



UNIVERSITAT POLITÈCNICA
DE CATALUNYA
BARCELONATECH

Sag effects on protection system in distributed generation grids

Mostafa Bakkar

ADVERTIMENT La consulta d'aquesta tesi queda condicionada a l'acceptació de les següents condicions d'ús: La difusió d'aquesta tesi per mitjà del repositori institucional UPCommons (<http://upcommons.upc.edu/tesis>) i el repositori cooperatiu TDX (<http://www.tdx.cat/>) ha estat autoritzada pels titulars dels drets de propietat intel·lectual **únicament per a usos privats** emmarcats en activitats d'investigació i docència. No s'autoritza la seva reproducció amb finalitats de lucre ni la seva difusió i posada a disposició des d'un lloc aliè al servei UPCommons o TDX. No s'autoritza la presentació del seu contingut en una finestra o marc aliè a UPCommons (*framing*). Aquesta reserva de drets afecta tant al resum de presentació de la tesi com als seus continguts. En la utilització o cita de parts de la tesi és obligat indicar el nom de la persona autora.

ADVERTENCIA La consulta de esta tesis queda condicionada a la aceptación de las siguientes condiciones de uso: La difusión de esta tesis por medio del repositorio institucional UPCommons (<http://upcommons.upc.edu/tesis>) y el repositorio cooperativo TDR (<http://www.tdx.cat/?locale-attribute=es>) ha sido autorizada por los titulares de los derechos de propiedad intelectual **únicamente para usos privados enmarcados** en actividades de investigación y docencia. No se autoriza su reproducción con finalidades de lucro ni su difusión y puesta a disposición desde un sitio ajeno al servicio UPCommons No se autoriza la presentación de su contenido en una ventana o marco ajeno a UPCommons (*framing*). Esta reserva de derechos afecta tanto al resumen de presentación de la tesis como a sus contenidos. En la utilización o cita de partes de la tesis es obligado indicar el nombre de la persona autora.

WARNING On having consulted this thesis you're accepting the following use conditions: Spreading this thesis by the institutional repository UPCommons (<http://upcommons.upc.edu/tesis>) and the cooperative repository TDX (<http://www.tdx.cat/?locale-attribute=en>) has been authorized by the titular of the intellectual property rights **only for private uses** placed in investigation and teaching activities. Reproduction with lucrative aims is not authorized neither its spreading nor availability from a site foreign to the UPCommons service. Introducing its content in a window or frame foreign to the UPCommons service is not authorized (*framing*). These rights affect to the presentation summary of the thesis as well as to its contents. In the using or citation of parts of the thesis it's obliged to indicate the name of the author.



DEPARTAMENT D'ENGINYERIA
ELÈCTRICA



UNIVERSITAT POLITÈCNICA DE
CATALUNYA

SAG EFFECTS ON PROTECTION SYSTEM IN DISTRIBUTED GENERATION GRIDS

Doctoral Thesis

Author: Mostafa Ahmed Ahmed Mahmoud Ahmed Bakkar

Directors: Santiago Bogarra, Felipe Córcoles

Electrical Engineering Department (DEE)

Thesis presented to obtain the degree of doctorate
Polytechnic University of Catalonia (UPC)
Escuela Superior de Ingenierías Industrial, Aeroespacial y Audiovisual de
Terrassa (ESEIAAT)
Terrassa, December 2021

<u>Table of Contents</u>		<u>Page</u>
Acknowledgment.....		i
Abstract		iii
Table of contents.....		vi
List of figures		xi
List of tables		xxii
List of symbols		xxv
List of abbreviations		xxix
CHAPTER 1	Introduction	1
	1.1. Overview.....	1
	1.2. DG techniques	5
	1.3. Protective devices	5
	1.4. Motivation	7
	1.5. Thesis Objectives	7
	1.6. Thesis Outline	8
CHAPTER 2	State of the art of DG penetration impact on MV DS protection systems.....	10
	2.1. DGs impact on MV distribution grid.....	10
	2.1.1. Impact of fault ride-through requirements.....	10
	2.1.2. Impact of DG on MV distribution grid protection.....	10
	2.2. State of the art.....	12
	2.2.1. State of the art on the reference current control strategies of VSI during grid faults.....	12
	2.2.2. State of the art of the protection schemes of MV DS with DGs penetration.....	14
CHAPTER 3	Medium voltage distribution system construction, modeling, and analysis during faults with DG penetration	21
	3.1. Modeling of DS components	21
	3.2. Analysis of PV penetration impact on the DS behaviour	28
CHAPTER 4	Analysis of a three-phase grid-connected converter under voltage sags according to the Spanish grid code	35
	4.1. Spanish grid code P.0. 12.2 application with symmetrical and unsymmetrical sags	35
	4.2. Three-phase grid-connected inverter	37
	4.2.1. Reference current control strategies using <i>Park</i>	

	transformation.....	37
	4.2.2. Reference current control strategies in Ku transformation..	43
	4.3. Analysis and discussion.....	45
CHAPTER 5	Proposed fault protection scheme.....	58
	5.1. Introduction	58
	5.2. Conventional protections (OCR/DR).....	59
	5.3. Proposed fault protection algorithms.....	61
	5.3.1. Centralize control algorithm (CE).....	67
	5.3.2. Zone control algorithm (ZO).....	69
	5.3.3. Local control algorithm (LO).....	71
	5.3.3.1. Fault classification algorithm.....	72
	5.3.3.2. LO algorithm in case symmetrical and unsymmetrical faults and the MV side of the (HV/MV) transformer is not isolated.....	75
	5.3.3.3. LO algorithm in case of symmetrical and unsymmetrical faults and the MV side of the (HV/MV) transformer grounded through a zigzag.....	86
	5.3.4. PD priority strategy.....	93
CHAPTER 6	Analysis and test results of the proposed protection algorithms....	97
	6.1. Analytical and test results for CE, ZO, and LO protection algorithms.....	97
	6.1.1. CE-ZO protection algorithms.....	98
	6.1.2. LO protection algorithm.....	102
	6.2. Comparative study.....	117
CHAPTER 7	Experimental implementation and results.....	124
	7.1. Experimental implementation of the three-phase grid-connected converter.....	124
	7.1.1. Experimental implementation of the current control strategies.....	124
	7.2. Experimental implementation of the proposed protection algorithms.....	128
	7.2.1. Protection algorithms practical verification using dSPACETM and DSP.....	131
	7.2.2. Experimental implementation and verification of the proposed protection algorithms using the physical scaled grid.....	133
	7.2.2.1. Calculation of system parameters.....	134
	7.2.2.2. Experimental results discussion of the proposed	

	protection algorithms (CE, ZO, and LO)	136
	7.2.2.3. Simplified radial grid without DG.....	141
	7.2.2.4. Simplified radial grid with DG.....	144
	7.2.2.5. Complete radial grid without DG.....	147
	7.2.2.6. Complete radial grid with DG.....	152
	7.2.2.7. Complete ring grid without DG.....	158
	7.2.2.8. Complete ring grid with DG.....	166
CHAPTER 8	Conclusions and recommendation future work.....	176
	8.1. Conclusions.....	176
	8.2. Recommendation for future work.....	177
List of references	180
Appendix A	Analysis of the ring grid behaviour during faults.....	193
	A.1. System behaviour with isolated transformer and different types of faults.....	193
	A.2. Test the algorithm with different types of HV/MV Transformer configurations.....	195
	A.3. Examples for analysed ring grid with faults in different locations.	197
	A.4. The behaviour of the ring grid during fault and disconnection.....	202
Appendix B	Tested cases and simulation results.....	210
	B.1. Tested cases.....	210
	B.2. Results.....	214
	B.3. Demonstration of DPF in various grid scenarios.....	235
	B.4. ANN fault classification.....	244
Appendix C	Solid State Relay and Mechanical breaker demonstration.....	247
	C.1. Solid-state relay features.....	247
	C.2. Available topologies.....	248
	C.3. Evaluation of SSR response.....	248
	C.4. Troubleshooting.....	249
Appendix D	Experimental verification of the protection algorithms.....	253
	D.1. Total number of analysed cases.....	253
	D.2. Implementation on dSPACE.....	257
	D.3. Experimental results (Continue).....	268
Appendix E	Converter control.....	286
	E.1. Mathematical model of grid-connected inverter system in <i>Park</i> transformation.....	286
	E.2. Mathematical model of grid-connected inverter system in <i>Ku</i> transformation.....	291

E.3.	Relation between Ku and Park components.....	293
E.4.	Phase Lock Loop (PLL).....	298
E.5.	Modification of the current control strategy.....	299
Appendix F	Experimental setup.....	304
F.1.	System connection.....	304
Appendix G	Calculation of the system parameters and pu values.....	313
G.1.	Calculation of line parameters.....	313
G.2.	Calculation of zigzag impedance.....	314
G.3.	Calculation of fault resistance.....	314
G.4.	Calculation of pu values.....	315
Appendix H	Proposed MPPT technique during partial shading.....	318
H.1.	State of the art of the MPPT techniques during partial shading...	318
H.2.	Chopper control employing MPPT control.....	319
H.3.	MPPT employing adaptive FLC and DSM (practical Case Study)	324
H.4.	Mathematical inference of the MPPT under partial shading mode.....	327
List of publications.....		331

A. Appendix A

Analysis of the ring grid behaviour during faults

In this section, ring grid behaviour has been studied by simulation. Its behavior is analysed considering different fault types and locations. In the figures, the steady-state (S-S) conditions and fault conditions (F) are highlighted. In addition, the loads' consumption change has been considered for low and high values.

A.1. System behaviour with isolated transformer and different types of faults

➤ **Low load consumption with isolated MV transformer**

Fig. A.1 and Fig. A.2 show the behaviour of the system using positive, negative and zero values of voltages and currents during a single-phase to ground fault at DL3 and DL5, with low load consumption (L1= 0.5 MVAR; L2= 1 MVAR; L3= 2 MVAR; L4= 0.25 MVAR; L5= 2 MVAR). As seen, the values of the short-circuit currents are varied when the fault changes from DL3 to DL6. When the fault is at DL5, the short-circuit currents are higher as the impedance between the fault point and the grid is less when the fault is at DL3. Fig. A.3 shows the behaviour of the system during a three-phase fault.

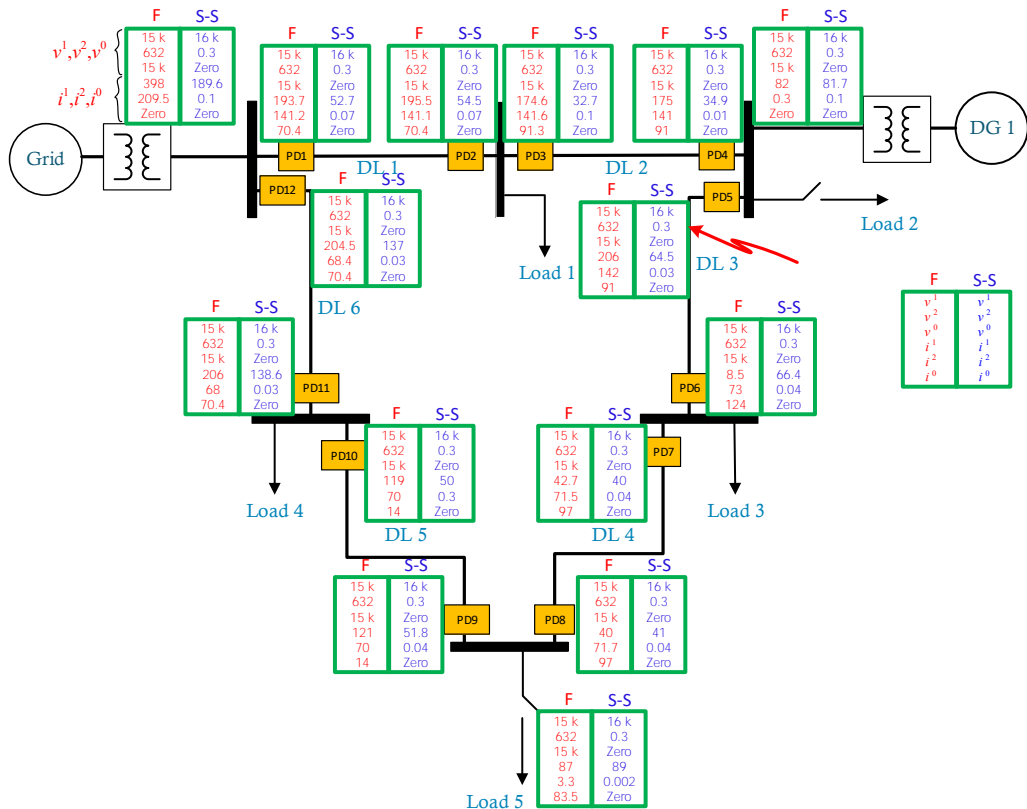


Fig. A.1 Single-phase to ground fault at DL3, when the secondary part of the MV transformer is isolated, and low load consumption

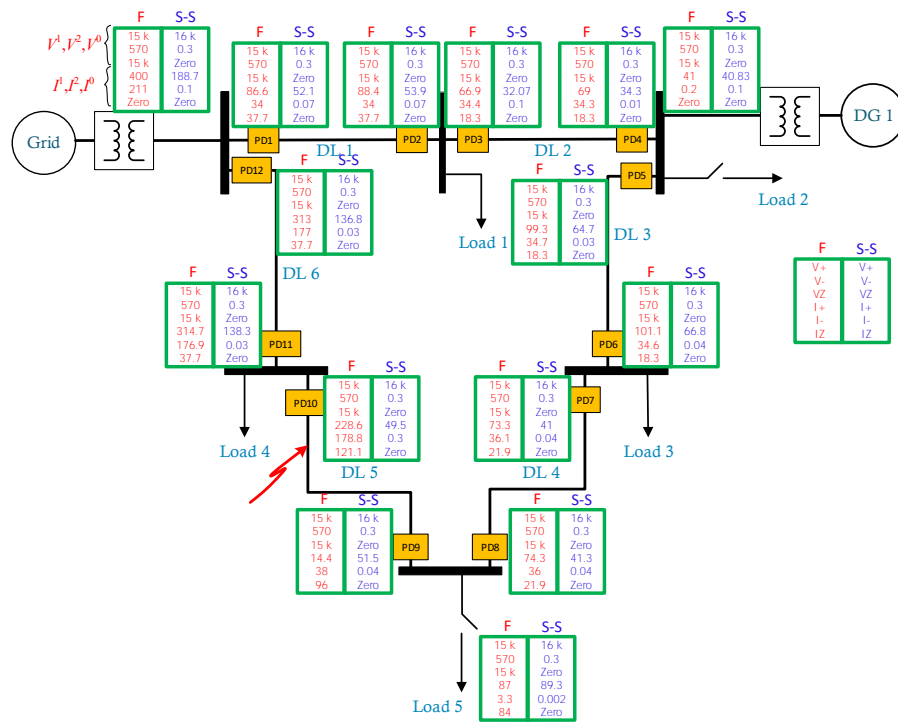


Fig. A.2 Single-phase to ground fault at DL6, when the secondary part of the MV transformer is isolated, and low load consumption

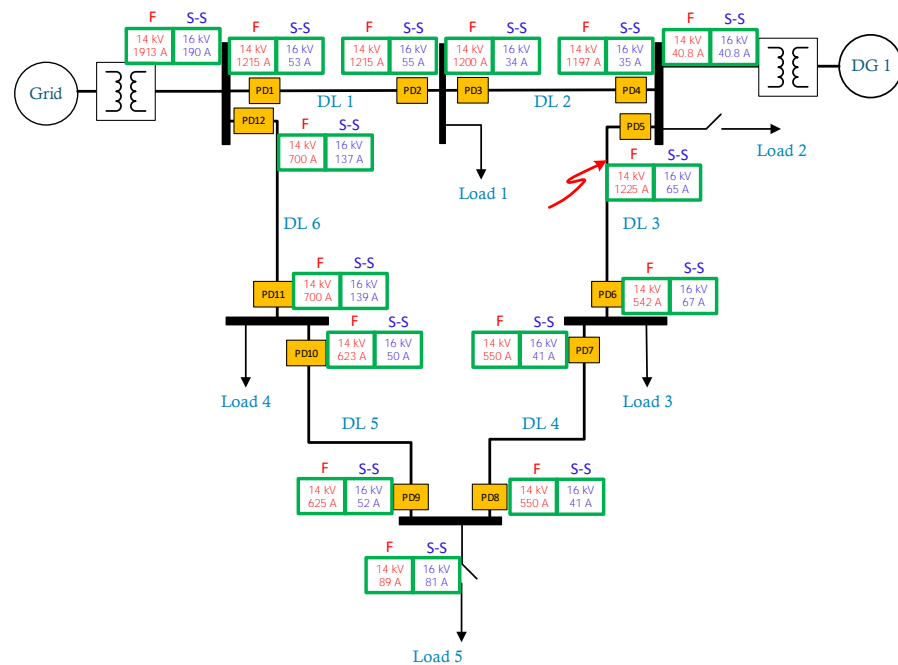


Fig. A.3 Three-phase to ground fault at DL6, when the secondary part of the MV transformer is isolated, and low load consumption

➤ **High load consumption with isolated MV transformer**

Fig. A.4 shows the behaviour of the system during a three-phase fault with high load consumption ($L1=10$ MVAR; $L2=5$ MVAR; $L3=4$ MVAR; $L4=2$ MVAR; $L5=1$ MVAR). As seen, the load consumption changes between low (Fig. A.3) and high (Fig. A.4) do not affect the short-circuit current values.

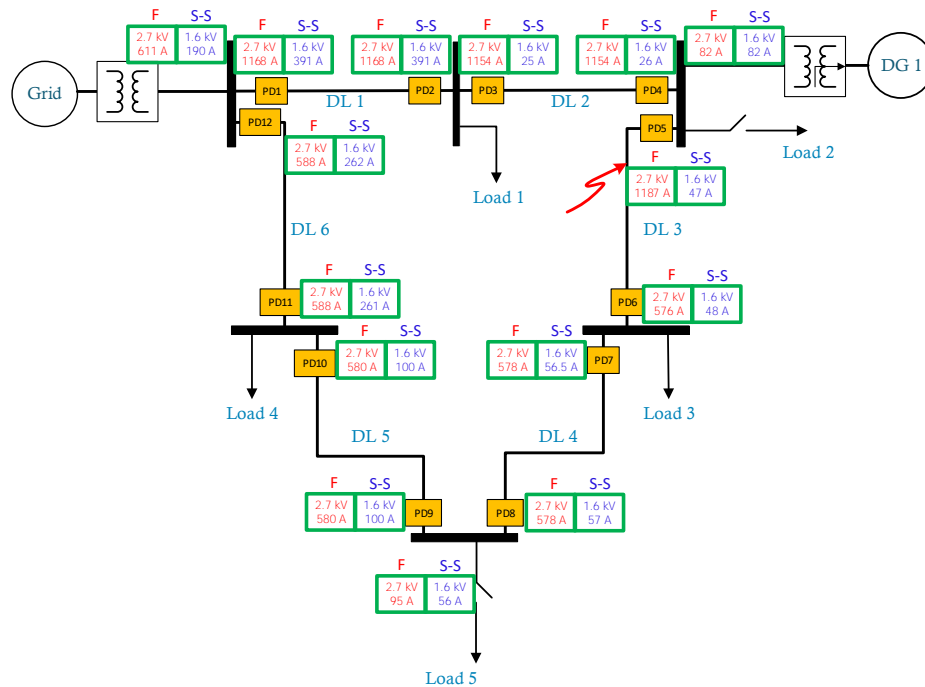


Fig. A.4 Three-phase fault at DL3, when the secondary part of the MV transformer is isolated, and high voltage consumption

A.2. System behaviour with different types of HV/MV transformer configurations

In this section, the grid behaviour is tested by changing the HV/MV transformer configuration, and the effects on the sequence voltages.

➤ **YNd11 transformer configuration**

In the case of a single-phase fault, the short-circuit current variations before and during the fault are minimal. So, this condition cannot be considered a fault, so there is no need for disconnection. Although, the single-phase fault can be recognized by using the fault classification algorithm.

The short-circuit currents of the other fault types (two-phase, two-phase to ground, and three-phase) are different from the single-phase fault because the fault currents have different paths, and the impedance of the zigzag transformer does not limit the fault current in these cases. Fig. A.5 shows the sequence voltages in the case of two-phase to ground fault with YNd11 transformer configuration.

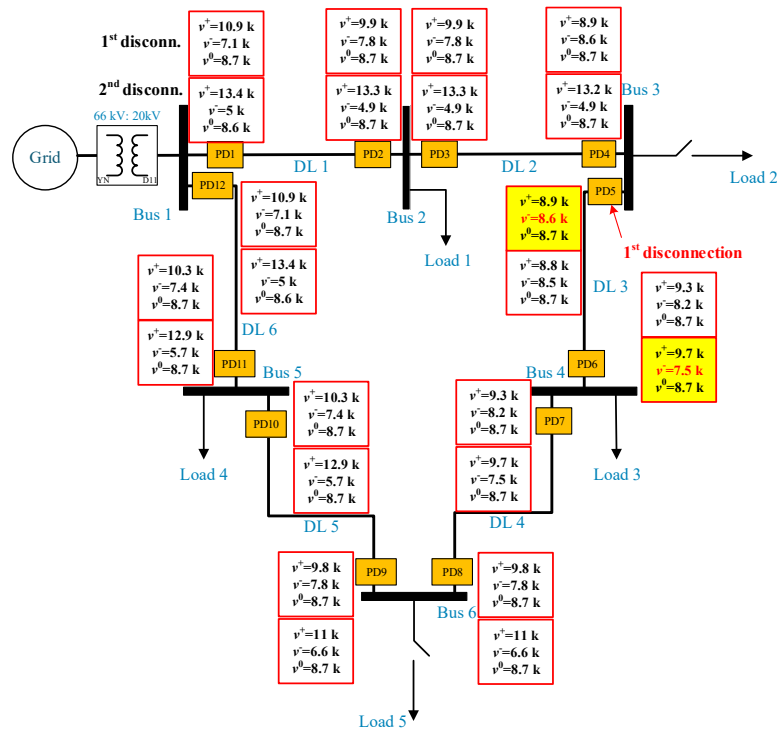


Fig. A.5 Two-phase to ground fault at DL3, $r = 0.1 \Omega$ (Transformer connection YNd11 “grounded”)

➤ **YNyn transformer configuration**

Fig. A.6 shows the values of the sequence voltages in the case of two-phase to ground fault with YNyn transformer configuration. As seen, the same conclusion as the YNd11 transformer configuration can be obtained.

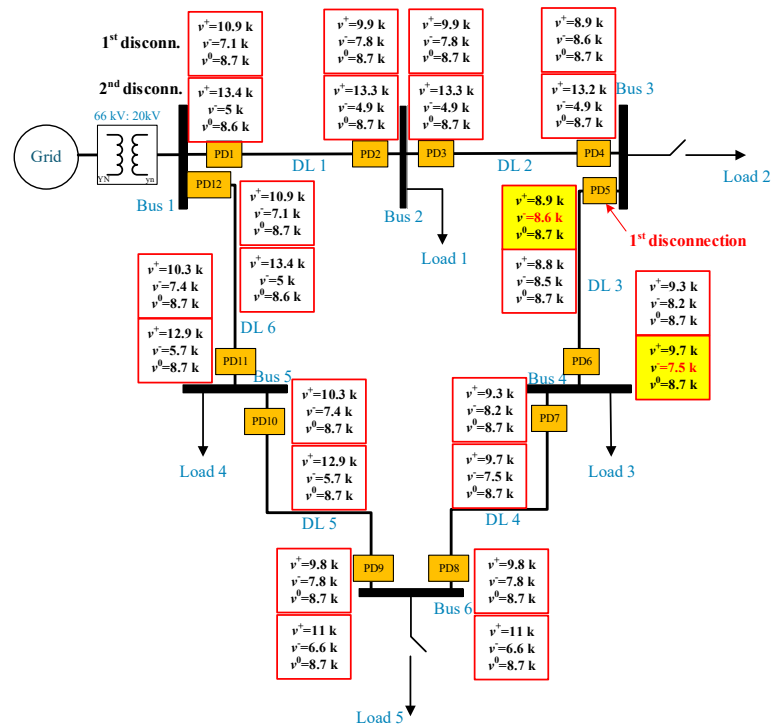


Fig. A.6 Two-phase to ground fault at DL3, $r = 0.1 \Omega$ (Transformer connection YNyn)

➤ YNyg grounded through resistor transformer configuration

In this case, the single-phase fault can be recognized using the sequence voltages, in the same way used in the case of the YNd11 with zigzag transformer. Fig. A.7 shows the positive, negative, and zero sequence voltages during a single-phase to ground fault at DL3 with transformer connection YNyg grounded through a resistor. For the first disconnection, the value of the negative-sequence voltage at PD5 is the highest, and after the second disconnection, the highest value of the negative-sequence voltage is at PD6.

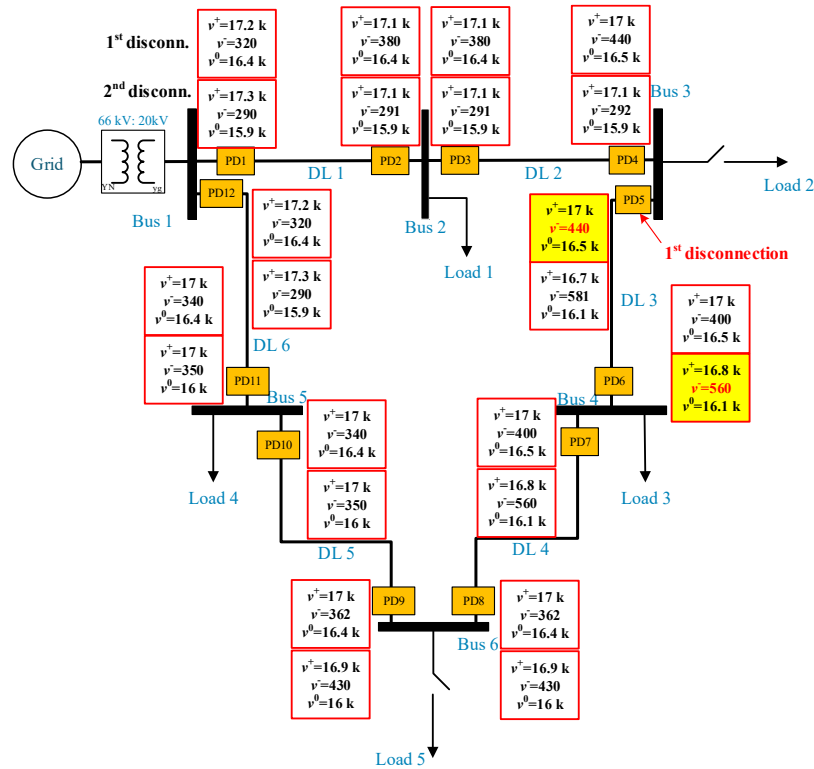


Fig. A.7 Single-phase to ground fault at DL3, $r = 0.1 \Omega$ (transformer connection YNyg grounded through a resistor)

A.3. Examples for analysed ring grid with faults in different locations

The following figures (Fig. A.8 ~ Fig. A.16) show the positive, negative, and zero sequence currents of the analysed ring grid when the MV transformer is grounded through a zigzag transformer. In order to study the analysed ring grid in different scenarios, the grid has been analysed during different faults types in different locations. Moreover, the fault resistance is changed, and the DGs penetrations have been considered in different locations.

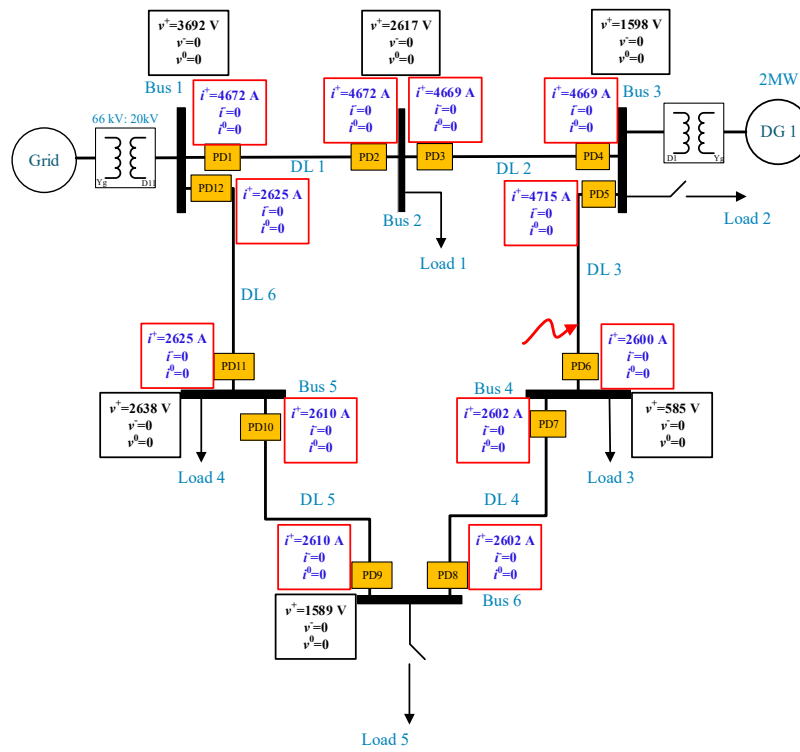


Fig. A.8 Short-circuit current during three-phase fault at DL3, with $r = 0.1 \Omega$ fault resistance

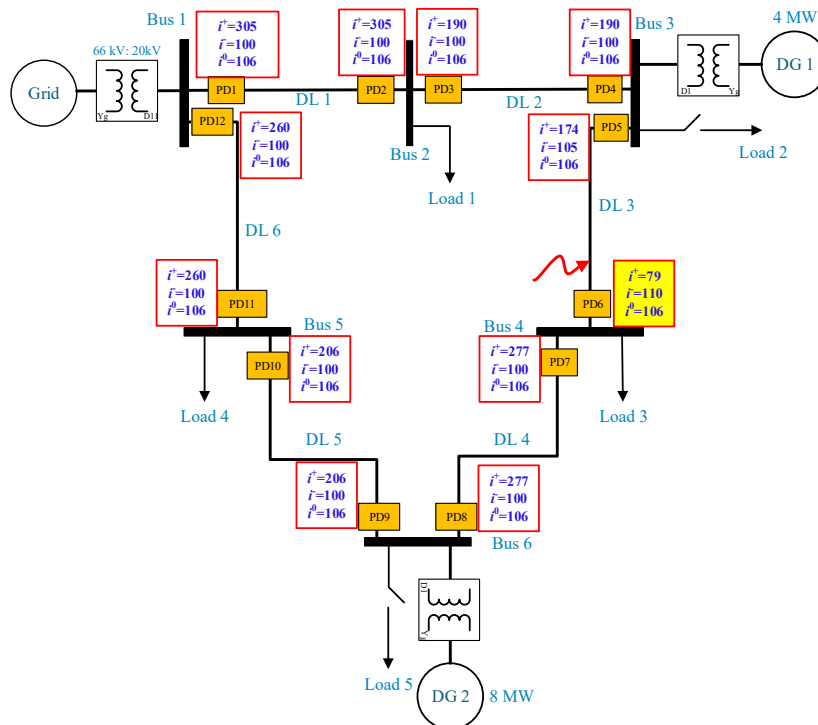


Fig. A.9 Short-circuit current during single-phase to ground fault at DL3, with $r = 0.1 \Omega$ fault resistance

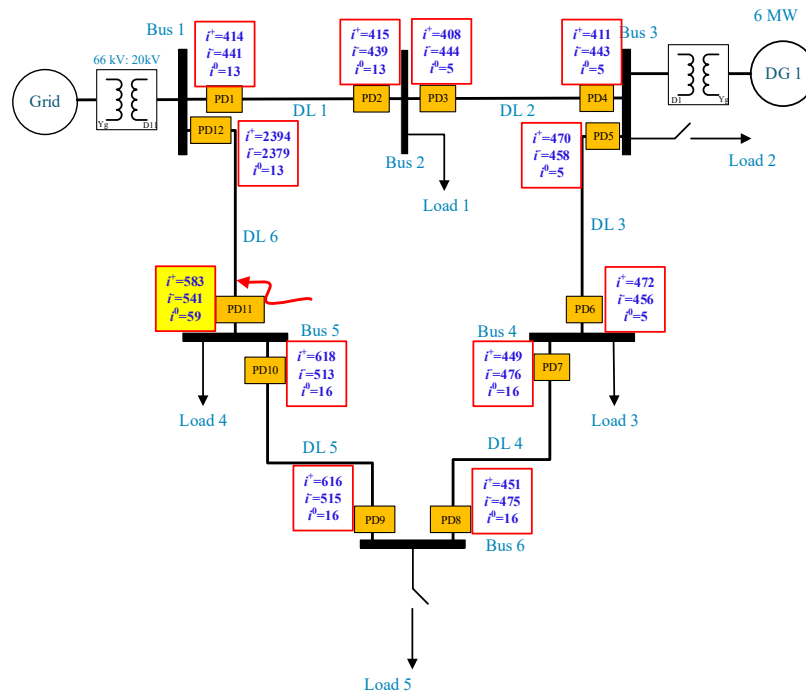


Fig. A.10 Short-circuit current during two-phase to ground fault at DL6, with $r=0.1 \Omega$ fault resistance

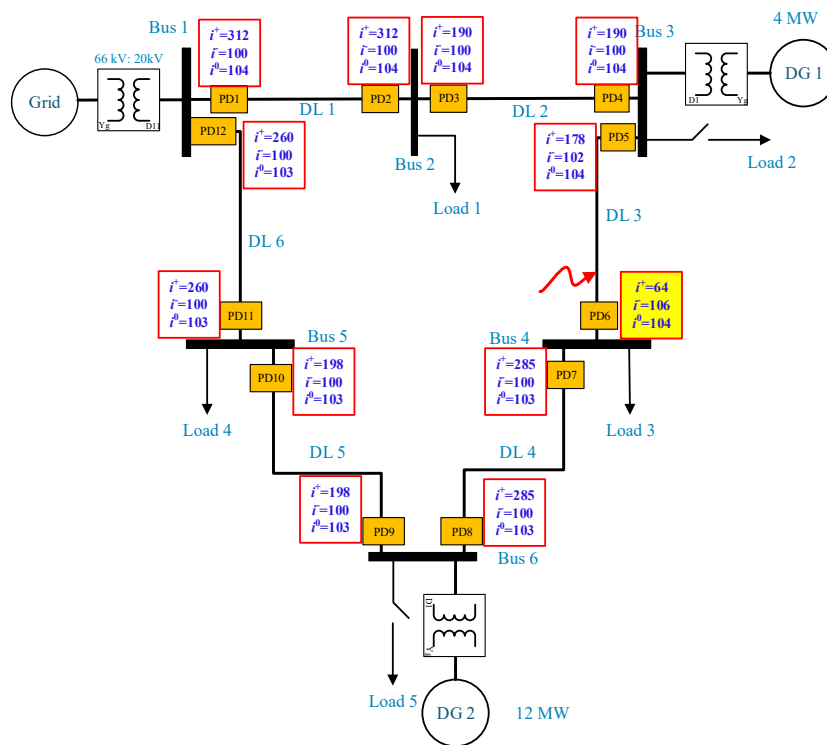


Fig. A.11 Short-circuit current during single-phase to ground fault at DL3, with $r = 4 \Omega$ fault resistance

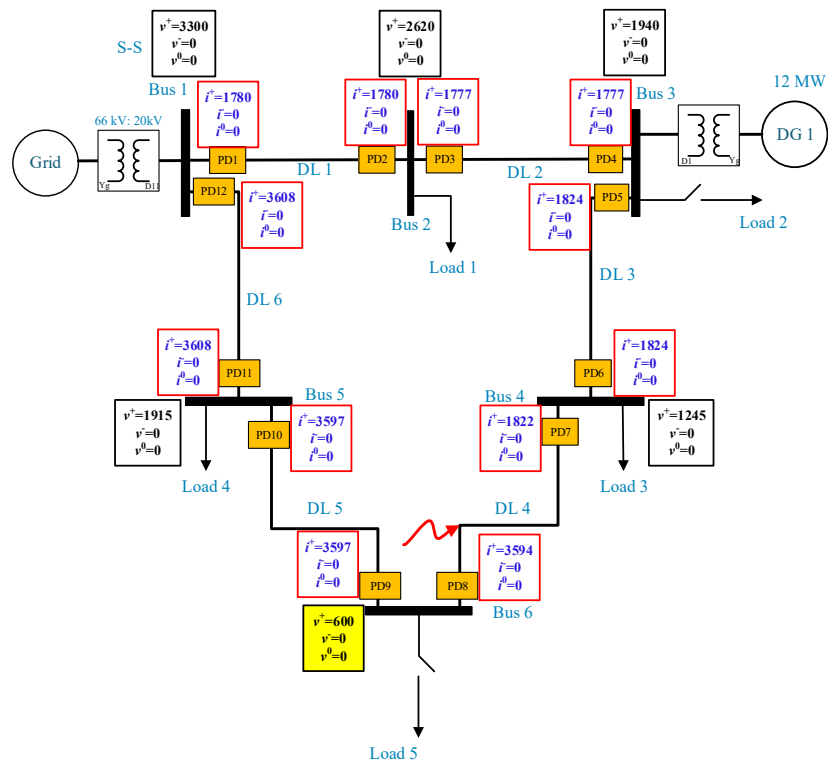


Fig. A.12 Short-circuit current during three-phase fault to ground at DL4, with $r = 0.1 \Omega$ fault resistance

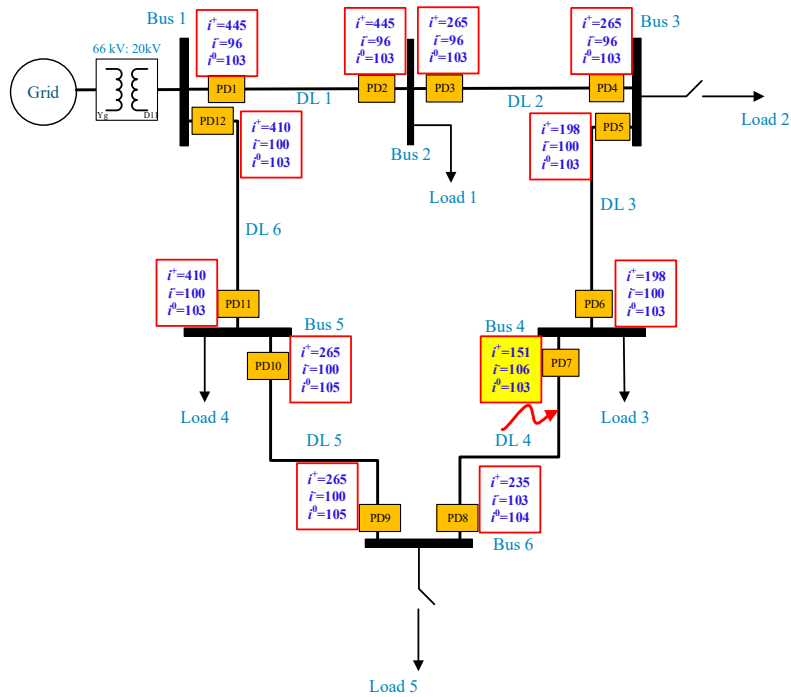


Fig. A.13 Short-circuit current during single-phase to ground fault at DL4, with $r = 0.1 \Omega$ fault resistance

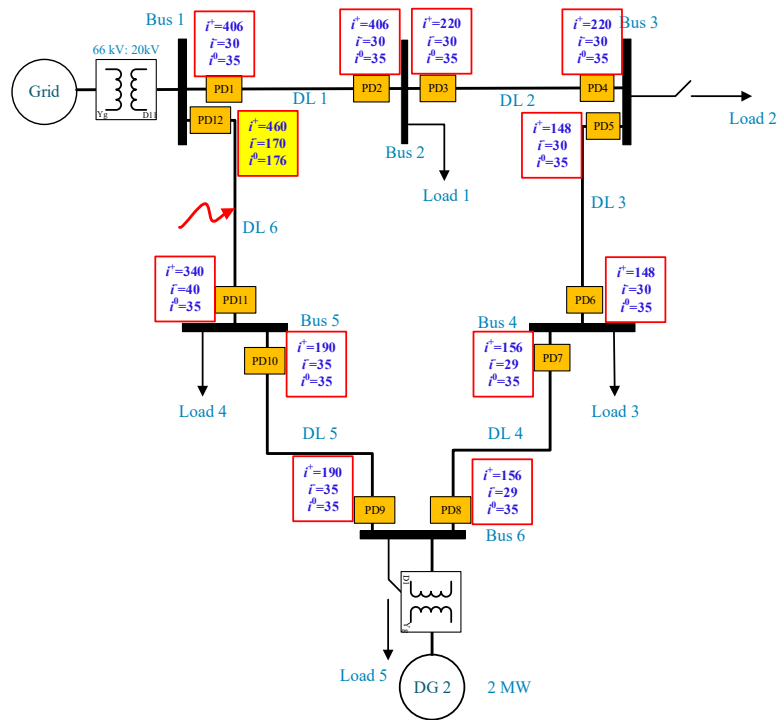


Fig. A.14 Short-circuit current during single-phase to ground fault at DL6, with $r=0.1 \Omega$ fault resistance

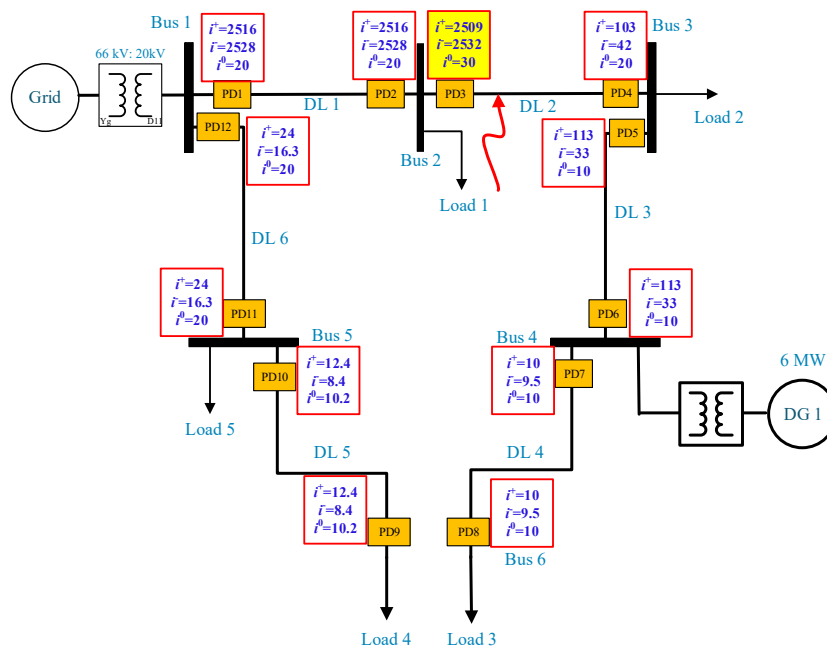


Fig. A.15 Short-circuit current during two-phase to ground fault at DL2, with $r =0.1 \Omega$ fault resistance

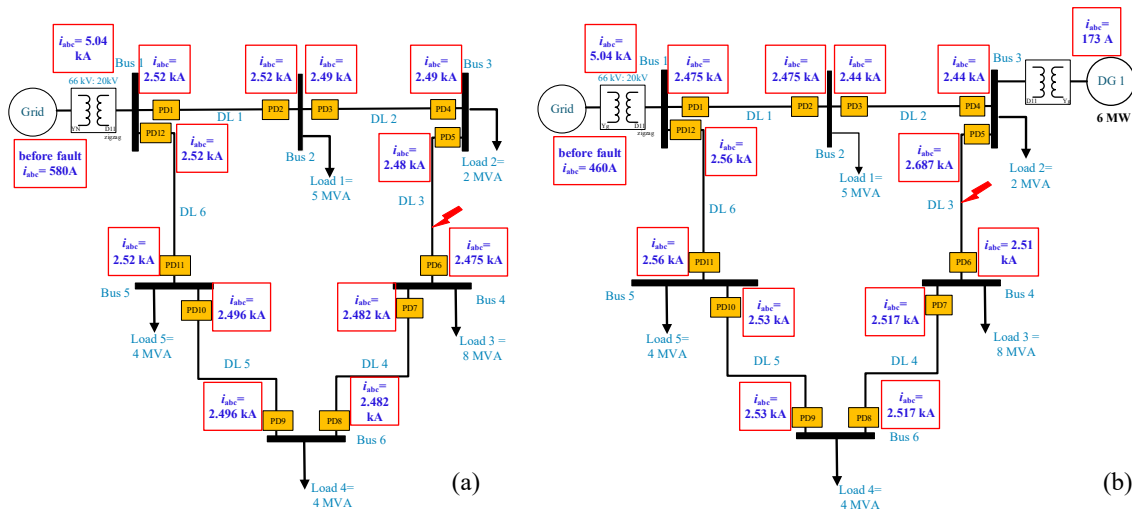


Fig. A.16 RMS short-circuit currents during three-phase fault at DL3, with $r = 0.1 \Omega$ (a) without DG (b) with DG penetration

Previous figures are obtained and studied to understand the effect of the DG penetration on the short-circuit faults with different types of faults in different locations.

A.4. The behaviour of the ring grid during fault and disconnection

In this part, the analysed ring grid is studied by analyzing the sequence voltages and currents before the first disconnection, after the first disconnection, and after the second disconnection. In the case of a single-phase fault, by using negative-sequence voltage during the fault (as mentioned in chapter 5), one end of the faulted line can be located. The negative-sequence voltage at one end of the faulted line is higher than any other zero-sequence value of other lines. Therefore, the highest value means faster disconnection.

The figures (Fig. A.17, Fig. A.18, Fig. A.19, Fig. A.21, Fig. A.22, Fig. A.23, Fig. A.25, Fig. A.26, Fig. A.27, and Fig. A.28) show that during unsymmetrical faults, the negative-sequence voltage is the highest value at one end of the line near the fault. Then, after the first disconnection, the negative-sequence voltage at the other end of the faulted line is the highest value; so, using this criterion and the definite-time curve, the disconnection of the faulted line can be achieved. The same idea can be used with symmetrical faults (Fig. A.20 and Fig. A.24) but with the positive-sequence voltage and the definite-time curve (as mentioned in chapter 5).

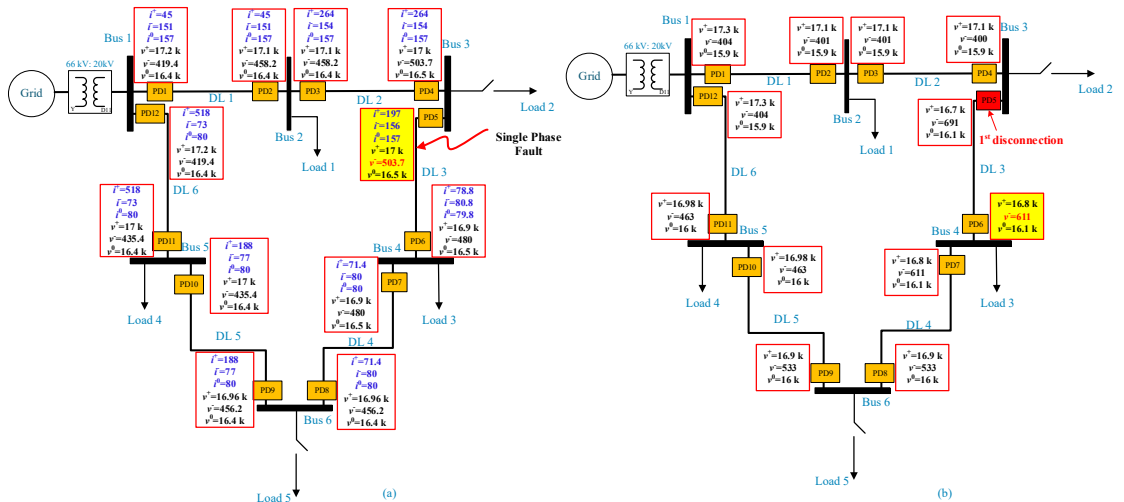


Fig. A.17 Single-phase to ground fault at DL3, $r=0.1 \Omega$ (Transformer connection YNd11 zigzag) (a) before disconnection, (b) after 1st disconnection

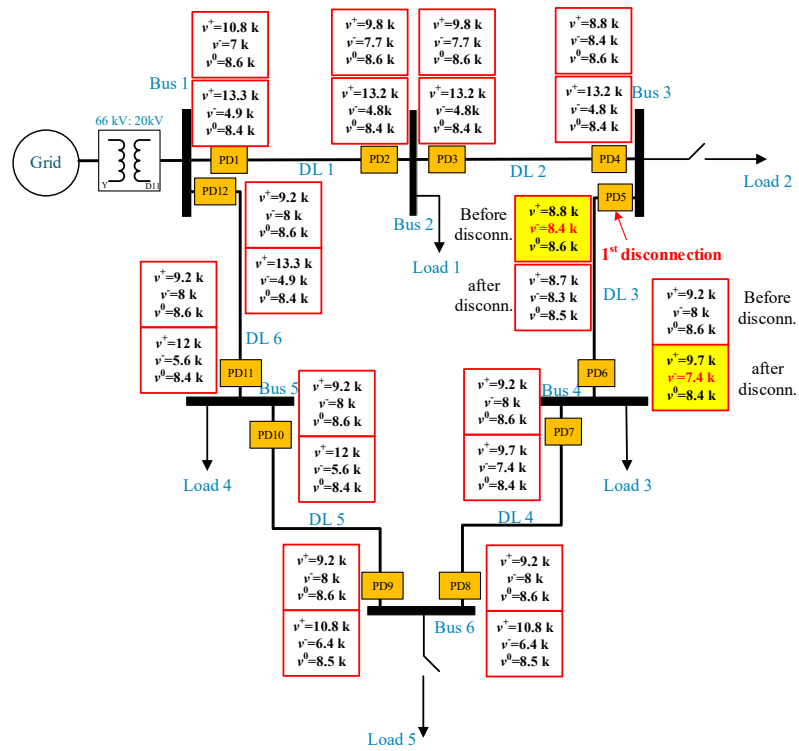


Fig. A.18 Two-phase to ground fault at DL3, $r=0.1 \Omega$ (Transformer connection YNd11 zigzag)

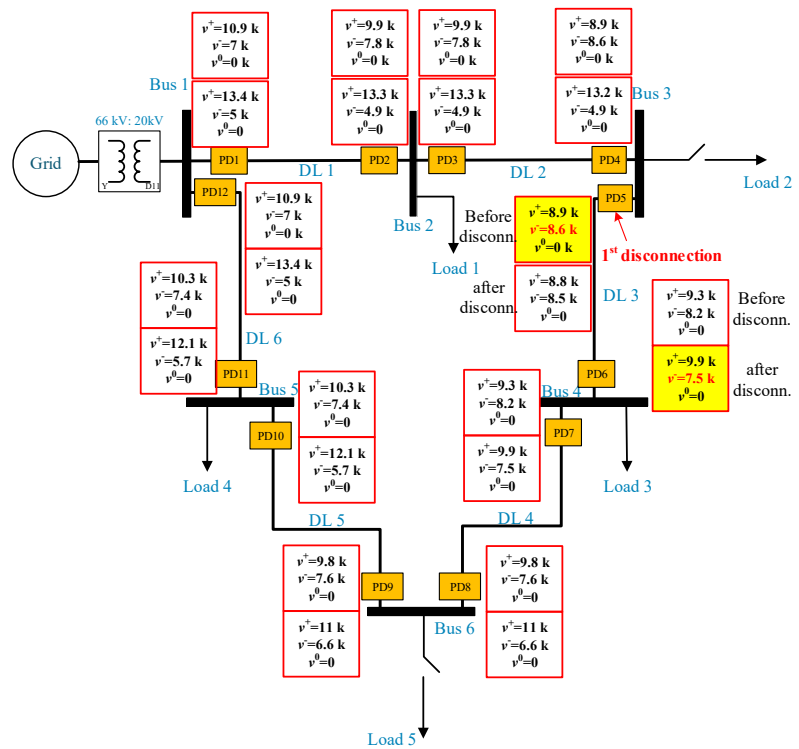


Fig. A.19 Two-phase fault at DL3, $r=0.1 \Omega$ (Transformer connection YNd11 zigzag)

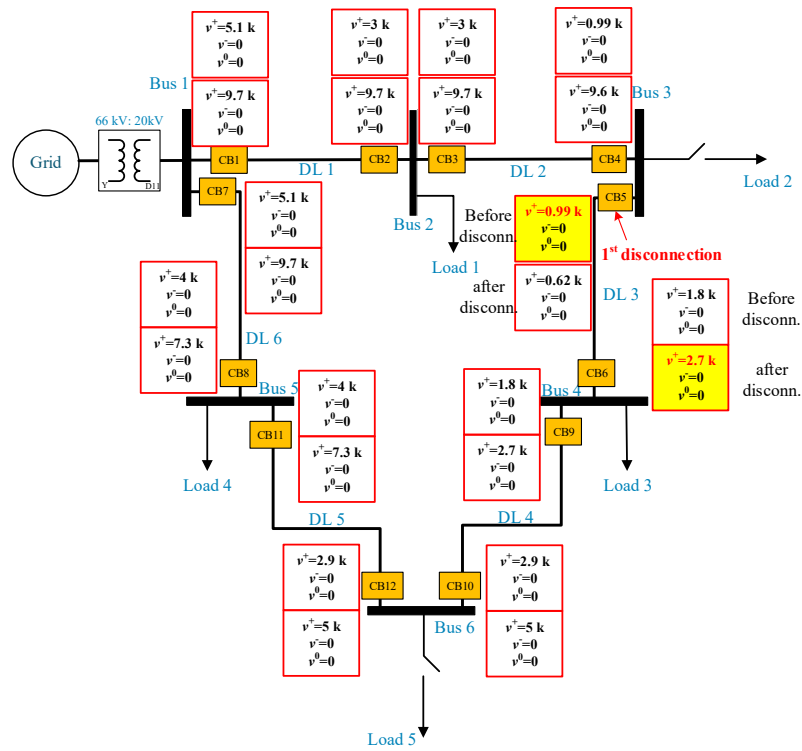


Fig. A.20 Three-phase to ground fault at DL3, $r=0.1 \Omega$ (Transformer connection YNd11 zigzag)

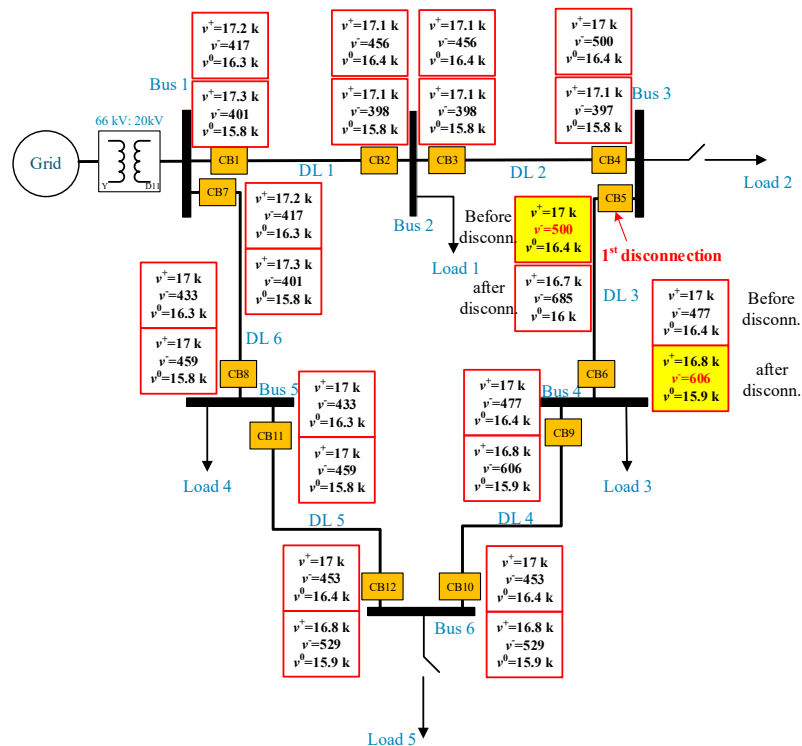


Fig. A.21 Single-phase to ground fault at DL3, $r=2 \Omega$ (Transformer connection YNd11 zigzag)

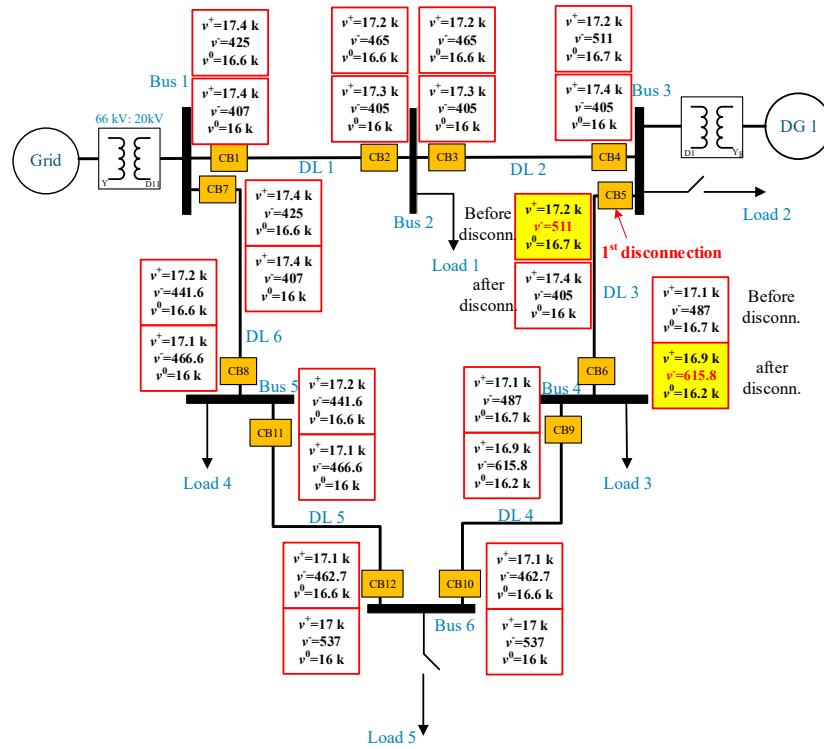


Fig. A.22 Single-phase to ground fault at DL3, $r=0.1 \Omega$ with one DG (Transformer connection YNd11 zigzag)

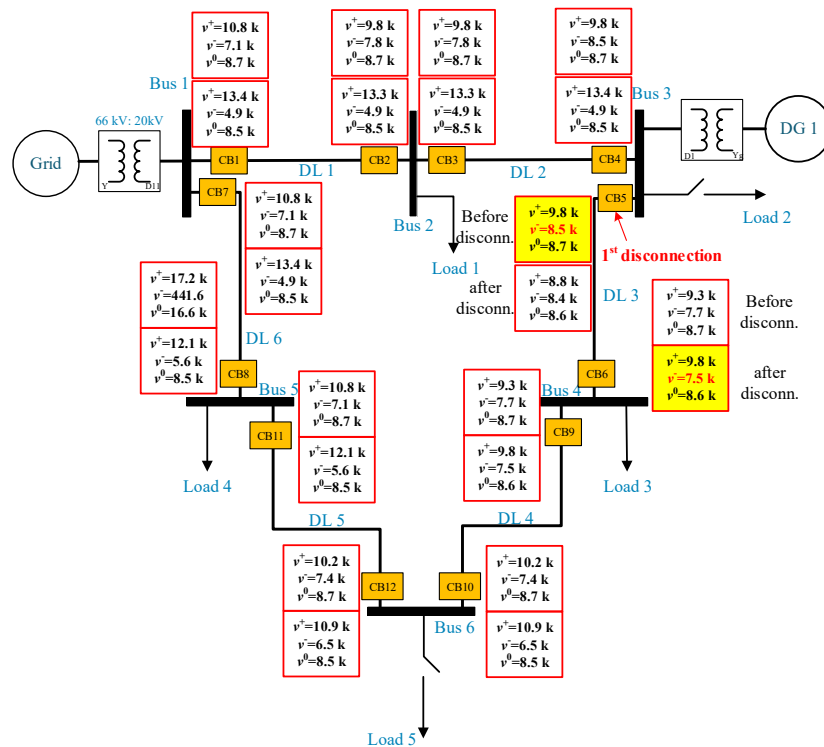


Fig. A.23 Two-phase to ground fault at DL3, $r=0.1 \Omega$ with one DG (Transformer connection YNd11 zigzag)

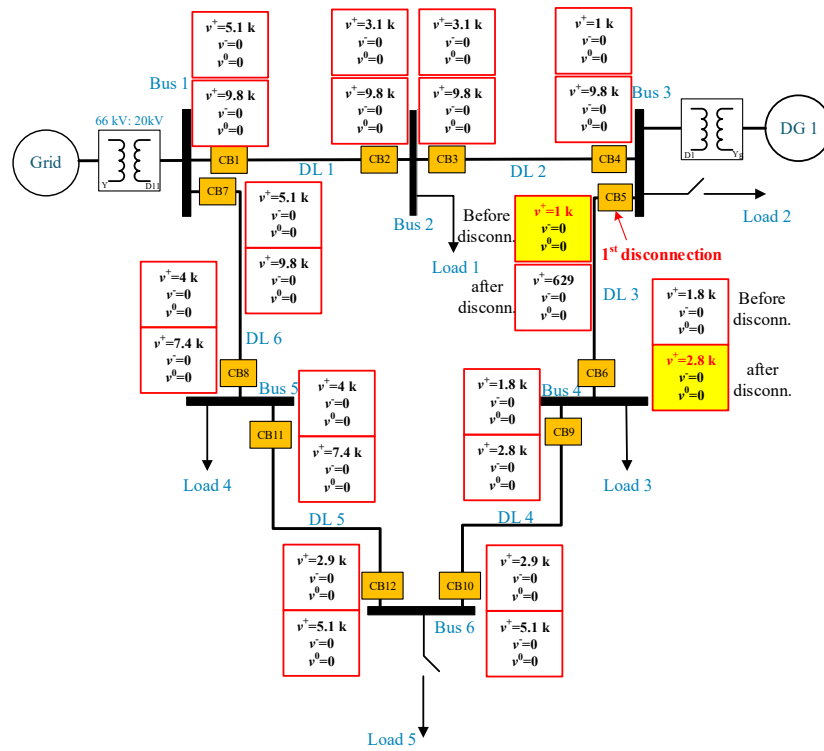


Fig. A.24 Three-phase to ground fault at DL3, $r=0.1 \Omega$ with one DG (Transformer connection YNd11 zigzag)

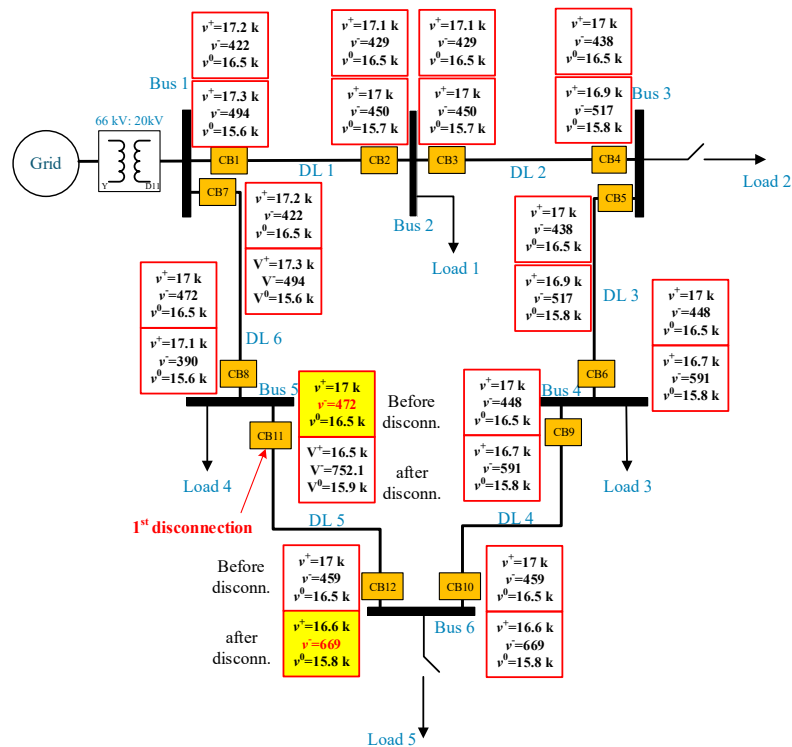


Fig. A.25 Single-phase to ground fault at DL5, $r=0.1 \Omega$ (Transformer connection YNd11 zigzag)

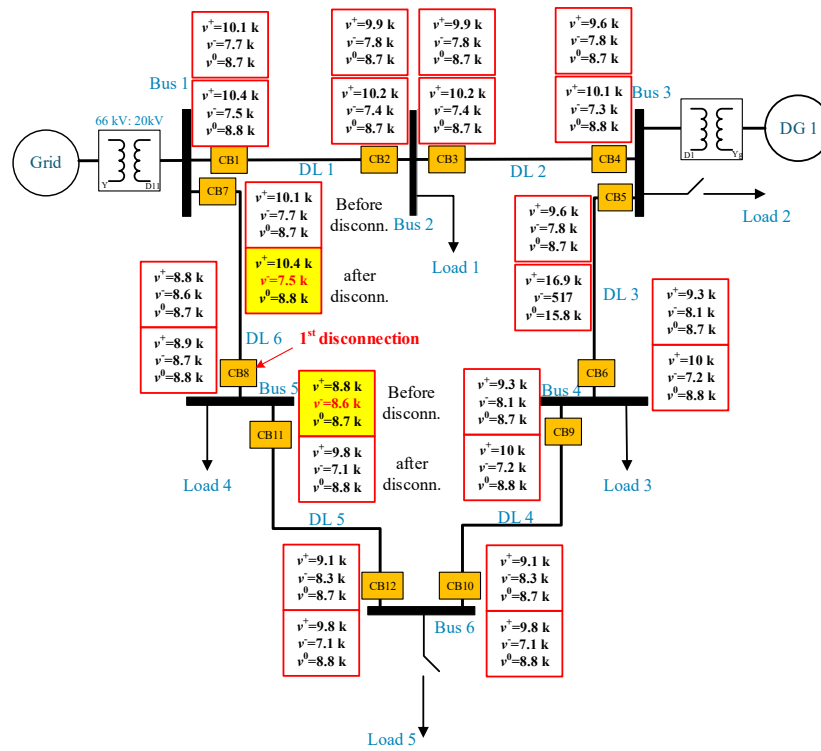


Fig. A.26 Two-phase to ground fault at DL6, $r=0.1 \Omega$ with one DG (Transformer connection YNd11 zigzag)

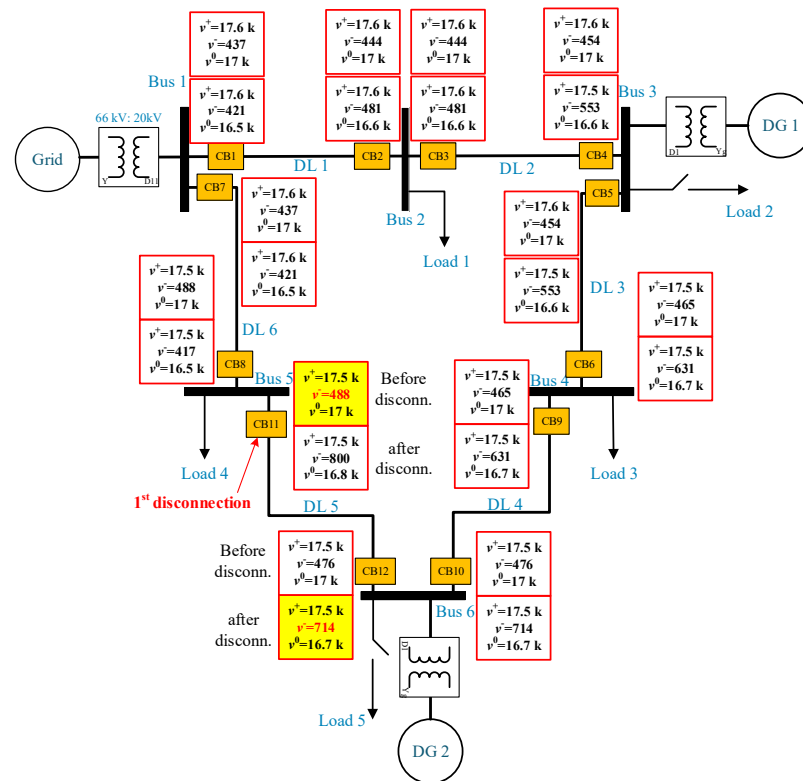


Fig. A.27 Single-phase to ground fault at DL5, $r=0.1 \Omega$ with two DG (Transformer connection YNd11 zigzag)

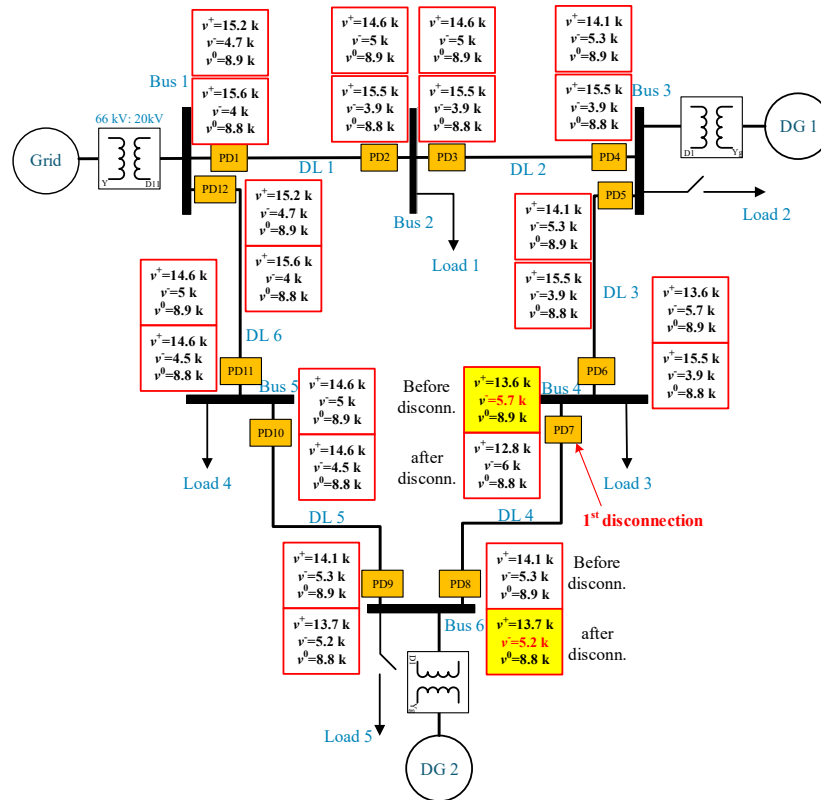


Fig. A.28 Two-phase to ground fault at DL4, $r = 2 \Omega$ with two DG (Transformer connection YNd11 zigzag)

B. Appendix B

Tested cases and simulation results

The tested cases used to validate the algorithms and the simulation results are presented in this section.

B.1. Tested cases

Table B.1 and Table B.2 show the number of cases taken into account to train the ANN fault location algorithm. In order to train this system, the number of cases and number of possibilities must be identified first as seen below.

Table B.1 number of cases considering fault resistance

No. of generators	Fault type	Fault resistance		Load changes														
		$r = 0.1$ Ω	$r = 8$ Ω	L1 (MW)			L2 (MW)			L3 (MW)			L4 (MW)			L5 (MW)		
DG1 = 0, DG2 = 0	AG	X	X	0.5	5	10	1	1	5	2	4	4	0.25	3	2	2	2	1
	BG	X	X	0.5	5	10	1	1	5	2	4	4	0.25	3	2	2	2	1
	CG	X	X	0.5	5	10	1	1	5	2	4	4	0.25	3	2	2	2	1
	ABG	X	X	0.5	5	10	1	1	5	2	4	4	0.25	3	2	2	2	1
	BCG	X	X	0.5	5	10	1	1	5	2	4	4	0.25	3	2	2	2	1
	CAG	X	X	0.5	5	10	1	1	5	2	4	4	0.25	3	2	2	2	1
	AB	X	X	0.5	5	10	1	1	5	2	4	4	0.25	3	2	2	2	1
	BC	X	X	0.5	5	10	1	1	5	2	4	4	0.25	3	2	2	2	1
	CA	X	X	0.5	5	10	1	1	5	2	4	4	0.25	3	2	2	2	1
	ABC	X	X	0.5	5	10	1	1	5	2	4	4	0.25	3	2	2	2	1
DG1 = 1, DG2 = 0	AG	X	X	Same changes as before														
	BG	X	X															
	CG	X	X															
	ABG	X	X															
	BCG	X	X															
	CAG	X	X															
	AB	X	X															

Table B.1 Cont'd

	BC	X	X	
	CA	X	X	
	ABC	X	X	
DG1 = 0, DG2 = 1	AG	X	X	Same changes as before
	BG	X	X	
	CG	X	X	
	ABG	X	X	
	BCG	X	X	
	CAG	X	X	
	AB	X	X	
	BC	X	X	
	CA	X	X	
	ABC	X	X	
DG1 = 3.5 DG2 = 0	AG	X	X	Same changes as before
	BG	X	X	
	CG	X	X	
	ABG	X	X	
	BCG	X	X	
	CAG	X	X	
	AB	X	X	
	BC	X	X	
	CA	X	X	
	ABC	X	X	
DG1 = 0,	AG	X	X	Same changes as before
	BG	X	X	
	CG	X	X	
	ABG	X	X	
	BCG	X	X	

Table B.1 Cont'd

DG2 = 3.5	CAG	X	X	
	AB	X	X	
	BC	X	X	
	CA	X	X	
	ABC	X	X	
DG1 = 1, DG2 = 3.5	AG	X	X	Same changes as before
	BG	X	X	
	CG	X	X	
	ABG	X	X	
	BCG	X	X	
	CAG	X	X	
	AB	X	X	
	BC	X	X	
	CA	X	X	
	ABC	X	X	
DG1 = 3.5 DG2 = 1	AG	X	X	Same changes as before
	BG	X	X	
	CG	X	X	
	ABG	X	X	
	BCG	X	X	
	CAG	X	X	
	AB	X	X	
	BC	X	X	
	CA	X	X	
	ABC	X	X	

Table B.2 Total number of cases

#	Number of lines	Generation unit	Loads	Contribution of DG	Load changes (Low – high)	Fault resistance (0.01 - 6) Ω	Fault location (1 - 6)
1	DL1	Grid (G)	L1		X	X	
2	DL1, DL2	G, DG1	L1	X	X	X	X
3	DL1, DL2	G	L1, L4		X	X	X
4	DL4	G	L3		X	X	
5	DL4, DL6	G, DG2	L3	X	X	X	X
6	DL4, DL6	G	L3, L5		X	X	X
7	DL1, DL2, DL3	G	L1, L2, L4		X	X	X
8	DL1, DL2, DL3	G, DG1	L1, L2	X	X	X	X
9	DL1, DL2, DL3, DL5	G	L1, L2, L4, L5		X	X	X
10	DL1, DL2, DL3, DL5	G, DG1	L1, L2, L5	X	X	X	X
11	DL1, DL2, DL3, DL5	G, DG2	L1, L2, L4	X	X	X	X
12	DL1, DL2, DL3, DL5	G, DG1, DG2	L1, L2	X	X	X	X
13	DL1, DL2, DL4	G	L1, L3, L4		X	X	X
14	DL1, DL2, DL4	G, DG1	L1, L3	X	X	X	X
15	DL1, DL2, DL3, DL4	G	L1, L2, L3, L4		X	X	X
16	DL1, DL2, DL3, DL4	G, DG1	L1, L2, L3	X	X	X	X
17	DL1, DL2, DL4, DL6	G	L1, L2, L3, L4, L5		X	X	X
18	DL1, DL2, DL4, DL6	G, DG1	L1, L2, L3, L5	X	X	X	X
19	DL1, DL2, DL4, DL6	G, DG2	L1, L2, L3, L4	X	X	X	X
20	DL1, DL2, DL4, DL6	G, DG1, DG2	L1, L2, L3	X	X	X	X
21	DL1, DL2, DL3, DL4, DL6	G	L1, L2, L3, L4, L5		X	X	X
22	DL1, DL2, DL3, DL4, DL6	G, DG1	L1, L2, L3, L5	X	X	X	X
23	DL1, DL2, DL3, DL4, DL6	G, DG2	L1, L2, L3	X	X	X	X
24	DL1, DL2, DL3, DL4, DL5, DL6	G, DG1, DG2	L1, L2, L3, L4, L5	X	X	X	X
25	DL1, DL2, DL3, DL4, DL5, DL6	G	L1, L2, L3, L4, L5		X	X	X

Table B.2 Cont'd

26	DL1, DL2, DL3, DL4, DL5, DL6	G, DG1	L1, L2, L3, L5	X	X	X	X
27	DL1, DL2, DL3, DL4, DL5, DL6	G, DG2	L1, L2, L3, L4	X	X	X	X
28	DL1,DL2, DL3,DL4, DL5, DL6	G, DG1, DG2	L1, L2, L3	X	X	X	X
29	DL1,DL2, DL3,DL4, DL5	G	L1, L2, L3, L4, L5		X	X	X
30	DL1,DL2, DL3,DL4, DL5	G, DG1	L1, L2, L3, L5	X	X	X	X
31	DL1,DL2, DL3,DL4, DL5	G, DG2	L1, L2, L3, L4	X	X	X	X
32	DL1,DL2, DL3,DL4, DL5	G, DG1, DG2	L1, L2, L3	X	X	X	X
33	DL1,DL2, DL4,DL5, DL6	G	L1, L2, L3, L4, L5		X	X	X
34	DL1,DL2, DL4,DL5, DL6	G, DG1	L1, L2, L3, L5	X	X	X	X
35	DL1,DL2, DL4,DL5, DL6	G, DG1	L1, L2, L3, L4	X	X	X	X
36	DL1,DL2, DL4,DL5, DL6	G, DG1, DG2	L1, L2, L3	X	X	X	X
37	DL1,DL2, DL3,DL5, DL6	G	L1, L2, L3, L4, L5		X	X	X
38	DL1,DL2,DL3, DL5, DL6	G, DG1	L1, L2, L3, L5	X	X	X	X
39	DL1, DL2, DL3, DL5, DL6	G, DG2	L1, L2, L3, L4	X	X	X	X
40	DL1, DL2, DL3, DL5, DL6	G, DG1, DG2	L1, L2, L3	X	X	X	X

X – refer to do not care logic (can be different values).

B.2. Results

In the next part, the results of the fault classification and location algorithms will be presented. Table B.3 shows the results of the fault classification algorithms under some operation conditions, and Table B.4 shows the results of the cases used to verify the CE algorithm.

Table B.3 Fault identifier results for some operation conditions

Fault type	Fault location	Fault resistance	Number of DG	Contribution of DG	Load changes	Fault identifier decision
AG	DL1	0.1 Ω	None	Zero	L1 = 0.5 MVA, L2 = 0.25 MVA, L3 = 1 MVA, L4 = 2 MVA, L5 = 1 MVA	1
AG	DL6	0.1 Ω	1	2 MW	L1 = 2 MVA, L3 = 1 MVA, L4 = 4 MVA, L5 = 0.5 MVA	1
AG	DL3	6 Ω	2	2 MW 2 MW	L1 = 2 MVA, L3 = 4 MVA, L4 = 0.5 MVA,	1
BG	DL2	4 Ω	None	Zero	L1 = 1 MVA, L2 = 0.25 MVA, L3 = 4 MVA, L4 = 2 MVA, L5 = 1 MVA	2
BG	DL3	3 Ω	1	1 MW	L1 = 0.5 MVA, L3 = 2 MVA, L4 = 3 MVA, L5 = 1 MVA	2
BG	DL1	0.1 Ω	2	1 MW 2 MW	L1 = 4 MVA, L3 = 1 MVA, L4 = 2 MVA,	2
CG	DL5	1 Ω	None	Zero	L1 = 1 MVA, L2 = 0.25 MVA, L3 = 4 MVA, L4 = 2 MVA, L5 = 1 MVA	3
CG	DL2	4.5 Ω	1	3 MW	L1 = 1 MVA, L3 = 0.5 MVA, L4 = 4 MVA, L5 = 0.25 MVA	3
CG	DL5	0.5 Ω	2	3 MW 2 MW	L1 = 2 MVA, L3 = 0.5 MVA, L4 = 4 MVA,	3
AB	DL2	6 Ω	None	Zero	L1 = 4 MVA, L2 = 0.25 MVA, L3 = 2 MVA, L4 = 3 MVA, L5 = 1 MVA	4
AB	DL3	0.6 Ω	1	1 MW	L1 = 2 MVA, L3 = 2 MVA, L4 = 3 MVA, L5 = 0.5 MVA	4
AB	DL1	0.4 Ω	2	1 MW 2 MW	L1 = 5 MVA, L3 = 1 MVA, L4 = 0.5 MVA,	4

Table B.3 Cont'd

BC	DL5	6 Ω	None	Zero	L1 = 1 MVA, L2 = 0.25 MVA, L3 = 4 MVA, L4 = 2 MVA, L5 = 1 MVA	5
BC	DL4	5 Ω	1	5 MW	L1 = 3 MVA, L3 = 3 MVA, L4 = 5 MVA, L5 = 1 MVA	5
BC	DL6	4 Ω	2	5 MW 1 MW	L1 = 2 MVA, L3 = 1 MVA, L4 = 4 MVA,	5
CA	DL5	1.5 Ω	None	Zero	L1 = 1 MVA, L2 = 0.25 MVA, L3 = 4 MVA, L4 = 2 MVA, L5 = 1 MVA	6
CA	DL1	0.2 Ω	1	1 MW	L1 = 0.5 MVA, L3 = 2 MVA, L4 = 3 MVA, L5 = 1 MVA	6
CA	DL6	5.5 Ω	2	2 MW 2 MW	L1 = 2 MVA, L3 = 1 MVA, L4 = 2 MVA,	6
ABG	DL4	0.1 Ω	None	Zero	L1 = 1 MVA, L2 = 0.25 MVA, L3 = 2 MVA, L4 = 4 MVA, L5 = 0.5 MVA	7
ABG	DL2	6 Ω	1	1 MW	L1 = 2 MVA, L3 = 0.5 MVA, L4 = 1 MVA, L5 = 1 MVA	7
ABG	DL6	0.9 Ω	2	2 MW 2 MW	L1 = 0.5 MVA, L3 = 1 MVA, L4 = 2 MVA,	7
BCG	DL5	3 Ω	None	Zero	L1 = 1 MVA, L2 = 2 MVA, L3 = 0.2 MVA, L4 = 2 MVA, L5 = 4 MVA	8
BCG	DL4	5 Ω	1	4 MW	L1 = 6 MVA, L3 = 3 MVA, L4 = 5 MVA, L5 = 10 MVA	8
BCG	DL6	0.1 Ω	2	3 MW 2 MW	L1 = 5 MVA, L3 = 10 MVA, L4 = 3 MVA,	8
CAG	DL5	1 Ω	None	Zero	L1 = 5 MVA, L2 = 1 MVA, L3 = 0.5 MVA, L4 = 2 MVA, L5 = 2 MVA	9

Table B.3 Cont'd

CAG	DL1	2 Ω	1	3 MW	L1 = 5 MVA, L3 = 2 MVA, L4 = 3 MVA, L5 = 1 MVA	9
CAG	DL6	0.3 Ω	2	1 MW 1 MW	L1 = 2 MVA, L3 = 2 MVA, L4 = 2 MVA, L5 = 1 MVA	9
ABC	DL5	6 Ω	None	Zero	L1 = 1 MVA, L2 = 1 MVA, L3 = 3 MVA, L4 = 2 MVA, L5 = 2 MVA	10
ABC	DL2	0.1 Ω	1	3 MW	L1 = 2 MVA, L3 = 2 MVA, L4 = 1 MVA, L5 = 1 MVA	10
ABC	DL3	5 Ω	2	1 MW 1 MW	L1 = 2 MVA, L3 = 0.5 MVA, L4 = 2 MVA,	10

Table B.4 Fault location results for some operation conditions

Fault location	Fault type	Fault resistance (Ω)	Number of DG	Load Changes	Fault location decision
None	None	0.1	--	L1 = 2 MVA, L2 = 2 MVA, L3 = 2 MVA, L4 = 1 MVA, L5 = 1 MVA	0
None	None	2	--	L1 = 8 MVA, L2 = 0.25 MVA, L3 = 2 MVA, L4 = 1 MVA, L5 = 2 MVA	0
DL 1	AG	0.1	1	L1 = 2 MVA, L2 = 2 MVA, L3 = 2 MVA, L4 = 1 MVA, L5 = 1 MVA	1
DL 1	AB	4	2	L1 = 2 MVA, L2 = 2 MVA, L3 = 4 MVA, L4 = 1 MVA, L5 = 1 MVA	1
DL 1	ABC	0.1	--	L1 = 2 MVA, L2 = 2 MVA, L3 = 2 MVA, L4 = 1 MVA, L5 = 1 MVA	1
DL 1	AG	2	--	L1 = 2 MVA, L2 = 2 MVA, L3 = 2 MVA, L4 = 5 MVA, L5 = 1 MVA	1
DL 1	AB	0.1	2	L1 = 2 MVA, L2 = 2 MVA, L3 = 4 MVA, L4 = 1 MVA, L5 = 1 MVA	1
DL 1	ABC	2	1	L1 = 8 MVA, L2 = 2 MVA, L3 = 0.5 MVA, L4 = 1 MVA, L5 = 1 MVA	1
DL 2	AG	4	--	L1 = 6 MVA, L2 = 0.4 MVA, L3 = 2 MVA, L4 = 1 MVA, L5 = 1 MVA	2
DL 2	AB	0.1	--	L1 = 2 MVA, L2 = 2 MVA, L3 = 4 MVA, L4 = 1 MVA, L5 = 1 MVA	2
DL 2	ABC	0.1	2	L1 = 8 MVA, L2 = 2 MVA, L3 = 2 MVA, L4 = 2 MVA, L5 = 0.25 MVA	2
DL 2	AG	2	--	L1 = 2 MVA, L2 = 2 MVA, L3 = 2 MVA, L4 = 1 MVA, L5 = 6 MVA	2
DL 2	AB	0.1	3	L1 = 2 MVA, L2 = 2 MVA, L3 = 2 MVA, L4 = 1 MVA, L5 = 1 MVA	2
DL 2	ABC	4	1	L1 = 6 MVA, L2 = 2 MVA, L3 = 2 MVA, L4 = 1 MVA, L5 = 1 MVA	2
DL 3	ABC	2	2	L1 = 2 MVA, L2 = 2 MVA, L3 = 2 MVA, L4 = 1 MVA, L5 = 1 MVA	3
DL 4	AB	1	3	L1 = 8 MVA, L2 = 0.25 MVA, L3 =	4

Table B.4 Cont'd

DL 5	BCG	0.01	3	2 MVA, L4 = 1 MVA, L5 = 2 MVA L1 = 2 MVA, L2 = 2 MVA, L3 = 2 MVA, L4 = 1 MVA, L5 = 1 MVA	5
DL 1	AG	6	1	L1 = 2 MVA, L2 = 2 MVA, L3 = 4 MVA, L4 = 1 MVA, L5 = 1 MVA	1
DL 4	CAG	0.1	2	L1 = 2 MVA, L2 = 2 MVA, L3 = 2 MVA, L4 = 1 MVA, L5 = 1 MVA	4
DL 6	ABC	2	1	L1 = 2 MVA, L2 = 2 MVA, L3 = 2 MVA, L4 = 5 MVA, L5 = 1 MVA	6
DL 2	CA	1	--	L1 = 2 MVA, L2 = 2 MVA, L3 = 4 MVA, L4 = 1 MVA, L5 = 1 MVA	2
DL 5	AB	6	3	L1 = 8 MVA, L2 = 2 MVA, L3 = 0.5 MVA, L4 = 1 MVA, L5 = 1 MVA	5
DL 3	AG	0.1	2	L1 = 6 MVA, L2 = 0.4 MVA, L3 = 2 MVA, L4 = 1 MVA, L5 = 1 MVA	3
DL 1	ABC	0.01	3	L1 = 2 MVA, L2 = 2 MVA, L3 = 4 MVA, L4 = 1 MVA, L5 = 1 MVA	1
DL 6	CAG	6	1	L1 = 8 MVA, L2 = 2 MVA, L3 = 2 MVA, L4 = 2 MVA, L5 = 0.25 MVA	6
DL 1	BC	1	1	L1 = 2 MVA, L2 = 2 MVA, L3 = 2 MVA, L4 = 1 MVA, L5 = 6 MVA	1
DL 5	CA	2	2	L1 = 2 MVA, L2 = 2 MVA, L3 = 2 MVA, L4 = 1 MVA, L5 = 1 MVA	5
DL 1	AB	0.1	--	L1 = 8 MVA, L2 = 0.25 MVA, L3 = 2 MVA, L4 = 1 MVA, L5 = 2 MVA	1
DL 5	ABC	1	3	L1 = 2 MVA, L2 = 2 MVA, L3 = 2 MVA, L4 = 1 MVA, L5 = 1 MVA	5
DL 3	BCG	6	2	L1 = 2 MVA, L2 = 2 MVA, L3 = 4 MVA, L4 = 1 MVA, L5 = 1 MVA	3
DL 1	AG	0.01	3	L1 = 2 MVA, L2 = 2 MVA, L3 = 2 MVA, L4 = 1 MVA, L5 = 1 MVA	1
DL 4	AG	0.1	2	L1 = 2 MVA, L2 = 2 MVA, L3 = 2 MVA, L4 = 5 MVA, L5 = 1 MVA	4
DL 2	BG	2	3	L1 = 2 MVA, L2 = 2 MVA, L3 = 4 MVA, L4 = 1 MVA, L5 = 1 MVA	2
DL 5	AB	0.1	1	L1 = 8 MVA, L2 = 2 MVA, L3 = 0.5 MVA, L4 = 1 MVA, L5 = 1 MVA	5
DL 1	ABC	0.01	--	L1 = 6 MVA, L2 = 0.4 MVA, L3 = 2 MVA, L4 = 1 MVA, L5 = 1 MVA	1
DL 3	BC	0.1	1	L1 = 2 MVA, L2 = 2 MVA, L3 = 4 MVA, L4 = 1 MVA, L5 = 1 MVA	3
DL 1	CAG	2	1	L1 = 8 MVA, L2 = 2 MVA, L3 = 2 MVA, L4 = 2 MVA, L5 = 0.25 MVA	1
DL 2	BCG	0.1	2	L1 = 2 MVA, L2 = 2 MVA, L3 = 2 MVA, L4 = 1 MVA, L5 = 6 MVA	2
DL 3	AG	0.01	3	L1 = 2 MVA, L2 = 2 MVA, L3 = 2 MVA, L4 = 1 MVA, L5 = 1 MVA	3
DL 6	AB	0.1	2	L1 = 6 MVA, L2 = 2 MVA, L3 = 2 MVA, L4 = 1 MVA, L5 = 1 MVA	6
DL 5	ABC	2	--	L1 = 2 MVA, L2 = 2 MVA, L3 = 2 MVA, L4 = 1 MVA, L5 = 1 MVA	5
DL 6	BCG	6	3	L1 = 8 MVA, L2 = 0.25 MVA, L3 = 2 MVA, L4 = 1 MVA, L5 = 2 MVA	6
DL 1	CA	0.1	3	L1 = 2 MVA, L2 = 2 MVA, L3 = 2 MVA, L4 = 1 MVA, L5 = 1 MVA	1
DL 3	BCG	2	3	L1 = 2 MVA, L2 = 2 MVA, L3 = 4 MVA	3

Table B.4 Cont'd

DL 3	AG	4	2	MVA, L4 = 1 MVA, L5 = 1 MVA L1 = 2 MVA, L2 = 2 MVA, L3 = 2	3
DL 1	AB	6	3	MVA, L4 = 1 MVA, L5 = 1 MVA L1 = 2 MVA, L2 = 2 MVA, L3 = 2	1
DL 5	ABC	2	3	MVA, L4 = 5 MVA, L5 = 1 MVA L1 = 2 MVA, L2 = 2 MVA, L3 = 4	5
DL 2	BG	0.1	3	MVA, L4 = 1 MVA, L5 = 1 MVA L1 = 8 MVA, L2 = 2 MVA, L3 = 0.5	2
DL 3	CG	0.1	--	MVA, L4 = 1 MVA, L5 = 1 MVA L1 = 2 MVA, L2 = 2 MVA, L3 = 2	3
DL 3	ABC	2	3	MVA, L4 = 1 MVA, L5 = 1 MVA L1 = 8 MVA, L2 = 0.25 MVA, L3 = 2	3
DL 1	AB	2	2	MVA, L4 = 1 MVA, L5 = 1 MVA L1 = 2 MVA, L2 = 2 MVA, L3 = 2	1
DL 6	CAG	4	1	MVA, L4 = 1 MVA, L5 = 1 MVA L1 = 2 MVA, L2 = 2 MVA, L3 = 4	6
DL 5	ABC	2	3	MVA, L4 = 1 MVA, L5 = 1 MVA L1 = 2 MVA, L2 = 2 MVA, L3 = 2	5
DL 6	AG	0.1	1	MVA, L4 = 1 MVA, L5 = 1 MVA L1 = 2 MVA, L2 = 2 MVA, L3 = 2	6
DL 5	BCG	1	2	MVA, L4 = 5 MVA, L5 = 1 MVA L1 = 2 MVA, L2 = 2 MVA, L3 = 4	5
DL 5	BG	0.1	1	MVA, L4 = 1 MVA, L5 = 1 MVA L1 = 8 MVA, L2 = 2 MVA, L3 = 0.5	5
DL 3	ABG	4	1	MVA, L4 = 1 MVA, L5 = 1 MVA L1 = 6 MVA, L2 = 0.4 MVA, L3 = 2	3
DL 2	ABC	2	1	MVA, L4 = 1 MVA, L5 = 1 MVA L1 = 2 MVA, L2 = 2 MVA, L3 = 4	2
DL 4	BCG	0.1	2	MVA, L4 = 1 MVA, L5 = 1 MVA L1 = 8 MVA, L2 = 2 MVA, L3 = 2	4
DL 5	AB	0.01	1	MVA, L4 = 2 MVA, L5 = 0.25 MVA L1 = 2 MVA, L2 = 2 MVA, L3 = 2	5
DL 6	CG	0.1	2	MVA, L4 = 1 MVA, L5 = 6 MVA L1 = 2 MVA, L2 = 2 MVA, L3 = 2	6
DL 1	CA	4	1	MVA, L4 = 1 MVA, L5 = 1 MVA L1 = 6 MVA, L2 = 2 MVA, L3 = 2	1
DL 4	ABC	0.1	--	MVA, L4 = 1 MVA, L5 = 1 MVA L1 = 2 MVA, L2 = 2 MVA, L3 = 2	4
DL 4	CAG	1	2	MVA, L4 = 1 MVA, L5 = 1 MVA L1 = 8 MVA, L2 = 0.25 MVA, L3 = 2	4
DL 1	AB	0.1	1	MVA, L4 = 1 MVA, L5 = 1 MVA L1 = 2 MVA, L2 = 2 MVA, L3 = 2	1
DL 5	AG	2	2	MVA, L4 = 1 MVA, L5 = 1 MVA L1 = 2 MVA, L2 = 2 MVA, L3 = 4	5
DL 3	AG	0.1	1	MVA, L4 = 1 MVA, L5 = 1 MVA L1 = 2 MVA, L2 = 2 MVA, L3 = 2	3
DL 4	ABC	1	2	MVA, L4 = 1 MVA, L5 = 1 MVA L1 = 2 MVA, L2 = 2 MVA, L3 = 2	4
DL 2	BG	6	1	MVA, L4 = 5 MVA, L5 = 1 MVA L1 = 2 MVA, L2 = 2 MVA, L3 = 4	2
DL 5	BC	2	--	MVA, L4 = 1 MVA, L5 = 1 MVA L1 = 2 MVA, L2 = 2 MVA, L3 = 2	5
DL 3	BCG	0.1	2	MVA, L4 = 1 MVA, L5 = 1 MVA L1 = 8 MVA, L2 = 0.25 MVA, L3 = 2	3
DL 4	ABC	6	1	MVA, L4 = 1 MVA, L5 = 1 MVA L1 = 2 MVA, L2 = 2 MVA, L3 = 2	4

Table B.4 Cont'd

DL 2	AG	0.1	1	MVA, L4 = 1 MVA, L5 = 1 MVA L1 = 2 MVA, L2 = 2 MVA, L3 = 4	2
DL 5	CAG	0.01	1	MVA, L4 = 1 MVA, L5 = 1 MVA L1 = 2 MVA, L2 = 2 MVA, L3 = 2	5
DL 1	CA	2	1	MVA, L4 = 1 MVA, L5 = 1 MVA L1 = 2 MVA, L2 = 2 MVA, L3 = 2	1
DL 4	ABC	0.1	2	MVA, L4 = 5 MVA, L5 = 1 MVA L1 = 2 MVA, L2 = 2 MVA, L3 = 4	4
DL 2	AG	4	--	MVA, L4 = 1 MVA, L5 = 1 MVA L1 = 8 MVA, L2 = 2 MVA, L3 = 0.5	2
DL 6	BCG	0.1	1	MVA, L4 = 1 MVA, L5 = 1 MVA L1 = 6 MVA, L2 = 0.4 MVA, L3 = 2	6
DL 5	BG	2	1	MVA, L4 = 1 MVA, L5 = 1 MVA L1 = 2 MVA, L2 = 2 MVA, L3 = 4	5
DL 4	ABC	6	2	MVA, L4 = 1 MVA, L5 = 1 MVA L1 = 8 MVA, L2 = 2 MVA, L3 = 2	4
DL 6	AG	0.1	1	MVA, L4 = 2 MVA, L5 = 0.25 MVA L1 = 2 MVA, L2 = 2 MVA, L3 = 2	6
DL 4	AB	0.01	1	MVA, L4 = 1 MVA, L5 = 1 MVA L1 = 8 MVA, L2 = 0.25 MVA, L3 = 2	4
DL 1	CA	0.1	1	MVA, L4 = 1 MVA, L5 = 1 MVA L1 = 2 MVA, L2 = 2 MVA, L3 = 2	1
DL 4	ABC	4	--	MVA, L4 = 1 MVA, L5 = 1 MVA L1 = 2 MVA, L2 = 2 MVA, L3 = 4	4
DL 6	CAG	6	2	MVA, L4 = 1 MVA, L5 = 1 MVA L1 = 2 MVA, L2 = 2 MVA, L3 = 2	6
DL 5	CG	0.01	1	MVA, L4 = 1 MVA, L5 = 1 MVA L1 = 2 MVA, L2 = 2 MVA, L3 = 2	5
DL 2	CA	2	2	MVA, L4 = 5 MVA, L5 = 1 MVA L1 = 2 MVA, L2 = 2 MVA, L3 = 4	2
DL 4	ABC	0.1	1	MVA, L4 = 1 MVA, L5 = 1 MVA L1 = 8 MVA, L2 = 2 MVA, L3 = 0.5	4
DL 3	AB	4	--	MVA, L4 = 1 MVA, L5 = 1 MVA L1 = 6 MVA, L2 = 0.4 MVA, L3 = 2	3
DL 4	BCG	2	2	MVA, L4 = 1 MVA, L5 = 1 MVA L1 = 2 MVA, L2 = 2 MVA, L3 = 4	4
DL 6	ABG	0.1	3	MVA, L4 = 1 MVA, L5 = 1 MVA L1 = 8 MVA, L2 = 2 MVA, L3 = 2	6
DL 1	ABC	4	2	MVA, L4 = 2 MVA, L5 = 0.25 MVA L1 = 2 MVA, L2 = 2 MVA, L3 = 2	1
DL 4	CAG	6	2	MVA, L4 = 1 MVA, L5 = 6 MVA L1 = 2 MVA, L2 = 2 MVA, L3 = 2	4
DL 2	AG	0.1	--	MVA, L4 = 1 MVA, L5 = 1 MVA L1 = 6 MVA, L2 = 2 MVA, L3 = 2	2
DL 6	BG	4	3	MVA, L4 = 1 MVA, L5 = 1 MVA L1 = 2 MVA, L2 = 2 MVA, L3 = 2	6
DL 3	ABC	2	2	MVA, L4 = 1 MVA, L5 = 1 MVA L1 = 8 MVA, L2 = 0.25 MVA, L3 = 2	3
DL 5	CG	4	3	MVA, L4 = 1 MVA, L5 = 2 MVA L1 = 2 MVA, L2 = 2 MVA, L3 = 2	5
DL 1	CAG	0.01	2	MVA, L4 = 1 MVA, L5 = 1 MVA L1 = 2 MVA, L2 = 2 MVA, L3 = 4	1
DL 6	AB	4	1	MVA, L4 = 1 MVA, L5 = 1 MVA L1 = 2 MVA, L2 = 2 MVA, L3 = 2	6
DL 4	ABC	0.01	--	MVA, L4 = 1 MVA, L5 = 1 MVA L1 = 2 MVA, L2 = 2 MVA, L3 = 2	4

Table B.4 Cont'd

DL 3	BC	1	3	MVA, L4 = 5 MVA, L5 = 1 MVA L1 = 2 MVA, L2 = 2 MVA, L3 = 4	3
DL 2	BCG	0.1	3	MVA, L4 = 1 MVA, L5 = 1 MVA L1 = 8 MVA, L2 = 2 MVA, L3 = 0.5	2
DL 5	CA	0.01	1	MVA, L4 = 1 MVA, L5 = 1 MVA L1 = 6 MVA, L2 = 0.4 MVA, L3 = 2	5
				MVA, L4 = 1 MVA, L5 = 1 MVA	

0 - No-fault, 1 - fault at DL 1, 2 – fault at DL 2, 3 - fault at DL 3, 4 – fault at DL 4, 5 - fault at DL 5, 6 – fault at DL 6.

In order to demonstrate and test the proposed protection algorithms during different scenarios, the analysed radial and ring grids have been analysed during symmetrical and unsymmetrical faults in different fault locations. The following figures show the behaviour of CE and ZO algorithms for the analysed radial and ring grids.

Fig. B.1 shows the *abc* voltages, *abc* currents, DPF, fault classification signal (ANN_CL), protection algorithm signal, and trip signal for the analysed ring grid in the case of CE algorithm. Fig. B.1(a) represents the case with two DGs during a single-phase to ground fault at DL5, and Fig. B.1(b) represents the case without DGs during a two-phase fault at DL1. In addition, Fig. B.2 shows the same signals as Fig. B.1 but for the analysed radial grid. Fig. B.2(a) represents the case with two DGs during a single-phase to ground fault at DL4, and Fig. B.2(b) represents the case without DGs during a two-phase to ground fault at DL2.

Fig. B.3 ~ Fig. B.11 show the entire analysed ring grid during different types of faults in various locations. Fig. B.12 and Fig. B.13 represent the same cases shown in Fig. B.1 and Fig. B.2 for ZO algorithm.

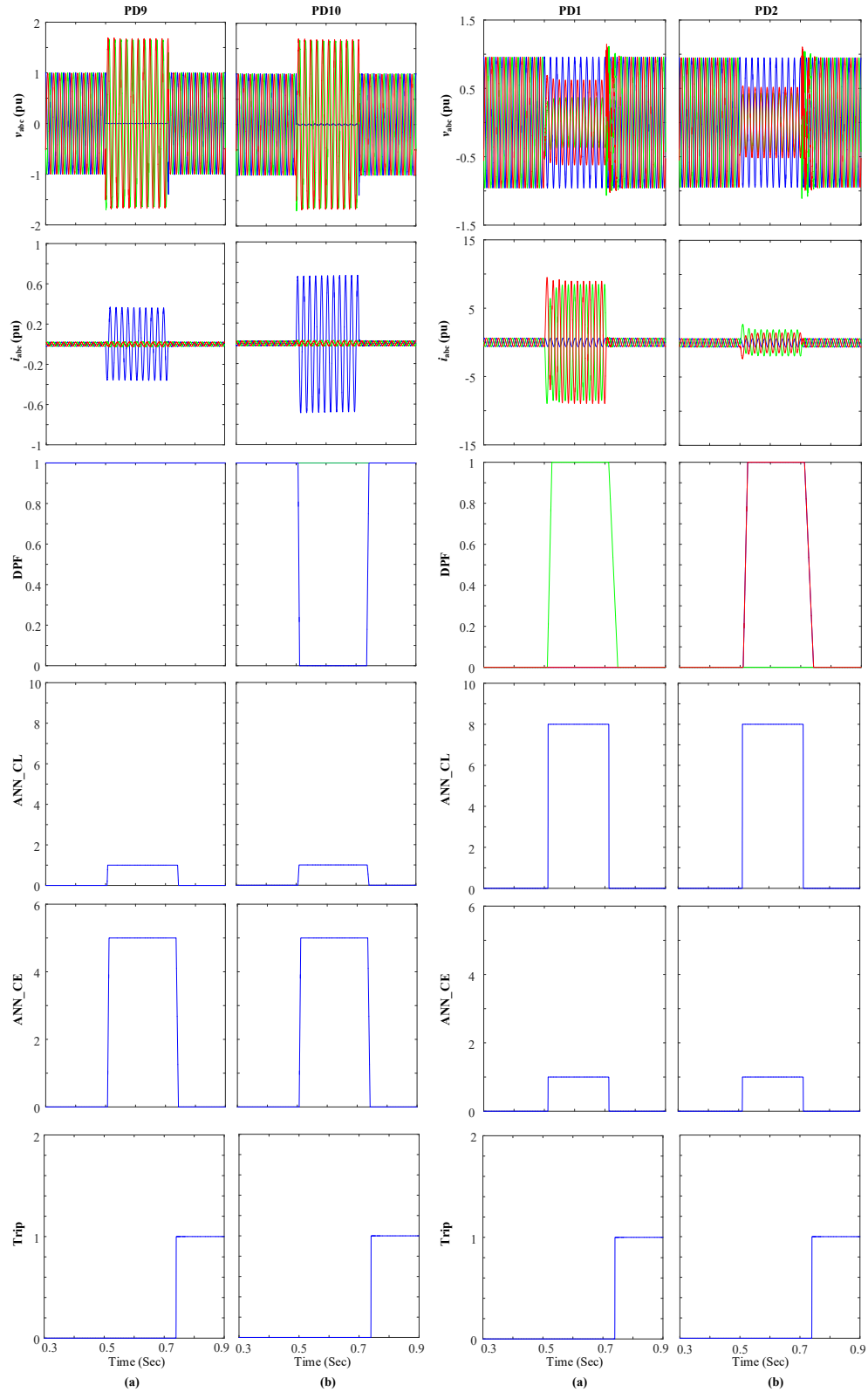


Fig. B.1 Analyzed ring grid with CE (a) 2 DGs during single-phase to ground fault (AG) at DL5, (b) No DG during two-phase fault (BC) at DL1

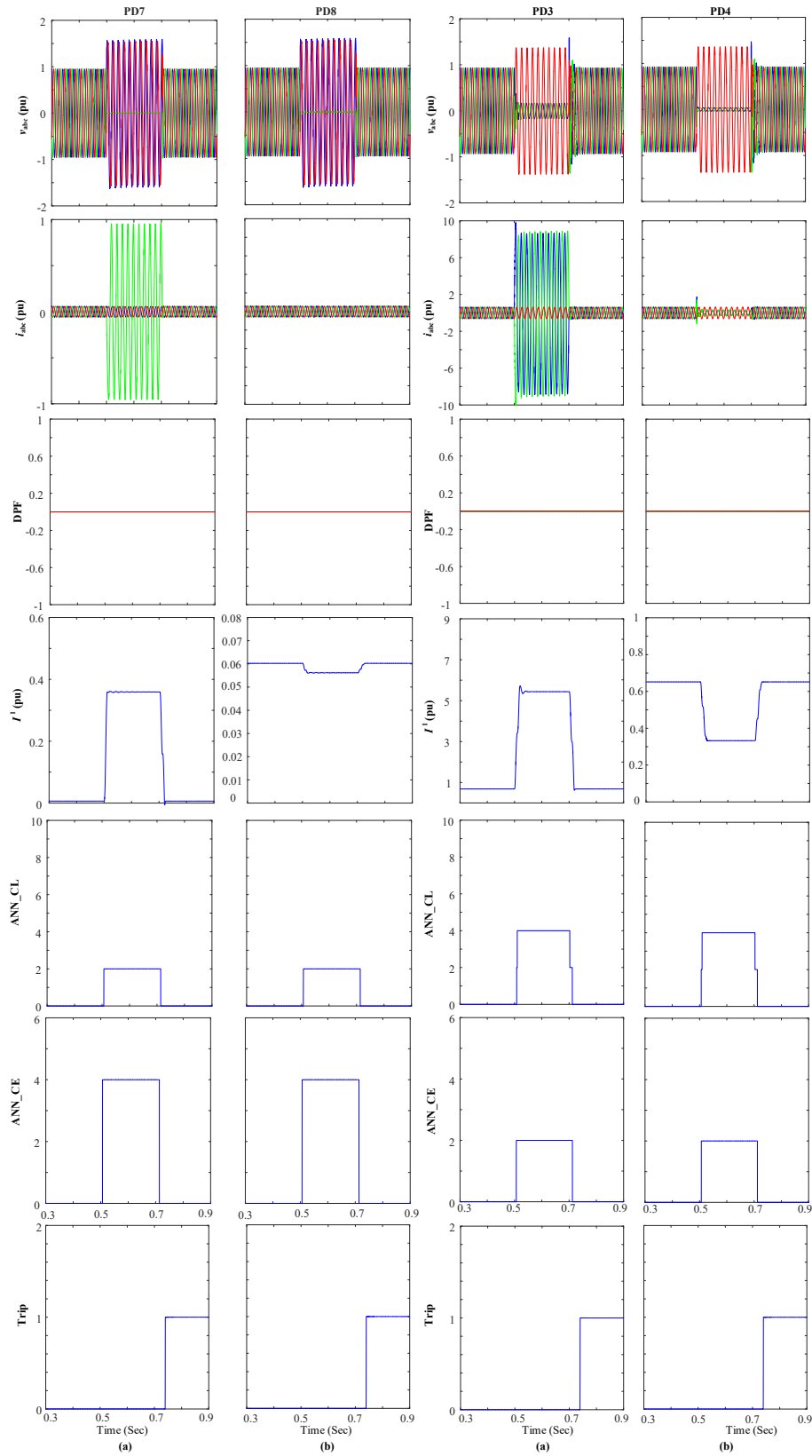


Fig. B.2 Analysed radial grid with CE (a) 2 DGs during single-phase to ground fault (BG) at DL4, (b) No DG during two-phase to ground fault (ABG) at DL2

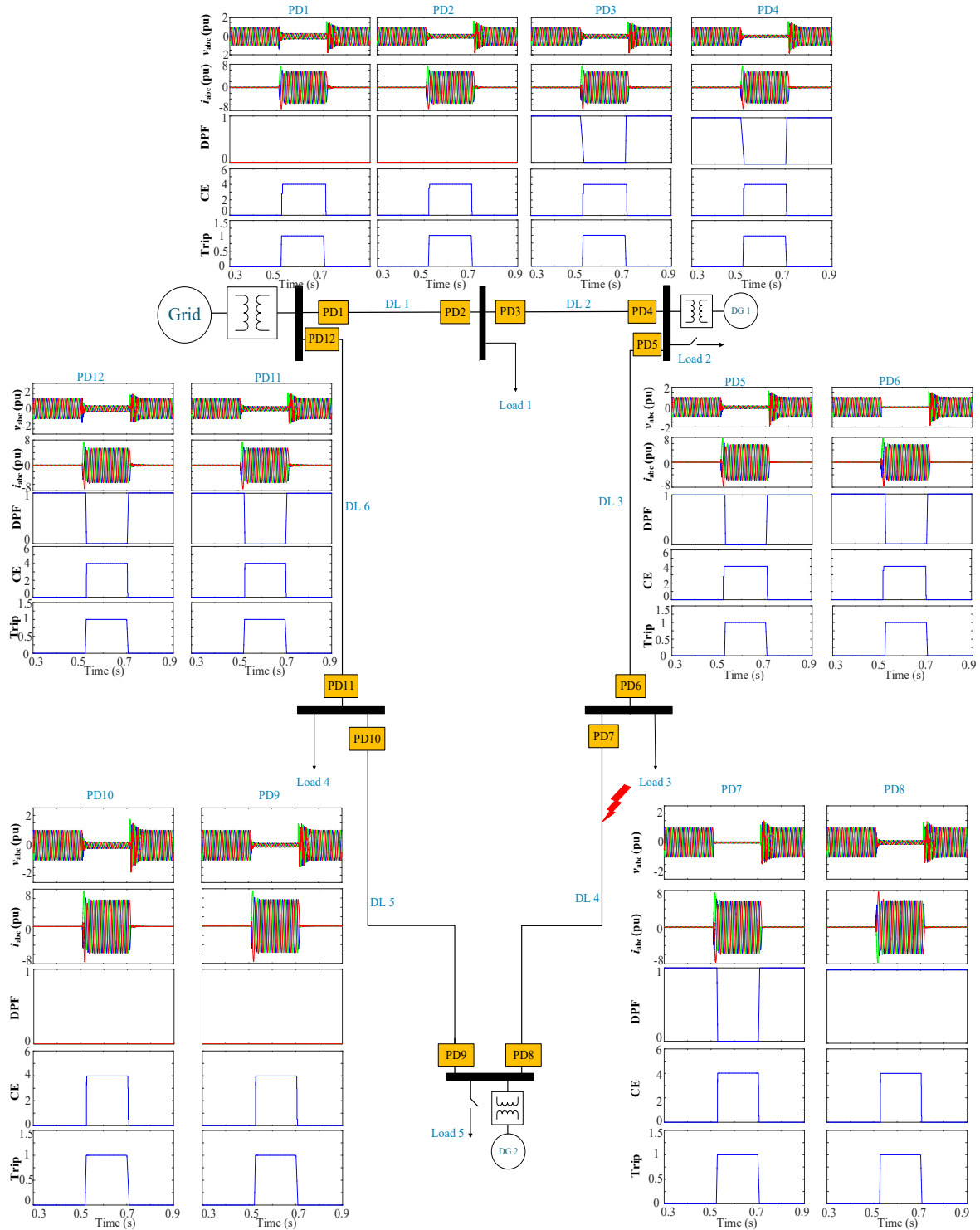


Fig. B.3 Analysed ring grid behaviour during symmetrical fault at DL4 with CE-ZO with $r = 0.1 \Omega$

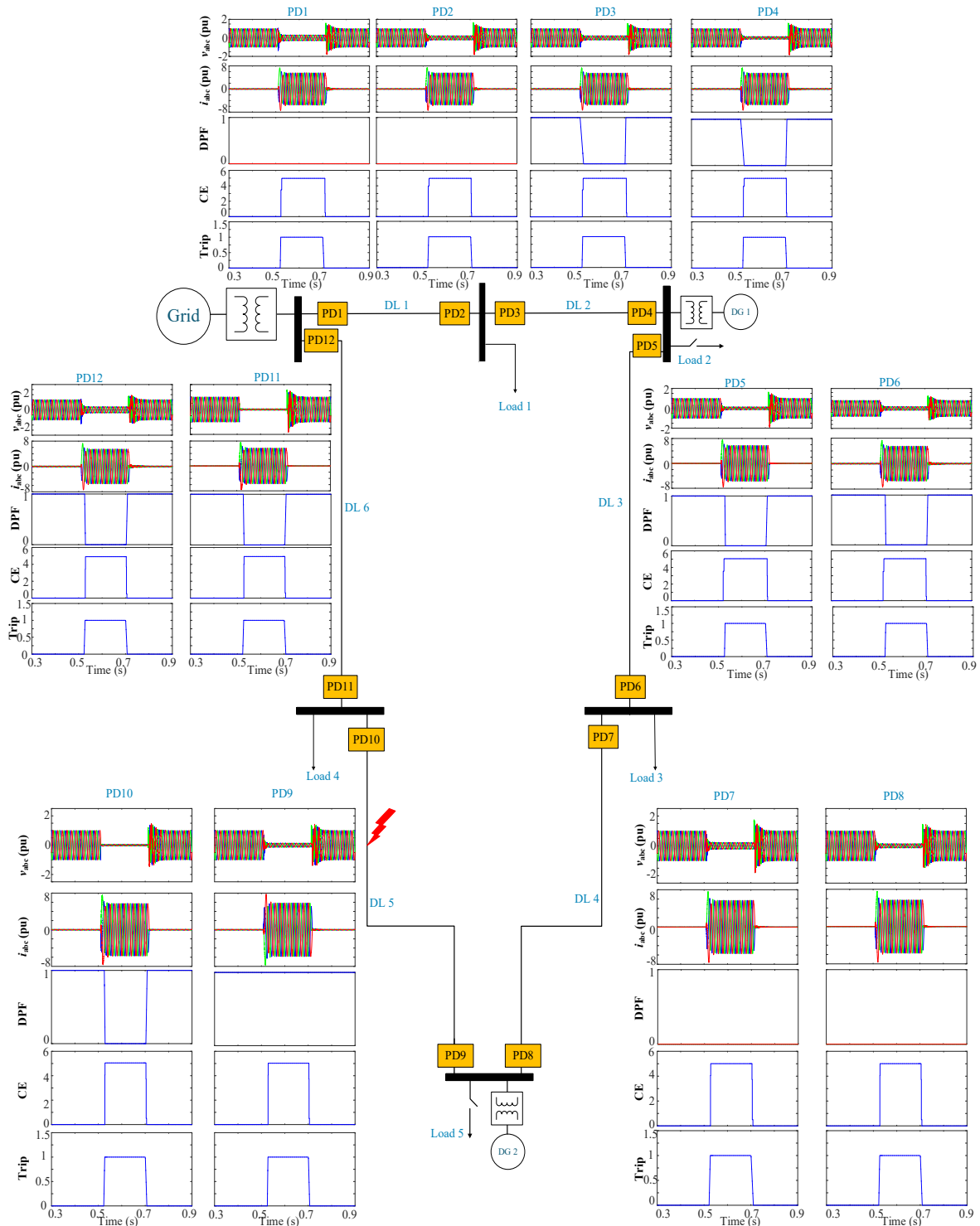


Fig. B.4 Analysed ring grid behaviour during symmetrical fault at DL5 with CE-ZO with $r = 0.1 \Omega$

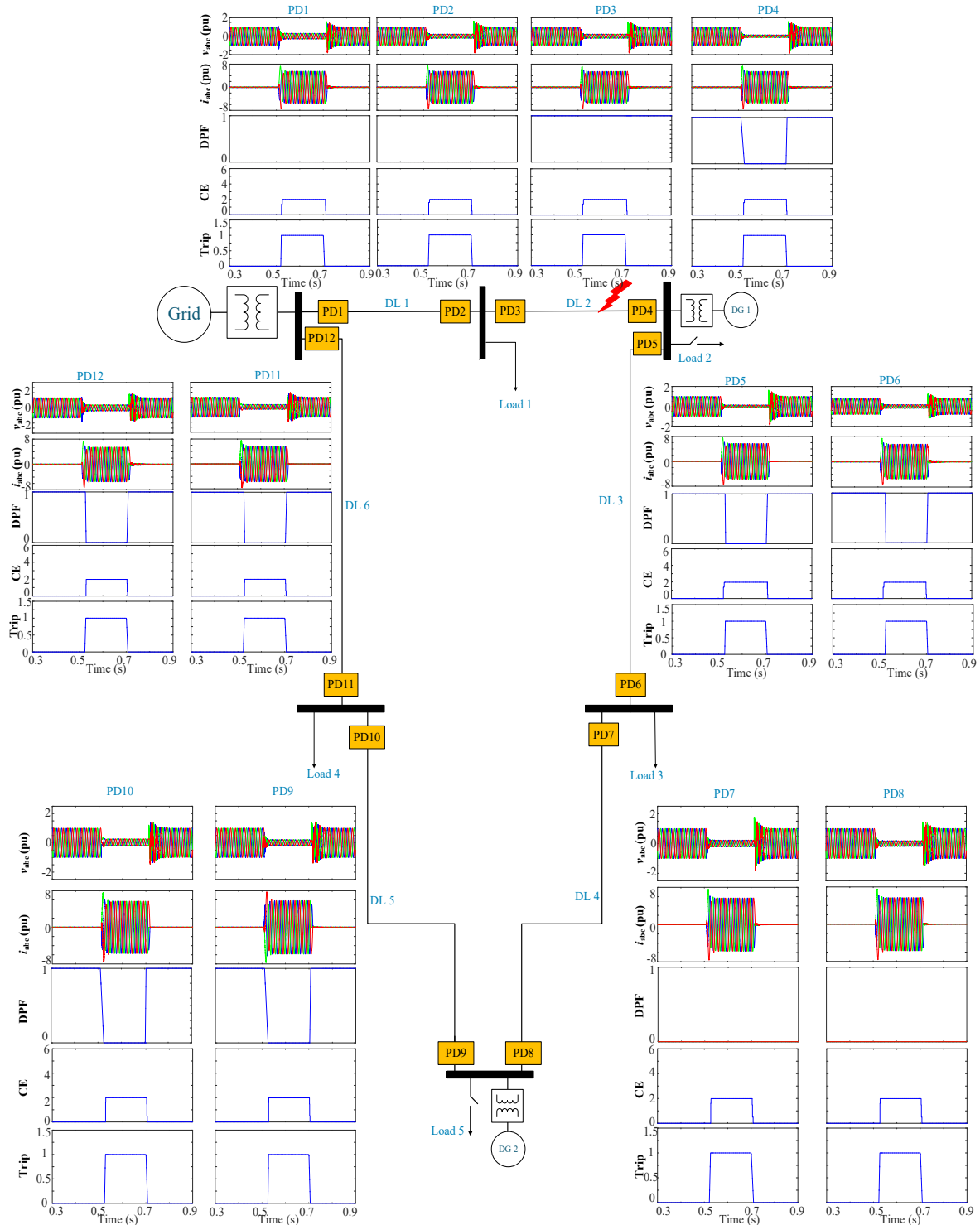


Fig. B.5 Analysed ring grid behaviour during symmetrical fault at DL2 with CE-ZO with $r = 0.1 \Omega$

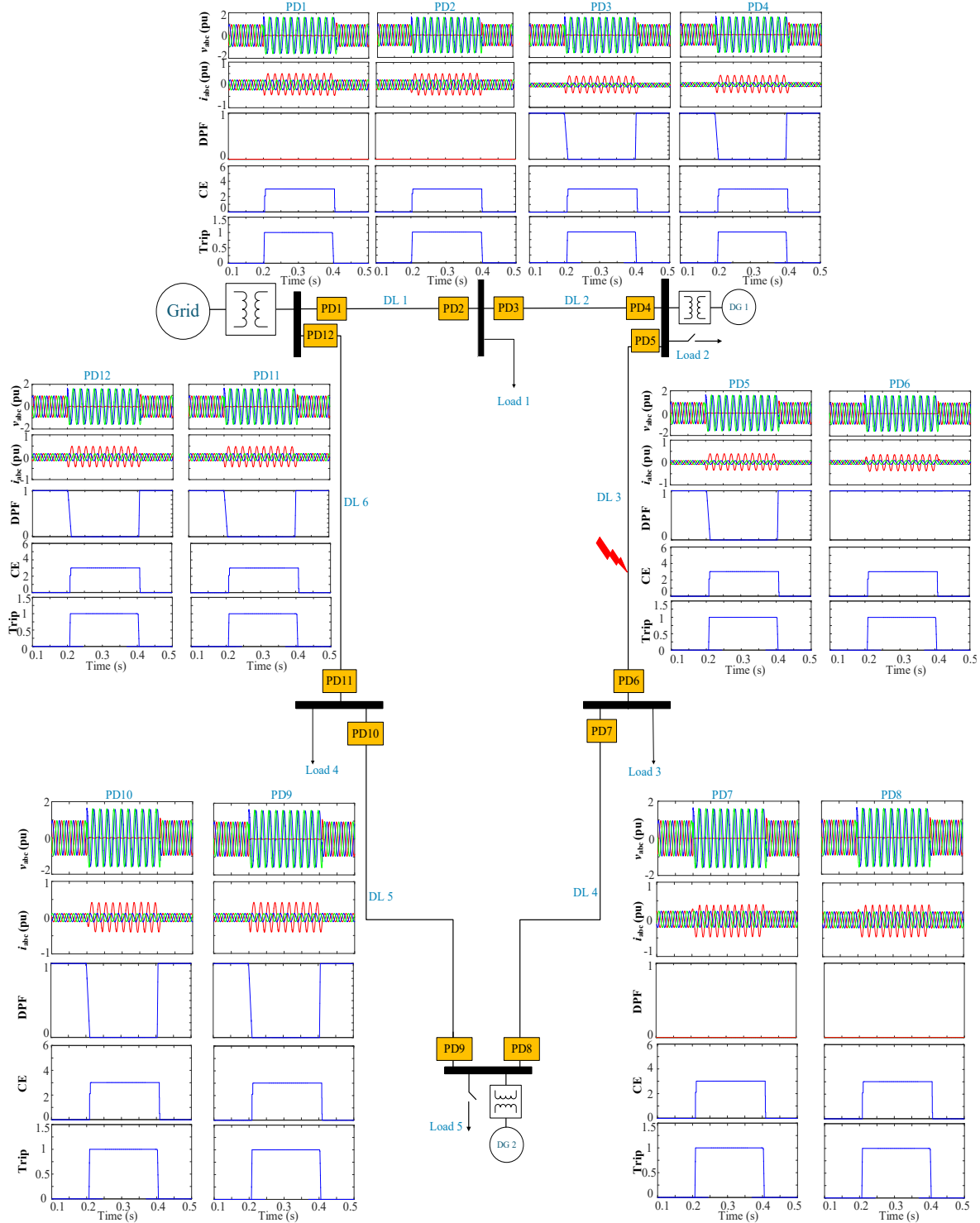


Fig. B.6 Analysed ring grid behaviour during single-phase to ground fault at DL3 with CE-ZO with fault resistance $r = 0.1 \Omega$

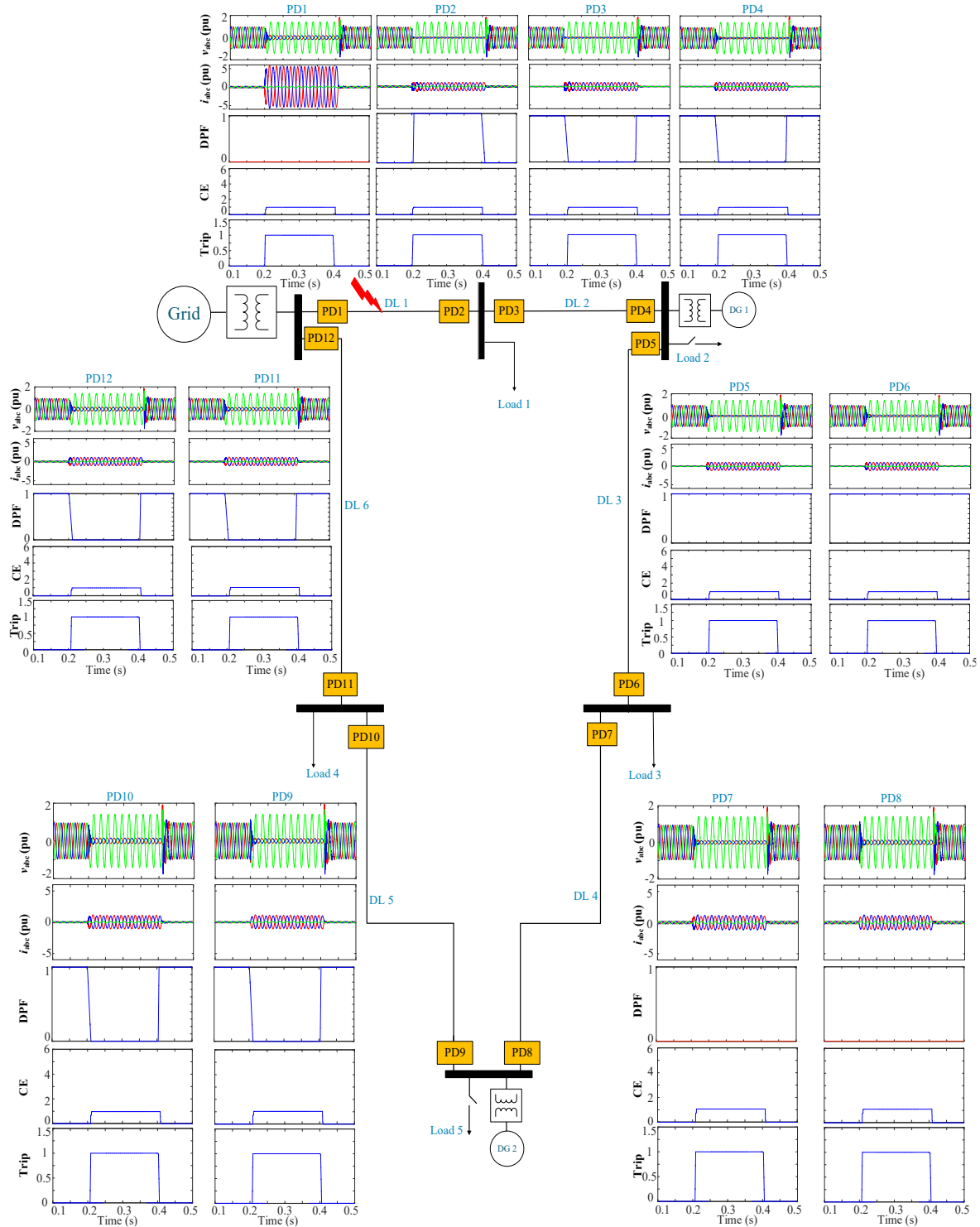


Fig. B.7 Analysed ring grid behaviour during two-phase to ground fault at DL1 with CE-ZO with fault resistance $r = 0.1 \Omega$

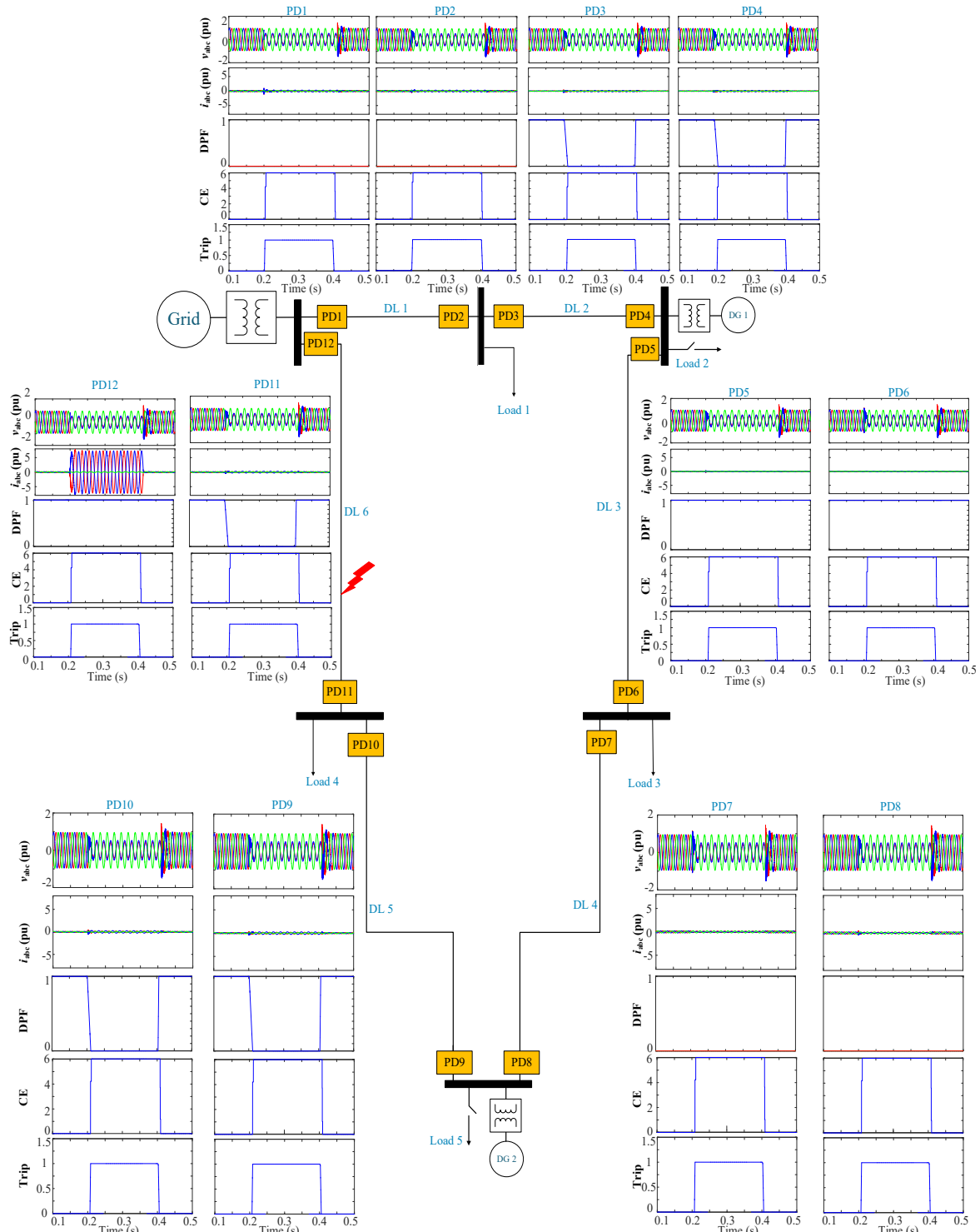


Fig. B.8 Analysed ring grid behaviour during two-phase fault at DL6 with CE-ZO with fault resistance $r = 0.1 \Omega$

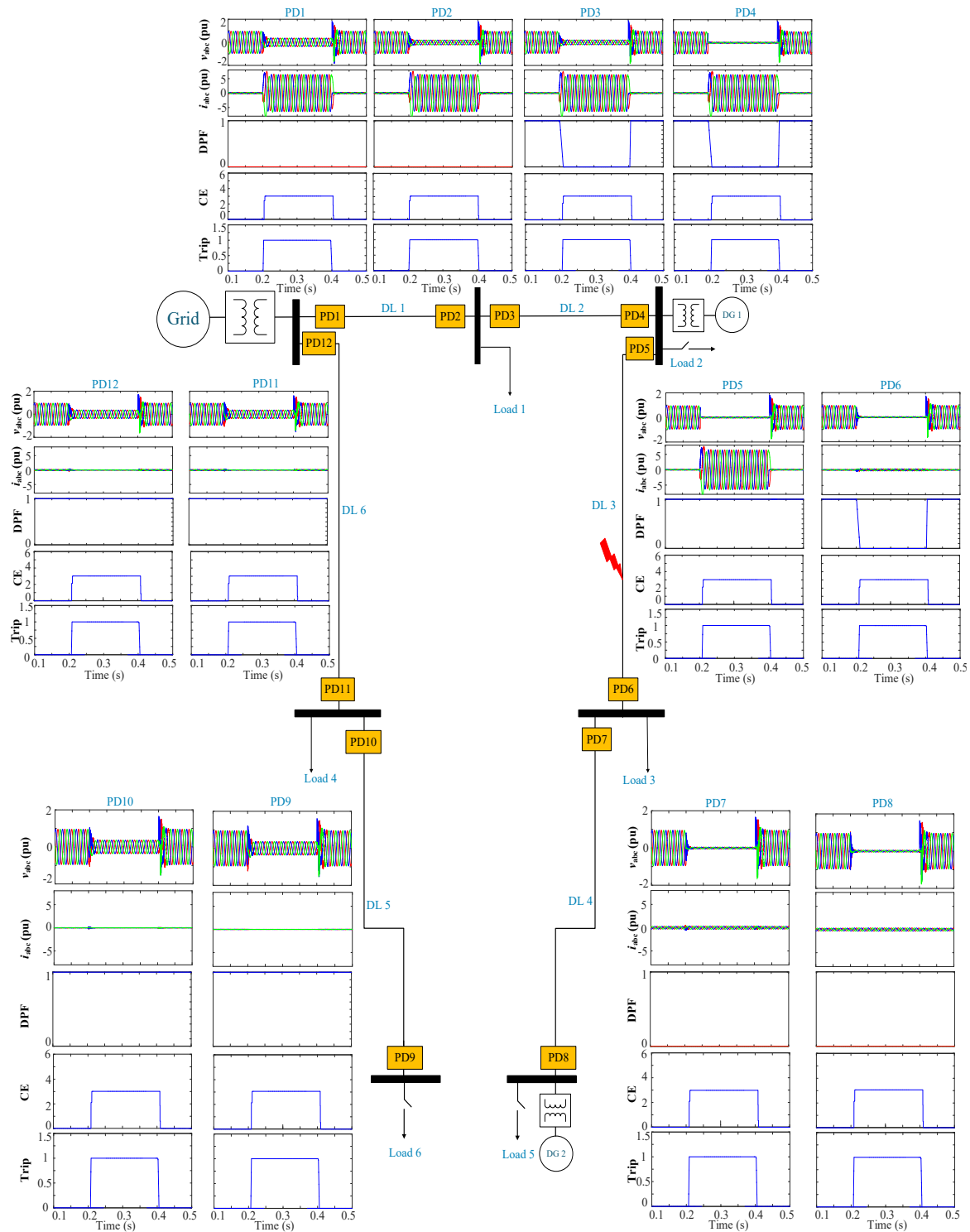


Fig. B.9 Analysed radial grid behaviour during symmetrical fault at DL3 with CE-ZO with fault resistance $r = 0.1 \Omega$

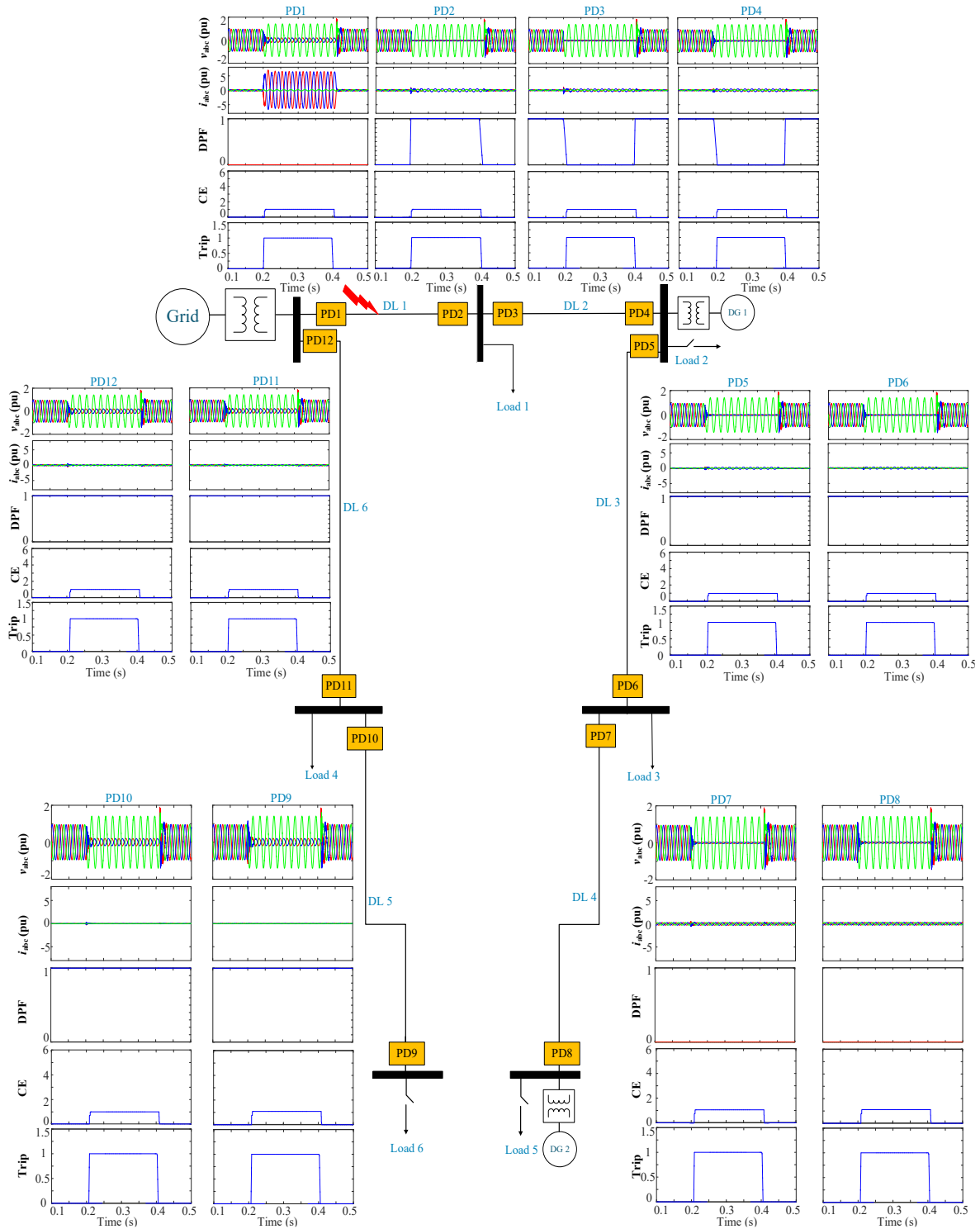


Fig. B.10 Analysed radial grid behaviour during two-phase to ground fault at DL1 with CE-ZO with fault resistance $r = 0.1 \Omega$

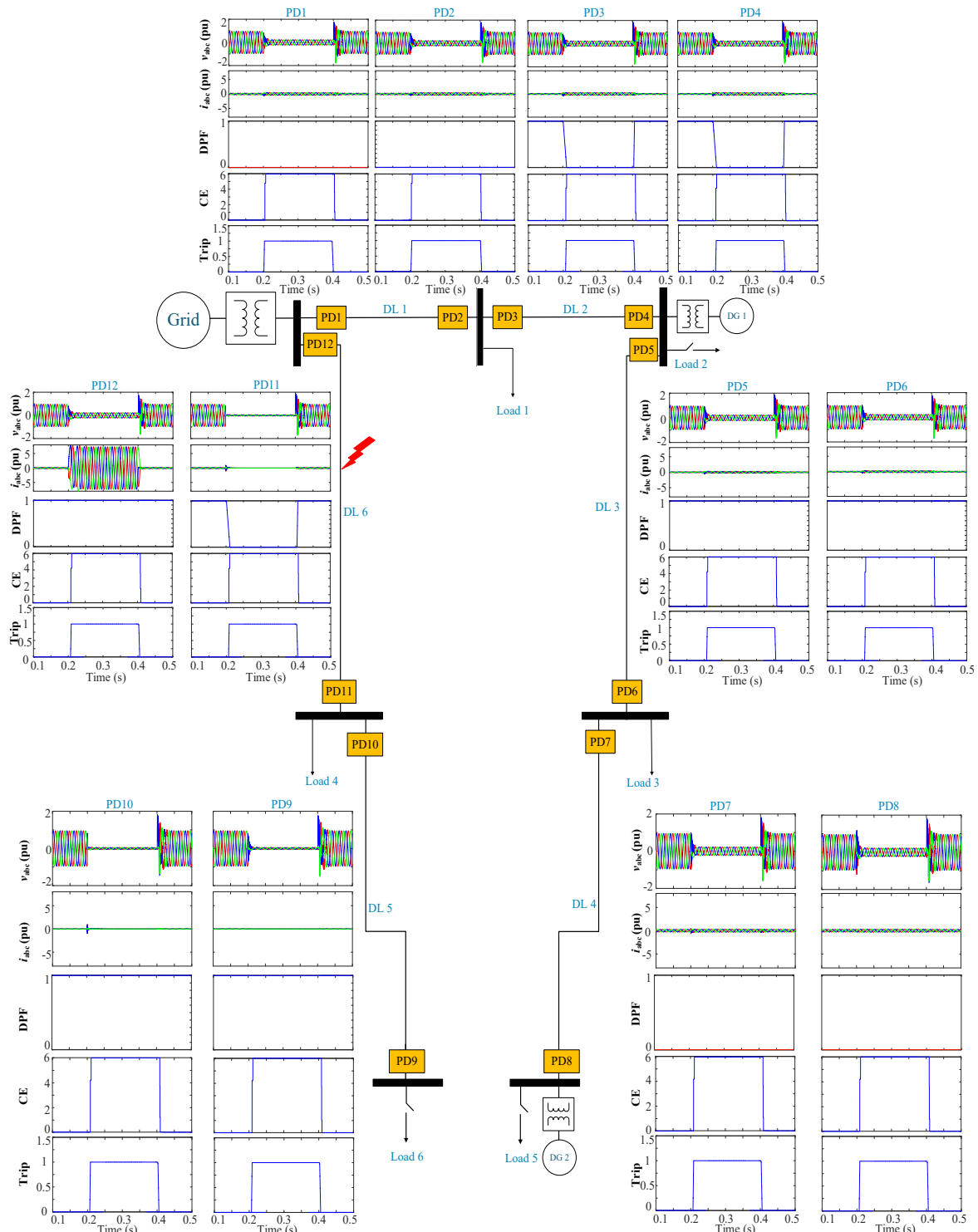


Fig. B.11 Analysed radial grid behaviour during symmetrical fault at DL6 with CE-ZO with fault resistance $r = 0.1 \Omega$

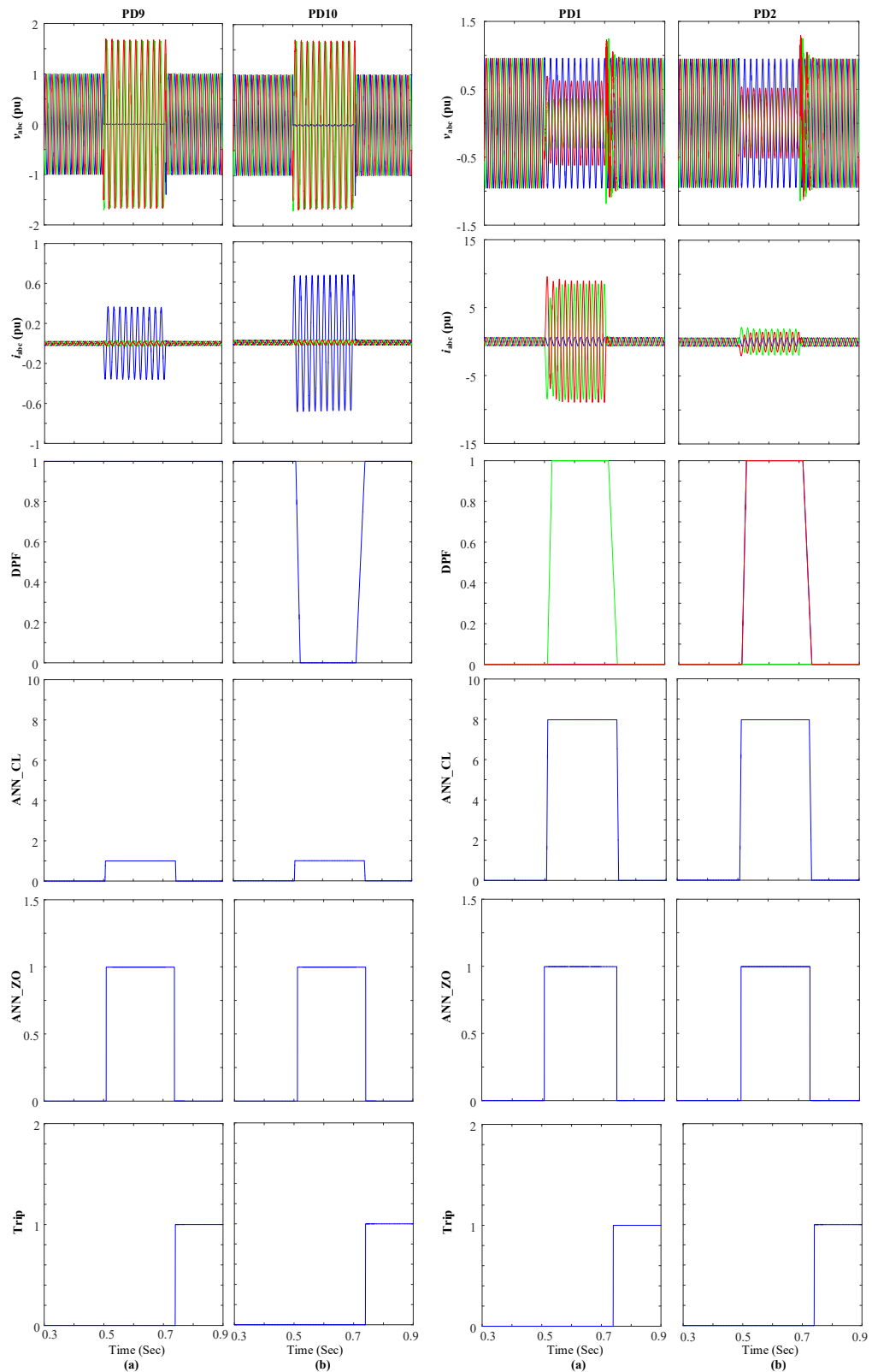


Fig. B.12 Analysed ring grid with ZO (a) 2 DGs during single-phase to ground fault (AG) at DL5, (b) No DG during two-phase fault (BC) at DL1

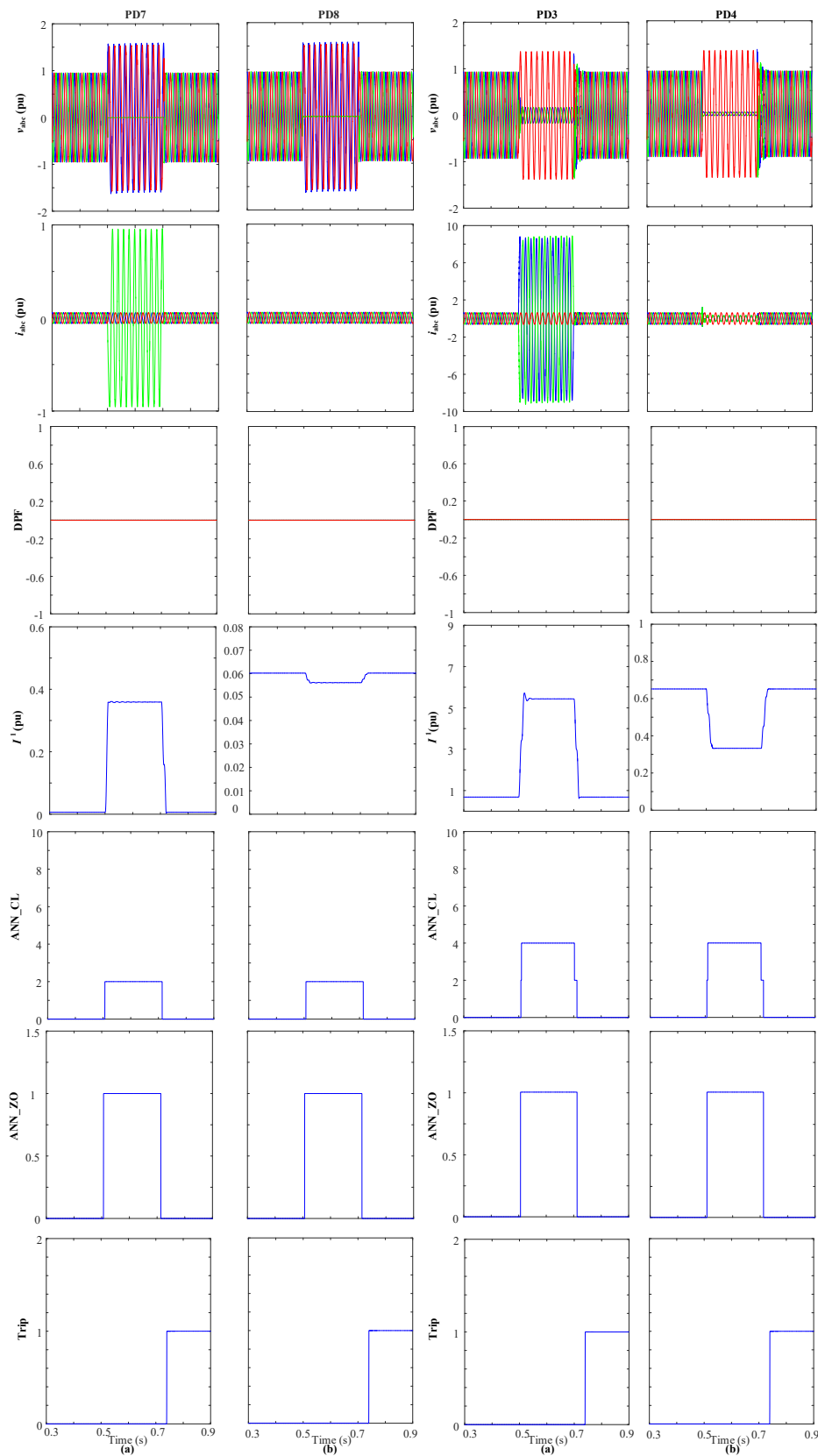


Fig. B.13 Analysed radial grid with ZO (a) 2 DGs during single-phase to ground fault (BG) at DL4, (b) No DG during two-phase to ground fault (ABG) at DL2

B.3. Demonstration of DPF in various grid scenarios

In this section, the behaviour of DPF is analysed during different fault types and locations with and without DGs, also with low and high load consumption. This analysis is done to understand the effect of DGs on the DPF. Several cases have been presented to show the methodology of the protection algorithms.

➤ **Ring grid without DG**

For CE controller, during faults, the DPF will change at one end of the faulted line, for example, when the fault is at DL2 (red arrows) or is at DL5 (green arrows), as seen in Fig. B.14, the DPF at one end equals to zero (downstream direction) and at the other end equals to 1 (upstream direction), as shown in Table B.5. In this case, ANN can identify the fault and the location of the fault in all situations, with high or low loads consumption.

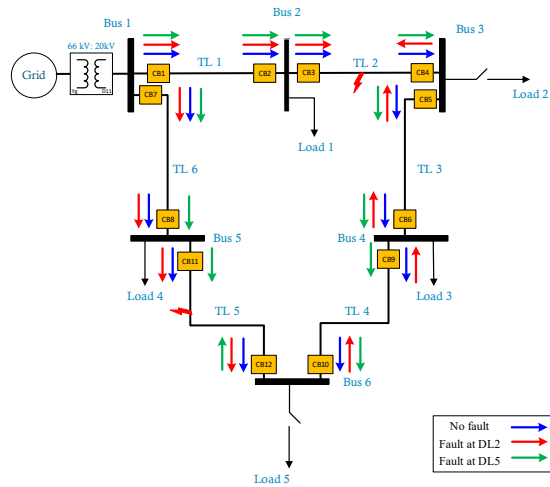


Fig. B.14 Ring grid

Table B.5 CE decision for the analysed ring grid without DG

Fault	Direction Relays												CE Decision
	PD1	PD2	PD3	PD4	PD5	PD6	PD7	PD8	PD9	PD10	PD11	PD12	
No	0	0	0	0	0	0	0	0	0	0	0	0	0
DL2	0	0	0	1	1	1	1	1	0	0	0	0	2
DL5	0	0	0	0	0	0	0	0	0	1	1	0	5

In the case of ZO, the decision of the ANN depends on the DPF at each line. In this case, each PD has its own ZO controller and gives the decision depending on the communication between the two PDs at the same line, as shown in Table B.6. For example, when the fault is at DL2, ZO decision for PD3 and PD4 give a value equal to (1), which means there is a fault in that line, and ZO decision for PD1 and PD2 give a value equal to (2), which means the fault is in the downstream direction; also, ZO decision for PD5 and PD6 give a value equals to (3), which means the fault is in the upstream direction.

Table B.6 ZO decision for the analysed ring grid without DG

Fault	Direction Relays											
	PD1	PD2	PD3	PD4	PD5	PD6	PD7	PD8	PD9	PD10	PD11	PD12
No	0	0	0	0	0	0	0	0	0	0	0	0
DL2	2	2	1	1	3	3	3	3	2	2	2	2
DL5	2	2	2	2	2	2	2	2	1	1	2	2

➤ Ring grid with one DG at bus 3 with low and high loads consumption

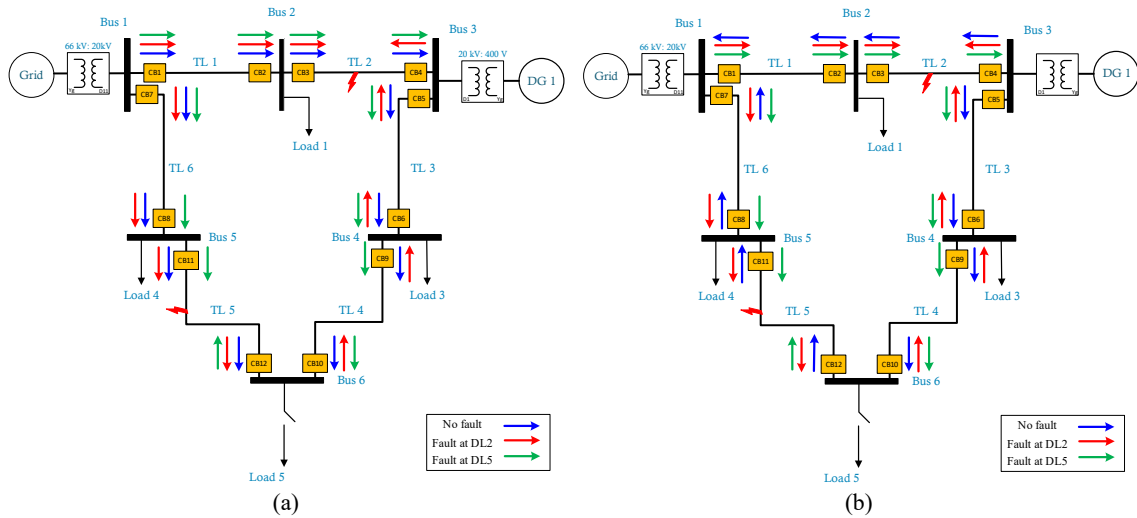


Fig. B.15 Ring grid

When a DG is connected at bus 3 with power penetration equals 1 MW, as seen in Fig. B.15(a), the DPF is the same as the previous case because the loads are higher than the power of DG. No more training is needed in this case, and the results are the same as shown in Table B.5.

When a DG connected at bus 3 with power penetration equals 4 MW, as seen in Fig. B.15(b), in this case, the DG injects more power than the loads need, the remaining power will transfer to the grid, and in this case, the DPF will change due to this reason. More training is needed to identify the fault location in this case. Table B.7 shows the DPF behaviour before and after the fault and the decision of CE, and Table B.8 for ZO.

Table B.7 CE decision for the analysed ring grid with DG

Fault	Direction Relays												CE Decision
	PD1	PD2	PD3	PD4	PD5	PD6	PD7	PD8	PD9	PD10	PD11	PD12	
No	0	0	0	0	0	0	0	0	0	0	0	0	0
DL2	0	0	0	1	1	1	1	1	0	0	0	0	2
DL5	0	0	0	0	0	0	0	0	1	0	0	0	5

Table B.8 ZO decision for the analysed ring grid with DG

Fault	Direction Relays											
	PD1	PD2	PD3	PD4	PD5	PD6	PD7	PD8	PD9	PD10	PD11	PD12
No	0	0	0	0	0	0	0	0	0	0	0	0
DL2	2	2	1	1	3	3	3	3	2	2	2	2
DL 5	2	2	2	2	2	2	2	2	1	1	2	2

➤ Ring grid with two DG1= 1 MW, DG1= 2 MW with low loads and high loads consumption

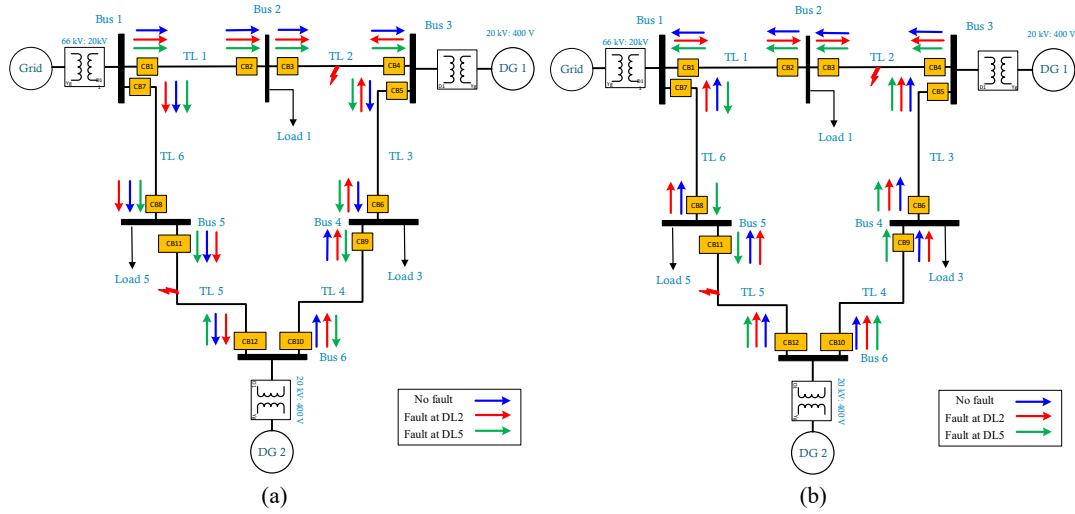


Fig. B.16 Ring grid

When two DGs are connected at buses 3 and 6, the power flow changes depending on the load consumptions shown in Fig. B.16(a) and Fig. B.16 (b) and Table B.9 and Table B.10. In these cases, the ANN must be trained in similar situations. Table B.11 and Table B.12 show the behaviour of ZO.

Table B.9 CE decision for the analysed ring grid with DG and high load consumption

Fault	Direction Relays												NN Decision
	PD1	PD2	PD3	PD4	PD5	PD6	PD7	PD8	PD9	PD10	PD11	PD12	
No	0	0	0	0	0	0	0	0	0	0	0	0	0
DL2	0	0	0	1	1	1	1	1	0	0	0	0	2
DL5	0	0	0	0	0	0	0	0	1	0	0	0	5

Table B.10 CE decision for the analysed ring grid with DG and low load consumption

Fault	Direction Relays												NN Decision
	PD1	PD2	PD3	PD4	PD5	PD6	PD7	PD8	PD9	PD10	PD11	PD12	
No	0	0	0	0	0	0	0	0	0	0	0	0	0
DL2	0	0	0	1	1	1	1	1	1	1	1	1	2
DL5	1	1	1	1	1	1	1	1	1	0	0	0	5

Table B.11 ZO decision for the analysed ring grid with DG and high load consumption

Fault	Direction Relays											
	PD1	PD2	PD3	PD4	PD5	PD6	PD7	PD8	PD9	PD10	PD11	PD12
No	0	0	0	0	0	0	0	0	0	0	0	0
DL2	2	2	1	1	3	3	3	3	3	3	3	3
DL5	2	2	2	2	2	2	2	2	1	1	2	2

Table B.12 ZO decision for the analyzed ring grid with DG and low load consumption

Fault	Direction Relays											
	PD1	PD2	PD3	PD4	PD5	PD6	PD7	PD8	PD9	PD10	PD11	PD12
No	0	0	0	0	0	0	0	0	0	0	0	0
DL2	2	2	1	1	3	3	3	3	3	3	3	3
DL5	3	3	3	3	3	3	3	3	1	1	2	2

➤ Radial grid without DG

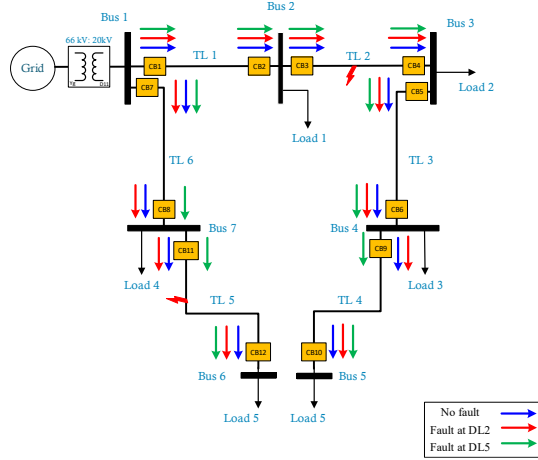


Fig. B.17 Radial grid

In the case of radial grids, seen in Fig. B.17, the DPF will not change due to – in some cases – the generation will be only from the main grid. Therefore, another strategy depends on the use of the positive-sequence current at both ends of the line. If the positive-sequence current at both ends of the line is approximately the same, then the fault is in another line. If the values of positive-sequence current at both ends of the line are not the same, as seen in Table B.13 for CE and Table B.14 for ZO, then the fault is located at that line .

Table B.13 CE decision for the analysed radial grid without DG

Fault	Direction Relays											NN Decision	
	PD1	PD2	PD3	PD4	PD5	PD6	PD7	PD8	PD9	PD10	PD11		PD12
No	0	0	0	0	0	0	0	0	0	0	0	0	0
DL2(DPF)	0	0	0	0	0	0	0	0	0	0	0	0	0
DL5(DPF)	0	0	0	0	0	0	0	0	0	0	0	0	0
	$i^+1 \approx i^+2$		$i^+3 \approx i^+4$		$i^+5 \approx i^+6$		$i^+7 \approx i^+8$		$i^+10 \approx i^+9$		$i^+12 \approx i^+14$		Algorithm Decision
DL2 (i^+)	0	$i^+3 \neq i^+4$ 1		0	0	0	0	0	0	0	0	0	2
DL5 (i^+)	0	0	0	0	0	0	0	$i^+10 \neq i^+9$ 1		0	0	0	5

Table B.14 ZO decision for the analysed radial grid without DG

Fault	Direction Relays											
	PD1	PD2	PD3	PD4	PD5	PD6	PD7	PD8	PD9	PD10	PD11	PD12
No	0	0	0	0	0	0	0	0	0	0	0	0
DL2 (DPF)	2	2	2	2	2	2	2	2	2	2	2	0
DL5(DPF)	2	2	2	2	2	2	2	2	2	2	2	2
	0	$i^+3 \neq i^+4$ 1		0	0	0	0	0	0	0	0	0
DL2 (i^+)	2	2	1	1	2	2	2	2	2	2	2	2
	0	0	0	0	0	0	0	$i^+10 \neq i^+9$ 1		0	0	0
DL5 (i^+)	2	2	2	2	2	2	2	2	1	1	2	2

➤ Radial grid with one DG= 1 MW

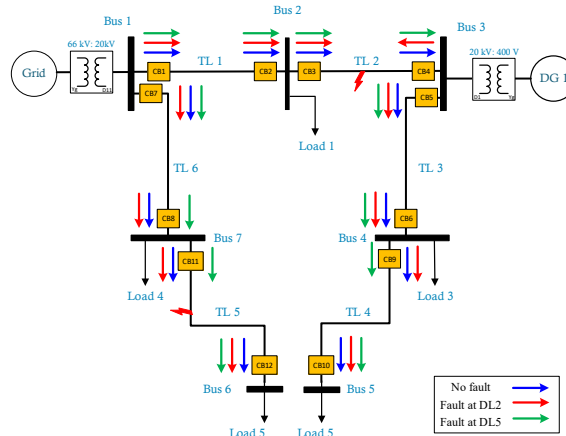


Fig. B.18 Radial grid with one DG

When one DG is connected at bus 3, as shown in Fig. B.18, and when a fault occurs at DL2, the DPF is changing because DL2 is fed from both ends of the line. However, when the fault is at DL5, the DPF will not change as the line is supplied only from one end. In this case, the decision will be based on the positive-sequence currents at both ends of the faulted line, as shown in Table B.15 for CE and Table B.16 for ZO.

Table B.15 CE decision for the analysed radial grid with one DG

Fault	Direction Relays												NN Decision
	PD1	PD2	PD3	PD4	PD5	PD6	PD7	PD8	PD9	PD10	PD11	PD12	
No	0	0	0	0	0	0	0	0	0	0	0	0	0
DL2(DPF)	0	0	0	1	0	0	0	0	0	0	0	0	2
DL5(DPF)	1	1	1	1	0	0	0	0	0	0	0	0	0
	$i^+1 \approx i^+2$		$i^+3 \approx i^+4$		$i^+5 \approx i^+6$		$i^+7 \approx i^+8$		$i^+10 \approx i^+9$		$i^+12 \approx i^+14$		Algorithm Decision
DL2 (i^+)	0	$i^+3 \neq i^+4$ 1		0	0	0	0	0	0	0	0	0	2
DL5 (i^+)	0	0	0	0	0	0	0	$i^+10 \neq i^+9$ 1		0	0	0	5

Table B.16 ZO decision for the analysed radial grid with one DG

Fault	Direction Relays											
	PD1	PD2	PD3	PD4	PD5	PD6	PD7	PD8	PD9	PD10	PD11	PD12
No	0	0	0	0	0	0	0	0	0	0	0	0
DL2	2	2	1	1	2	2	2	2	2	2	2	2
DL5	3	3	3	3	2	2	2	2	2	2	2	2
	0	0	$i^+3 \neq i^+4$ 1		0	0	0	0	0	0	0	0
DL2 (i^+)	2	2	1	1	2	2	2	2	2	2	2	2
	0	0	0	0	0	0	0	$i^+10 \neq i^+9$ 1		0	0	0
DL5 (i^+)	2	2	2	2	2	2	2	2	1	1	2	2

➤ Radial grid with two DG= DG1= 1 MW, and DG2= 2 MW

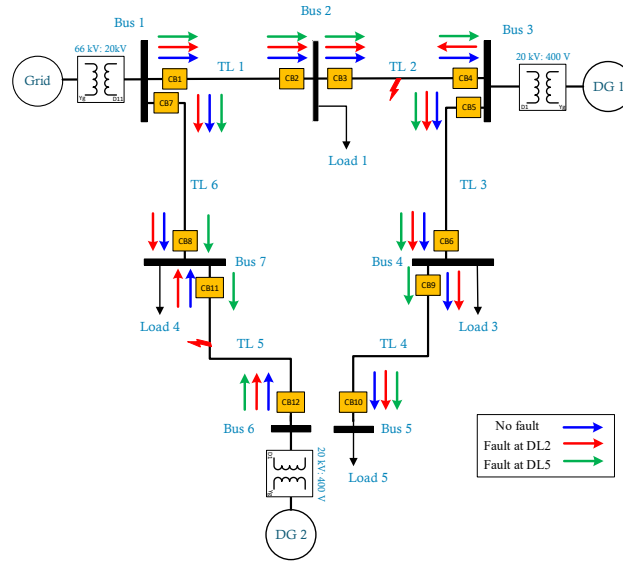


Fig. B.19 Radial grid with two DG

When two DGs are connected at buses 3 and 6 (Fig. B.19), and the fault occurs at DL2 or DL5, the lines are supplied from two line ends. Therefore, the DPF will change in both cases, as seen in Table B.17 for CE, and Table B.18 for ZO.

Table B.17 CE decision for the analysed radial grid with two DG

Fault	Direction Relays												NN Decision
	PD1	PD2	PD3	PD4	PD5	PD6	PD7	PD8	PD9	PD10	PD11	PD12	
No	0	0	0	0	0	0	0	0	0	0	0	0	0
DL2	0	0	0	1	0	0	0	0	1	1	1	1	2
DL5	1	1	1	1	0	0	0	0	1	0	0	0	5

Table B.18 ZO decision for the analysed radial grid with two DG

Fault	Direction Relays											
	PD1	PD2	PD3	PD4	PD5	PD6	PD7	PD8	PD9	PD10	PD11	PD12
No	0	0	0	0	0	0	0	0	0	0	0	0
DL2(DPF)	2	2	1	1	2	2	2	2	3	3	3	3
DL5(DPF)	3	3	3	3	2	2	2	2	1	1	2	2

➤ Ring grid with one DG= 4 MW connected at Bus 2 and low loads values

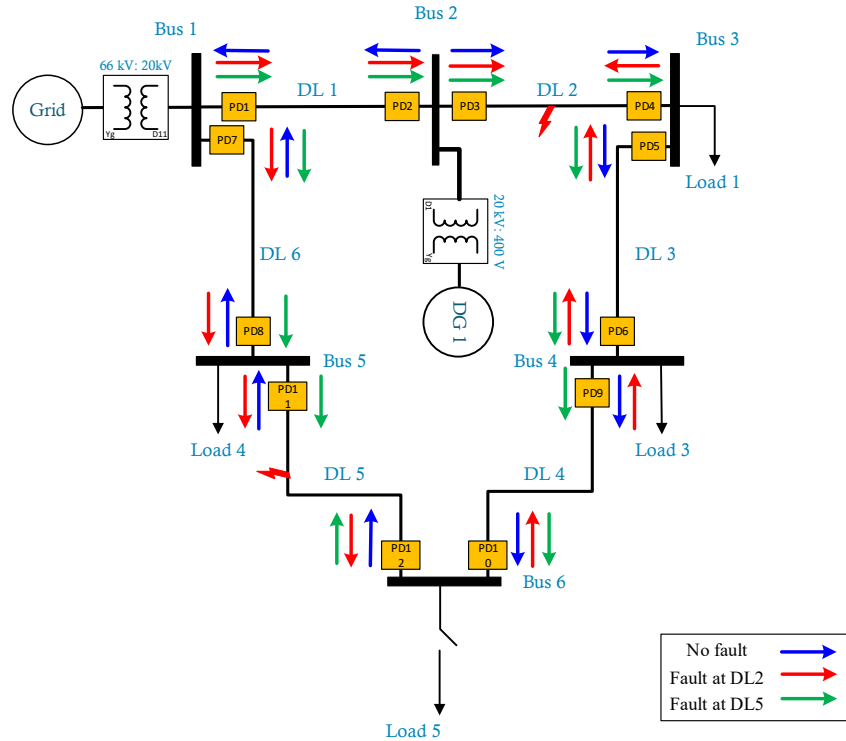


Fig. B.20 Analysed ring grid with one DG = 4 MW connected at bus 2

If the fault is located at DL2, then the DPFs at both ends of DL2 are different. Similar behaviour can be concluded when the fault is located at DL5, as seen in Fig. B.20.

Table B.19 shows the ZO decision of all the PDs located at each end of the DL. It can be recognized that when the DPF is different, the ZO can identify the fault correctly. For example, when the fault is at DL2, the ZO decision of PD3 and PD4 equals 3, which means there is a fault in this line; however, for the other lines, the decision is 1 that indicates the fault is downstream the line, or 2 which indicated the fault upstream the line.

Table B.19 ZO decision

Fault	Direction Relays											
	PD1	PD2	PD3	PD4	PD5	PD6	PD7	PD8	PD9	PD10	PD11	PD12
No	0	0	0	0	0	0	0	0	0	0	0	0
DL2	0	0	0	1	1	1	1	1	0	0	0	0
NN Decision	NN 1 = 2		NN 2 = 1		NN 3 = 3		NN 4 = 3		NN 5 = 2		NN 6 = 2	
DL5	0	0	0	0	0	0	0	0	1	0	0	0
NN Decision	NN 1 = 2		NN 2 = 2		NN 3 = 2		NN 4 = 2		NN 5 = 1		NN 6 = 2	

➤ Ring grid with one DG= 4 MW connected at Bus 4 and low loads values

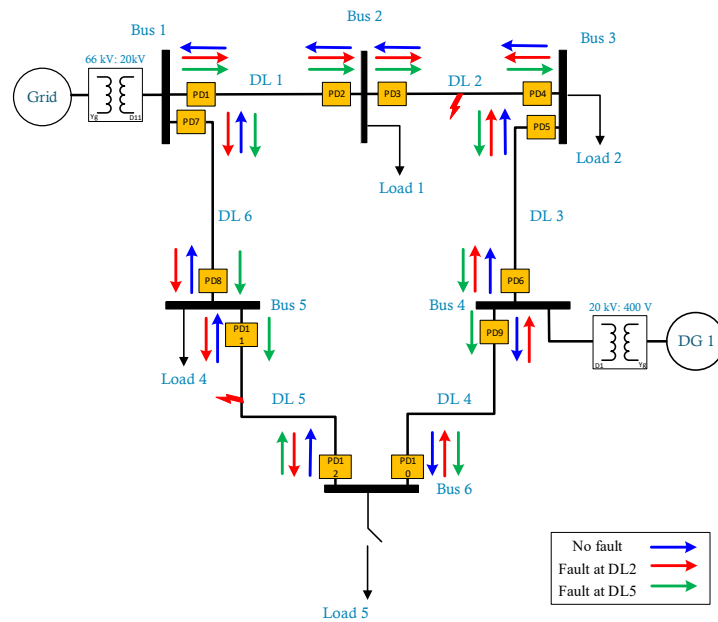


Fig. B.21 Analysed ring grid with one DG = 4 MW connected at bus 4

In the case analysed in Fig. B.21, the DPF is changed before the fault (blue arrows); this situation is different from the analysed case shown in Fig. B.20. Table B.20 shows the CE decision for all the PDs located at each end of all lines. It can be recognized that when the DPF is different the CE can identify the fault correctly. For example, when the fault is at DL2, the CE decision equals 2, which corresponds to the faulted line number (DL2), and when the fault is at DL5, the CE decision equals 5, corresponding to the faulted line number (DL5).

Table B.21 shows the ZO decision of all the PDs located at each end of all lines. It can be recognized that when the DPF is different the ZO can identify the fault correctly. For example, when the fault is at DL2, the ZO decision of PD3 and PD4 equals 3 which means there is a fault in this line, however, for the other lines, the decision is 1 that indicates the fault is downstream the line, or 2 which indicated the fault upstream the line.

Table B.20 CE decision

Fault	Direction Relays												NN Decision
	PD1	PD2	PD3	PD4	PD5	PD6	PD7	PD8	PD9	PD10	PD11	PD12	
No	0	0	0	0	0	0	0	0	0	0	0	0	0
DL2	0	0	0	1	1	1	1	1	0	0	0	0	2
DL5	0	0	0	0	1	1	0	0	1	0	0	0	5

Table B.21 ZO decision

Fault	Direction Relays											
	PD1	PD2	PD3	PD4	PD5	PD6	PD7	PD8	PD9	PD10	PD11	PD12
No	0	0	0	0	0	0	0	0	0	0	0	0
DL2	0	0	0	1	1	1	1	1	0	0	0	0
NN Decision	NN 1 = 2		NN 2 = 1		NN 3 = 3		NN 4 = 3		NN 5 = 2		NN 6 = 2	
DL5	0	0	0	0	1	1	0	0	1	0	0	0
NN Decision	NN 1 = 2		NN 2 = 2		NN 3 = 3		NN 4 = 2		NN 5 = 1		NN 6 = 2	

➤ Ring grid with one DG= 4 MW connected at Bus 5 and low loads values

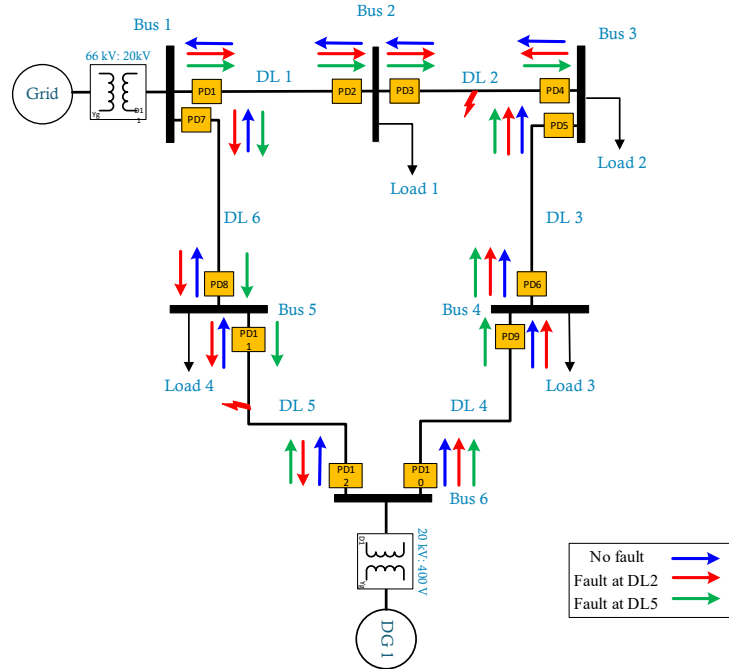


Fig. B.22 Ring grid

In Fig. B.22, the location of the DG is changed to be connected to bus 6. The same conclusions from previous cases are obtained here as seen in Table B.22 and Table B.23.

Table B.22 CE decision

Fault	Direction Relays												NN Decision
	PD1	PD2	PD3	PD4	PD5	PD6	PD7	PD8	PD9	PD10	PD11	PD12	
No	0	0	0	0	0	0	0	0	0	0	0	0	0
DL2	0	0	0	1	1	1	1	1	0	0	0	0	2
DL5	0	0	0	0	1	1	1	1	1	0	0	0	5

Table B.23 ZO decision

Fault	Direction Relays											
	PD1	PD2	PD3	PD4	PD5	PD6	PD7	PD8	PD9	PD10	PD11	PD12
No Fault	0	0	0	0	0	0	0	0	0	0	0	0
DL2	0	0	0	1	1	1	1	1	0	0	0	0
NN Decision	NN 1 = 2		NN 2 = 1		NN 3 = 3		NN 4 = 3		NN 5 = 2		NN 6 = 2	
DL5	0	0	0	0	1	1	1	1	1	0	0	0
NN Decision	NN 1 = 2		NN 2 = 2		NN 3 = 3		NN 4 = 3		NN 5 = 1		NN 6 = 2	

➤ Ring grid with one DG= 4 MW connected at Bus 6 and low loads values

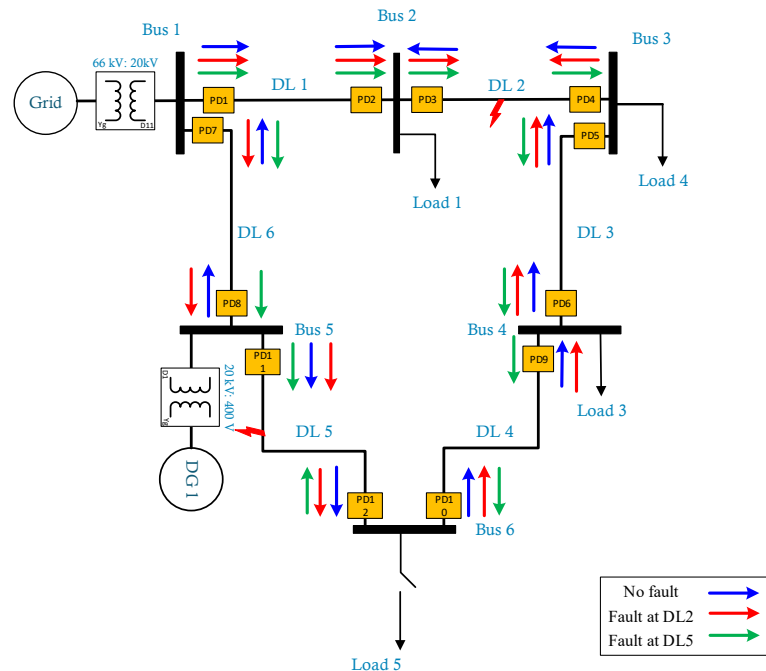


Fig. B.23 Ring grid

In Fig. B.23, the location of the DG is changed to be connected to bus 6. The same conclusions from previous cases are obtained here as seen in Table B.24 and Table B.25.

Table B.24 CE decision

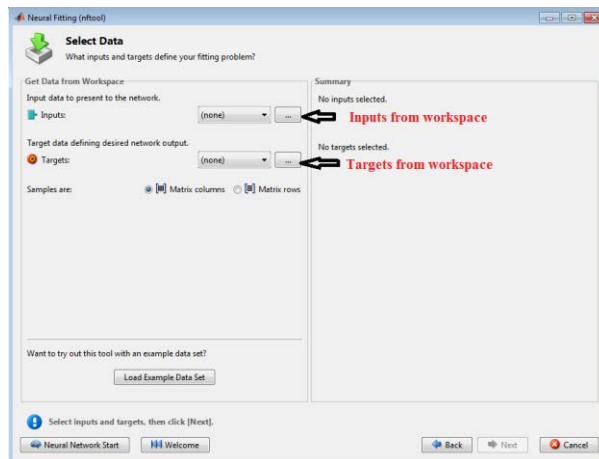
Fault	Direction Relays												NN Decision
	PD1	PD2	PD3	PD4	PD5	PD6	PD7	PD8	PD9	PD10	PD11	PD12	
No	0	0	0	0	0	0	0	0	0	0	0	0	0
DL2	0	0	0	1	1	1	1	1	1	1	0	0	2
DL5	0	0	0	0	0	0	0	0	1	0	0	0	5

Table B.25 ZO decision

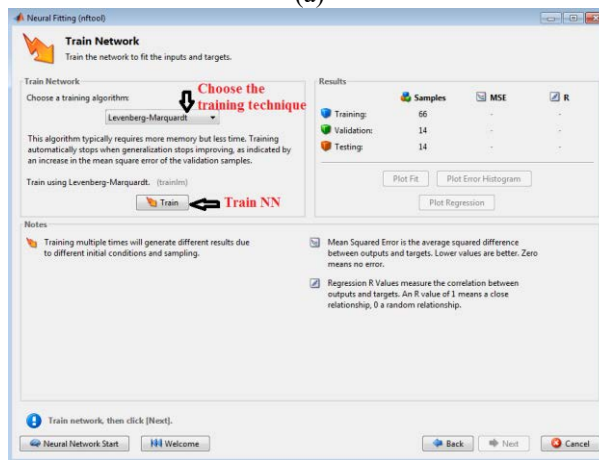
Fault	Direction Relays											
	PD1	PD2	PD3	PD4	PD5	PD6	PD7	PD8	PD9	PD10	PD11	PD12
No	0	0	0	0	0	0	0	0	0	0	0	0
DL2	0	0	0	1	1	1	1	1	1	1	1	1
NN Decision	NN 1 = 2		NN 2 = 1		NN 3 = 3		NN 4 = 3		NN 5 = 3		NN 6 = 3	
DL5	0	0	0	0	0	0	0	0	1	0	0	0
NN Decision	NN 1 = 2		NN 2 = 2		NN 3 = 2		NN 4 = 2		NN 5 = 1		NN 6 = 2	

B.4. ANN fault classification

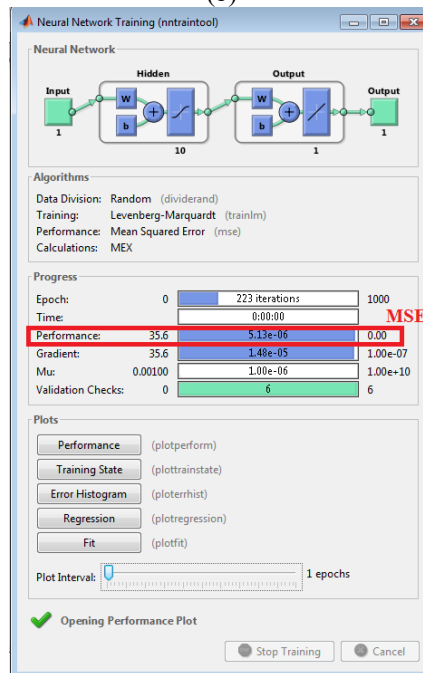
As shown in Fig. B.24, ANN can be trained using “nftool” by entering the desired inputs to the tool through the workspace (Fig. B.24(a)). Next, the most appropriate training method is chosen, which is “Levenberg Marquardt”, this technique takes more memory but less time, (Fig. B.24(b)). Finally, the ANN is trained and tested, in order to obtain satisfactory results, (Fig. B.24(c)).



(a)



(b)



(c)

Fig. B.24 ANN training steps

C. Appendix C

Solid State Relay and Mechanical breaker demonstration

C.1. Solid-state relay features

SSR has advantages over electromagnetic relays: high reliability, no contact, no spark, long service life, fast switching speed, strong anti-interference capability, and small size. This has been commonly used in large applications such as Computer Numerical Control (CNC) machines, remote control systems, and industrial automation systems, chemical industry, medical equipment, network protection, etc. In the next subsections, the most important features of SSR is explained.

➤ Principle of operation

An SSR is an electronic switching device that turns on or off when connected through its control terminals with a small external voltage. SSRs consist of an appropriate input (control signal), a solid-state electronic switching device that switches power to the load circuitry, and a coupling mechanism that allows the control signal to activate this switch without mechanical parts, as shown in Fig. C.1. The relay may be designed to switch either AC or DC to charging. It serves the same function as an electromechanical relay but it does not have moving components. Packaged solid-state relays use power semiconductor devices like thyristors and transistors to switch currents to approximately a hundred amperes. SSR response times can typically be as low as 1 ms.

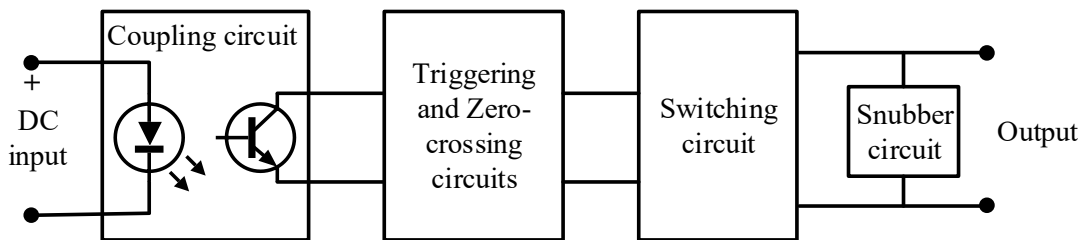


Fig. C.1 SSR block diagram

When functioning, the AC output will control the on-off state by adding the desired control signal to the SSR input circuit and then achieving the switching function. The coupling circuit provides a path for control signal feedback between input and output terminals but blocks off the electrical link between input and output to keep the output from affecting inputs. Components used in the coupling circuits are "optical couplers" which have strong sensitivity for action, fast response speed, high input/output insulation level (withstanding voltage). A light-emitting diode is a load at the input terminal (galvanic separation), which makes SSR input very easy to match the input signal level. In usage, it can be attached directly to the output interface of the controller, which is controlled by the logic level of "1" and "0". The purpose of the trigger circuit is to produce the desired signal to drive the switching circuit operation. However, the switching circuit can generate Radio Frequency Interference (RFI) and create high harmonics or peaks without a special control circuit, so a zero-crossing control circuit is designed for this purpose. Zero crossing means, by placing the control signal and AC voltage crossing zero, SSR becomes on-state; after switching off the control signal, SSR is not off-state until the AC current becomes the positive half cycle and the negative half cycle (zero potential) at the junction. That design prevents higher harmonics from interfering. The snubber circuit is designed to avoid effect and interruption from the surges and spikes (voltage) from the power supply when switching Triac part. Normally snubber circuit or non-linear resistance Metal-Oxide Varistor (MOV) of the RC series is used.

C.2. Evaluation of SSR response

The performance of the Crydom SSR was examined to evaluate its response to sudden changes in the input voltage. The relay was tested using a pulse signal with frequency = 1 kHz. As seen in Fig. C.2(a) and Fig. C.2(b), the output of the SSR follows the input signal with a minimal delay time (approximately 50 μ s). Moreover, as shown in Fig. C.3, the relay ensures zero-crossing detection. This step is essential to protect the relay from sparks and mechanical failure.

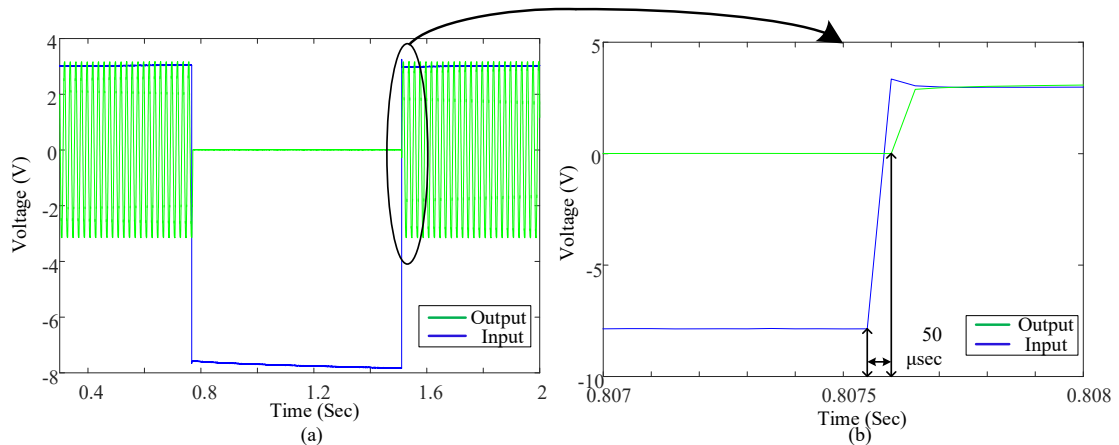


Fig. C.2 SSR response vs. input pulse signal (a) during on/off state, (b) On-state zooming

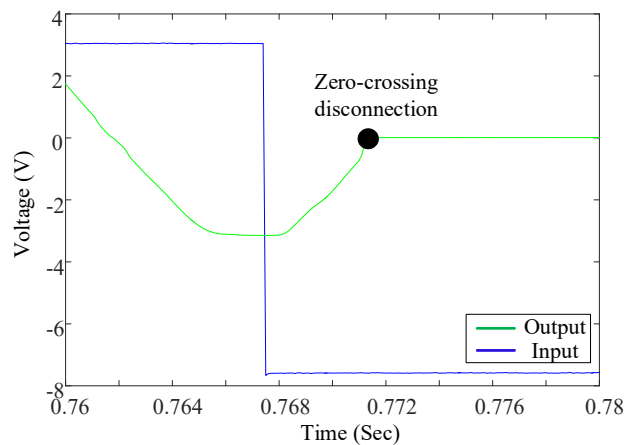


Fig. C.3 disconnection SSR disconnect at zero-crossing

C.3. Troubleshooting

In this section, the troubleshooting with SSR is explained, and the solutions for these problems are discussed.

In the case shown in Fig. C.4 with one line only, the SSR can be controlled without problems.

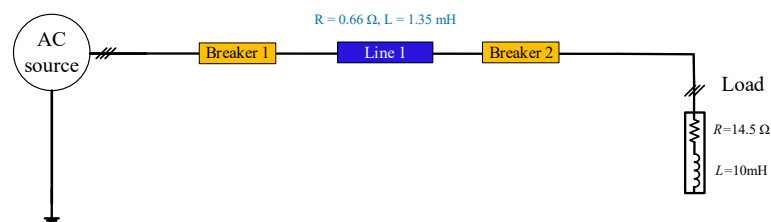


Fig. C.4 One line radial grid

However, when one or two lines are connected in parallel with line 1, as shown in Fig. C.5, the SSR does not work; as the voltage difference at the SSR is less than 48 V, which is the value needed to operate the SSR, if the voltage difference value is below 48 V then the SSR is always open.

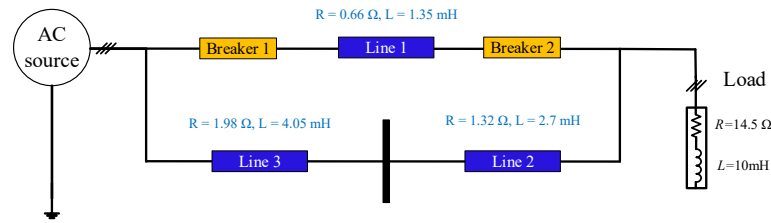


Fig. C.5 ring grid

The problem is due to the low impedance of the two lines connected in parallel with Line 1, as shown in Fig. C.5, so the voltage difference across the SSR terminals is lower than the minimum voltage difference required to operate correctly, as shown in Fig. C.6.

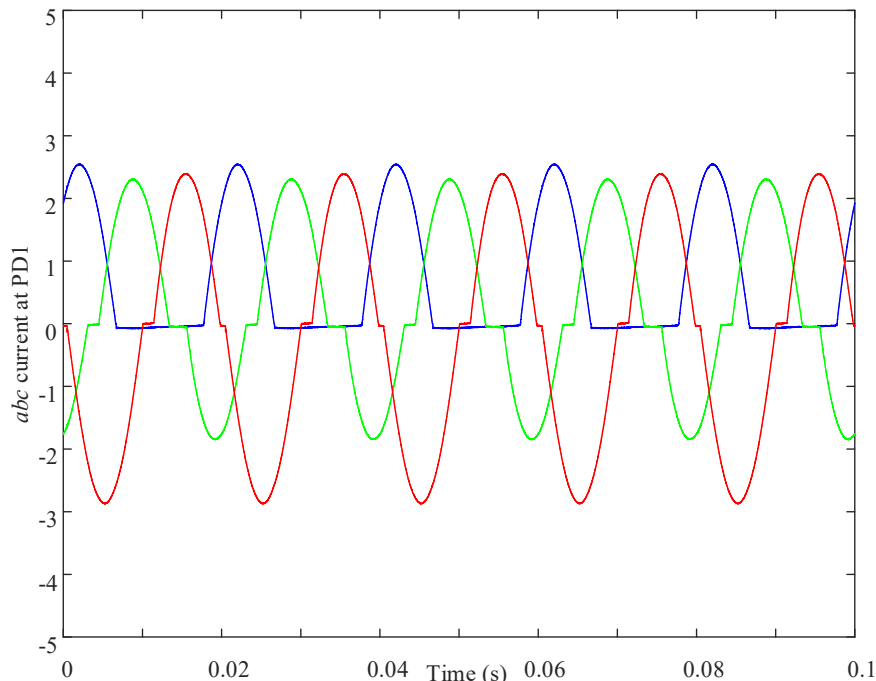


Fig. C.6 Current at PDI

As a solution for this problem, the SSR is replaced with a mechanical relay since they were the available components and no-additional time was required to perform the tests, without affecting the validation of the proposed algorithms. However, the main disadvantages of the mechanical relays are discussed in the following section.

C.4. Mechanical breaker demonstration

In this section, the explanation of the disconnection of the mechanical breaker is discussed in order to understand the behaviour of the breaker, especially during disconnection.

Fig. C.7 shows the behaviour of CE-ZO for single-phase to ground fault when the fault is at DL1, as seen in Fig. C.8.

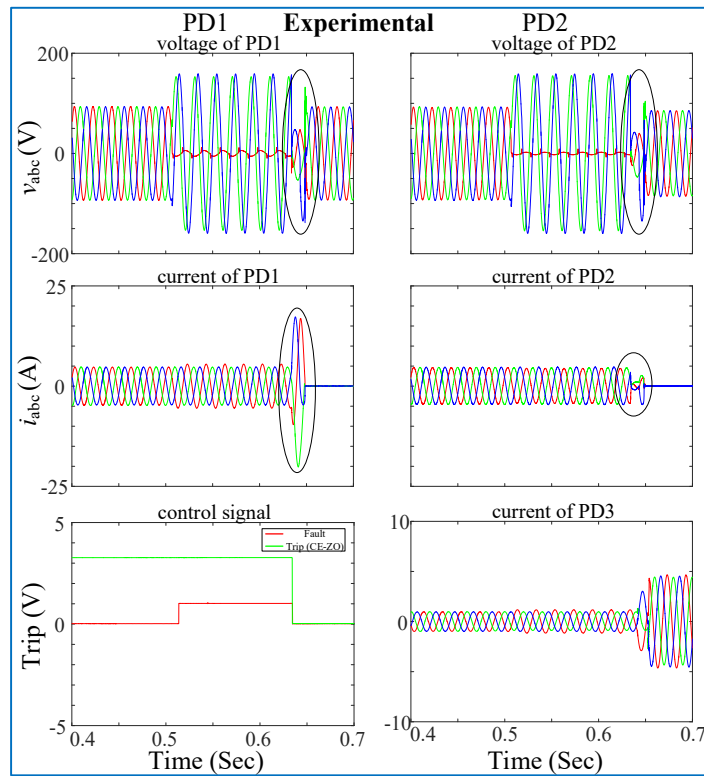


Fig. C.7 Behaviour of CE-ZO for single-phase to ground fault when the fault at DL1

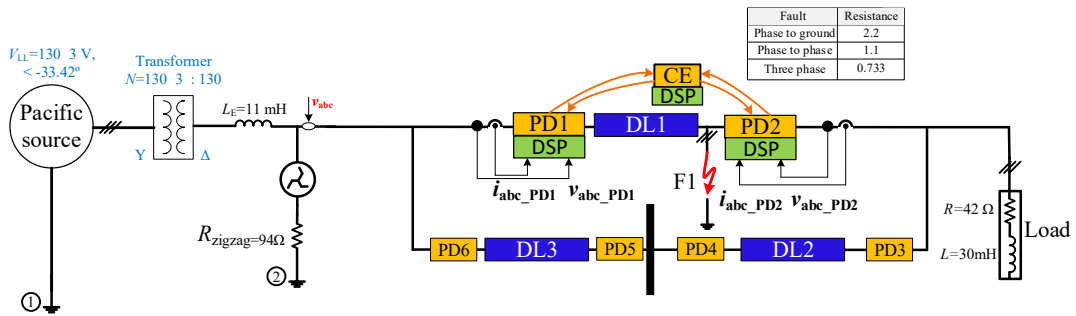


Fig. C.8 Scheme of ring grid without DG

An overshoot in the abc current in PD1 is produced during the tripping (black in Fig. C.7). This overshoot is produced from the arcing process during the disconnection. Therefore, the disconnection will last for two or more cycles, which is a disadvantage compared with the SSR that disconnects fast and at the first zero-crossing current. Fig. C.9 shows the abc voltage and current of PD1 during the tripping of the breaker. As seen, there is a drop of voltage in the three phases, which means the single-phase fault during the sag is transformed to a three-phase fault. The ionized air creates low impedance pathways, forming a three-phase fault that increases the abc currents [194]–[196].

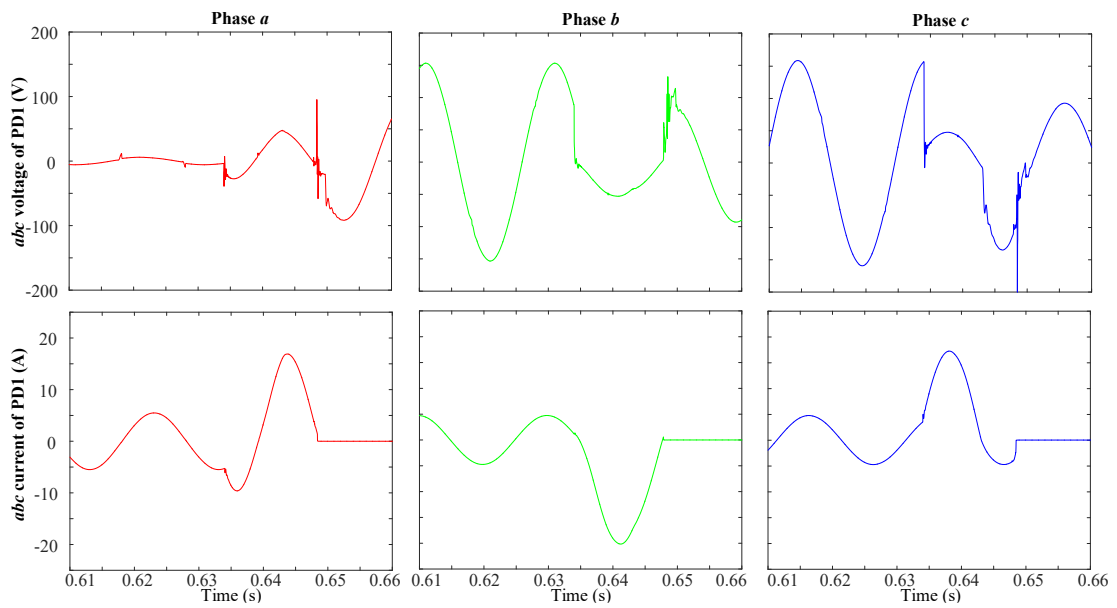


Fig. C.9 *abc* voltage, current and impedance of PD1

As explained in chapter 7, the implemented grid in the laboratory is a scaled grid to emulate the analyzed MV grid and validate the algorithms. Therefore, the problem with the mechanical contactor that appears in the scaled laboratory grid, an LV grid, could not appear in the MV grid because they are constructively different [197].

D. Appendix D

Experimental verification of the protection algorithms

D.1. Total number of analysed cases

Fig. D.1, Fig. D.2, and Fig. D.3 show the simplified radial grid, the complete radial grid and the ring grid, respectively. Table D.1 shows the total number of experimentally implemented cases in the laboratory.

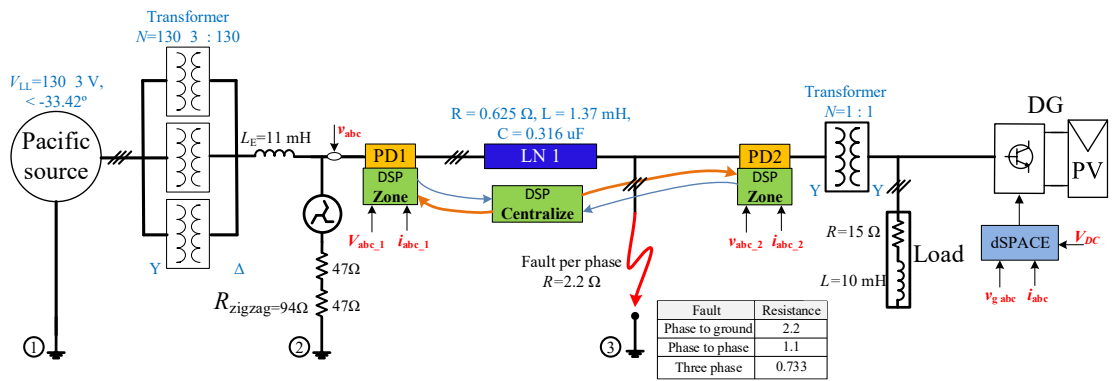


Fig. D.1 Scheme of the Simplified radial grid with DG

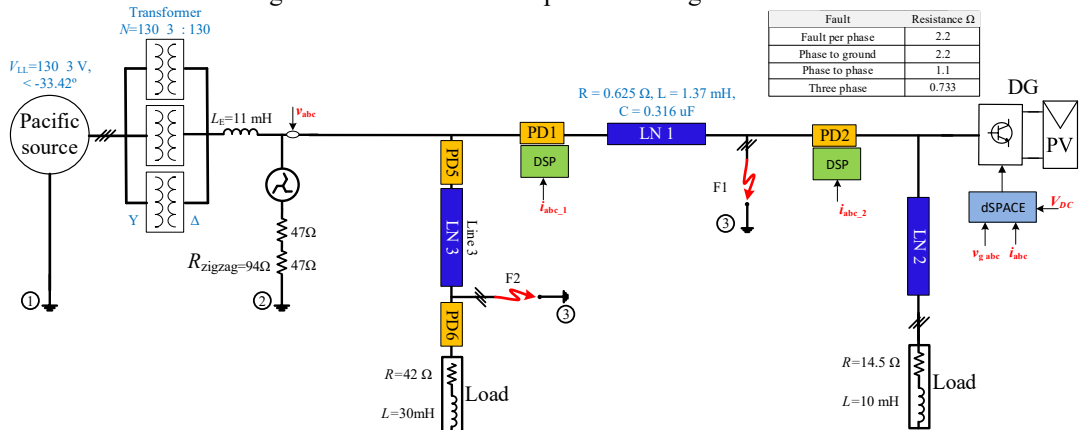


Fig. D.2 Scheme of the complete radial grid with DG

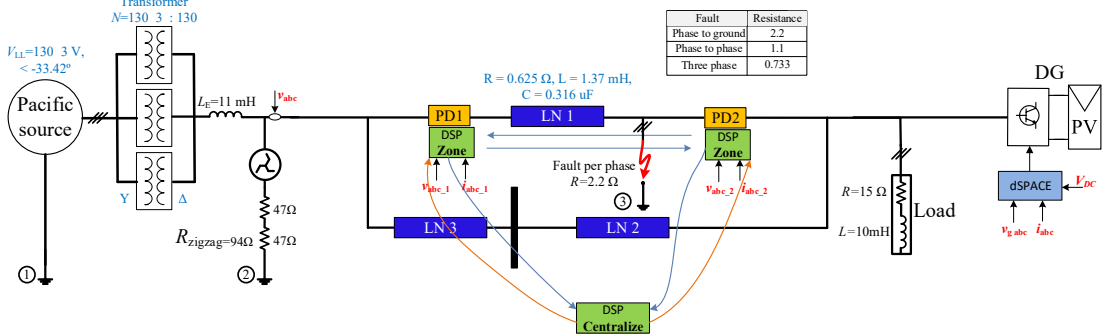


Fig. D.3 Scheme of ring grid with DG

Table D.1 shows the total number of the implemented cases in the laboratory

Case No.	Grid configuration	Fault type	Fault location	DG penetration	Protection algorithm	Current control strategy
1	Radial (one line)	Single-phase to ground	DL1	No DG	CE-ZO	--
2	Radial (one line)	Three-phase	DL1	No DG	CE-ZO	--
3	Radial (one line)	Single-phase to ground	DL1	No DG	LO	--
4	Radial (one line)	Three-phase	DL1	No DG	LO	--
5	Radial (one line)	Single-phase to ground	DL1	With DG	CE-ZO	BCC
6	Radial (one line)	Three-phase	DL1	With DG	CE-ZO	BCC
7	Radial (one line)	Single-phase to ground	DL1	With DG	LO	BCC
8	Radial (one line)	Three-phase	DL1	With DG	LO	BCC
9	Radial (one line)	Single-phase to ground	DL1	With DG	CE-ZO	CPC
10	Radial (one line)	Three-phase	DL1	With DG	CE-ZO	CPC
11	Radial (one line)	Single-phase to ground	DL1	With DG	CE-ZO	CRC
12	Radial (one line)	Three-phase	DL1	With DG	CE-ZO	CRC
13	Radial (three line)	Single-phase to ground	DL1	No DG	OCR	--
14	Radial (three-line)	Three-phase	DL1	No DG	OCR	--
15	Radial (three-line)	Single-phase to ground	DL1	No DG	DR	--
16	Radial (three-line)	Three-phase	DL1	No DG	DR	--
17	Radial (three-line)	Single-phase to ground	DL3	No DG	OCR	--
18	Radial (three-line)	Three-phase	DL3	No DG	OCR	--
19	Radial (three-line)	Single-phase to ground	DL3	No DG	DR	--
20	Radial (three-line)	Three-phase	DL3	No DG	DR	--
21	Radial (three	Single-	DL3	with DG	OCR	BCC

Table D.1 Cont'd

22	Radial (three line)	Three-phase to ground	DL3	with DG	OCR	BCC
23	Radial (three line)	Single-phase to ground	DL3	with DG	DR	BCC
24	Radial (three line)	Three-phase to ground	DL3	with DG	DR	BCC
25	Radial (three line)	Single-phase to ground	DL3	No DG	CE-ZO	--
26	Radial (three line)	Three-phase to ground	DL3	No DG	CE-ZO	--
27	Radial (three line)	Single-phase to ground	DL3	with DG	CE-ZO	BCC
28	Radial (three line)	Three-phase to ground	DL3	with DG	CE-ZO	BCC
29	Radial (three line)	Single-phase to ground	DL1	with DG	OCR	BCC
30	Radial (three line)	Three-phase to ground	DL1	with DG	OCR	BCC
31	Radial (three line)	Single-phase to ground	DL1	with DG	DR	BCC
32	Radial (three line)	Three-phase to ground	DL1	with DG	DR	BCC
33	Radial (three line)	Single-phase to ground	DL1	No DG	CE-ZO	--
34	Radial (three line)	Three-phase to ground	DL1	No DG	CE-ZO	--
35	Radial (three line)	Single-phase to ground	DL1	with DG	CE-ZO	BCC
36	Radial (three line)	Three-phase to ground	DL1	with DG	CE-ZO	BCC
37	Ring grid	Single-phase to ground	DL1	No DG	CE-ZO	--
38	Ring grid	Three-phase to ground	DL1	No DG	CE-ZO	--
39	Ring grid	Single-phase to ground	DL1	No DG	LO	--
40	Ring grid	Three-phase to ground	DL1	No DG	LO	--
41	Ring grid	Single-phase to ground	DL1	with DG	CE-ZO	BCC
42	Ring grid	Three-	DL1	with DG	CE-ZO	BCC

Table D.1 Cont'd

43	Ring grid	phase to ground Single-phase to ground	DL1	with DG	LO	BCC
44	Ring grid	Three-phase to ground	DL1	with DG	LO	BCC
45	Ring grid	Single-phase to ground	DL3	No DG	CE-ZO	--
46	Ring grid	Three-phase to ground	DL3	No DG	CE-ZO	--
47	Ring grid	Single-phase to ground	DL3	No DG	LO	--
48	Ring grid	Three-phase to ground	DL3	No DG	LO	--
49	Ring grid	Single-phase to ground	DL3	with DG	CE-ZO	BCC
50	Ring grid	Three-phase to ground	DL3	with DG	CE-ZO	BCC
51	Ring grid	Single-phase to ground	DL3	with DG	LO	BCC
52	Ring grid	Three-phase to ground	DL3	with DG	LO	BCC
53	Ring grid	two-phase to ground	DL1	No DG	LO	--
54	Ring grid	two-phase to ground	DL1	with DG	LO	BCC
55	Ring grid	Single-phase to ground	DL2	No DG	CE-ZO	--
56	Ring grid	Three-phase to ground	DL2	No DG	CE-ZO	--
57	Ring grid	Single-phase to ground	DL2	with DG	CE-ZO	BCC
58	Ring grid	Three-phase to ground	DL2	with DG	CE-ZO	BCC
59	Ring grid	Single-phase to ground	DL1	No DG	LO (No recloser)	--
60	Ring grid	Three-phase	DL1	No DG	LO (No recloser)	--
61	Ring grid	Single-phase to	DL1	No DG	LO (with recloser)	--

Table D.1 Cont'd

62	Ring grid	ground Three-phase	DL1	No DG	LO (with recloser)	--
63	Ring grid	Single-phase to ground	DL1	With DG	LO (No recloser)	BCC
64	Ring grid	Three-phase	DL1	With DG	LO (No recloser)	BCC
65	Ring grid	Single-phase to ground	DL1	With DG	LO (with recloser)	BCC
66	Ring grid	Three-phase	DL1	With DG	LO (with recloser)	BCC
67	Ring grid	Single-phase to ground	DL1	with DG	CE-ZO	CPC
68	Ring grid	Three-phase to ground	DL1	with DG	CE-ZO	CPC
69	Ring grid	Single-phase to ground	DL1	with DG	CE-ZO	CRC
70	Ring grid	Three-phase to ground	DL1	with DG	CE-ZO	CRC

D.2. Implementation on dSPACE

The values of the abc voltages and currents of the faulted line are implemented in the dSPACE to emulate the faulted line in the grid.

➤ Description of SIMULINK file in ControlDesk

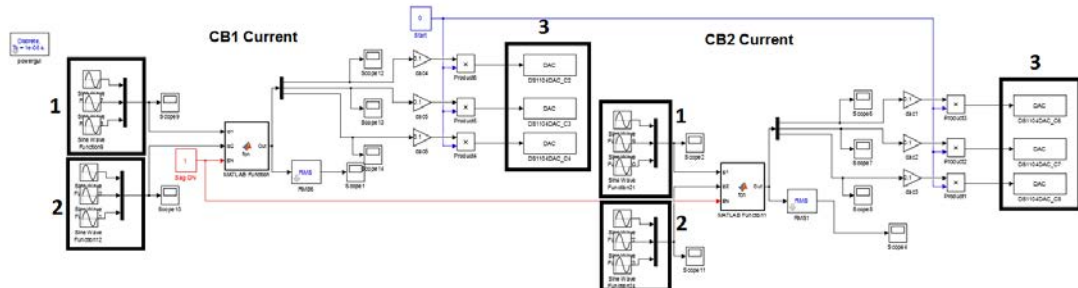


Fig. D.4 Simulink file of the currents at each PD located at the faulted line

- Generation of the abc voltages and currents before the fault, for both breakers at each end of the faulted line.
- Generation of the abc voltages and currents during the fault, for both breakers at each end of the faulted line.
- Digital to Analog Converter (DAC) of dSPACE.

The abc voltage and current signals of the two PDs located at the faulted line are generated in two different files. Then, these data are stored inside the DSP. This is because the dSPACE has only 8 DACs; so, it is not possible to generate 12 signals at the same time (Fig. D.4). The voltages and currents are used to identify the type of fault, and to identify power flow to identify the location of the fault.

➤ Communication between dSPACE and DSP

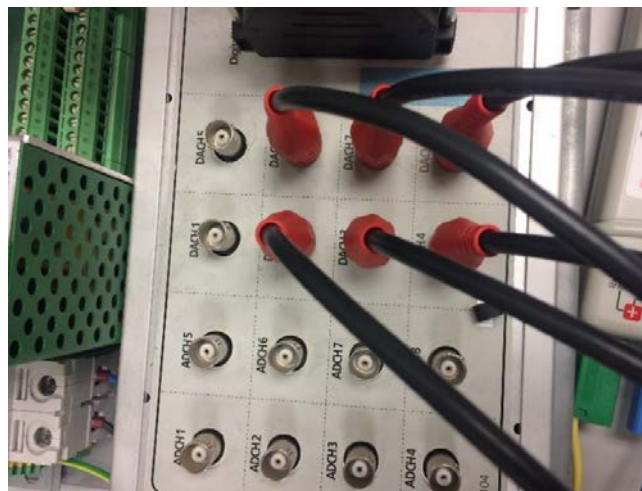
After the signals generation from the dSPACE using DAC, these signals are sent to the DSP via the Op-Amp circuit (Fig. D.5). The Op-Amp circuit has two tasks 1) to offset the input signal above zero. 2) to margin the input signal to a value between (0 - 3.3 V). Next, these signals are sent to the DSP's ADC.



(a) Op-Amp circuit



(b) Inputs to DSP



(c) Outputs of dSPACE

Fig. D.5 Connection of dSPACE 1104, OP-AMP, and DSP

➤ DSP program

In this step, the algorithms of all strategies will be implemented (CE, ZO, and LO).

- Centralize control (CE)

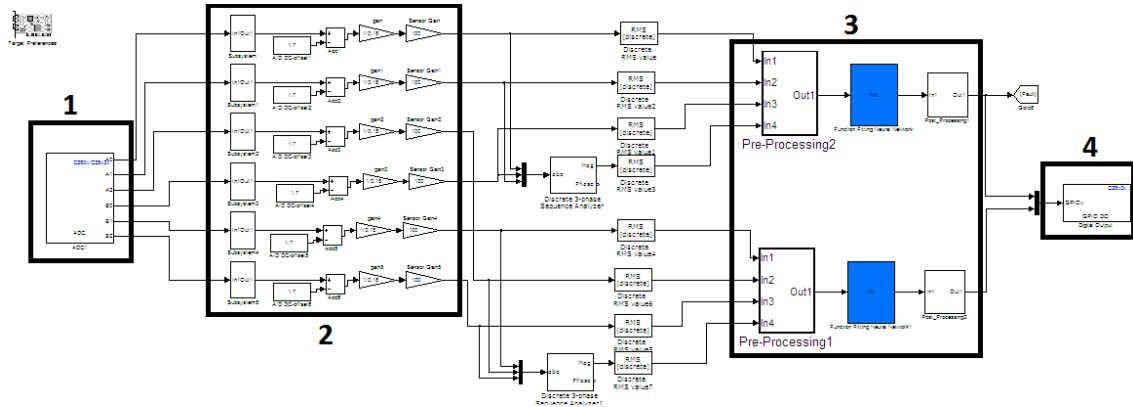


Fig. D.6 SIMULINK program for fault type identification

Fig. D.6 shows the SIMULINK program used to identify the type of fault. The numerations in the figure are corresponding to:

- 1- Inputs: *abc* voltages of both breakers at the faulted line.
- 2- Signal configuration, to obtain the actual signal before sending it to the algorithm.
- 3- ANN.
- 4- Output decision.

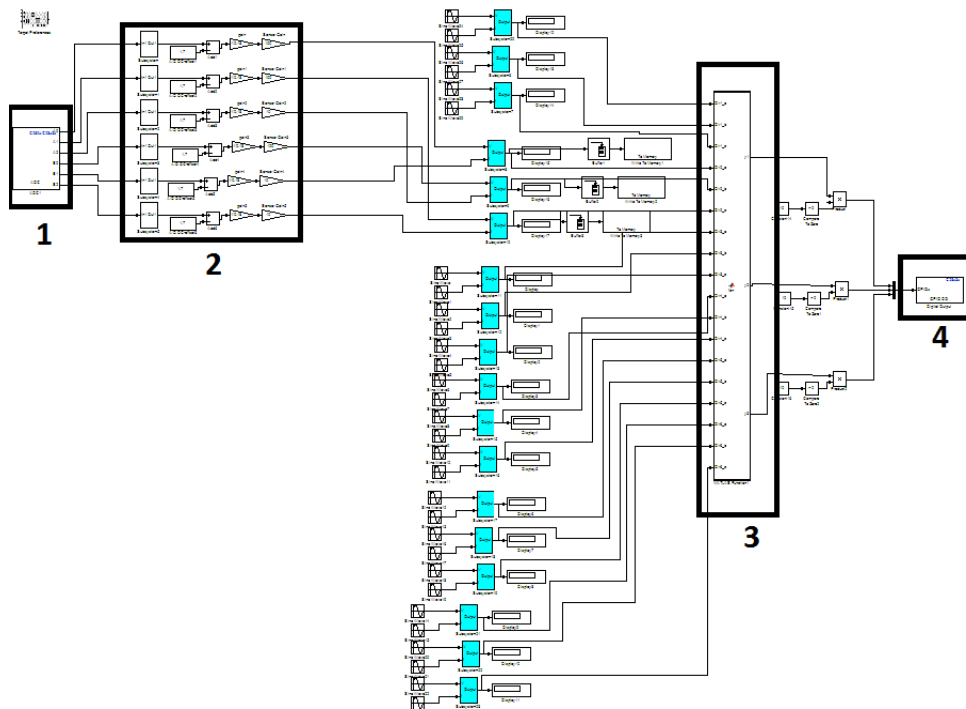


Fig. D.7 SIMULINK program for fault location (CE)

Fig. D.7 the SIMULINK program used to locate the fault. The numerations in the figure are corresponding to:

- 1- Inputs: *abc* currents of both breakers at the faulted line.
 - 2- Signal configuration, to obtain the actual signal before sending it to the algorithm.
 - 3- power flow Calculation and ANN
 - 4- Output decision.
- Zone control (ZO)

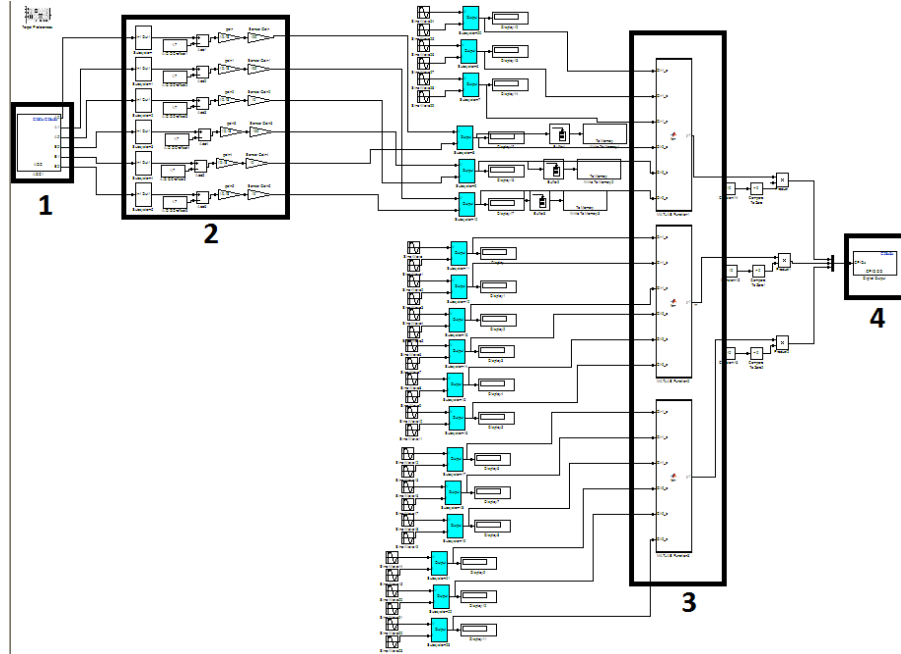


Fig. D.8 SIMULINK program for fault location (ZO)

Fig. D.8 the SIMULINK program used to locate the fault. The numerations in the figure are corresponding to:

- 1- Inputs: *abc* currents of both breakers at the faulted line.
 - 2- Signal configuration, to obtain the actual signal before sending it to the algorithm.
 - 3- power flow Calculation and ANN for each line
 - 4- Output decision.
- Local control

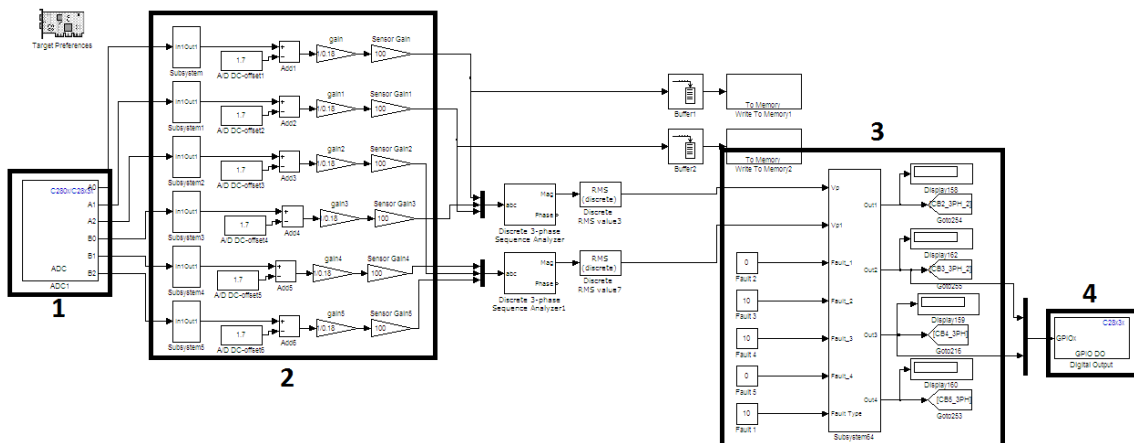


Fig. D.9 SIMULINK program for fault location (LO)

Fig. D.9 the SIMULINK program used to locate the fault. The numerations in the figure are corresponding to:

- 1- Inputs: *abc* voltages of both breakers at the faulted line.
- 2- Signal configuration, to obtain the actual signal before sending it to the algorithm.
- 3- Positive and negative sequence components of the *abc* voltage at both ends of the faulted line. Then the algorithm is based on these values.
- 4- Output decision.

➤ Results

All the following results are for the ring grid. The following figures show the results of the measurement signals at the inputs of the DSP, Op-Amp, and the outputs of DSP.

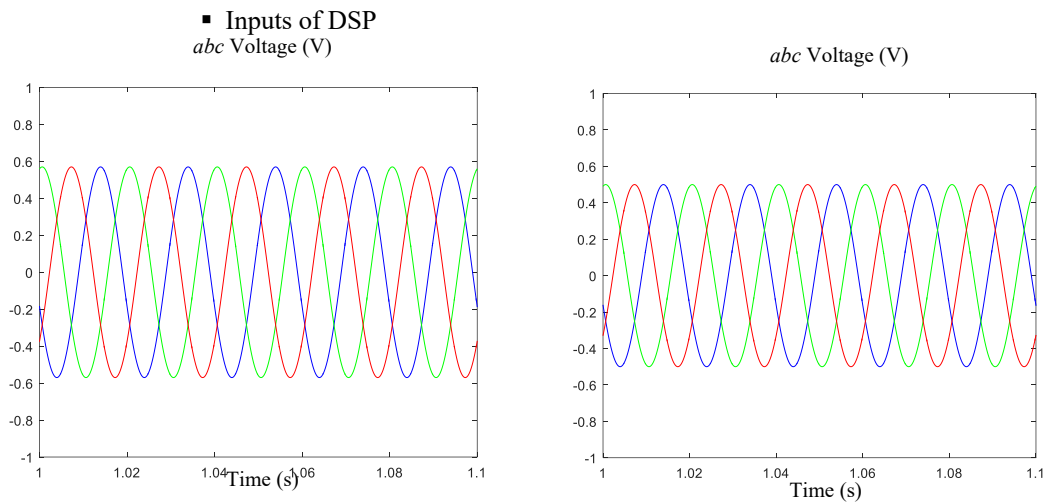


Fig. D.10 *abc* voltages from dSPACE in case of a three-phase fault (Control desk) (PD1 and PD2)

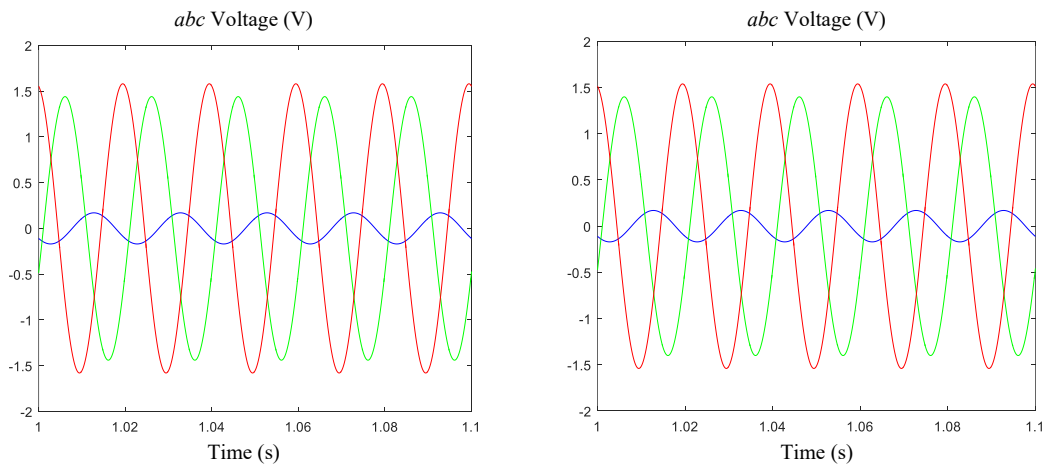


Fig. D.11 *abc* voltages from dSPACE in case of single-phase to ground fault (Control desk) (PD1 and PD2)

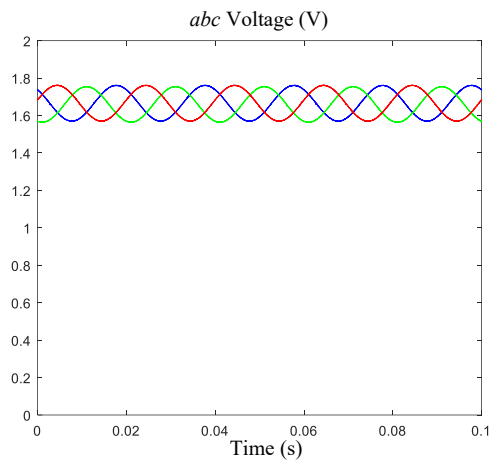


Fig. D.12 *abc* voltages to ADC of DSP in case of a three-phase fault (Scope) (PD1)

As seen in Fig. D.12 ~ Fig. D.15, the *abc* voltage or current must be amplified and boosted before transmitted to the ADC of the DSP, then inside the DSP and using the SIMULINK code this signal is modified and scaled to return to its original value, as seen in Fig. D.16.

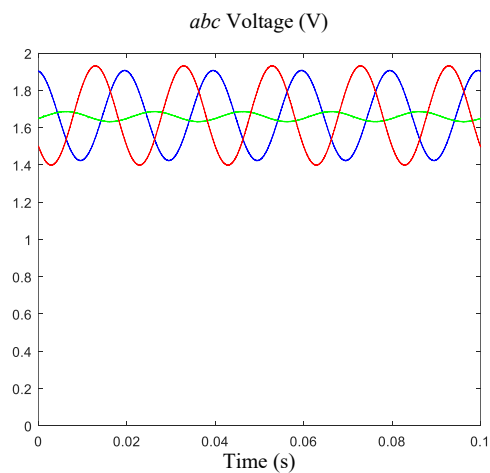


Fig. D.13 *abc* voltages to ADC of DSP in case of single-phase fault to the ground (Scope) (PD1)

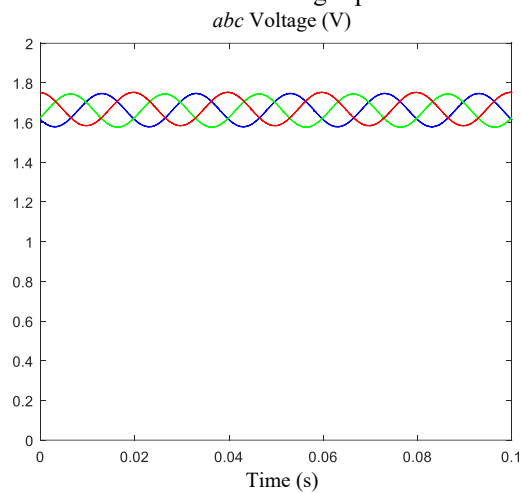


Fig. D.14 *abc* voltages to ADC of DSP in case of a three-phase fault (Scope) (PD2)

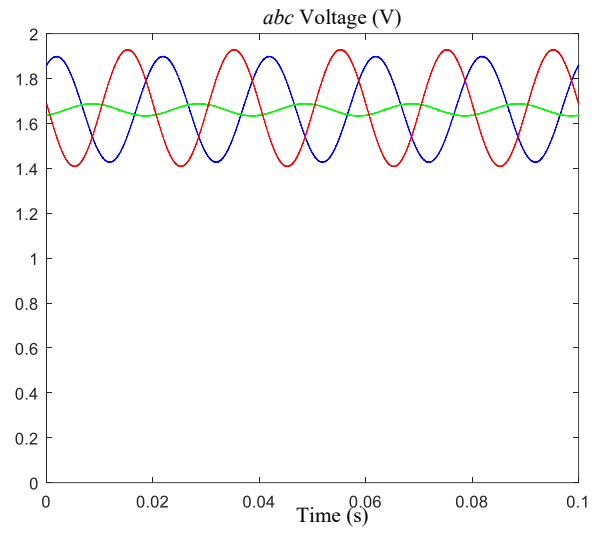
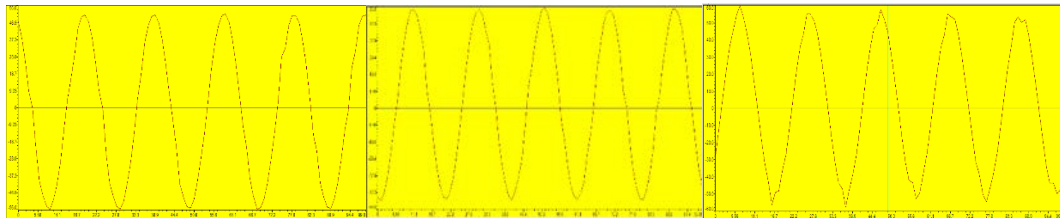
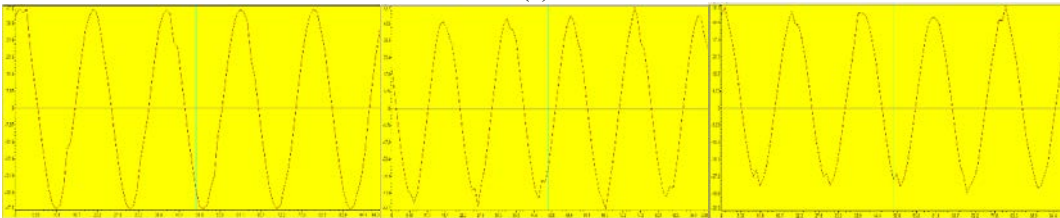


Fig. D.15 *abc* voltages to ADC of DSP in case of single-phase fault to the ground (Scope) (PD2)

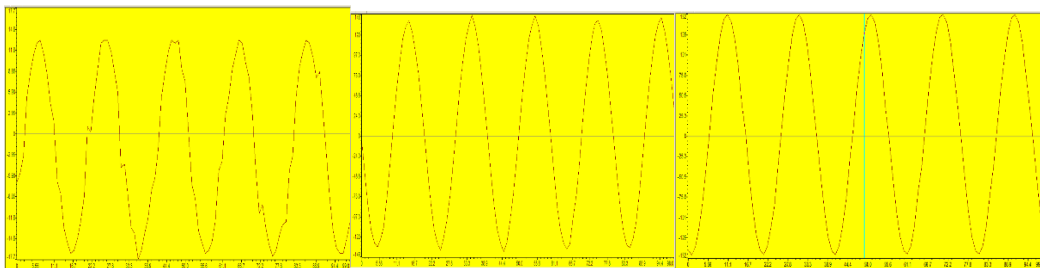


(a)



(b)

Fig. D.16 *abc* voltages to DSP in case of a three-phase fault (inside Code Composer) (a) for PD1, (b) for PD2



(a)

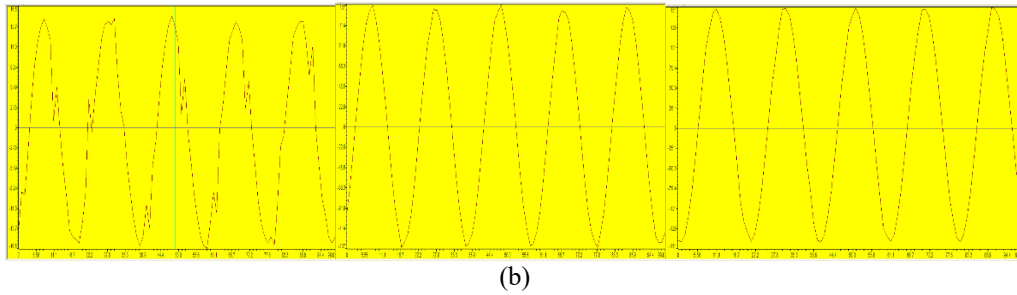


Fig. D.17 *abc* voltages to DSP in case of single-phase fault to the ground (inside Code Composer) (a) for PD1, (b) for PD2

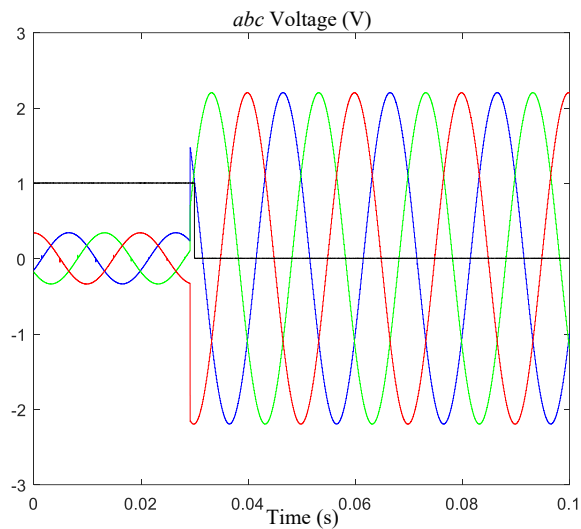


Fig. D.18 *abc* voltages vs. fault occurrence for three-phase voltage

Fig. D.18 shows the fault signal and the *abc* voltage before and during a three-phase fault, the figure shows the match between the two signals with a small delay (2 ms) due to the speed of the ADC of the dSPACE1104.

■ Outputs of DSP

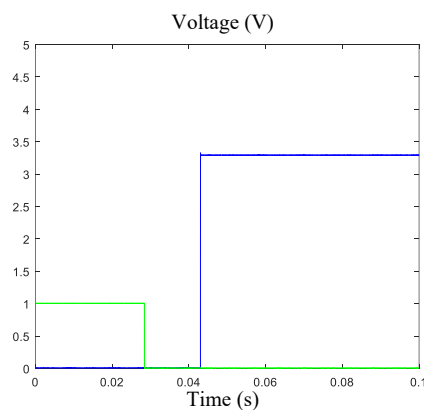


Fig. D.19 Digital output of the algorithm decision vs. fault occurrence (Three-phase fault)
Voltage (V)

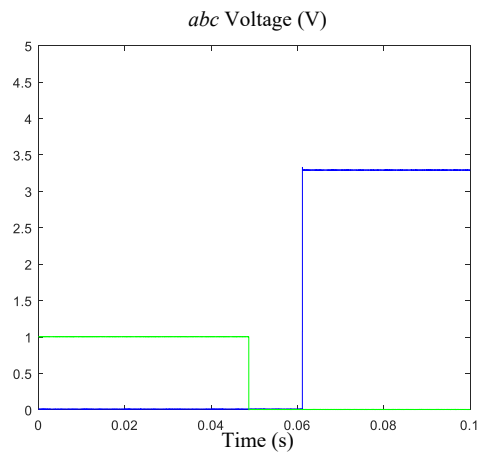


Fig. D.20 Digital output of the algorithm decision vs. fault occurrence (Single-phase fault)

Fig. D.19 and Fig. D.20 show the decision of the DSP vs. a fault.

○ Location of fault

The following figures show the inputs of DSP (output of dSPACE) (Fig. D.21 ~ (b)

Fig. D.28).

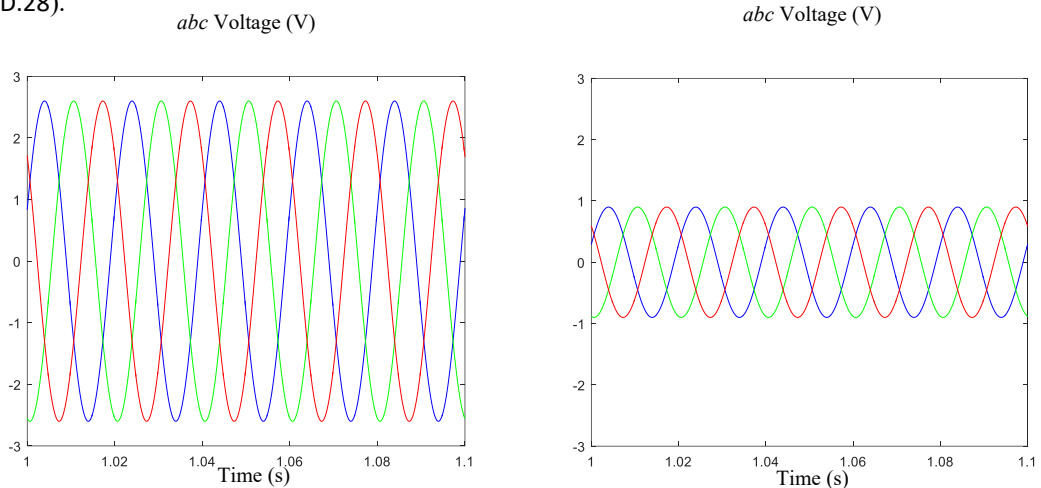


Fig. D.21 *abc* current from dSPACE in case of a three-phase fault (Control desk)

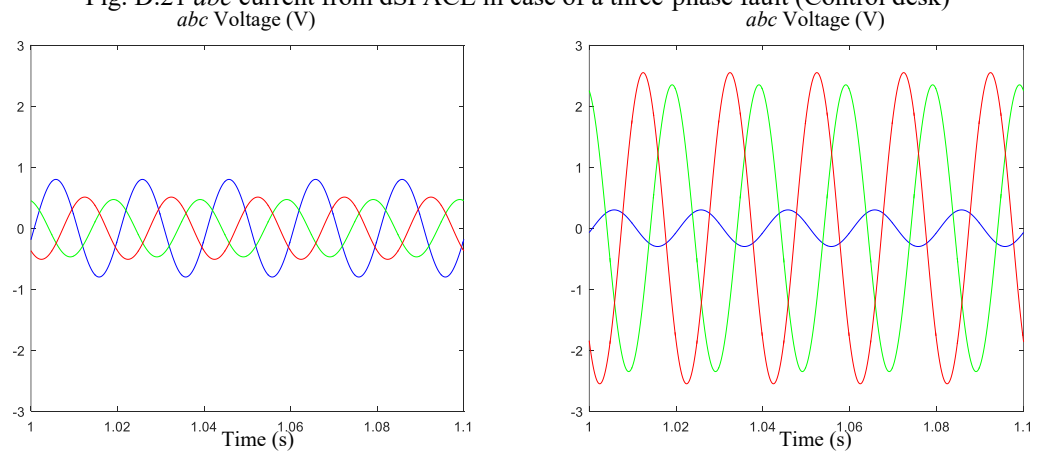


Fig. D.22 *abc* current from dSPACE in case of single-phase fault to the ground (Control desk)

abc Voltage (V)

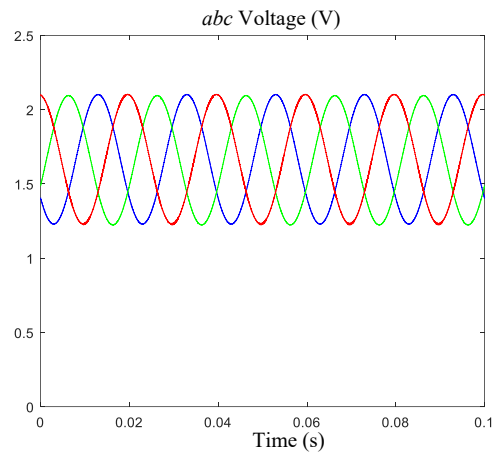


Fig. D.23 *abc* current to ADC of DSP in case of a three-phase fault (Scope) (PD1)

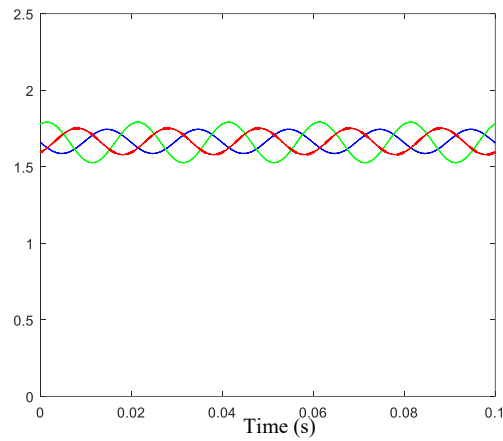


Fig. D.24 *abc* current to ADC of DSP in case of single-phase fault to the ground (Scope) (PD1)

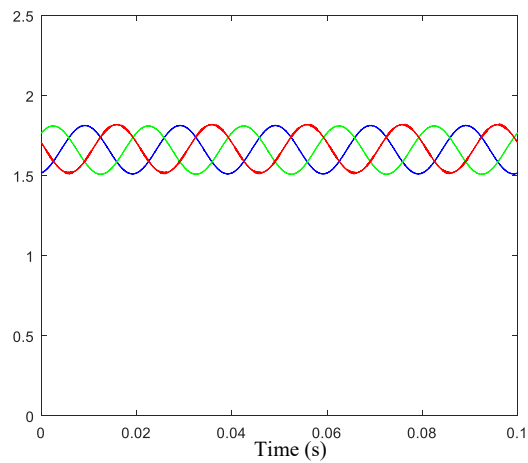


Fig. D.25 *abc* current to ADC of DSP in case of a three-phase fault (Scope) (PD2)

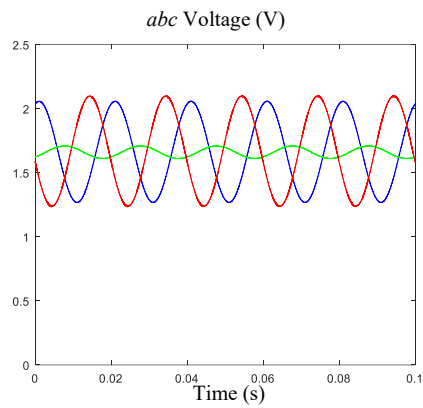
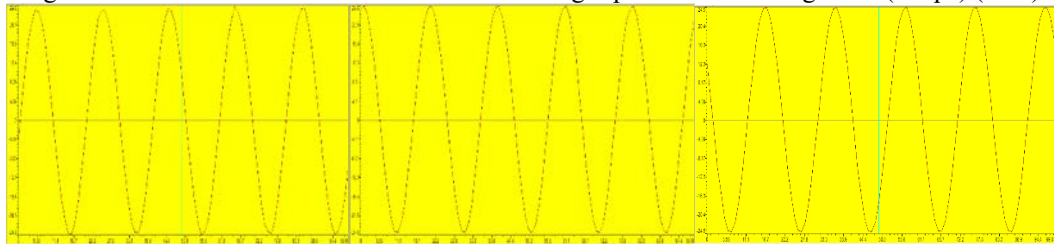
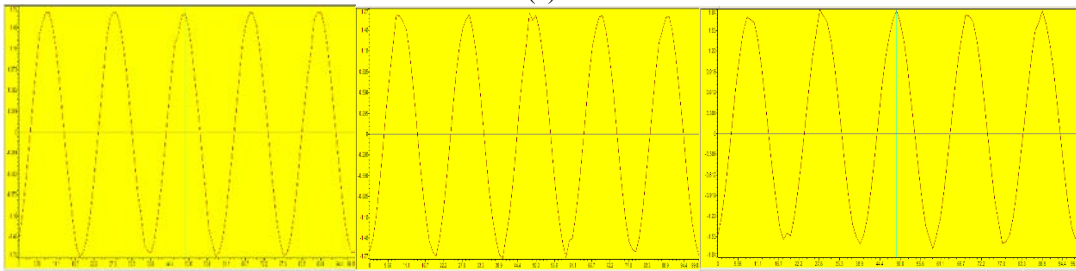


Fig. D.26 *abc* current to ADC of DSP in case of single-phase fault to the ground (Scope) (PD2)

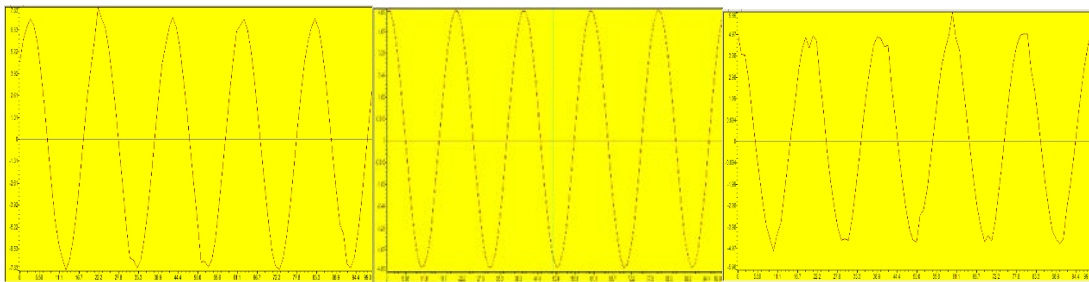


(a)

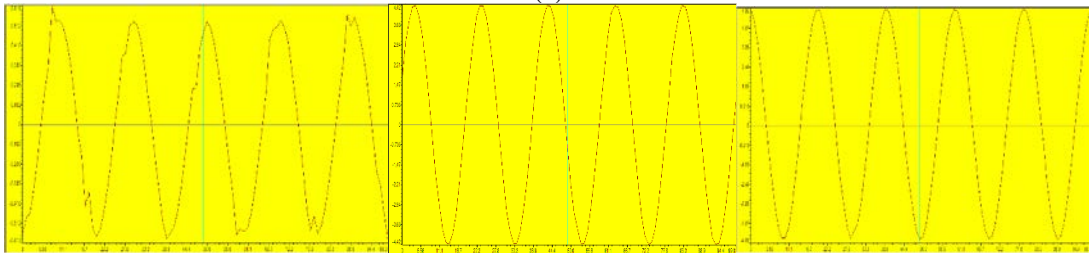


(b)

Fig. D.27 *abc* current to DSP in case of a three-phase fault (inside Code Composer) (a) for PD1, (b) for PD2



(a)



(b)

Fig. D.28 *abc* current to DSP in case of single-phase fault to the ground (inside Code Composer) (a) for PD1, (b) for PD2

○ Outputs of DSP

The following figures (Fig. D.29 and Fig. D.30) show the outputs of DSP.

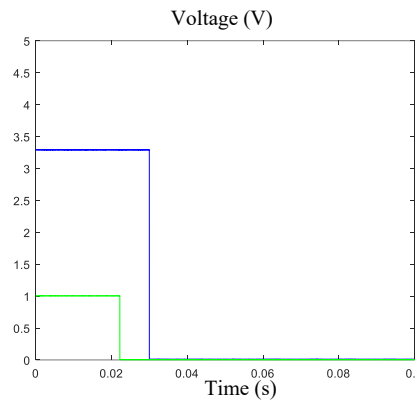


Fig. D.29 Digital output of the algorithm decision vs. fault occurrence (Three-phase fault)

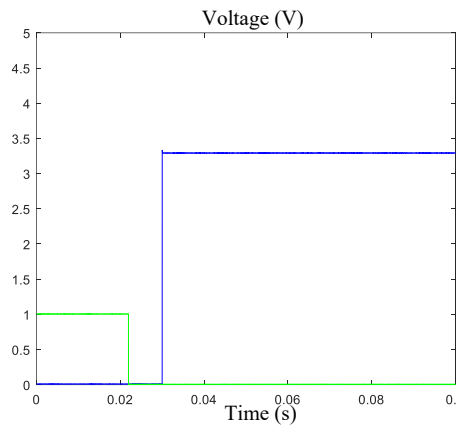


Fig. D.30 Digital output of the algorithm decision vs. fault occurrence (Single-phase fault)

Fig. D.29 and Fig. D.30 show the algorithm decision in the case of single-phase and three-phase faults.

D.3. Experimental results (Continue)

The rest of the experimental results are shown in this section for the simplified radial grid, complete radial grid, and ring grid, as follows:

D.3.1. Simplified radial grid without DG

➤ **Scheme**

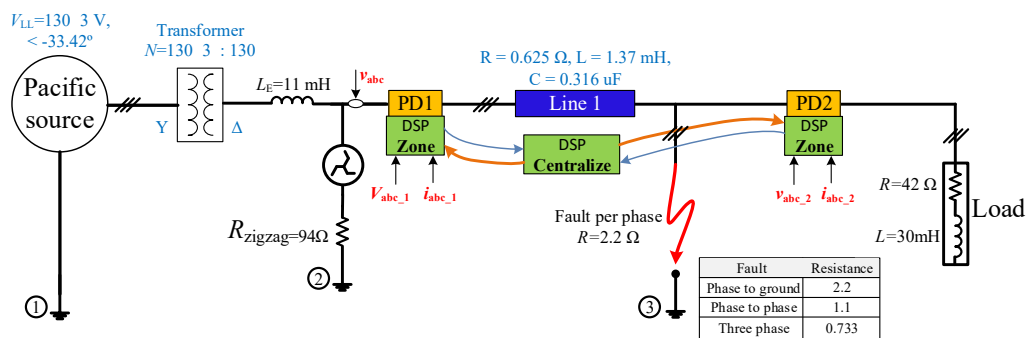


Fig. D.31 Scheme of Simplified radial grid (one line) without DG

➤ **LO control**

- Single-phase fault

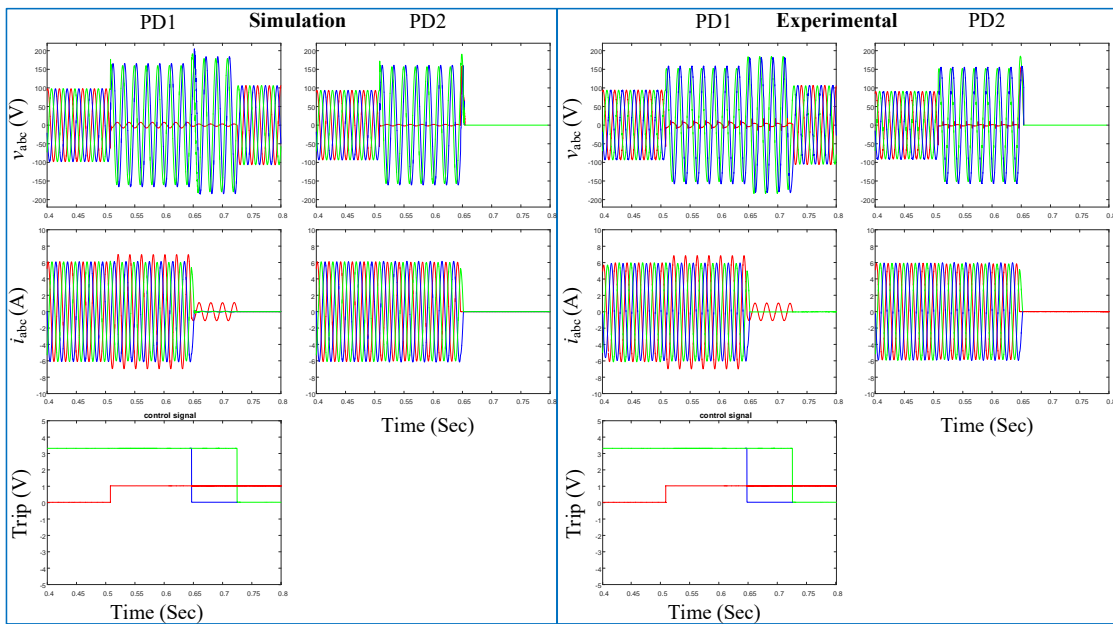


Fig. D.32 LO control in case of single-phase to ground without DG

D.3.2. Simplified radial grid with DG

➤ **LO control with BCC**

- Single-phase fault

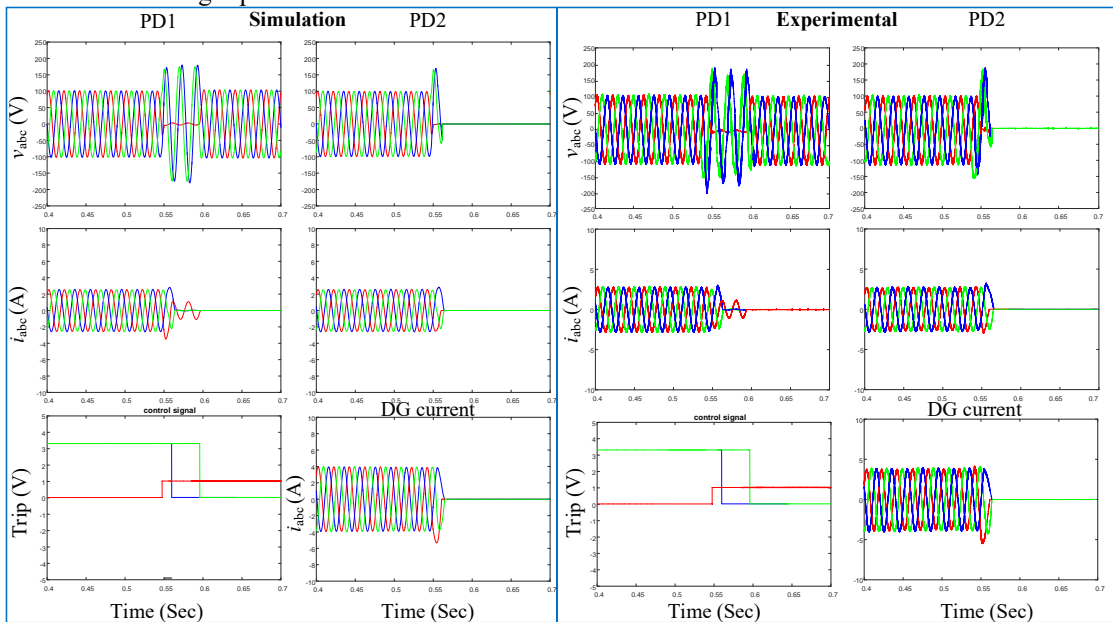


Fig. D.33 LO control in case of single-phase to ground with DG and BCC control

➤ **CE-ZO control with CPC**

• Three-phase fault

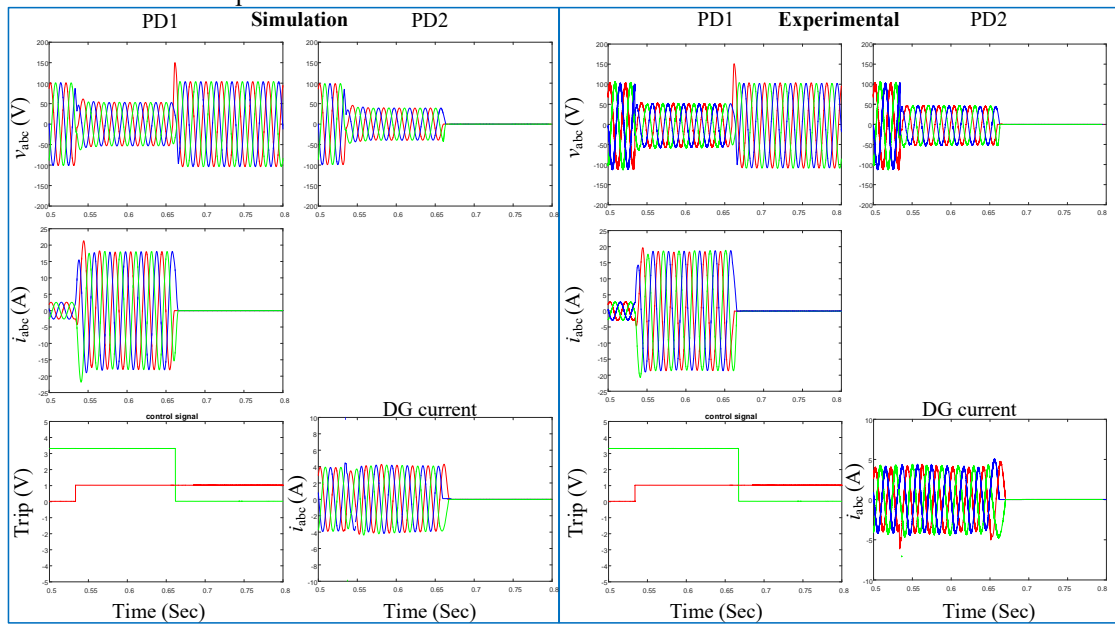


Fig. D.34 CE-ZO control in case of three-phase with DG and CPC control

➤ **CE-ZO control with CRC**

• Three-phase fault

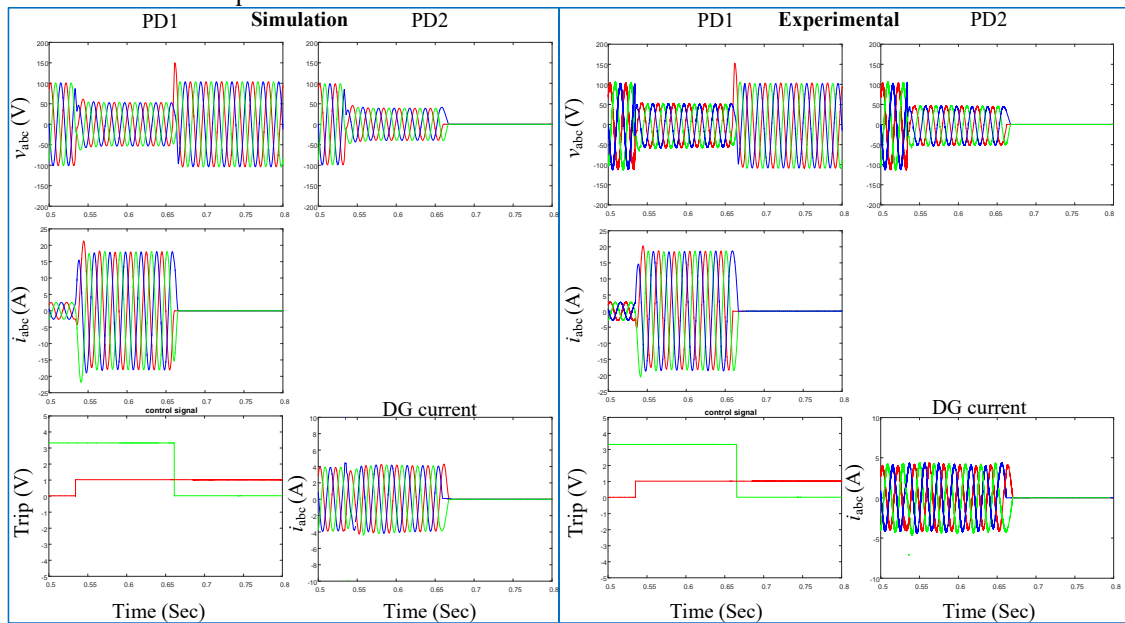


Fig. D.35 CE-ZO control in case of three-phase with DG and CRC control

D.3.3. Complete radial grid without DG

➤ Scheme (F1 and F2)

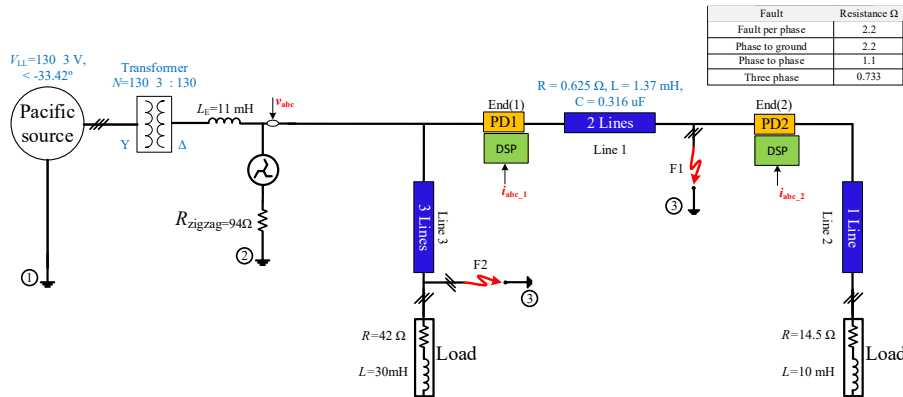


Fig. D.36 Scheme of the radial grid (three-line) without DG

➤ Fault at F1

- With contactor (Overcurrent relay)
- Single-phase fault

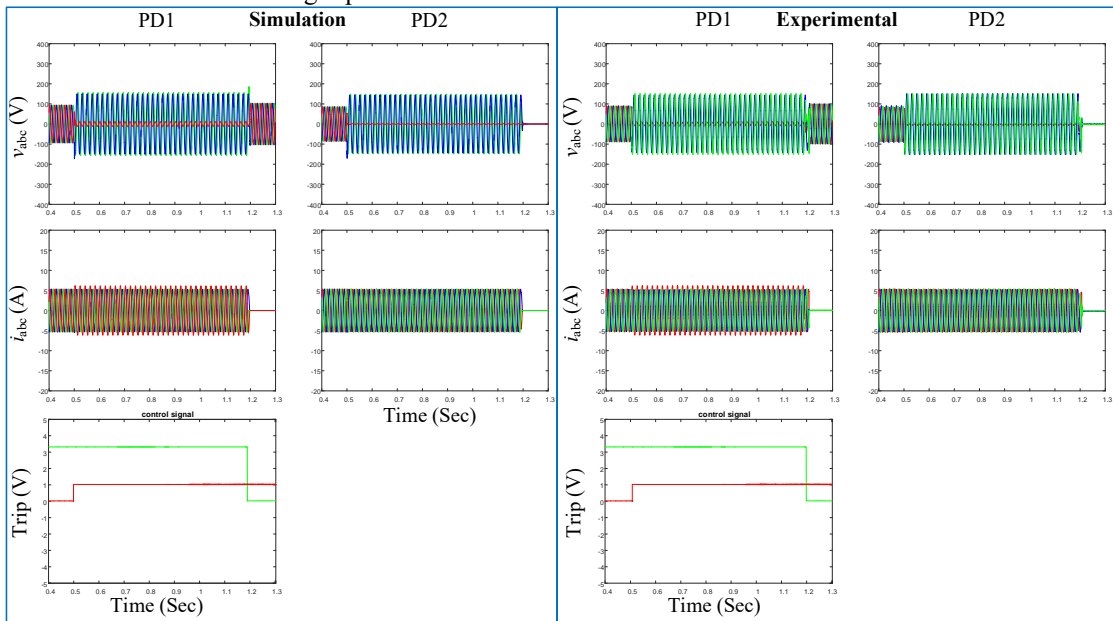


Fig. D.37 OCR control in case of single-phase to ground without DG

■ Three-phase fault

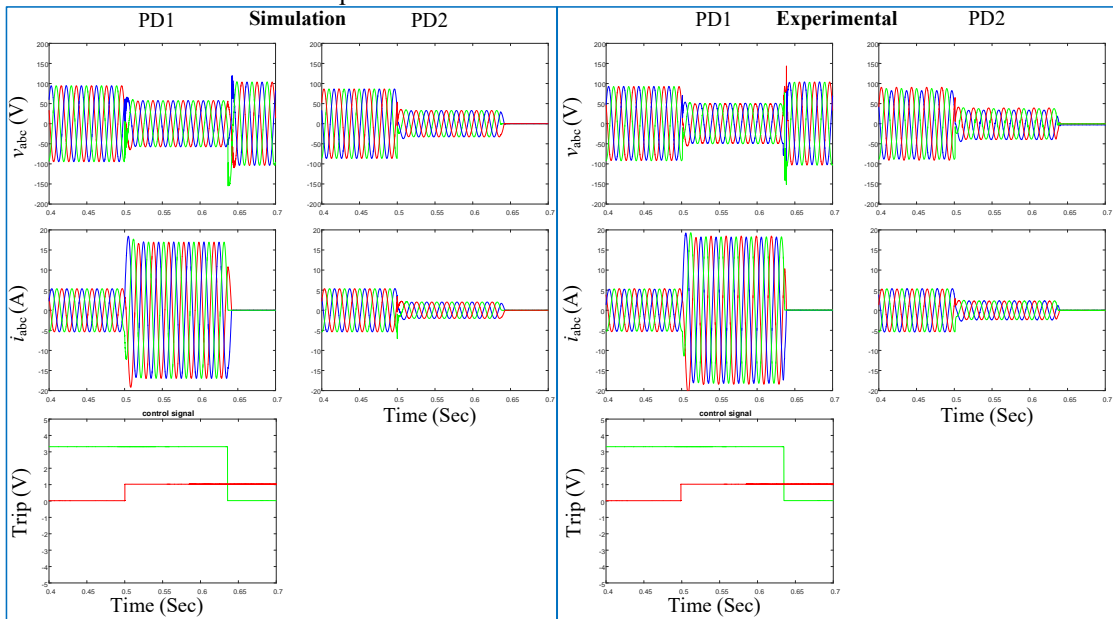


Fig. D.38 OCR control in case of three-phase without DG

● With contactor (Differential relay)

■ Single-phase fault

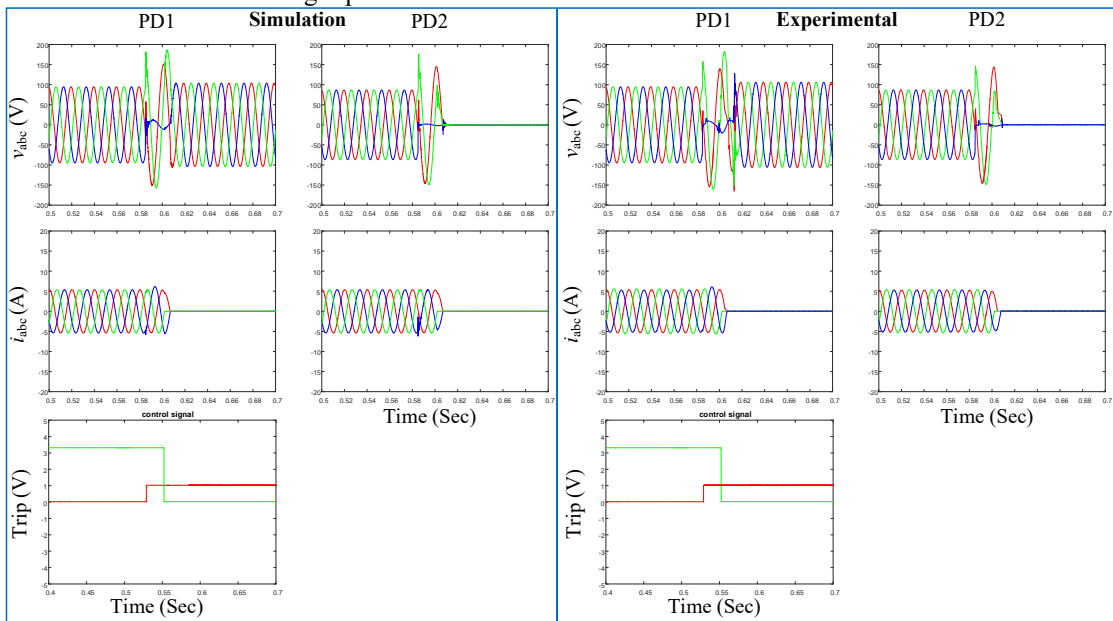


Fig. D.39 DR control in case of single-phase to ground without DG

▪ Three-phase fault

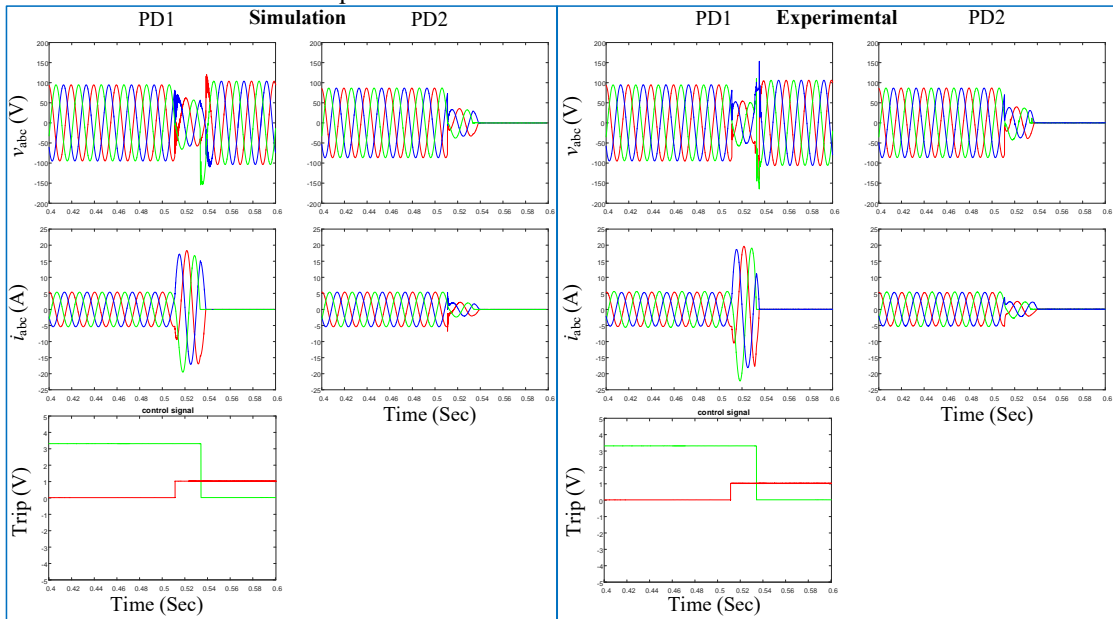


Fig. D.40 DR control in case of three-phase to the ground without DG

➤ **Fault at F2**

- Overcurrent relay
 - Single-phase fault

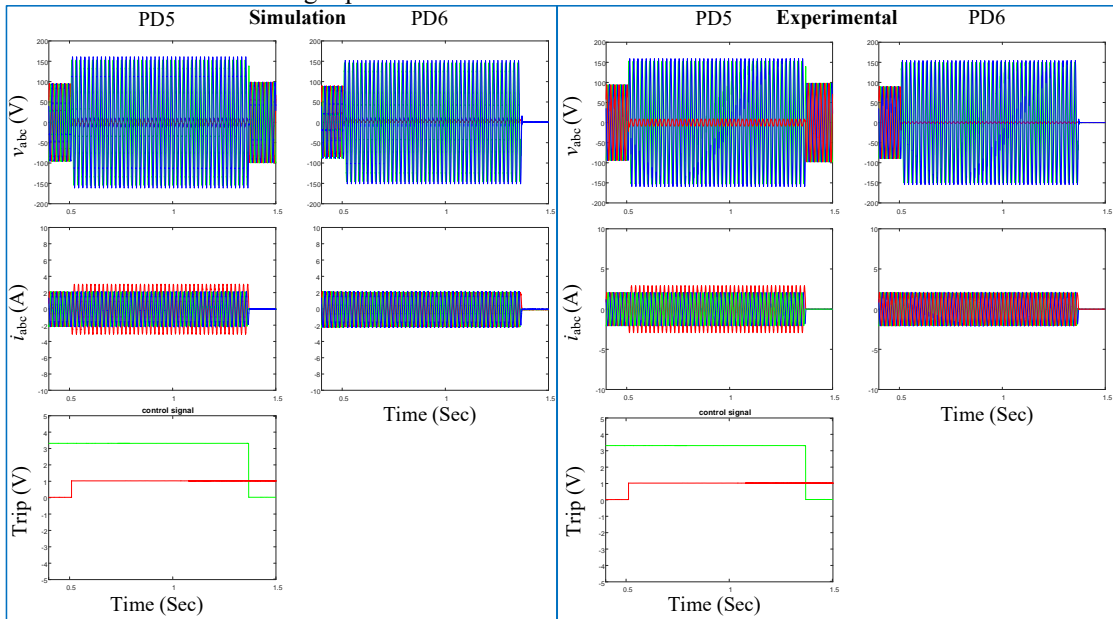


Fig. D.41 OCR control in case of single-phase to ground without DG

- Differential relay
 - Single-phase fault

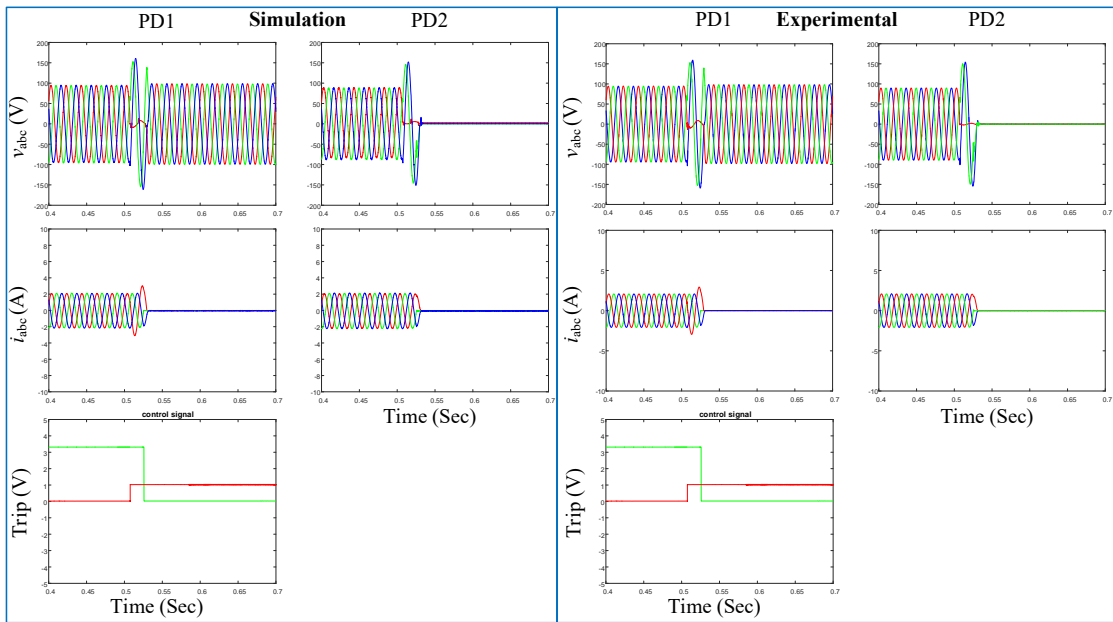


Fig. D.42 DR control in case of single-phase to ground without DG

- CE-ZO control
 - Single-phase fault

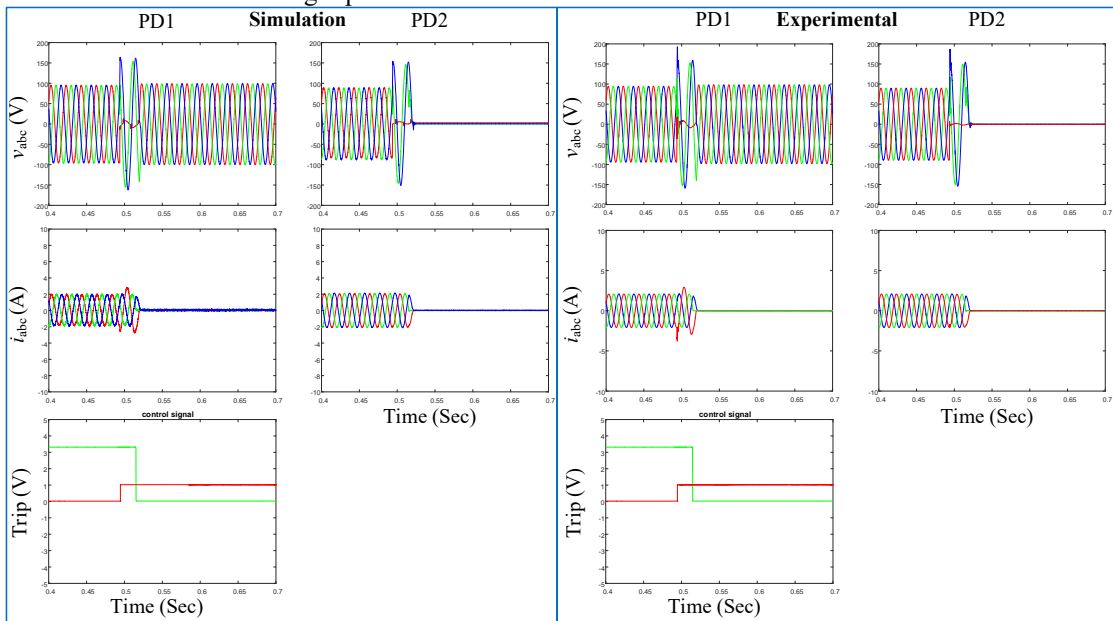


Fig. D.43 CE-ZO control in case of single-phase to ground without DG

D.3.4. Complete radial grid with DG

➤ **Scheme (F1 and F2)**

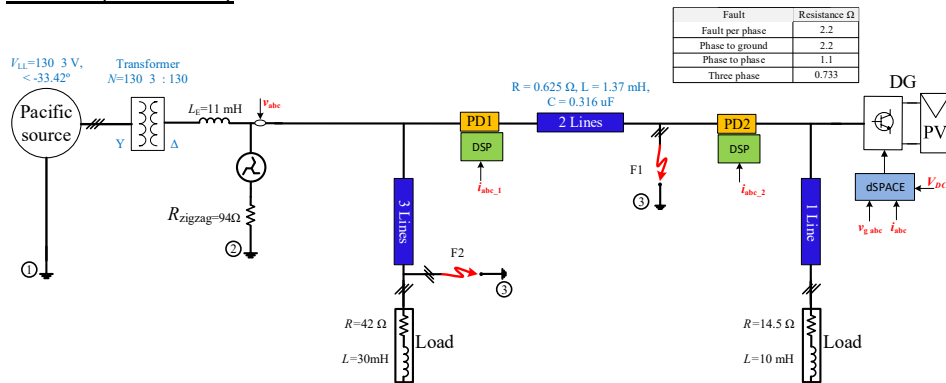


Fig. D.44 Scheme of the radial grid (three-line) with DG

➤ **Fault at F2**

- Overcurrent relay
 - Single-phase fault

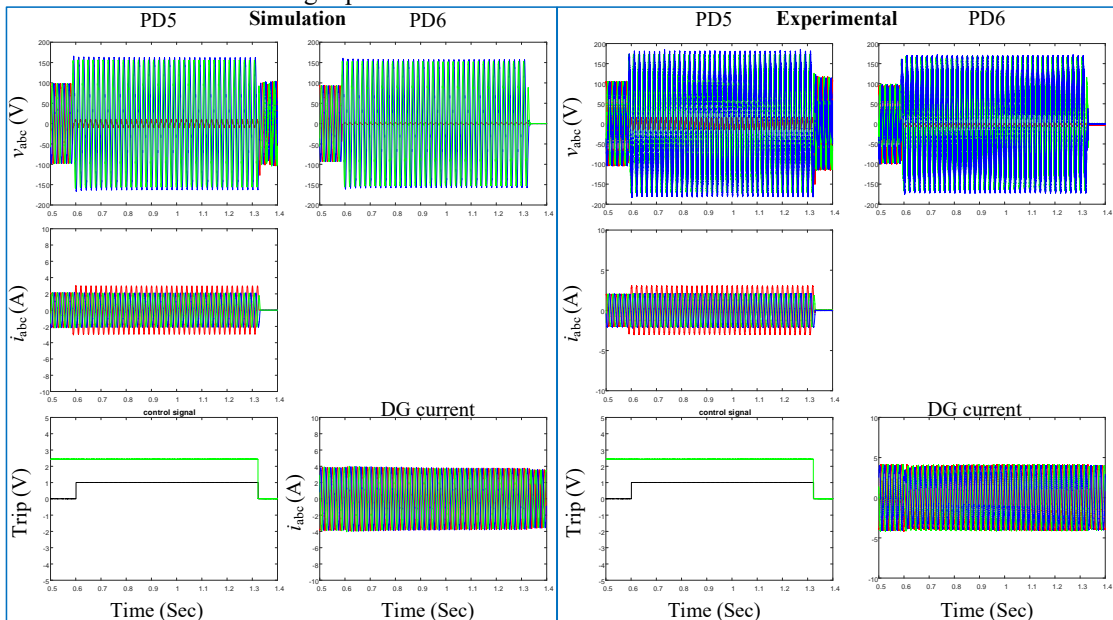


Fig. D.45 OCR control in case of single-phase to ground with DG

- Differential relay
 - Single-phase fault

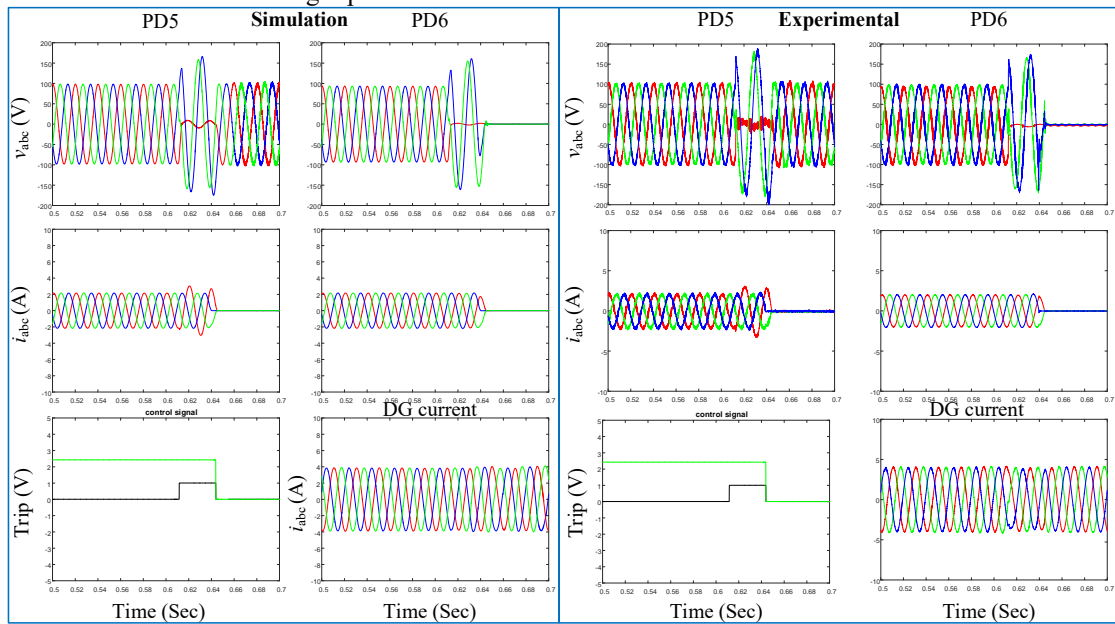


Fig. D.46 DR control in case of single-phase to ground with DG

- CE-ZO control with BCC
 - Single-phase fault

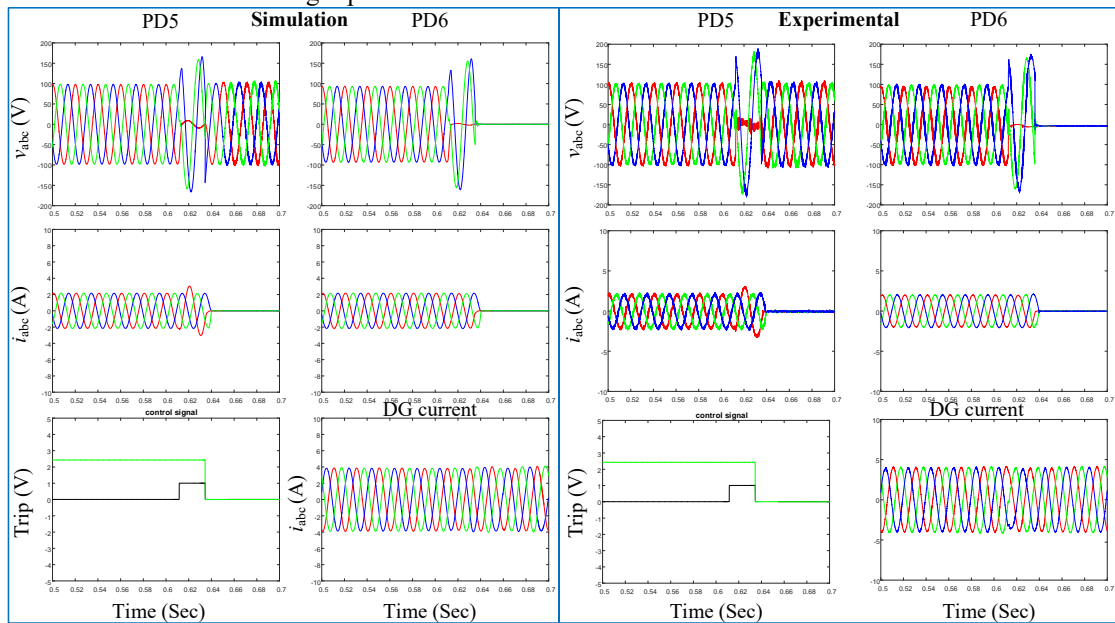


Fig. D.47 CE-ZO control in case of single-phase to ground with DG and BCC

D.3.5. Ring grid without DG

➤ **Breakers in DL1 and fault in DL1**

• Scheme

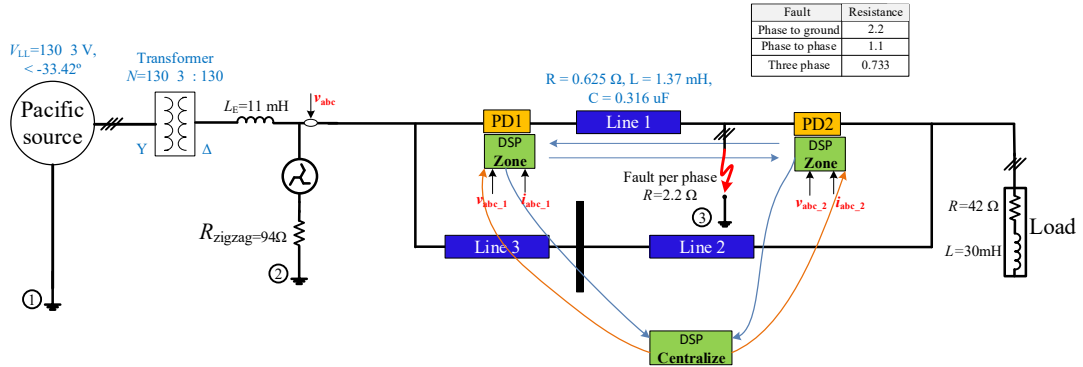


Fig. D.48 Scheme of ring grid without DG

• CE-ZO control

▪ Two-phase fault

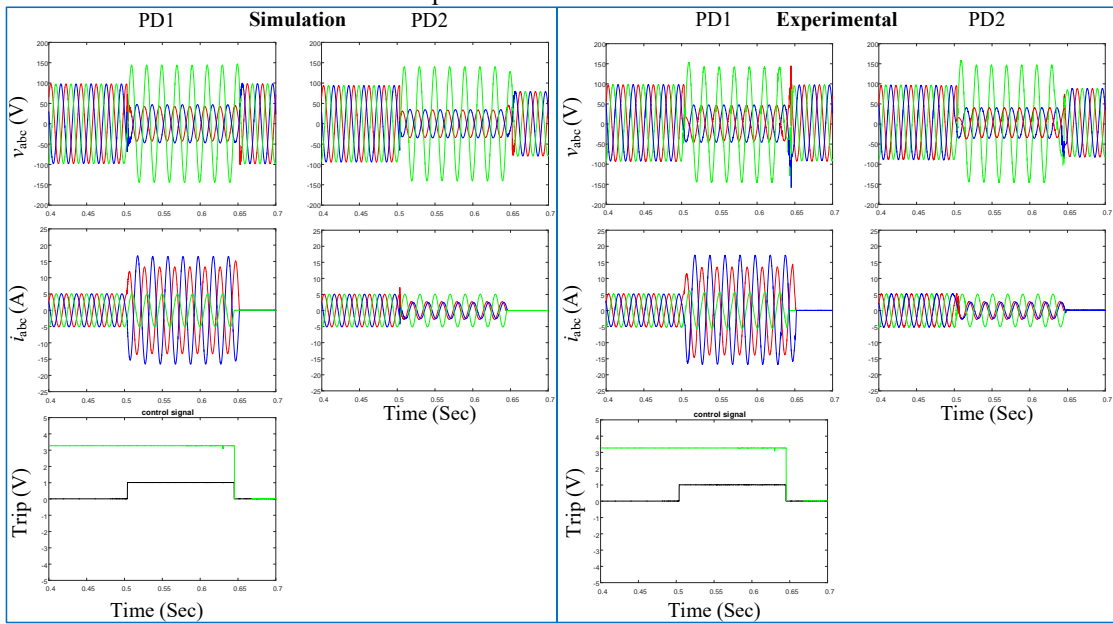


Fig. D.49 CE-ZO control in case of two-phase to ground

➤ **Breakers in DL1 and fault in DL3**
 • Scheme

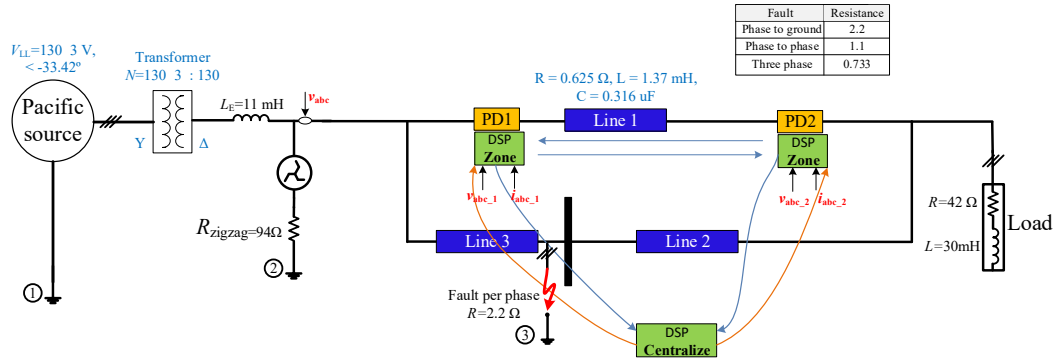


Fig. D.50 Scheme of ring grid without DG when fault DL3

• CE-ZO control
 ▪ Single-phase fault

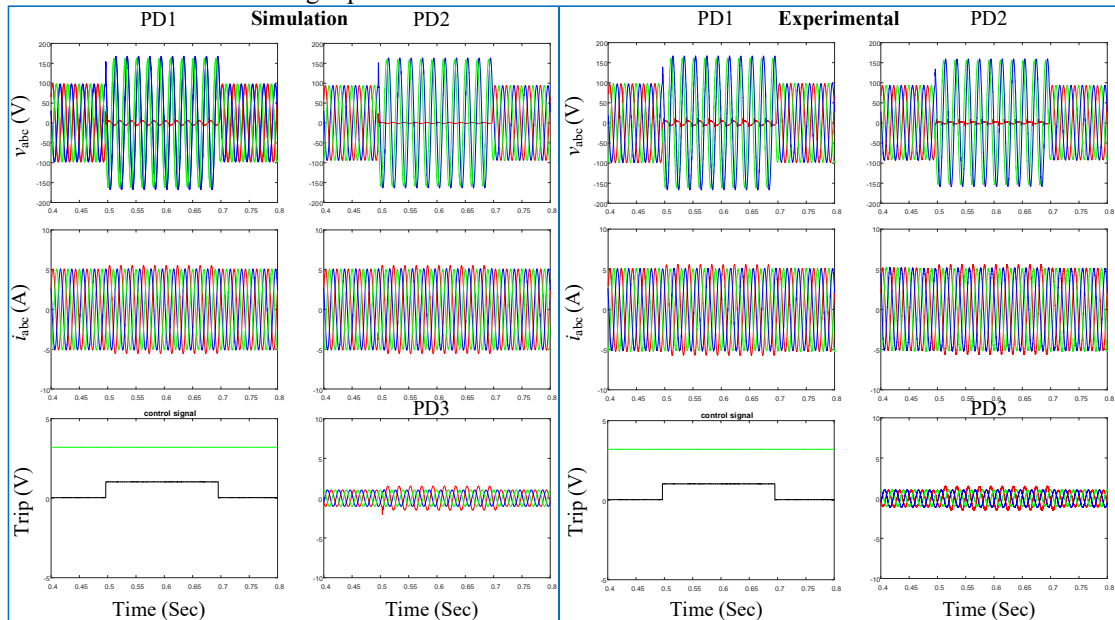


Fig. D.51 CE-ZO control in case of single-phase to ground

• LO control
 ■ Single-phase fault

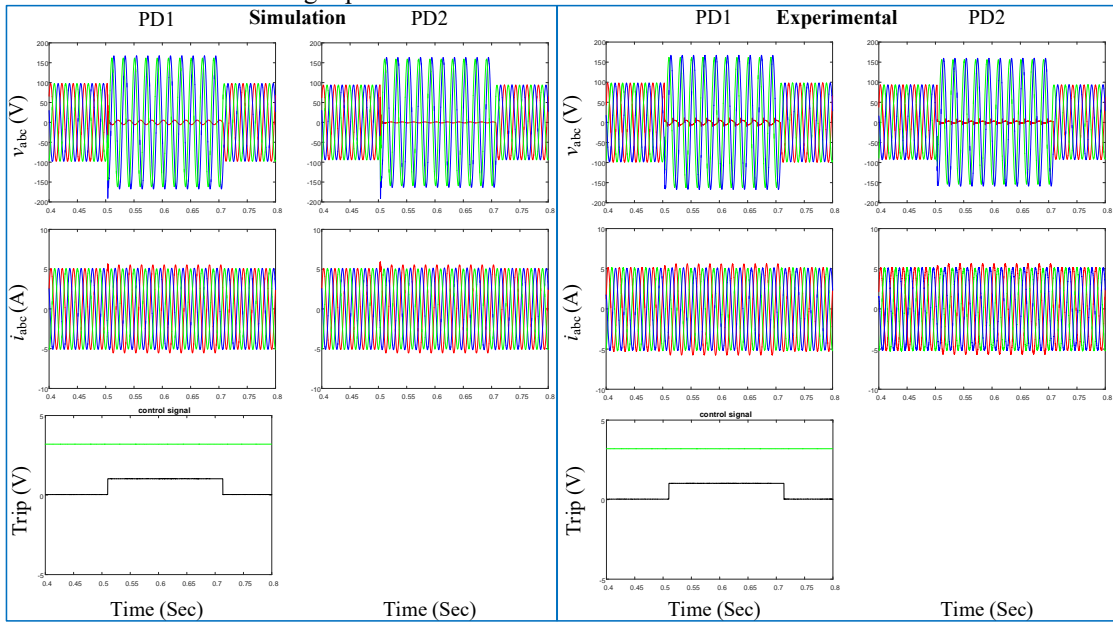


Fig. D.52 LO control in case of single-phase to ground

■ Three-phase fault

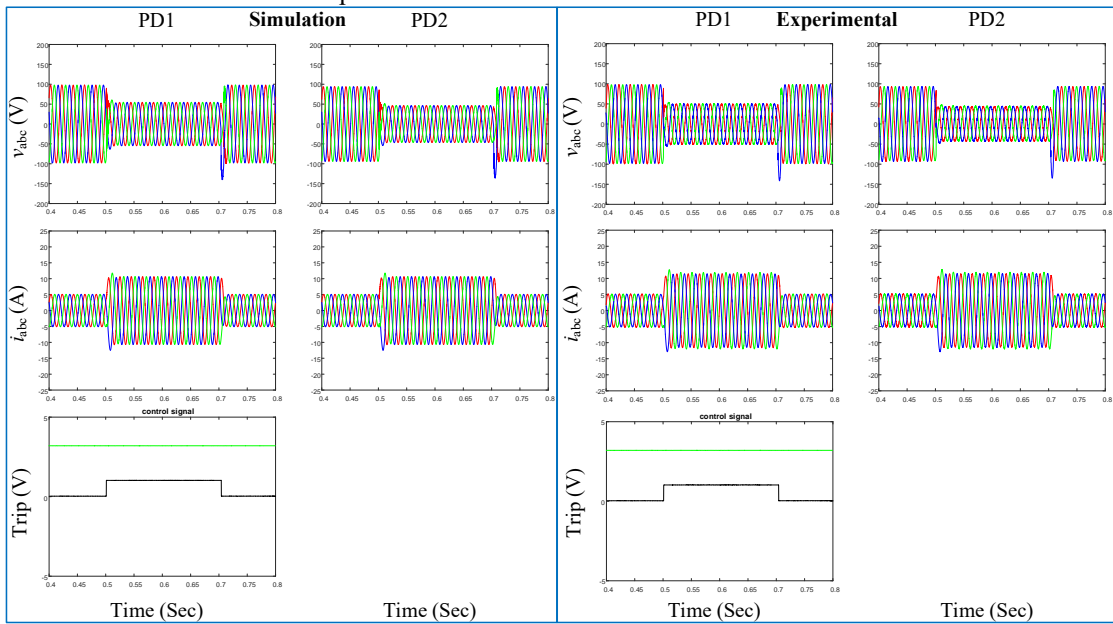


Fig. D.53 LO control in case of three-phase to ground

➤ **Breakers in DL2 and fault in DL2**

• **Scheme**

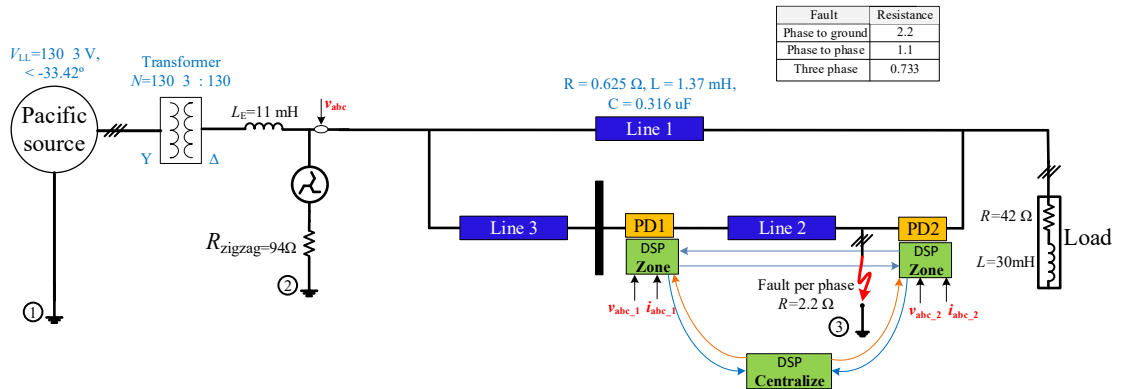


Fig. D.54 Scheme of ring grid without DG when fault DL2

• **CE-ZO control**

▪ **Three-phase fault**

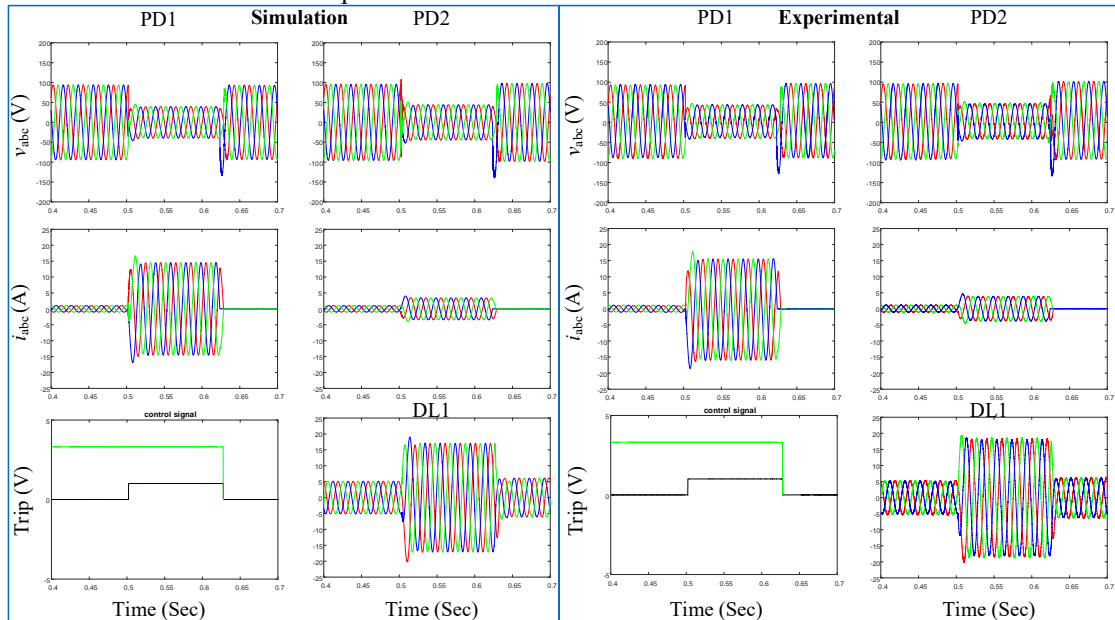


Fig. D.55 CE-ZO control in case of three-phase to ground

D.3.6. Ring grid with DG

➤ **Breakers in DL1 and fault in DL1**

• Scheme

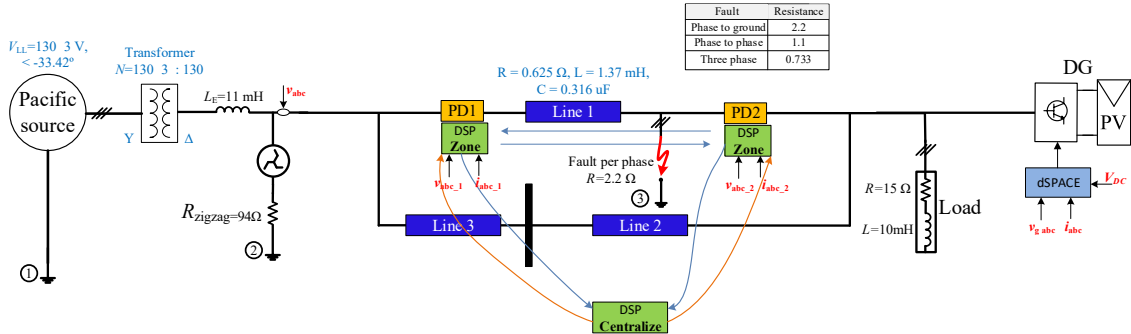


Fig. D.56 Scheme of ring grid with DG

• CE-ZO control with BCC

• Two-phase fault

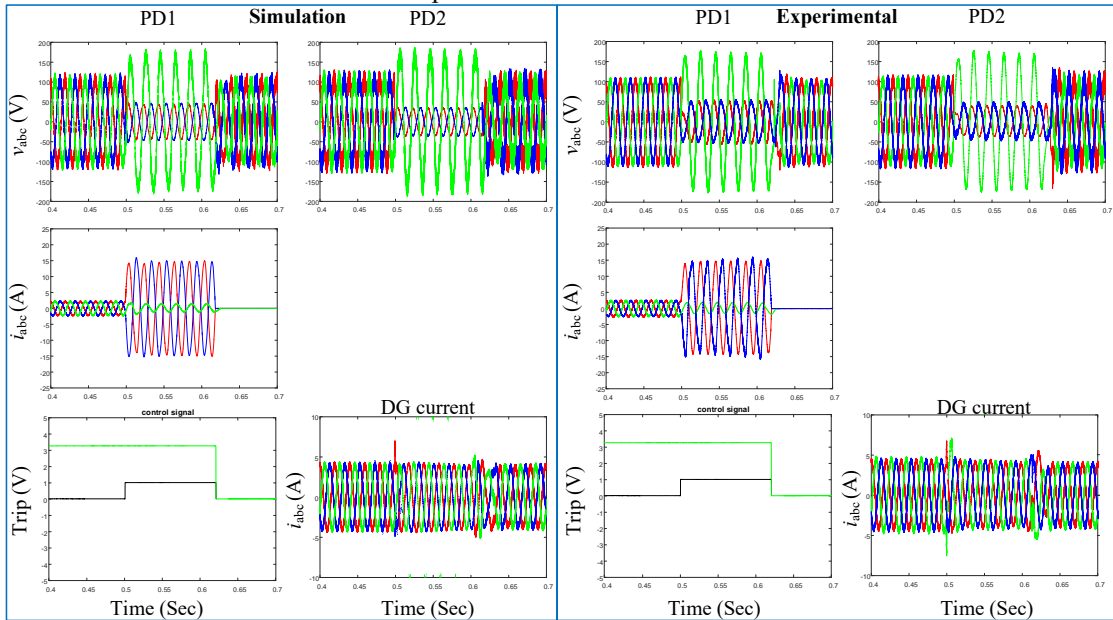


Fig. D.57 CE-ZO control in case of two-phase to ground with DG and BCC

•CE-ZO control with CPC
 ■ Three-phase fault

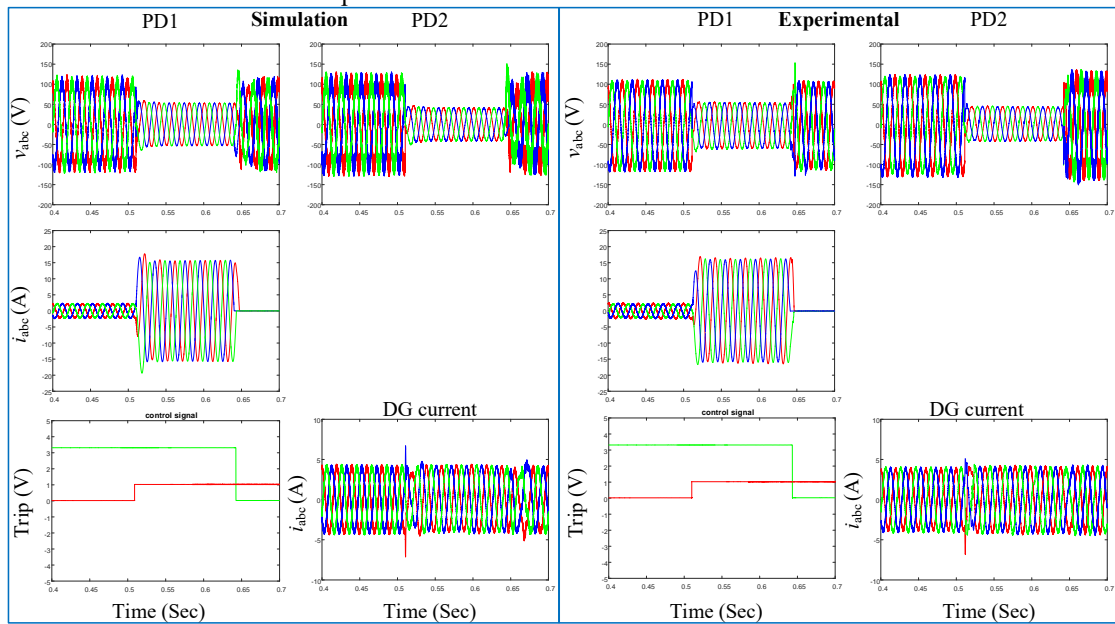


Fig. D.58 CE-ZO control in case of three-phase with DG and CPC

•CE-ZO control with CRC
 ■ Three-phase fault

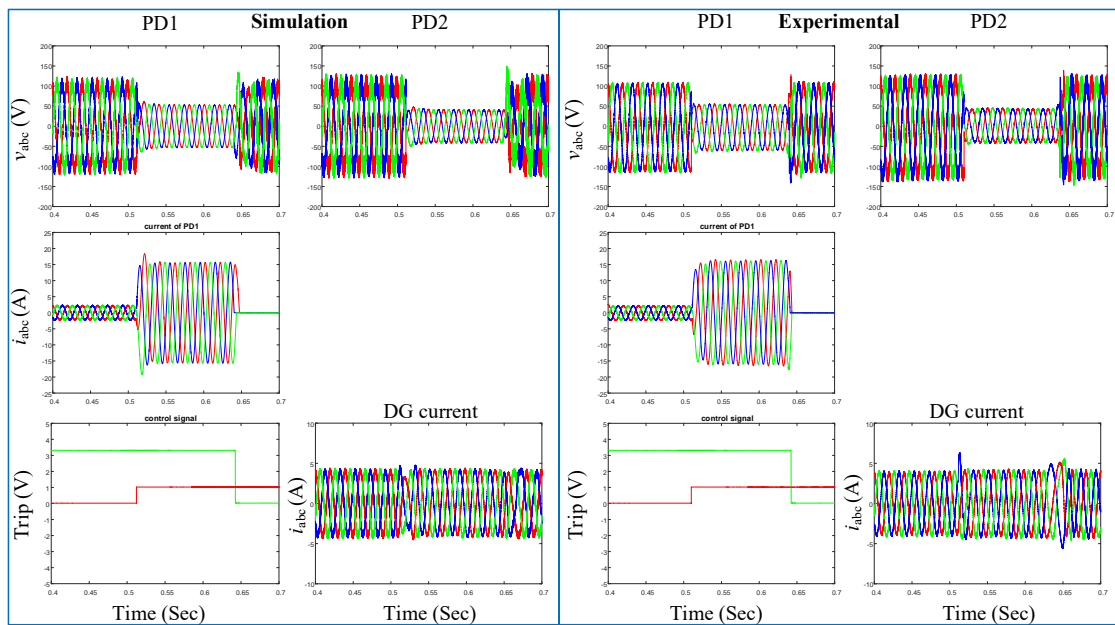


Fig. D.59 CE-ZO control in case of three-phase with DG and CRC

➤ **Breakers in DL1 and fault in DL3**

• **Scheme**

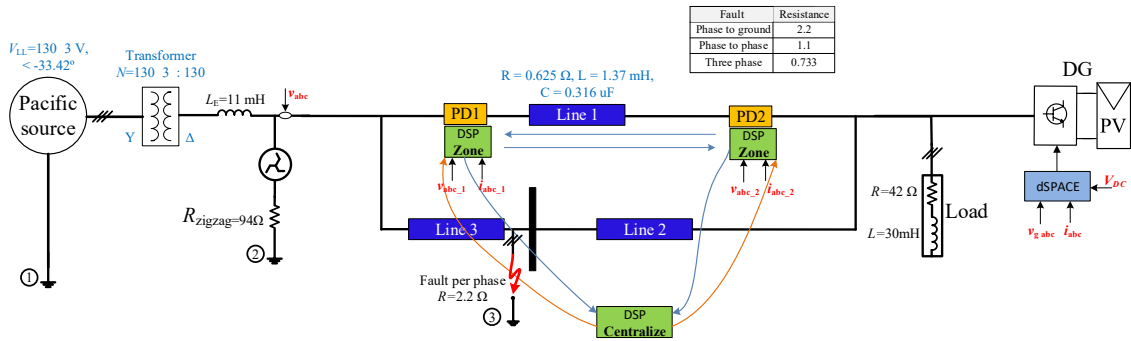


Fig. D.60 Scheme of ring grid with DG

• **CE-ZO control with BCC**

▪ **Single-phase fault**

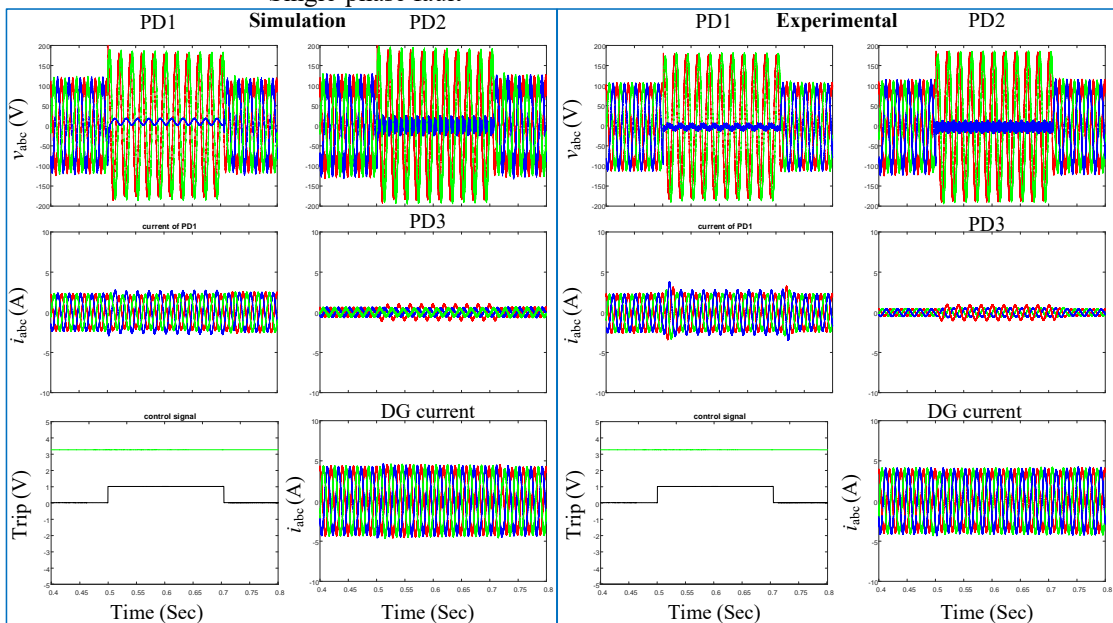


Fig. D.61 CE-ZO control in case of single-phase to ground with DG and BCC

➤ **Breakers in DL2 and fault in DL2**

• **Scheme**

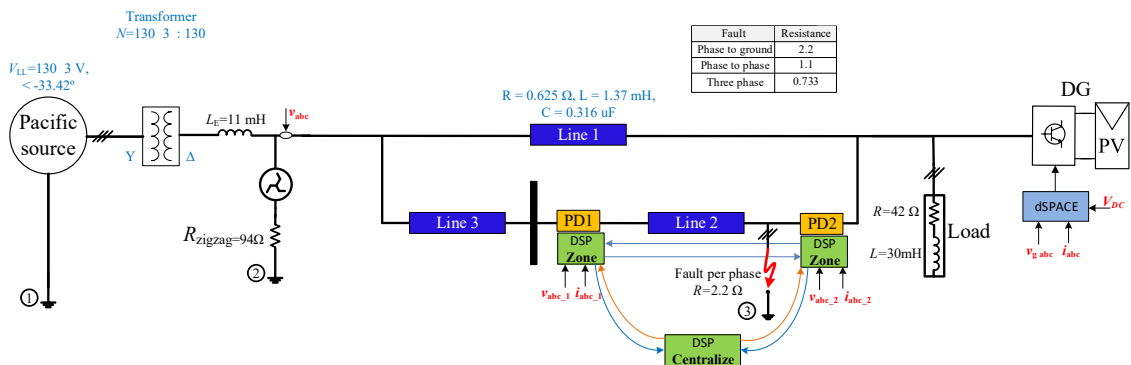


Fig. D.62 Scheme of ring grid with DG

•CE-ZO control with BCC
 ■ Single-phase fault

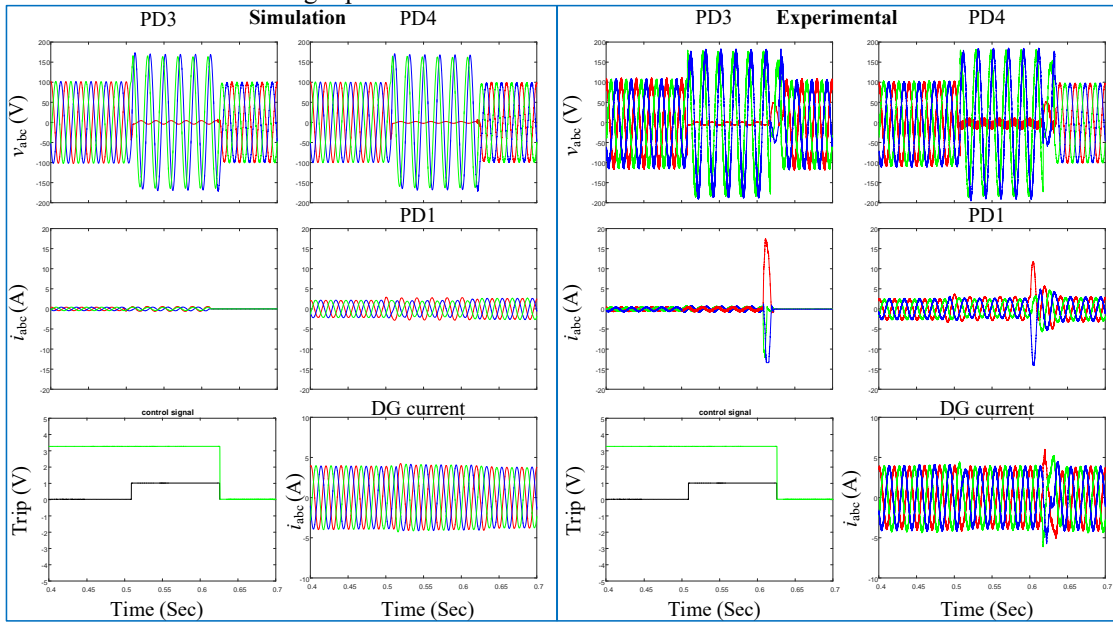


Fig. D.63 CE-ZO control in case of single-phase to ground with DG and BCC

E. Appendix E

Converter control

In this section, the basic information for the inverter control is presented.

E.1. Mathematical model of grid-connected inverter system in *Park* transformation

The model of the grid is implemented using a voltage source, as shown in Fig. E.1. The inverter switches are assumed to be ideal switches, and the model of the PV system is modeled as a DC supply and a capacitor.

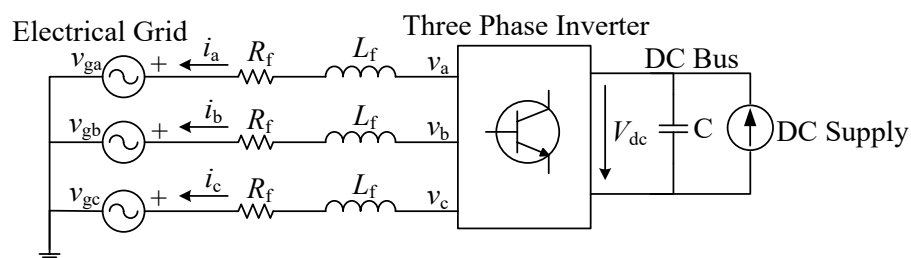


Fig. E.1 Three-Phase grid-connected VSC with RL filter

From Fig. E.1, the following equations can be written for the voltages and currents:

$$\begin{aligned} v_a &= i_a \left(R_f + L_f \frac{d}{dt} \right) + v_{ga} \\ v_b &= i_b \left(R_f + L_f \frac{d}{dt} \right) + v_{gb} \\ v_c &= i_c \left(R_f + L_f \frac{d}{dt} \right) + v_{gc}, \end{aligned} \quad (47)$$

where: v_a , v_b and v_c are the inverter voltages; i_a , i_b and i_c are the inverter currents; R_f and L_f are the R-L filter resistance and inductance; v_{ga} , v_{gb} and v_{gc} are the grid voltages.

These equations can be written in terms of the grid voltages. In matrix form the equations are given below:

$$\begin{bmatrix} v_a \\ v_b \\ v_c \end{bmatrix} = \begin{bmatrix} R_f & 0 & 0 \\ 0 & R_f & 0 \\ 0 & 0 & R_f \end{bmatrix} \begin{bmatrix} i_a \\ i_b \\ i_c \end{bmatrix} + \frac{d}{dt} \begin{bmatrix} L_f & 0 & 0 \\ 0 & L_f & 0 \\ 0 & 0 & L_f \end{bmatrix} \begin{bmatrix} i_a \\ i_b \\ i_c \end{bmatrix} + \begin{bmatrix} v_{ga} \\ v_{gb} \\ v_{gc} \end{bmatrix}. \quad (48)$$

- **Calculation of filter inductance**

The inductance of the RL filter is calculated as:

$$L_f = \left(\frac{\frac{V_{dc}}{2} / \sqrt{2}}{2\pi f_s \left(\frac{3}{2}\right) i_{MAX}} \right), \quad (49)$$

where: L_f is the filter inductance, V_{dc} is the DC link voltage, f_s is the switching frequency, and i_{MAX} is the maximum permission current (< 10%).

- **Mathematical model of three-phase inverter in dq coordinates**

To design a control scheme, it is useful to have constant quantities. The electrical quantities in the abc reference frame are oscillating in nature. To convert them into constant quantities, $dq0$ is applied.

The following is the abc model coordinates written in matrix form:

$$[\mathbf{v}] = [\mathbf{R}_f][\mathbf{i}] + [\mathbf{L}_f] \frac{d}{dt} [\mathbf{i}] + [\mathbf{v}_g], \quad (50)$$

where: L_f is the inverter voltage and v_g is the grid voltage. The $dq0$ transformation is given by

$$[\mathbf{X}_{0dq}] = [\mathbf{P}(\Psi)][\mathbf{X}_{abc}],$$

where the transformation matrix $[\mathbf{P}(\Psi)]$ is given by

$$[\mathbf{P}(\Psi)] = \sqrt{\frac{2}{3}} \begin{bmatrix} \cos \Psi & \cos\left(\Psi - \frac{2\pi}{3}\right) & \cos\left(\Psi + \frac{2\pi}{3}\right) \\ -\sin(\Psi) & -\sin\left(\Psi - \frac{2\pi}{3}\right) & -\sin\left(\Psi + \frac{2\pi}{3}\right) \\ \frac{1}{\sqrt{2}} & \frac{1}{\sqrt{2}} & \frac{1}{\sqrt{2}} \end{bmatrix}. \quad (51)$$

Multiplying the system equation with the transformation matrix on both sides we get,

$$[\mathbf{P}(\Psi)][\mathbf{v}] = [\mathbf{P}(\Psi)][\mathbf{R}_f][\mathbf{i}] + [\mathbf{P}(\Psi)] \frac{d}{dt} \{[\mathbf{L}_f][\mathbf{i}]\} + [\mathbf{P}(\Psi)][\mathbf{v}_g] \quad (52)$$

$$\begin{aligned} [\mathbf{P}(\Psi)][\mathbf{v}] &= [\mathbf{P}(\Psi)][\mathbf{R}_f][\mathbf{P}(\Psi)]^{-1} [\mathbf{P}(\Psi)][\mathbf{i}] + \\ &[\mathbf{P}(\Psi)] \frac{d}{dt} \{[\mathbf{L}_f][\mathbf{P}(\Psi)]^{-1} [\mathbf{P}(\Psi)][\mathbf{i}]\} + [\mathbf{P}(\Psi)][\mathbf{v}_g] \end{aligned} \quad (53)$$

$$\begin{aligned} [\mathbf{v}_{dq0}] &= [\mathbf{R}_f][[\mathbf{i}_{dq0}]] + [\mathbf{P}(\Psi)] \frac{d}{dt} \{[\mathbf{L}_f][\mathbf{P}(\Psi)]^{-1} [\mathbf{i}_{dq0}]\} + [\mathbf{v}_{gdq0}] \\ [\mathbf{v}_{dq0}] &= [\mathbf{R}_f][[\mathbf{i}_{dq0}]] + [\mathbf{P}(\Psi)][\mathbf{L}_f] \frac{d}{dt} \{[\mathbf{P}(\Psi)]^{-1} [\mathbf{i}_{dq0}]\} + [\mathbf{v}_{gdq0}]. \end{aligned} \quad (54)$$

Applying the product rule on the derivative of two terms, we get

$$\begin{aligned}
[\mathbf{v}_{dq0}] &= [\mathbf{R}_f][[\mathbf{i}_{dq0}]] + [\mathbf{P}(\Psi)] \frac{d}{dt} \{[\mathbf{P}(\Psi)]^{-1}\} [\mathbf{L}_f][[\mathbf{i}_{dq0}]] + \\
&[\mathbf{P}(\Psi)][[\mathbf{L}_f][[\mathbf{P}(\Psi)]^{-1} \frac{d}{dt} \{[\mathbf{i}_{dq0}]\}] + [\mathbf{v}_{gdq0}] \\
[\mathbf{v}_{dq0}] &= [\mathbf{R}_f][[\mathbf{i}_{dq0}]] + [\boldsymbol{\omega}][[\mathbf{L}_f][[\mathbf{i}_{dq0}]] + [\mathbf{L}_f] \frac{d}{dt} \{[\mathbf{i}_{dq0}]\} + [\mathbf{v}_{gdq0}],
\end{aligned} \tag{55}$$

where: $[\mathbf{P}(\Psi)][[\mathbf{L}_f][[\mathbf{P}(\Psi)]^{-1}] = [\mathbf{L}_f]$

$$[\boldsymbol{\omega}] = [\mathbf{P}(\Psi)] \frac{d}{dt} \{[\mathbf{P}(\Psi)]^{-1}\} = \begin{bmatrix} 0 & 0 & 0 \\ 0 & 0 & -\frac{d\Psi}{dt} \\ 0 & \frac{d\Psi}{dt} & 0 \end{bmatrix} = \begin{bmatrix} 0 & 0 & 0 \\ 0 & 0 & -\omega_\Psi \\ 0 & \omega_\Psi & 0 \end{bmatrix}. \tag{56}$$

So,

$$\begin{aligned}
\begin{bmatrix} v_0 \\ v_d \\ v_q \end{bmatrix} &= \begin{bmatrix} R_f & 0 & 0 \\ 0 & R_f & 0 \\ 0 & 0 & R_f \end{bmatrix} \begin{bmatrix} i_0 \\ i_d \\ i_q \end{bmatrix} + \begin{bmatrix} 0 & 0 & 0 \\ 0 & 0 & -\omega_\Psi \\ 0 & \omega_\Psi & 0 \end{bmatrix} \begin{bmatrix} L_f & 0 & 0 \\ 0 & L_f & 0 \\ 0 & 0 & L_f \end{bmatrix} \begin{bmatrix} i_0 \\ i_d \\ i_q \end{bmatrix} \\
&+ \begin{bmatrix} L_f & 0 & 0 \\ 0 & L_f & 0 \\ 0 & 0 & L_f \end{bmatrix} \frac{d}{dt} \begin{bmatrix} i_0 \\ i_d \\ i_q \end{bmatrix} + \begin{bmatrix} v_{g0} \\ v_{gd} \\ v_{gq} \end{bmatrix}
\end{aligned} \tag{57}$$

$$\begin{bmatrix} v_0 \\ v_d \\ v_q \end{bmatrix} = \begin{bmatrix} R_f & 0 & 0 \\ 0 & R_f & -\omega_\Psi L_f \\ 0 & \omega_\Psi L_f & R_f \end{bmatrix} \begin{bmatrix} i_0 \\ i_d \\ i_q \end{bmatrix} + \begin{bmatrix} L_f & 0 & 0 \\ 0 & L_f & 0 \\ 0 & 0 & L_f \end{bmatrix} \frac{d}{dt} \begin{bmatrix} i_0 \\ i_d \\ i_q \end{bmatrix} + \begin{bmatrix} v_{g0} \\ v_{gd} \\ v_{gq} \end{bmatrix}. \tag{58}$$

The zero component voltage equation is: $v_0 = R_f i_0 + L_f \frac{di_0}{dt} + v_{g0}$,

where: $i_0 = 0$, $v_0 = v_{g0} = 0$.

From the transformation equation, $v_0 = \frac{v_a + v_b + v_c}{\sqrt{3}} = 0$.

So (58) can be simplified as

$$\begin{bmatrix} v_d \\ v_q \end{bmatrix} = \begin{bmatrix} R_f & -\omega_\Psi L_f \\ \omega_\Psi L_f & R_f \end{bmatrix} \begin{bmatrix} i_d \\ i_q \end{bmatrix} + \begin{bmatrix} L_f & 0 \\ 0 & L_f \end{bmatrix} \frac{d}{dt} \begin{bmatrix} i_d \\ i_q \end{bmatrix} + \begin{bmatrix} v_{gd} \\ v_{gq} \end{bmatrix}. \tag{59}$$

Similar equations can be derived for the d and q components of v_g

$$\Psi = \theta_e = \arctan \left(\frac{v_{g\beta}}{v_{g\alpha}} \right) \omega_\Psi = \frac{d\Psi}{dt} = \frac{d\theta_e}{dt} = \omega_g \tag{60}$$

$$\Psi = \omega_g t + \Psi_0 \omega_\Psi = \frac{d\Psi}{dt} = \frac{d\{\omega_g t + \Psi_0\}}{dt} = \omega_g, \quad (61)$$

where: $\omega_g = 2\pi f$.

So we have the following final set of equations,

$$\begin{aligned} v_d &= R_f i_d + L_f \frac{di_d}{dt} - \omega_g L_f i_q + v_{gd} \\ v_q &= R_f i_q + L_f \frac{di_q}{dt} - \omega_g L_f i_d + v_{gq}. \end{aligned} \quad (62)$$

The above equations can be represented by the circuits in Fig. E.2.

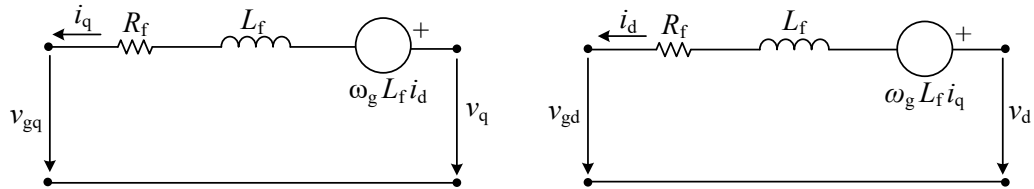


Fig. E.2 Equivalent electric circuits of three-phase inverter with RL filter in *Park* transformed variables

Using Park transformation (where: $[\mathbf{P}(\Psi)]$ is the matrix of the Park):

$$[\mathbf{P}(\Psi)] = \sqrt{\frac{2}{3}} \begin{bmatrix} \sqrt{\frac{1}{2}} & \sqrt{\frac{1}{2}} & \sqrt{\frac{1}{2}} \\ \cos(\Psi) & \cos\left(\Psi - \frac{2\pi}{3}\right) & \cos\left(\Psi + \frac{2\pi}{3}\right) \\ -\sin \Psi & -\sin\left(\Psi - \frac{2\pi}{3}\right) & -\sin\left(\Psi + \frac{2\pi}{3}\right) \end{bmatrix} \quad (63)$$

$$\mathbf{P}^{-1}(\Psi) = \sqrt{\frac{2}{3}} \begin{bmatrix} \sqrt{\frac{1}{2}} & \cos(\Psi) & -\sin \Psi \\ \sqrt{\frac{1}{2}} & \cos\left(\Psi - \frac{2\pi}{3}\right) & -\sin\left(\Psi - \frac{2\pi}{3}\right) \\ \sqrt{\frac{1}{2}} & \cos\left(\Psi + \frac{2\pi}{3}\right) & -\sin\left(\Psi + \frac{2\pi}{3}\right) \end{bmatrix}, \quad (64)$$

where it is observed that $[\mathbf{P}^{-1}(\Psi)] = [\mathbf{P}(\Psi)]^t$.

The reference in synchronism will be $\Psi = \omega_g t$.

The transformed variables when this transformation is applied will be as follow:

$$\begin{aligned} v_{sp} &= [\mathbf{P}(\Psi)]v_s ; v_{rp} = [\mathbf{P}(\Psi - \theta)]v_r \\ i_{sp} &= [\mathbf{P}(\Psi)]i_s ; i_{rp} = [\mathbf{P}(\Psi - \theta)]i_r. \end{aligned} \quad (65)$$

The components of each vector:

$$\begin{bmatrix} \mathbf{v}_{sp} \end{bmatrix} = \begin{bmatrix} v_{s0} \\ v_{sd} \\ v_{sq} \end{bmatrix} ; \begin{bmatrix} \mathbf{v}_{rp} \end{bmatrix} = \begin{bmatrix} v_{r0} \\ v_{rd} \\ v_{rq} \end{bmatrix} ; \begin{bmatrix} \mathbf{i}_{sp} \end{bmatrix} = \begin{bmatrix} i_{s0} \\ i_{sd} \\ i_{sq} \end{bmatrix} ; \begin{bmatrix} \mathbf{i}_{rp} \end{bmatrix} = \begin{bmatrix} i_{r0} \\ i_{rd} \\ i_{rq} \end{bmatrix}, \quad (66)$$

where: zero component (0), direct component (d), quadrature component (q), synchronous frame (s), and rotating frame (r).

- For the symmetrical case [198]::

$$\begin{aligned} v_{sa} &= \sqrt{2}V_s \cos(\omega_s t + \phi_{V_s}) \\ v_{sb} &= \sqrt{2}V_s \cos\left(\omega_s t + \phi_{V_s} - \frac{2\pi}{3}\right) \\ v_{sc} &= \sqrt{2}V_s \cos\left(\omega_s t + \phi_{V_s} + \frac{2\pi}{3}\right). \end{aligned} \quad (67)$$

These transformed voltages are:

$$\begin{aligned} v_{s0} &= \frac{1}{\sqrt{3}}(v_{sa} + v_{sb} + v_{sc}) \\ v_{sd} &= \sqrt{\frac{2}{3}}\left(\cos(\Psi)v_{sa} + \cos\left(\Psi - \frac{2\pi}{3}\right)v_{sb} + \cos\left(\Psi + \frac{2\pi}{3}\right)v_{sc}\right) \\ v_{sq} &= \sqrt{\frac{2}{3}}\left(-\sin(\Psi)v_{sa} - \sin\left(\Psi - \frac{2\pi}{3}\right)v_{sb} - \sin\left(\Psi + \frac{2\pi}{3}\right)v_{sc}\right). \end{aligned} \quad (68)$$

Substituting the three-phase voltages gives:

$$\begin{aligned} v_{s0} &= 0 \\ v_{sd} &= \sqrt{3}V_s \cos(\omega_s t + \phi_{V_s} - \Psi) \\ v_{sq} &= \sqrt{3}V_s \sin(\omega_s t + \phi_{V_s} - \Psi). \end{aligned} \quad (69)$$

Or the direct and quadrature voltages ($\Psi = \omega_s t$, $\omega_\Psi = \omega_s$):

$$\begin{aligned} v_{sd} &= \sqrt{3}V_s \cos(\phi_{V_s}) \\ v_{sq} &= \sqrt{3}V_s \sin(\phi_{V_s}). \end{aligned} \quad (70)$$

E.2. Mathematical model of grid-connected inverter system in Ku transformation

This section explains the mathematical model of the converter using Ku transformation.

Analytical expression of voltage sags: The Ku transformation relates the abc phase components of a three-phase system to the Ku transformed components.

$$[\mathbf{v}_{0fb}] = [\mathbf{K}(\Psi)][\mathbf{v}_{abc}] [\mathbf{v}_{abc}] = [\mathbf{K}(\Psi)]^{-1} [\mathbf{v}_{0fb}]. \quad (71)$$

The mathematical expressions of the abc variables that model the system of Fig. E.4 (considering the generator-sign convention) are given in (72):

$$\begin{bmatrix} v_{a \text{ Ref}} \\ v_{b \text{ Ref}} \\ v_{c \text{ Ref}} \end{bmatrix} = \begin{bmatrix} R & 0 & 0 \\ 0 & R & 0 \\ 0 & 0 & R \end{bmatrix} \begin{bmatrix} i_a \\ i_b \\ i_c \end{bmatrix} + \frac{d}{dt} \begin{bmatrix} L & 0 & 0 \\ 0 & L & 0 \\ 0 & 0 & L \end{bmatrix} \begin{bmatrix} i_a \\ i_b \\ i_c \end{bmatrix} + \begin{bmatrix} v_{ga} \\ v_{gb} \\ v_{gc} \end{bmatrix}, \quad (72)$$

where $v_{abc \text{ Ref}}$ is the abc components of the reference voltage of the inverter, $v_{g \text{ abc}}$ is the abc components of the grid voltage, i_{abc} are the injected abc currents from the inverter to the grid, and R and L are the resistance and the inductance of the filter, respectively.

The mathematical study is developed using the complex form of the *Park* transformation, i.e. Ku transformation, which gives the easiest representation that can be used to analyze the electrical variables. The power-invariant form of the Ku transformation is given by [199]:

$$[\mathbf{K}(\Psi)] = \frac{1}{\sqrt{3}} \begin{bmatrix} 1 & e^{j\Psi} & e^{-j\Psi} \\ 1 & a^2 e^{j\Psi} & a e^{-j\Psi} \\ 1 & a e^{j\Psi} & a^2 e^{-j\Psi} \end{bmatrix}; \quad a = e^{j2\pi/3} \quad (73)$$

$$[x_{abc}] = [\mathbf{K}(\Psi)][x_{0fb}] ; \quad [x_{0fb}] = [\mathbf{K}(\Psi)]^{-1}[x_{abc}],$$

where the subscripts a, b, and c stand for the abc components of the variable x (voltage or current). The subscripts 0, f, and b stand for the *zero*, *forward* and *backward* components respectively, and Ψ is the transformation angle provided by a PLL assuming the synchronous reference frame. *Backward* components are the complex conjugate of *forward* components, so only *forward* components need to be used. By applying the Ku transformation (73) into (72), and assuming the sag in its steady-state condition with sinusoidal waves, we obtain:

$$v_{f \text{ Ref}} = [R + L(s + j\omega)]i_f + v_{gf}, \quad (74)$$

where $v_{f \text{ Ref}}$ is the transformed inverter reference voltage, $s = d/dt$ is the derivative operator i_f is the transformed injected current, and v_{gf} is the transformed grid voltage. Under unbalanced conditions, transformed grid voltage can be represented by using the *Fortescue* transformation [198] as:

$$v_{gf}^+ = \frac{1}{\sqrt{6}} (V_a e^{j\phi_{r_a}} + aV_b e^{j\phi_{r_b}} + a^2 V_c e^{j\phi_{r_c}}) \quad (75)$$

$$v_{gf}^- = \frac{1}{\sqrt{6}} (V_a e^{-j\phi_{r_a}} + aV_b e^{-j\phi_{r_b}} + a^2 V_c e^{-j\phi_{r_c}}) \quad (76)$$

$$v_{gf} = v_{gf}^+ + v_{gf}^- e^{-j2\omega t}. \quad (77)$$

The same procedure can be followed to obtain the transformed injected current from the inverter to the grid, so:

$$i_f = i_f^+ + i_f^- e^{-j2\omega t}. \quad (78)$$

The transformed Ku components are given by:

$$\begin{aligned}
 v_0 &= \frac{1}{\sqrt{3}}(v_a + v_b + v_c) \\
 v_f &= \frac{e^{-j(\omega t + \Psi_0)}}{\sqrt{3}}(v_a + a v_b + a^2 v_c) \\
 v_b &= \frac{e^{j(\omega t + \Psi_0)}}{\sqrt{3}}(v_a + a^2 v_b + a v_c).
 \end{aligned}
 \tag{79}$$

It should be noted that the backward component, v_b , equals the complex conjugate of the forward component, v_f . Apart, if no zero component, v_0 , is considered (if the studied equipment has no neutral connections), only the forward component has to be studied [198].

Voltage sags form a set of unbalanced voltages

$$\begin{aligned}
 v_a &= \sqrt{2}V_a \cos(\omega t + \alpha_a) \\
 v_b &= \sqrt{2}V_b \cos(\omega t + \alpha_b) \\
 v_c &= \sqrt{2}V_c \cos(\omega t + \alpha_c).
 \end{aligned}
 \tag{80}$$

These unbalanced voltages can be transformed into three sets of symmetrical voltages (positive-, negative- and zero-sequence components) utilizing the Fortescue transformation [198], as illustrated in Fig. E.3. Next, we will calculate the Ku transformation of these unbalanced voltages in the function of the three sequence components (positive-, negative- and zero-sequence).

Substituting (79) in the expression of v_f in (73) and taking into account the trigonometric relation

$$\cos(\alpha) = \frac{e^{j\alpha} + e^{-j\alpha}}{2}.
 \tag{81}$$

Unbalanced system = Positive sequence + Negative sequence + Zero sequence

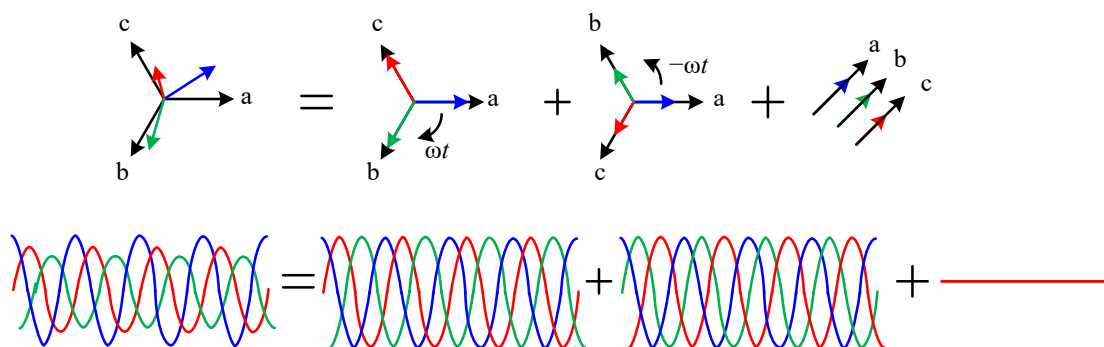


Fig. E.3 Obtaining the symmetric components of an unbalanced system

We have

$$v_f = (v_{f1} + v_{f2} e^{-j2\omega t}) e^{-j\Psi_0},
 \tag{82}$$

where v_{f1} and v_{f2} are

$$\begin{aligned}
v_{f1} &= \frac{1}{\sqrt{6}} \left(V_a e^{j\alpha_a} + a V_b e^{j\alpha_b} + a^2 V_c e^{j\alpha_c} \right) \\
v_{f2} &= \frac{1}{\sqrt{6}} \left(V_a e^{-j\alpha_a} + a V_b e^{-j\alpha_b} + a^2 V_c e^{-j\alpha_c} \right).
\end{aligned} \tag{83}$$

Comparing (82) with (78) it results in

$$\begin{aligned}
v_{f1} &= \sqrt{\frac{3}{2}} V_{-p} = \sqrt{\frac{3}{2}} V_p e^{j\alpha_p} \\
v_{f2} &= \sqrt{\frac{3}{2}} V_{-n} = \sqrt{\frac{3}{2}} V_n e^{-j\alpha_n},
\end{aligned} \tag{84}$$

where: V_p and V_n are the rms value of the positive- and negative-sequence voltages of sags and α_p and α_n are their angles [198]. Then, the equation (82) can be expressed in terms of the positive- and negative-sequence voltages as

$$v_f = \sqrt{\frac{3}{2}} \left(V_p e^{j\alpha_p} + V_n e^{-j(2\omega t + \alpha_n)} \right) e^{-j\Psi_0} \tag{85}$$

In the symmetrical case:

$$V_s = V_s e^{j\varphi_s} = \sqrt{\frac{2}{3}} v_{sf} \tag{86}$$

E.3. Relation between *Ku* and *Park* components

The transformed *Ku* forward component (x_f) is a complex notation of the Park *dq* components:

$$\begin{aligned}
x_d &= \sqrt{2} \operatorname{Re}(x_f) \\
x_q &= \sqrt{2} \operatorname{Im}(x_f).
\end{aligned} \tag{87}$$

Based on the discussion above, the overall control scheme is shown in Fig. E.4.

During asymmetric conditions appears the negative-sequence component of the voltages, the currents will also have a negative-sequence component.

For simplicity, it is important to have constant variables for the control. Park can be applied to balanced systems (positive- and negative-sequence) and thus obtain constant variables.

For the positive-sequence, apply Park with $\Psi = \omega t$ (reference synchronism, according to the direction of rotation of Fig. E.5. For the negative-sequence, apply Park with $\Psi = -\omega t$ (anti-synchronous reference, according to the direction of rotation of Fig. E.5.

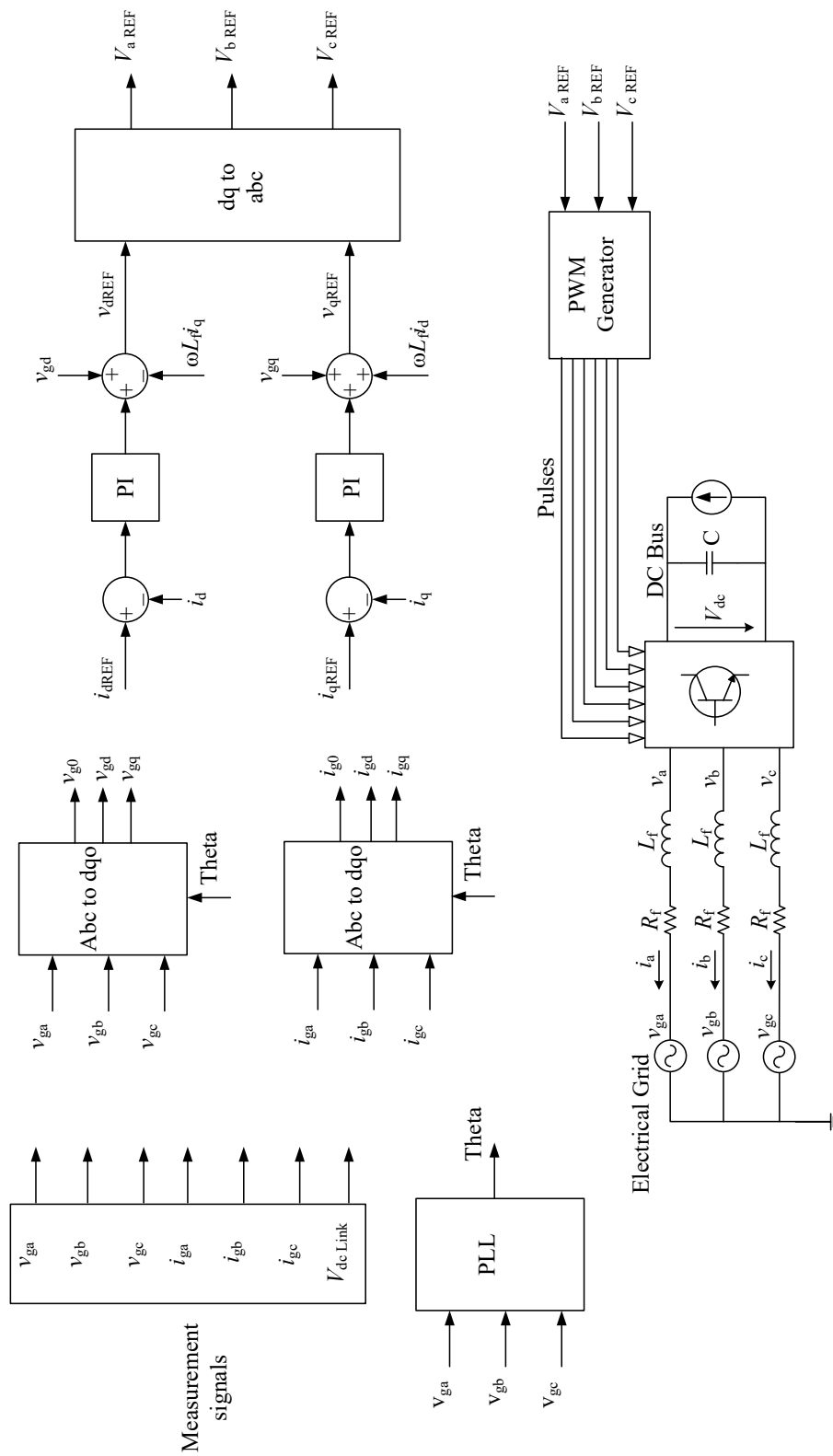


Fig. E.4 Three-phase inverter control for balanced conditions

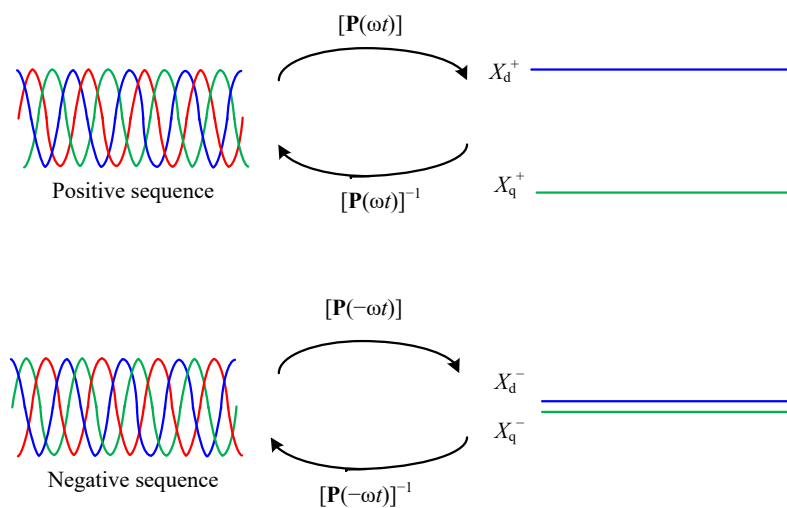


Fig. E.5 Park transformation of the symmetric components to obtain constant variables

This transformed pre-fault voltage can be chosen as the angle reference for all the transformed variables, i.e., $\Psi_0 = \alpha_a$. For example, the transformed pre-fault voltage at Table E.1 is the angle reference for the transformed variables if $\Psi_0 = \alpha_a = -90^\circ$ [200], for the unsymmetrical voltage sags in positive- and negative-sequence components [201]. The zero-, positive- and negative-sequence components of all sag types are shown in Table E.1 (adapted from [202]).

Table E.1 Unsymmetrical voltage sag types (obtained from [202]): faults of origin, phasors, and symmetrical components

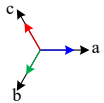
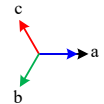
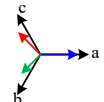
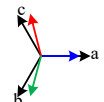
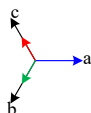
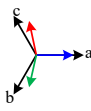

Type	Fault of origin	Phasor diagram	Phasor expressions	Zero-sequence	Positive-sequence	Negative-sequence
A	3 phase		$\underline{V}_{-a} = h\underline{V}_{-}$ $\underline{V}_{-b} = -\left(\frac{1}{2}\right)h\underline{V}_{-} - j\left(\frac{\sqrt{3}}{2}\right)h\underline{V}_{-}$ $\underline{V}_{-c} = -\left(\frac{1}{2}\right)h\underline{V}_{-} + j\left(\frac{\sqrt{3}}{2}\right)h\underline{V}_{-}$	0	$h\underline{V}_{-}$	0
B	1 phase-to-ground		$\underline{V}_{-a} = h\underline{V}_{-}$ $\underline{V}_{-b} = -\left(\frac{1}{2}\right)\underline{V}_{-} - j\left(\frac{\sqrt{3}}{2}\right)\underline{V}_{-}$ $\underline{V}_{-c} = -\left(\frac{1}{2}\right)\underline{V}_{-} + j\left(\frac{\sqrt{3}}{2}\right)\underline{V}_{-}$	$-\left(\frac{1-h}{3}\right)\underline{V}_{-}$	$\left(\frac{2+h}{3}\right)\underline{V}_{-}$	$-\left(\frac{1-h}{3}\right)\underline{V}_{-}$
C	2 phases or 1 phase-to-ground after a Dy transformer		$\underline{V}_{-a} = \underline{V}_{-}$ $\underline{V}_{-b} = -\left(\frac{1}{2}\right)\underline{V}_{-} - j\left(\frac{\sqrt{3}}{2}\right)h\underline{V}_{-}$ $\underline{V}_{-c} = -\left(\frac{1}{2}\right)\underline{V}_{-} + j\left(\frac{\sqrt{3}}{2}\right)h\underline{V}_{-}$	0	$\left(\frac{1+h}{3}\right)\underline{V}_{-}$	$\left(\frac{1-h}{2}\right)\underline{V}_{-}$
D	2 phases after a Dy transformer or ground after a two Dy transformer		$\underline{V}_{-a} = h\underline{V}_{-}$ $\underline{V}_{-b} = -\left(\frac{1}{2}\right)h\underline{V}_{-} - j\left(\frac{\sqrt{3}}{2}\right)\underline{V}_{-}$ $\underline{V}_{-c} = -\left(\frac{1}{2}\right)h\underline{V}_{-} + j\left(\frac{\sqrt{3}}{2}\right)\underline{V}_{-}$	0	$\left(\frac{1+h}{3}\right)\underline{V}_{-}$	$-\left(\frac{1-h}{2}\right)\underline{V}_{-}$

Table E.1 Cont'd

Type	Fault of origin	Phasor diagram	Phasor expressions	Zero-sequence	Positive-sequence	Negative-sequence
E	2 phases-two-ground		$V_{-a} = V_{-}$ $V_{-b} = -\left(\frac{1}{2}\right)hV_{-} - j\left(\frac{\sqrt{3}}{2}\right)hV_{-}$ $V_{-c} = -\left(\frac{1}{2}\right)hV_{-} + j\left(\frac{\sqrt{3}}{2}\right)hV_{-}$	$\left(\frac{1-h}{3}\right)V_{-}$	$\left(\frac{1+2h}{3}\right)V_{-}$	$\left(\frac{1-h}{3}\right)V_{-}$
F	2 phases-two-ground after a Dy transformer		$V_{-a} = hV_{-}$ $V_{-b} = -\left(\frac{1}{2}\right)hV_{-} - j\left[\frac{(2+h)}{\sqrt{12}}\right]V_{-}$ $V_{-c} = -\left(\frac{1}{2}\right)hV_{-} + j\left[\frac{(2+h)}{\sqrt{12}}\right]V_{-}$	c	$\left(\frac{1+2h}{3}\right)V_{-}$	$-\left(\frac{1-h}{3}\right)V_{-}$
G	2 phases-two-ground after a two Dy transformer		$V_{-a} = \left[\frac{(2+h)}{3}\right]V_{-}$ $V_{-b} = -\left[\frac{(2+h)}{6}\right]V_{-} - j\left(\frac{\sqrt{3}}{2}\right)hV_{-}$ $V_{-c} = -\left[\frac{(2+h)}{6}\right]V_{-} + j\left(\frac{\sqrt{3}}{2}\right)hV_{-}$	c	$\left(\frac{1+2h}{3}\right)V_{-}$	$\left(\frac{1-h}{3}\right)V_{-}$

E.4. Phase Lock Loop (PLL)

A phase lock loop (PLL) produces an output signal that synchronizes with the input signal, using a negative feedback loop, in-phase, and frequency. The PLL controls the internal signal such that, the error in phase between input and output is kept to a minimum, and the frequency is equal at input and output. A simple PLL circuit is often composed of three components, a phase detector, a loop filter, and a voltage-controlled oscillator. Phase detection is the main task for synchronization. The phase-detection block is used to measure the phase angle θ_m of the AC voltage. The angle is compared with $\theta_{\text{estimated}}$ from the look-up table used for waveform generation. This fundamental circuit is shown in Fig. E.6.

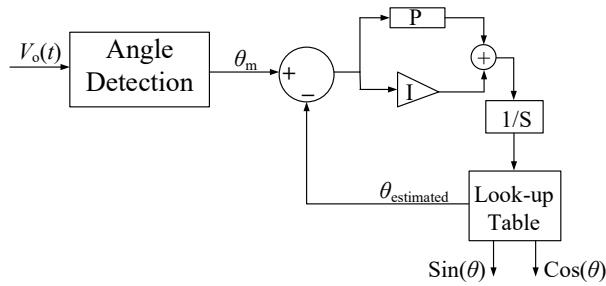


Fig. E.6 PLL Components

The difference between the calculated angle and the estimated angle is resolved with a PI controller. The PI-corrected performance needs another integrator to convert into an angle that provides the desired phase angle for $\sin(\theta)$ and $\cos(\theta)$ wave generation. If the integrator output gives an angle greater than 360° , it is reset to zero [203]. Phase-locked loops (PLL) with all dc / ac converters play an important role in delivering a synchronized reference phase signal to the ac system. This reference signal is used as a basic carrier wave in control circuits for the formulation of firing pulses. The actual instants of firing are determined using the PLL output as the base signal and adding the necessary firings [204].

In applications related to the three-phase systems, the PLL based on the synchronous reference frame is normally used. It is used in the conversion of the three-phase voltage vector from the abc reference frame to the dq reference frame using Park's Transformation. The angular position of the dq reference frame is controlled by a feedback loop that regulates the q component to zero. The abc to $dq0$ conversion needs the value of the angle θ that is determined by a phase-locked loop. The scheme of the phase-locked loop implemented here is shown in Fig. E.7.

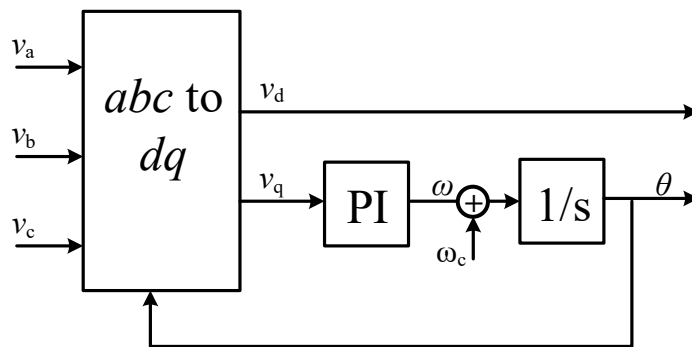


Fig. E.7 PLL using transformed quadrature voltage

The PLL can be adjusted keeping in view the fact that we align the d axis with v_{fd} which results in the voltage along the q-axis being null ($v_{fq} = 0$). A feedback loop controls the angular position of the dq frame and regulates the q component to zero. According to [201] the model for a three-phase PLL system is given below:

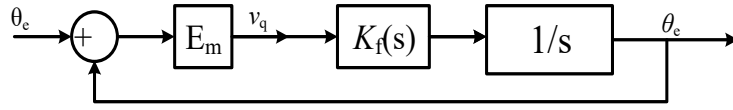


Fig. E.8 PLL Model according to [201]

The closed-loop transfer function of the previous figure is given by

$$H(s) = \frac{K_f(s)E_m}{s + K_f(s)E_m},$$

where $K_f(s)$ is the gain of the PI, given by:

$$K_f(s) = K_p + \frac{K_i}{s}.$$

Putting this value into the expression for the transfer function gives a second-order equation, whose poles are obtained by putting the denominator = 0.

$$s + K_f(s)E_m = s + \left(K_p + \frac{K_i}{s}\right)E_m = 0 \Rightarrow s^2 + K_pE_ms + K_iE_m = 0.$$

Comparing the above equation with the characteristic second order equation, we get,

$$K_p = \frac{2\xi\omega_n}{E_m}, K_i = \frac{\omega_n^2}{E_m} K_i = \frac{\omega_n^2}{E_m}.$$

The values of the parameters are

$$\xi = \frac{1}{\sqrt{2}} = \text{Damping factor.}$$

$$E_m = \frac{v_L}{\sqrt{3}} \sqrt{2} = \text{Peak value of the phase voltage.}$$

$$\omega_n = 100\pi \text{ rad/s} = \text{natural frequency of the voltage.}$$

The performances of all these schemes are evaluated considering two basic aspects. First of all, the tracking precision: the phase error between the output and input signals must converge to zero. Moreover, the system must exhibit a fast dynamic response that corresponds to considering a short transitory. Generally, a system characterized by a rapid dynamic response presents a greater tracking error and vice versa. For this reason, nowadays, the internal parameters of the schemes are derived as a trade-off between those two aspects making use of the settling time. The SRF-PLL behaviour is not very satisfactory in presence of harmonics or notches in the grid voltage.

E.5. Modification of the current control strategy

In this document, the modification of the Balanced Current Control (BCC) strategy is presented.

Fig. E.9 shows the initial condition of the abc injected current with BCC strategy. As seen in Fig. E.10, the short-circuit currents at the start and the recovery of the sag have an overshoot. The nominal current, in this case, is 2.7 A.

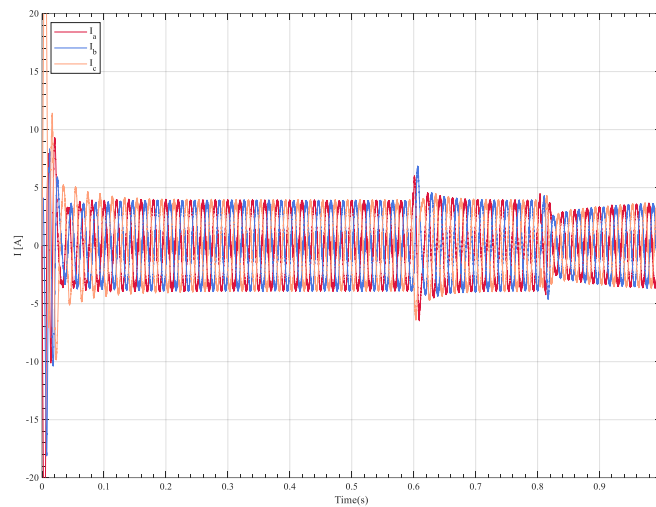
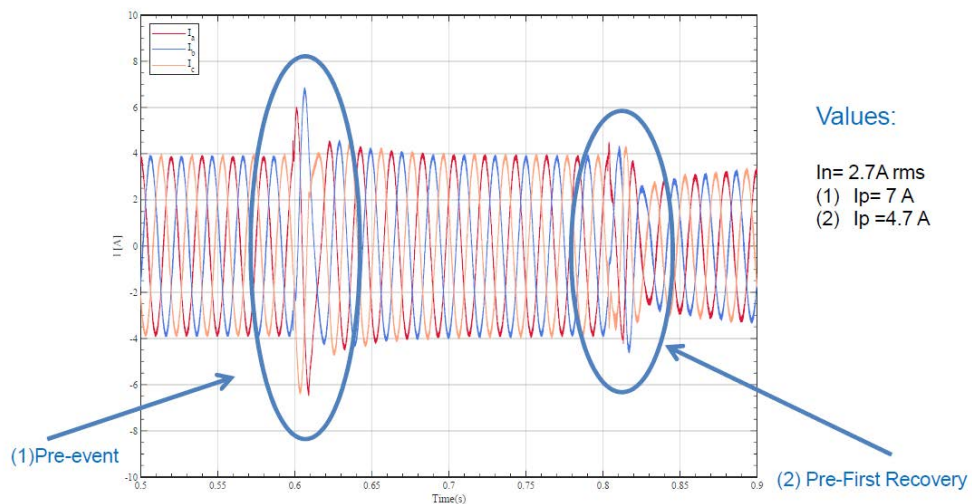
Fig. E.9 *abc* injected current (initial condition)

Fig. E.10 Short-circuit currents at the start and the recovery of the sag

As seen in Fig. E.11, the modifications on the grid code (highlighted in blue ellipse) are based on integrating the Spain grid code distribution voltage limit, and the current limit during the sag is increased from 1 to 1.1 pu.

Fig. E.12 shows the differences between initial condition and enhanced *abc* injected current with BCC strategy. As seen, the peaks at the beginning of the sag are reduced.

CONTROL CIRCUIT: NEW GRID CODE

```

1  function [idp_ref,iqp_ref,idn_ref,iqn_ref] = fcn(Va,Vb,Vc,I_N)
2  %#codegen
3
4  V = 75;           Grid voltage RMS
5  ip = 1;
6  iq = 0;
7
8
9  Vsag = sqrt(((Va).^2+(Vb).^2+(Vc).^2)/3)/V;   RMS Voltage [p.u.]
10
11  if (Va <= V*(1-0.075)) || (Vb <= V*(1-0.075)) || (Vc <= V*(1-0.075))
12      EN = 0;
13  else
14      EN = 1;
15  end
16
17  if (Vsag <= 0.5) && (EN ~= 1)
18      ir_p = ((-0.2*Vsag)+1);
19  elseif (Vsag > 0.5) && (EN ~= 1)
20      ir_p = ((-0.8571*Vsag)+1.3285);
21  else
22      ir_p = iq;
23  end

```

(a)

```

25  if (Vsag <= 0.925) && (EN ~= 1)
26      ia_p = ((ip/(1-0.075)^2)*Vsag);
27  else
28      ia_p = ip;
29  end
30
31
32  if (sqrt(ir_p^2+ia_p^2) > 1)
33      ir_ = ir_p*I_N*sqrt(3);
34      ia_ = sqrt(1-ir_p^2)*I_N*sqrt(3);
35  else
36      ir_ = ir_p*I_N*sqrt(3);
37      ia_ = ia_p*I_N*sqrt(3);
38  end
39  end
40  if (Vsag <= 0.925) && (EN ~= 1)
41
42  idp_ref = ia_*1.1;
43  iqp_ref = -ir_*1.1;
44  idn_ref = 0;
45  iqn_ref = 0;

```

47 else
48
49 idp_ref = ia_*1;
50 iqp_ref = -ir_*1;
51 idn_ref = 0;
52 iqn_ref = 0;
53 end

During the sag, the current value it's more than 2.7 A

(b)

Fig. E.11 Grid code modifications

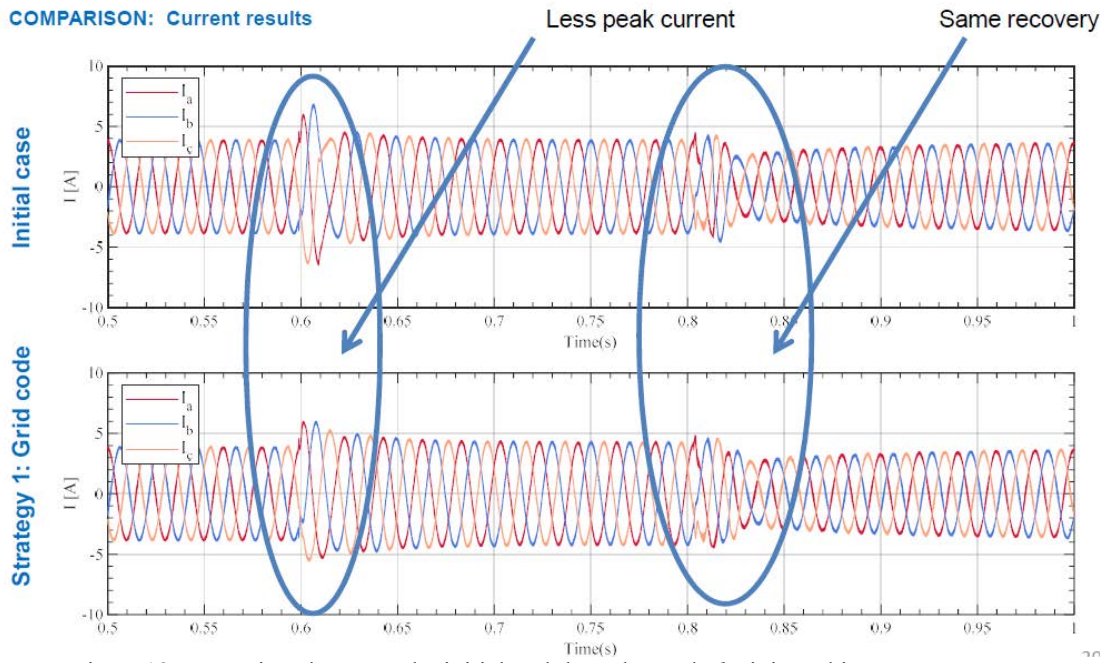


Fig. E.12 comparison between the initial and the enhanced abc injected inverter current

F. Appendix F

Experimental setup

The connection of the experimental setup is presented, also the devices used are commented on in this document.

F.1. System control connection

This section describes the hardware and controller connections of the system. To verify the chosen control strategies, an experimental model has been built in the laboratory as shown in Fig. F.1. The system consists of an AC supply connected to a transformer and rectifier to simulate the PV panel, Semikron three-phase inverter, 10 mH inductors, AC smart source to simulate different types of sags, and finally connected to (52Ω) resistive load, as shown in Fig. F.2.



Fig. F.1 Experimental setup

To ensure the perfect synchronization between the inverter and the smart source, a contactor has been used to connect the inverter to the smart source after PLL is working, as shown in Fig. F.2.

Fig. F.3 shows the controller connection, using dSPACE 1104 connected to three voltage sensors and three current sensors and using 6 PWM pulses to control the inverter. Fig. F.4 and Fig. F.5 show the experimental components used to implement the hardware connection.

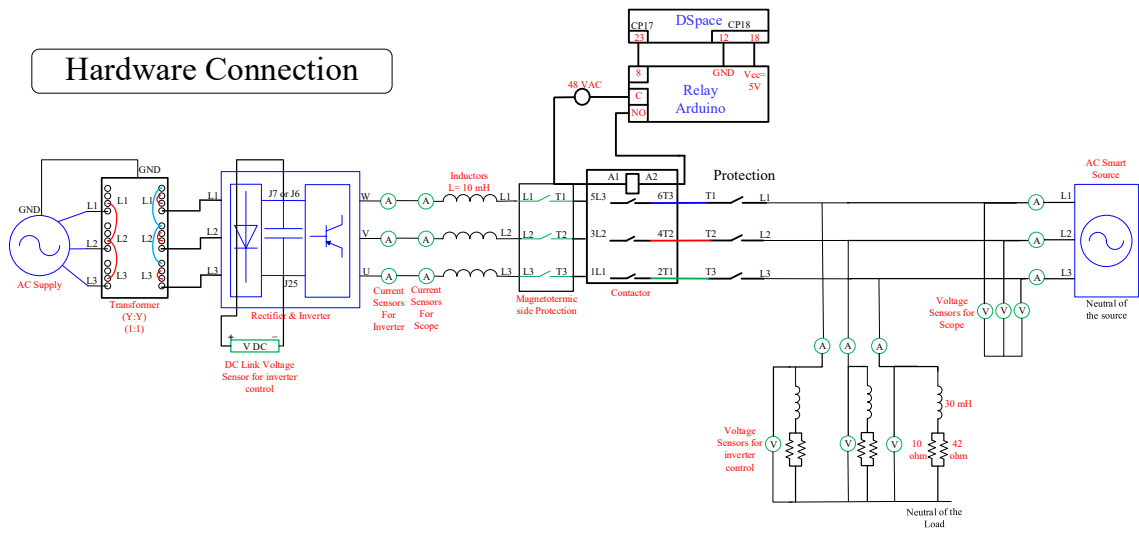


Fig. F.2 Hardware connection

Controller Connection

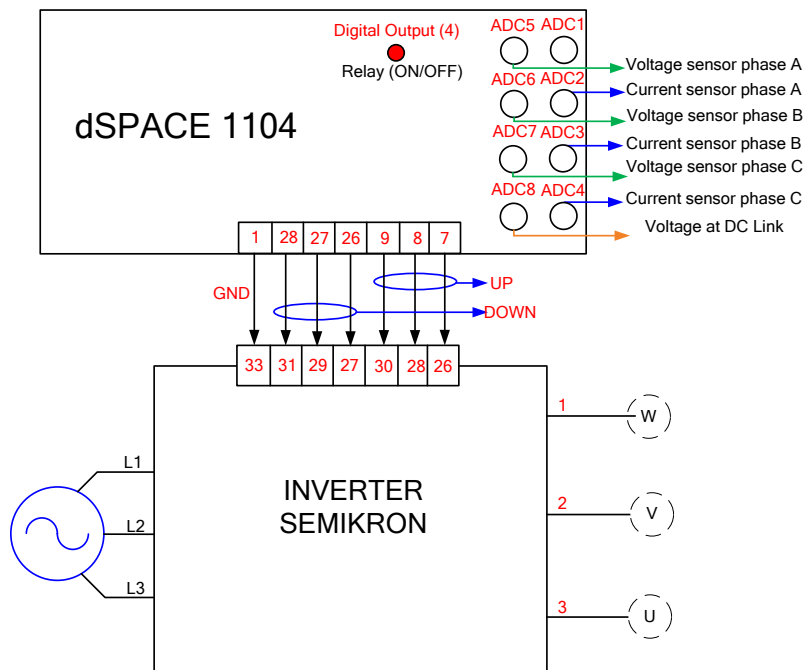


Fig. F.3 Controller connection

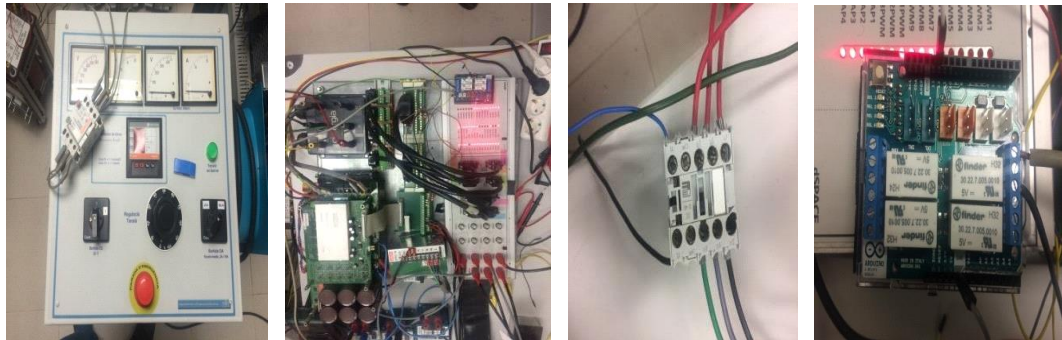
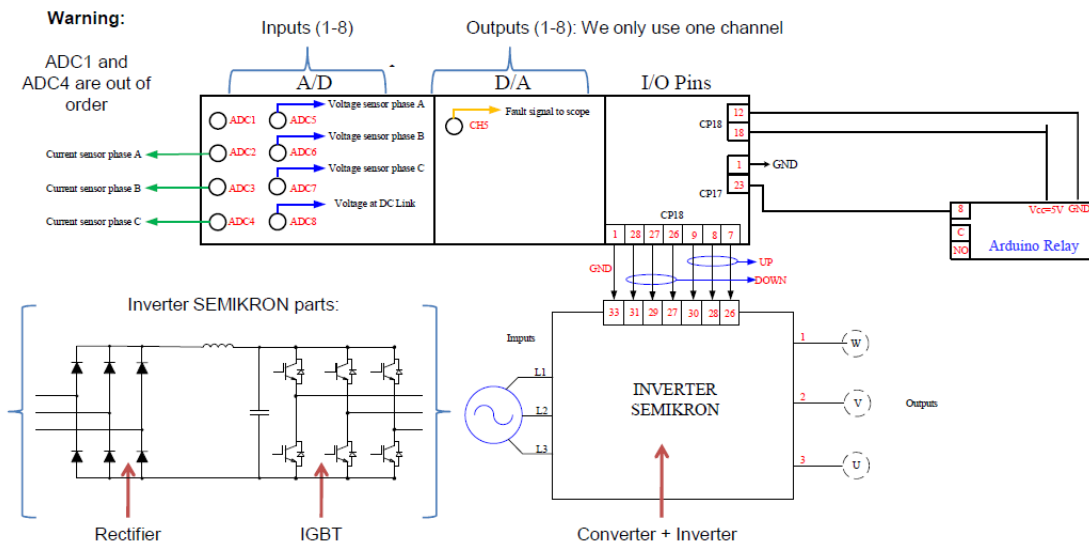


Fig. F.4 Experimental components (from left to right): AC Source, inverter, and dSPACE, contactor and relay



Fig. F.5 Experimental components smart source, resistive load, current and voltage sensors

Table F.1 shows the system parameters. The system consists of: a smart three-phase AC power source to emulate the grid and a converter connected to the grid through an RL filter.

Table F.1 Inverter system parameters

Inverter	Rated power	10 kVA
	Rated voltage	400 V
Filter	Inductance (L)	10 mH
	Resistance (R)	0.2 Ω
DC bus	DC rated voltage	800 V

The grid implemented in the laboratory is shown in Fig. F.6 that consists of a smart source, three transformers to achieve the required current, resistors, inductors, and capacitors to emulate the DLs, three DSPs to implement the protection algorithms, and an inverter, the parameters of the system can be seen in Table F.2.



Fig. F.6 Complete laboratory setup

Table F.2 System parameters

CINERGIA™ Inverter	Rated power	10 kVA
	Rated voltage	400 V
Filter	Inductance (L)	10 mH
	Resistance (R)	0.2 Ω
	DC bus	DC rated voltage
Three-phase Pacific™ Smart Power Source	345AMXT	4.5 kVA
SSR	Crydom H12WD4850	48-660 VAC
Distribution Lines (DL1, DL2, DL3)	Inductance (L_1, L_2, L_3)	1.37, 2.74, 4.11 mH
	Resistance (R_1, R_2, R_3)	625, 1250, 1875 m Ω
	Capacitance (C_1, C_2, C_3)	0.316, 0.632, 10, 30 μ F
Loads	Inductance (L_1, L_2)	10, 30 mH
	Resistance (R_1, R_2)	14.5, 42 Ω

The DSP and the Op-Amp circuit have been put in a box to ease the usage of the controller with BNCs and banana connections, as seen in Fig. F.7, and Fig. F.8.

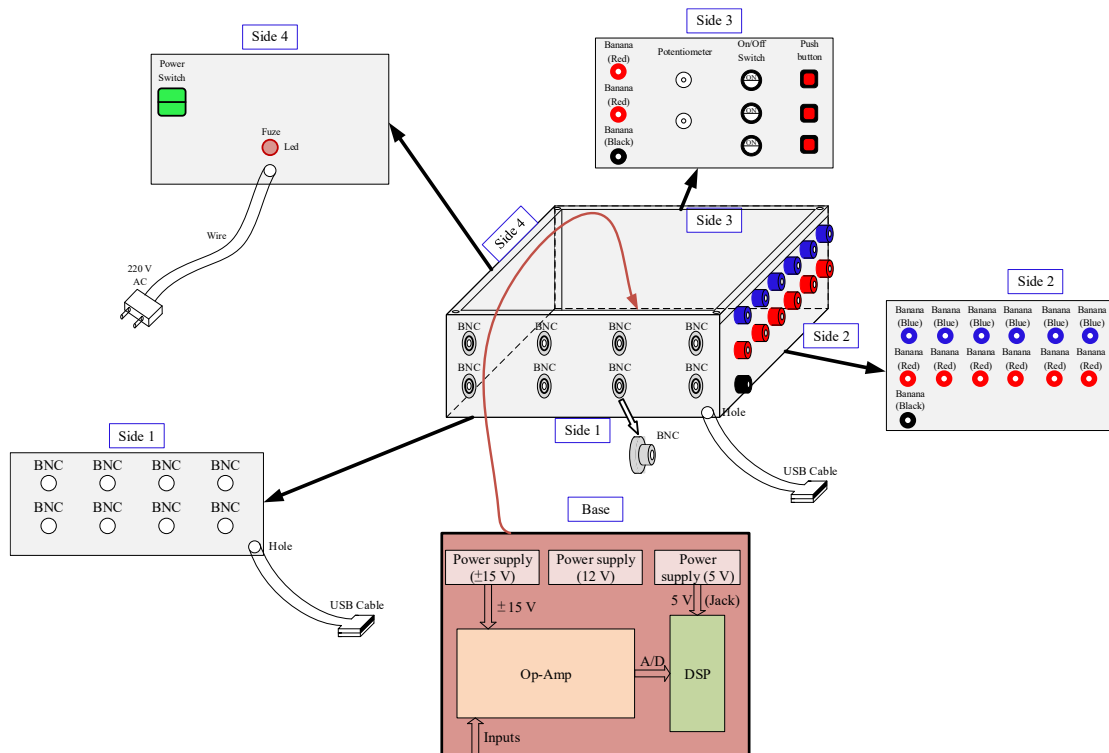


Fig. F.7 Box construction

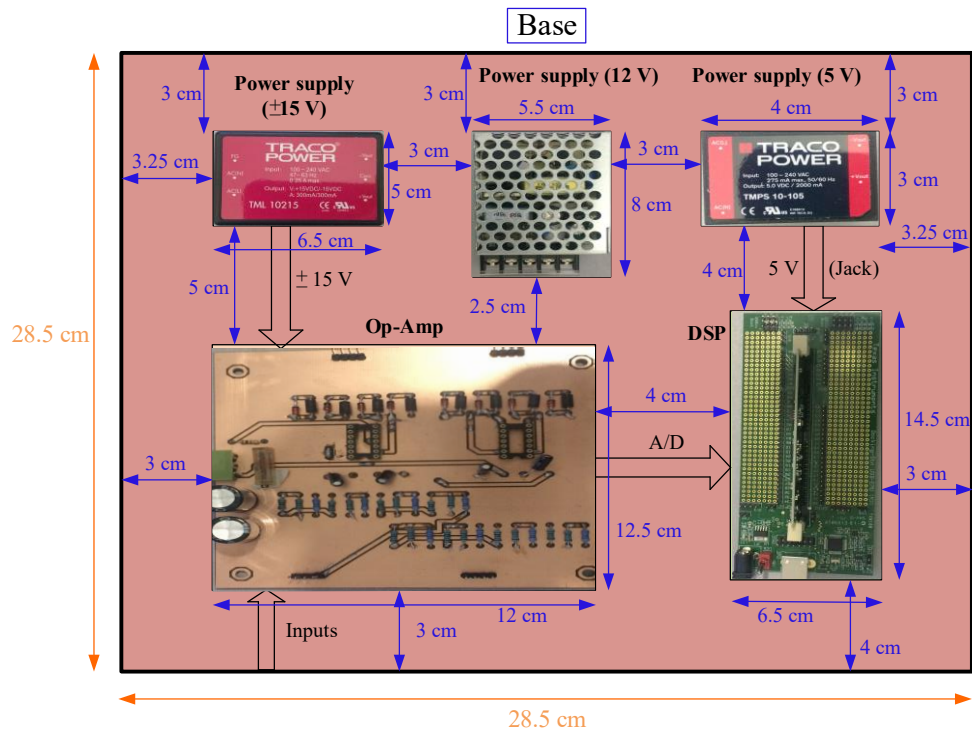


Fig. F.8 DSP, Op-Amp and power supply

In addition, Fig. F.9 shows the complete laboratory scheme of the complete ring grid, and Fig. F.10 shows the inverter connection scheme

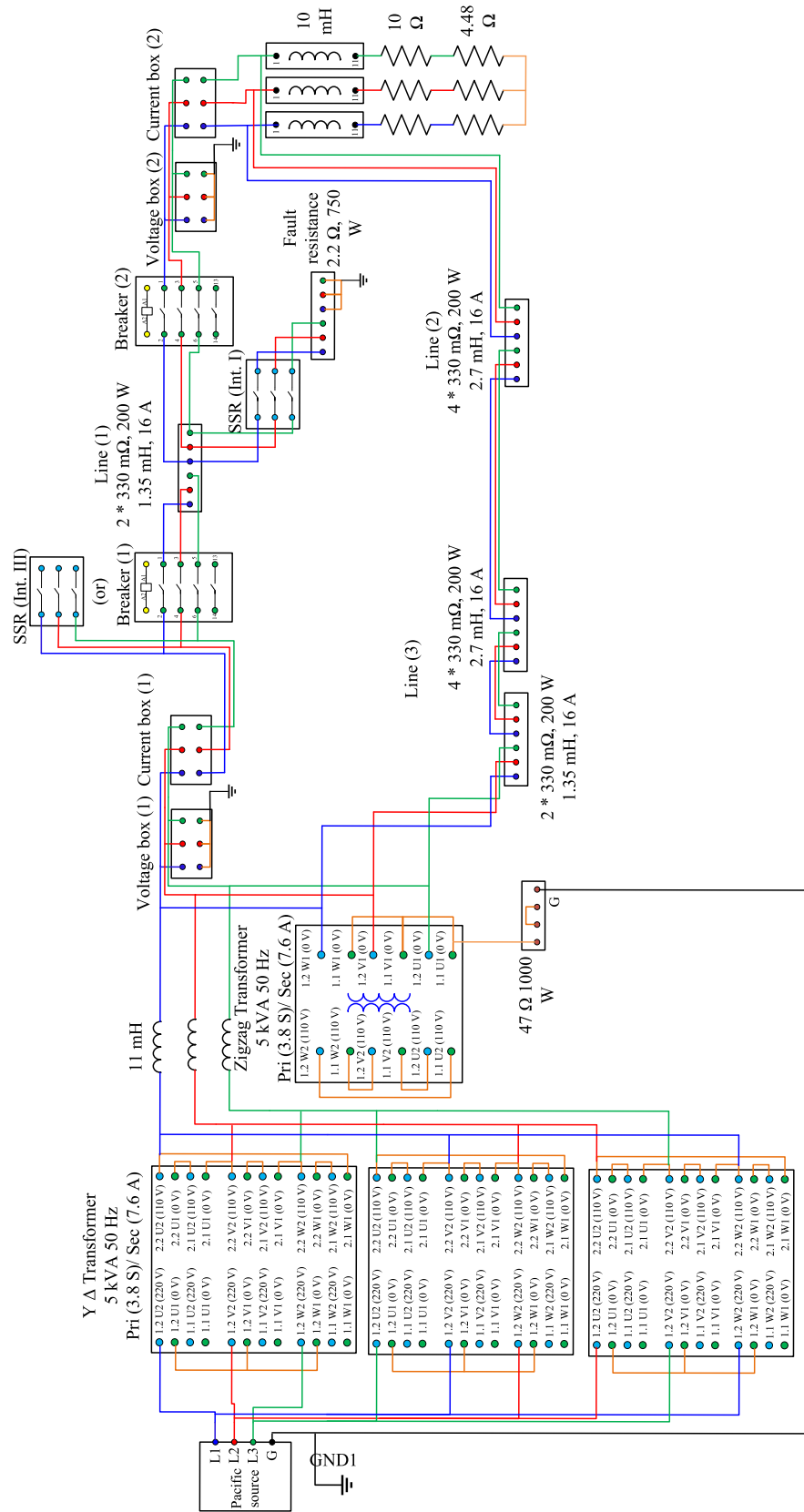


Fig. F.9 Scheme of the complete laboratory connection of the complete ring grid

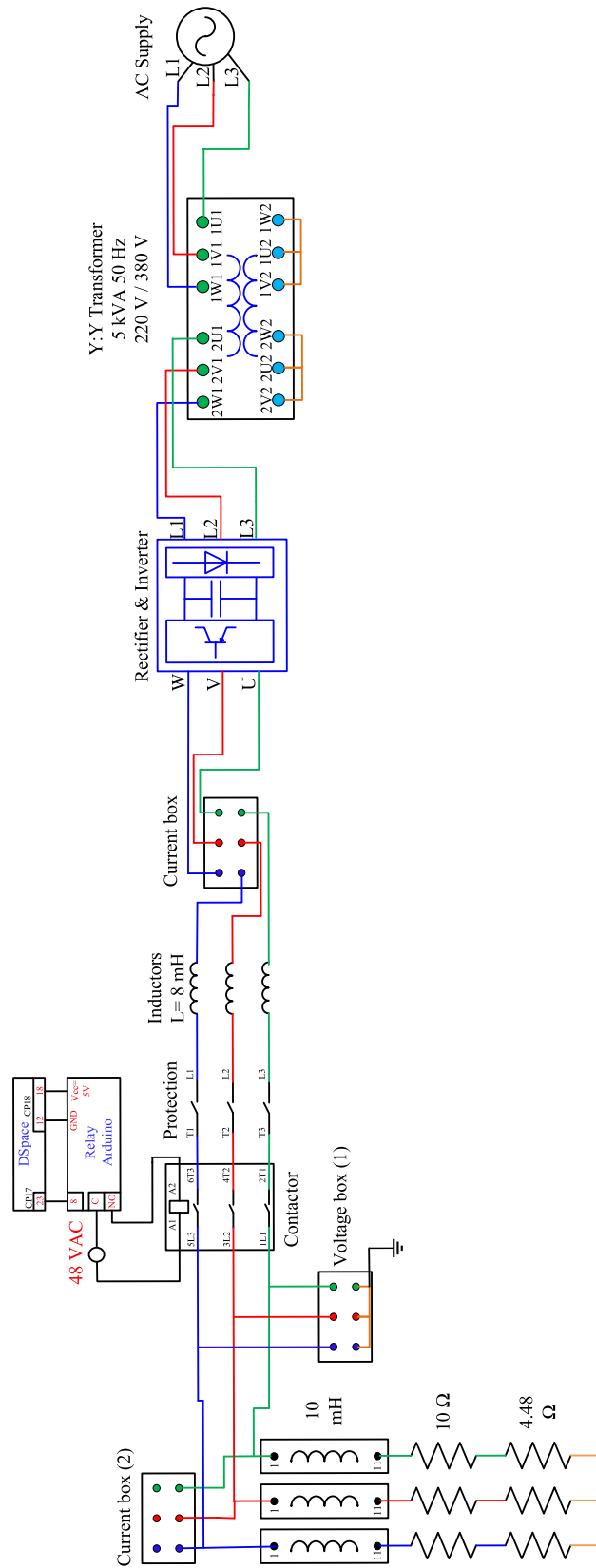


Fig. F.10 Scheme of the inverter connection

G. Appendix G

Calculation of the system parameters and pu values

In this document, the calculation of the systems parameters, pu, and experimental laboratory setup.

G.1. Calculation of line parameters

In order to calculate the base values of the grid implemented in the laboratory, the following equations are used, where V_{Base} , I_{Base} , S_{Base} , and Z_{Base} are the base voltage, current, apparent power, and impedance of the grid, respectively.

$$\begin{aligned} V_{\text{Base}} &= 75 \text{ V}, \quad I_{\text{Base}_{\text{ms}}} = 2.4 \text{ A}, \\ S_{\text{Base}} &= \sqrt{3} \cdot V_{\text{Base}} \cdot I_{\text{Base}_{\text{ms}}} = 540 \text{ W}, \quad Z_{\text{Base}} = \frac{V_{\text{Base}}}{I_{\text{Base}_{\text{ms}}}} = \frac{75}{2.4} = 31.25 \text{ } \Omega. \end{aligned} \quad (88)$$

The resistance of the analysed grid is $0.32 \text{ } \Omega$, for 2 km, and since the base value of the grid is $16 \text{ } \Omega$, as explained in chapter 3. Therefore, the pu value is

$$R_{\text{pu}} = \frac{0.32}{Z_{\text{Base}} = 16} = 0.02. \quad (89)$$

In order to calculate the corresponding resistance value for the grid implemented in the laboratory, the following equation is used

$$R_{\text{Lab}} = R_{\text{pu}} \cdot Z_{\text{Base}} = 0.02 \cdot 31.25 = 0.625 \text{ } \Omega \text{ or } R_{\text{Lab}} = \frac{0.32 \cdot 31.25}{16} = 0.625 \text{ } \Omega. \quad (90)$$

The inductance of the analysed grid is $2\pi f \cdot L$, $L = 3.4696\text{e-}04 \text{ H}$. So, $X_L = 0.218 \text{ } \Omega$ for 2 km. Since the base value of the real grid is $16 \text{ } \Omega$. So, the pu value is

$$X_{\text{Lpu}} = \frac{0.218}{16} = 0.0136. \quad (91)$$

Therefore, the inductance of the implemented grid in the laboratory is calculated using

$$X_{\text{LLab}} = X_{\text{Lpu}} \cdot Z_{\text{Base}} = 0.0136 \cdot 31.25 = 0.4304 \text{ } \Omega \text{ or } X_{\text{LLab}} = \frac{0.218 \cdot 31.25}{16} = 0.4304 \text{ } \Omega. \quad (92)$$

The capacitance of the analysed grid is $R_{\text{pu}} = \frac{1}{2\pi f C} = \frac{1}{2\pi(50)(0.309\text{e-}6)} = 1.0301\text{e+}04$. Since the base value of the real grid is $16 \text{ } \Omega$. Therefore, the pu value is

$$X_{\text{Cpu}} = \frac{10301}{16} = 643.8307. \quad (93)$$

Therefore, the capacitance of the implemented grid in the laboratory is calculated using

$$X_{\text{CLab}} = X_{\text{Cpu}} \cdot Z_{\text{Base}} = 643.83 \cdot 31.25 = 2.0120\text{e+}04 \text{ } \Omega \text{ or } X_{\text{CLab}} = \frac{10301 \cdot 31.25}{16} = 2.0120\text{e+}04 \text{ } \Omega. \quad (94)$$

$$C = \frac{1}{2\pi f X_C} = 0.158 \mu\text{F}. \quad (95)$$

G.2. Calculation of zigzag impedance

The impedance of the zigzag grounding transformer for a fault current (I_f) = 500 A is calculating using

$$X_{\text{zigzag_real}} = \frac{V_{\text{base_ph}}}{I_f/3} = \frac{20000/\sqrt{3}}{500/3} = 69.282 \Omega, \quad (96)$$

and the pu value is calculating using

$$X_{\text{zigzag_Lab}} = \frac{X_{\text{zigzag_real}}}{Z_{\text{base_real}}} * Z_{\text{base_Lab}} = \frac{69.282}{16} * 31.25 = 135.32 \Omega. \quad (97)$$

G.3. Calculation of fault resistance

As the studied grid is a distribution grid, and according to the standard, the ΔV is the allowable voltage drop (which equals 7.5% in distribution grids [157]). The calculation of the maximum fault resistance that can be considered as a fault is as follows:

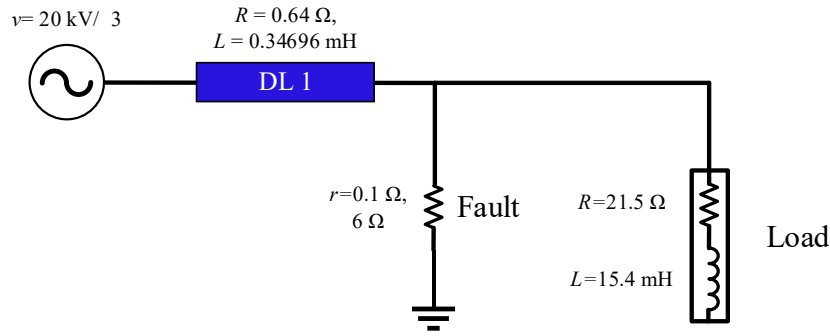


Fig. G.1 analysed grid with fault

If the voltage drop is less than the threshold calculated using (98), then it is considered as a fault.

$$v_{\text{grid}} = \frac{20}{\sqrt{3}} \text{ kV}, \Delta V = 7.5\%, v_{\text{drop}} = v_{\text{grid}} * \Delta V = \frac{1.5}{\sqrt{3}} \text{ kV}. \quad (98)$$

$$v_{\text{remain}} = v_{\text{grid}} - v_{\text{drop}} = \frac{18.5}{\sqrt{3}} \text{ kV} = 10.68 \text{ kV}.$$

When the fault resistance $r = 0.1 \Omega$, the short-circuit current equals 4.1 kA, and the voltage drop is 5.28 kV, and when the fault resistance $r = 6 \Omega$, the short-circuit current equals 1.83 kA, and the voltage drop is 10.62 kV, previous results are obtained using the simulation of the analysed grid. Therefore, the maximum fault resistance equals $r = 6 \Omega$.

The calculation of the fault resistance for the analysed grid and the grid implemented in the laboratory is obtained using

$$R_{\text{fault_real}} = 1.193 \Omega, R_{\text{fault_pu}} = \frac{R_{\text{fault_real}}}{Z_{\text{base_real}}} = \frac{1.193}{16} = 0.0746 \quad (99)$$

$$R_{\text{fault_Lab}} = R_{\text{fault_pu}} * Z_{\text{base_Lab}} = 0.0746 * 31.25 = 2.3312 \Omega.$$

Therefore, the pu values for the implemented grid in the laboratory can be summarized as follow

$$R_{\text{Line_pu}} = 0.02, X_{\text{L_Line_pu}} = j0.0138, R_{\text{fault_pu}} = 0.0746, V_{\text{fault_pu}} = 0.5911, I_{\text{fault_pu}} = 6.183. \quad (100)$$

G.4. Calculation of pu values

The calculation of the pu values of the voltage and current for the analysed grid and the grid implemented in the laboratory are obtained using

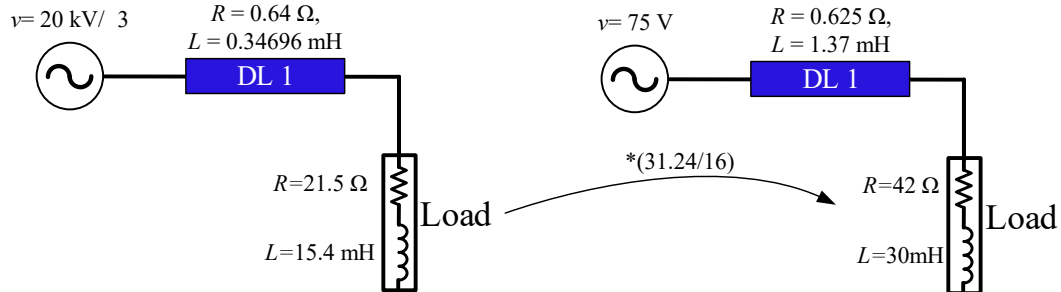


Fig. G.2 Analysed grids (a) Real grid, (b) Laboratory grid

$$\begin{aligned}
 v_{\text{real}} &= \frac{20\text{kV}}{\sqrt{3}}, \quad z_{\text{real}} = (0.32 + j0.218) \cdot 2 + (21.5 + j4.8381) \\
 i_{\text{real}} &= \frac{v_{\text{real}}}{z_{\text{real}}} = 506.1812 \text{ A}, \quad i_{\text{pu_real}} = \frac{506.1812}{i_{\text{base}} = 721.69} = 0.7014 \\
 v_{\text{lab}} &= 75, \quad z_{\text{lab}} = (0.66 + j0.4241) + (42 + j9.4248) \\
 i_{\text{lab}} &= \frac{v_{\text{lab}}}{z_{\text{lab}}} = 1.7 \text{ A}, \quad i_{\text{pu_lab}} = \frac{1.7}{i_{\text{base}} = 2.4} = 0.7083 \\
 i_{\text{pu_real}} &\approx i_{\text{pu_lab}}.
 \end{aligned} \tag{101}$$

Therefore, the pu values for the implemented grid in the laboratory can be summarized as follow

$$R_{\text{Line_pu}} = 0.02, \quad X_{L_{\text{Line_pu}}} = j0.0138, \quad R_{\text{fault_pu}} = 0.0746, \quad V_{\text{fault_pu}} = 0.5911, \quad I_{\text{fault_pu}} = 6.183. \tag{102}$$

Table G.1 and Table G.2 show the laboratory grid parameters and a comparison between the parameters of the analysed and the laboratory grids.

Table G.1 System parameters

CINERGIA™ Inverter	Rated power	10 kVA
	Rated voltage	400 V
Filter	Inductance (L)	10 mH
	Resistance (R)	0.2 Ω
DC bus	DC rated voltage	800 V
Three-phase Pacific™	345AMXT	4.5 kVA
Power Source		
SSR	Crydom H12WD4850	48-660 VAC
Distribution Lines	Inductance (L_1, L_2, L_3)	1.37, 2.74, 4.11 mH
(LN1, LN2, LN3)	Resistance (R_1, R_2, R_3)	625, 1250, 1875 mΩ
	Capacitance (C_1, C_2, C_3)	0.316, 0.632, 10, 30 μF
Loads	Inductance (L_1, L_2)	10, 30 mH
	Resistance (R_1, R_2)	14.5, 42 Ω

Table G.2 Comparison between the real grid and the laboratory grid parameters

	Analysed grid	Laboratory grid
Base voltage	$V_{\text{Base}} = 20 \text{ kV}$	$V_{\text{Base}} = 75 \text{ V}$
Base apparent power	$S_{\text{Base}} = 25 \text{ MVA}$	$S_{\text{Base}} = 540 \text{ W}$
Base current	$I_{\text{Base}_{\text{rms}}} = 721.69 \text{ A}$	$I_{\text{Base}_{\text{rms}}} = 2.4 \text{ A}$
Base impedance	$Z_{\text{Base}} = 16 \text{ } \Omega$	$Z_{\text{Base}} = 31.25 \text{ } \Omega$
Line resistance	$R_{\text{Line}_{\text{pu}}} = 0.02 \text{ pu}$	$R_{\text{Line}_{\text{pu}}} = 0.02 \text{ pu}$
Line inductance	$X_{\text{L}_{\text{Line}_{\text{pu}}}} = j0.0136 \text{ pu}$	$X_{\text{L}_{\text{Line}_{\text{pu}}}} = j0.0138 \text{ pu}$
Fault resistance	$R_{\text{fault}_{\text{pu}}} = 0.0746 \text{ pu}$	$R_{\text{fault}_{\text{pu}}} = 0.0746 \text{ pu}$

H. Appendix H

Proposed MPPT technique during partial shading

Due to the unexpected activity of solar energy sources, the PV system has a global maximum during normal weather conditions, while the PV system has several maximum points in partial shading. To address the constraints of MPPTs under shading conditions, this research proposes a Fuzzy Logic Tracking (FLC) based on Dynamic Safety Margin (DSM) as an MPPT approach for a PV system. However, it is important to note that during the study of the protection system in MV DS, the PV model has been simplified as a constant current source to simplify the whole system and reduce the total calculation time of the simulated cases. Furthermore, as the voltage dips considered only last for a few periods, it has been considered that the environmental conditions remain constant during the faults.

The next section gives a literature review regarding the most famous MPPT techniques especially in the case of partial shading conditions.

H.1. State of the art of the MPPT techniques during partial shading

Different PV MPPT approaches and algorithms for partial shading circumstances can be found across the literature [205]. A comprehensive analysis is presented in [206], to demonstrate the contributions and limitations of the MPPT techniques. New MPPT optimization algorithms, hybrid algorithms, modeling methodologies, and converter topologies are among them [207]. FLC [208], [209], ANN, and neuro-fuzzy algorithms [210] are used in several of these algorithms. The majority of them rely on a PV power-voltage (P-V) scanning to save the status at each observed shading condition. Other methods have been proposed in the previous, such as PSO [211], [212], Harris hawk optimization [213], bat algorithm [214], or implementing soft computing optimization techniques [207], [215]. The computational complexity, initial condition reliance, expense, and slow tracking are the most significant drawbacks of these approaches. Voltage and MPP oscillations may also occur as a result. Table H.1 gives a comparison between the most famous MPPT techniques. MPPT can be implemented in the DC/DC converter, or systems without a DC/DC converter are included in the DC/AC inverter control.

Table H.1 Comparison between different MPPT Techniques

MPPT Technique	PV Array Dependent	Analog or Digital	Convergence Speed	Implementation Complexity	Sensed Parameters
Hill-Climbing/P and O	No	Both	Varies	Low	Voltage, Current
Incremental Conductance	No	Digital	Varies	Medium	Voltage, Current
Fuzzy Logic Control	Yes	Digital	Fast	High	Varies
Neural Network	Yes	Digital	Fast	High	Varies

Under shaded conditions, FLC-based MPPT controllers can fail to track global maxima. As a result, research has described modified FLC algorithms. In [216] compares PSO with the integration of FLC with differential flatness control. In [210] implements an adaptive neuro-fuzzy system-based MPPT. Both approaches rely on P-V scan methods and require a longer time to reach a stable maximum operating point [217] proposes a type-2 FLC-based MPPT for partial shading. The fuzzy membership function is asymmetrical in this technique to avoid the uncertainty of generated power due to shading, and each membership has lower and upper boundaries. The key challenge with this method is determining the type-2 membership function. Furthermore, the majority of these methods are time-consuming and complicated. They also use a P-V scan method, which disrupts the supplied power and impacts grid stability while scanning. Reference [218] addresses FLC adaptation for MPPT by changing the FLC output depending

on the deviations of PV voltage and nominal open-circuit voltage. This approach is simple and reliable, although it does not perform well under partial shade in some cases.

As seen in the literature, an effective and reliable MPPT technique is still needed in order to assure the full power delivery of the PV system.

H.2. Chopper control employing MPPT control

Since the output power of a PV system is typically influenced by environmental conditions, the PV system has a global maximum during normal weather conditions, but in partial shading, the PV system has several maximum points, local and global peaks. As a result, if the MPPT controller is not robust enough, the MPPT may struggle to find the true maximum point and become trapped at a local maximum [219]. Because the bypass diodes offer an additional current path during the shaded mode, the characteristics of a bypass diode array differ from those of an array without such diodes. As a result, the P-V curve establishes several maxima. Consequently, an adaptive FLC based on the dynamic safety margin (DSM) performance index is developed. During transient and disturbance behaviours, the DSM-based controller has the benefit of maintaining a defined safety margin [220], [221]. Furthermore, in some cases of operational deviation, it can considerably improve performance recovery. The PV's safety region is selected to include all of the maximum operating points achievable under various weather conditions without shading. That indicates that after determining the safe operation zone, the operating monitoring point concerning the safe region shows abnormal behaviour due to shading or malfunction. Operating point deviation from the safe operation zone is used as a performance index to track the global maximum by adjusting the MPPT controller.

- Proposed MPPT employing adaptive Fuzzy Logic Controller (FLC) and Dynamic Safety Margin (DSM)

The DSM is a performance indicator in which the distance from a predetermined safety boundary is the independent variable. In Section H.4, the operation of the DSM is introduced. As a result, in the case of a PV system, PV voltage and power are chosen as the state variable relevant to the safety boundary, $\mathbf{x} = [V_{PV} P_{PV}]^T$, and the safe operating region, Φ , is chosen as the subspace that contains the state corresponding to the maximum power points for all possible weather, temperature, and irradiation conditions. If the PV operating point, which refers to a particular PV power, exceeds Φ , the PV system's extracted power will not achieve its maximum power, resulting in decreased PV system performance.

One of the following approaches can be used to identify a PV module's safe region: (1) offline, using the module's power and voltage (P-V) manufacturing characteristics. It does, however, necessitate having precise data on the PV modules and related connections; (2) online, by recording the highest power point achieved by FLC without shading conditions, however recording the border of the safe zone may take a long time; (3) by combining both offline and online approaches. Consider a commercial PV module of the KYOCERA KC200GT type with a 200 W rated power and a 30 V open-circuit voltage to demonstrate the concept. The safe region will be an elliptic shape, convex set, as illustrated in Fig. H.1, based on the P-V characteristic.

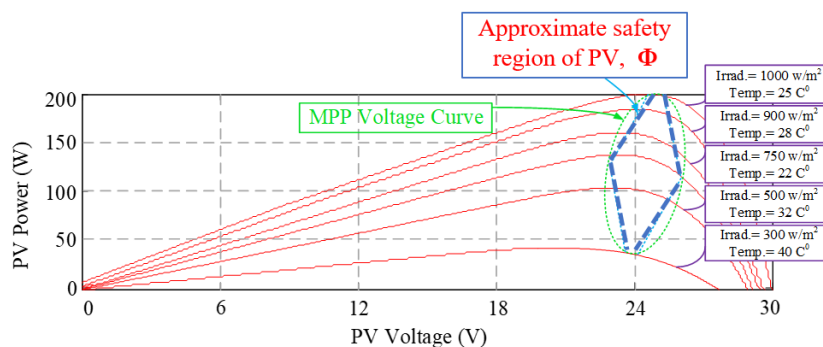


Fig. H.1 PV curve under different weather conditions for the KYOCERA KC200GT PV

The safe region of a multi-module PV system will be calculated by integrating the parameters of modules connected in series and parallel. When n_s modules are linked in series, the total safe region, Φ_s , is calculated by:

$$\Phi_s = \{\mathbf{x}_s \mid \mathbf{x}_s = n_s \mathbf{x}, \mathbf{x} \in \Phi\}, \quad (103)$$

where Φ is the safe region of a single module, $\mathbf{x} = [V_{PV} P_{PV}]^T$ is a single PV module's state vector, and $\mathbf{x}_s \in \mathbb{R}^2$, $\mathbf{x}_s = [V_s P_s]^T$ is the new string voltage and power condition variable.

When n_p modules are connected in parallel, the total safe region, Φ_p , is calculated by:

$$\Phi_p = \{\mathbf{x}_p \mid \mathbf{x}_p = A_p \mathbf{x}, \mathbf{x} \in \Phi\}, \quad (104)$$

where $A_p = \begin{bmatrix} 1 & 0 \\ 0 & n_p \end{bmatrix}$, $\mathbf{x}_p \in \mathbb{R}^2$, $\mathbf{x}_s = [V_p P_p]^T$ is the state variable of the new parallel voltage and power combination.

This safe operation zone may be approximated as a polytope, as illustrated in Fig. H.1, without any reduction in coherence, by a set of linear inequalities constraints, in the form of $\Phi = \{\mathbf{x} \mid \varphi_i(\mathbf{x}) \leq 0, i=1, \dots, 4\}$, where:

$$\Phi_i(\mathbf{x}) = \mathbf{a}_i^T \mathbf{x} - c_i \leq 0, i \dots 4, \quad (105)$$

where $\mathbf{a}_i^T \in \mathbb{R}^2$ and $c_i \in \mathbb{R}$ are constant, $\varphi_i(\cdot) = 0$ is a subspace of state vector boundary, $\partial\Phi$. These constraints can be arranged in a matrix (106):

$$\mathbf{A}\mathbf{x} \leq \mathbf{C}, \quad \text{where: } \mathbf{C} = \begin{bmatrix} c_1 \\ c_2 \\ \cdot \\ \cdot \\ \cdot \\ c_q \end{bmatrix}, \quad \mathbf{A} = \begin{bmatrix} \mathbf{a}_1^T \\ \mathbf{a}_2^T \\ \cdot \\ \cdot \\ \cdot \\ \mathbf{a}_q^T \end{bmatrix}. \quad (106)$$

The corresponding parameters of equation (106) for the characteristic indicated in Fig. H.1 are calculated for the specified KYOCERA KC200GT PV module type, such as:

$$\mathbf{C} = \begin{bmatrix} -2450 \\ -865 \\ 2195 \\ 737.5 \end{bmatrix}, \quad \mathbf{A} = \begin{bmatrix} -90 \\ -37.5 \\ 90 \\ 37.5 \end{bmatrix}. \quad (107)$$

The safe region boundary is $\partial\Phi(\mathbf{x}_p) = \{\mathbf{x}_p \mid \mathbf{A} \mathbf{x}_p = \mathbf{C}\}$. As the boundary is made up of four linear segments, the matrix equation indicates:

$$\mathbf{A}\mathbf{x}_p \leq \mathbf{C}. \quad (108)$$

The smallest distances between the current state \mathbf{x} and the number of a boundary segment i ($\delta_i(t)$) are provided by [220]:

$$\delta_i(t) = \frac{c_i - \mathbf{a}_i^T \mathbf{x}(t)}{\|\mathbf{a}_i\|_2} \begin{cases} \geq 0, & \text{if } \varphi_i(\mathbf{x}) < 0 \\ < 0, & \text{if } \varphi_i(\mathbf{x}) > 0 \end{cases} \quad (109)$$

For $\mathbf{d}(t) = [\delta_1(t), \delta_2(t), \dots, \delta_q(t)]^T$, all boundaries distance vector can be determined using the following formula:

$$\mathbf{d}(t) = \mathbf{D}_{ia} (\mathbf{C} - \mathbf{A}\mathbf{x}(t)) = \mathbf{d}_c - \mathbf{D}_a \mathbf{x}(t), \quad (110)$$

where: $D_a = \begin{bmatrix} \frac{1}{\|a_1\|_2^2} & \cdot & \cdot & 0 \\ \cdot & \cdot & \cdot & \cdot \\ \cdot & \cdot & \cdot & \cdot \\ 0 & \cdot & \cdot & \frac{1}{\|a_q\|_2^2} \end{bmatrix}$, is a diagonal matrix, $d_c = D_a C$, $D_a = D_{ia} A$, $d(\cdot) \in \mathfrak{R}^q$, $C \in \mathfrak{R}^q$, $d_c \in \mathfrak{R}^q$, $D_a \in \mathfrak{R}^{q \times n}$, and $D_{ia} \in \mathfrak{R}^{q \times q}$.

The safe region is a polytope since Φ is convex and the boundary constraints are linear, and the DSM, $\delta(\cdot)$, is the minimum element in $d(\cdot)$ [220], such as:

$$\delta(t) = \min_{1 \leq i \leq q} \delta_i(t) \quad (111)$$

Therefore, the steps to determine the safe region, Φ , of a PV system and the DSM can be stated as follows:

- 1) Obtain the safe region of a single PV module offline, using the PV manufacture's datasheet, as shown in Fig. H.1.
- 2) Calculate the boundary using (105), (106), (107), and (108).
- 3) Compute the overall safe region of all modules based on their parallel and series connections using (103) and (104).
- 4) Determine the online DSM by solving the optimization problem presented in section H.4 subject to constraints (108).
- 5) Overcome the approximation in steps 1 and 2, record the observed maximum point under normal conditions and, if necessary, alter the safe region boundary in step 3.

The general rule base structure of FLC can be seen in the author's previous work [222]. A generic FLC structure for MPPT could be used with normalized membership functions and a fixed rule base to avoid FLC redesign for varied PV system configurations and ratings. Only the FLC's input and output scale factors must be determined based on the PV system rating.

The MPPT controller's primary function is to determine the PV converter's gate signal. As a result, the DSM value may be utilized to control the FLC output as illustrated in Fig. H.2 to achieve the PV converter subsystem's appropriate gating signal duty cycle. The adaption of FLC based on DSM is accomplished in the following steps:

- 1) Obtain the FLC output according to the general rule base structure of FLC.
- 2) Determine the instantaneous value of the DSM, $\delta(\cdot)$, based on the defined safe region, Φ , of the PV, using the current state of the PV, $\mathbf{X} = [V_{PV} P_{PV}]^T$.
- 3) If the PV state, $\mathbf{X} = [V_{PV} P_{PV}]^T \in \Phi$, then the system is normal, and standalone FLC is sufficient to keep track of the global MPP. Otherwise, an abnormal condition has occurred (shading).
- 4) The control criteria are considered so that if the PV state, $\mathbf{X} = [V_{PV} P_{PV}]^T \notin \Phi$, then according to (112), the output of FLC is adjusted based on the value of $\delta(\cdot)$:

$$Duty = Duty_{FLC} [1 + S_g(t) \cdot \delta(t)], \quad (112)$$

and:

$$S_g(t) = \begin{cases} 0, & \text{if } x \text{ within the safe operatio region} \\ k, & \text{if } x \text{ out of the safe operatio region} \end{cases}$$

where $Duty$ is the duty cycle of the PWM, $k \in [0, 1]$ is the adaptation gain and $\delta(t)$ is the instantaneous DSM. When partial shading occurs, the operating point moves to the hazardous mode. Then FLC will then be enhanced by DSM to shift to another maximum point within Φ . Maximum operating points are recorded throughout the adaptation, and the DSM-based FLC adjusts the converter to perform at the global maximum point. Fig. H.3 shows the flowchart of the proposed DSM based FLC MPPT

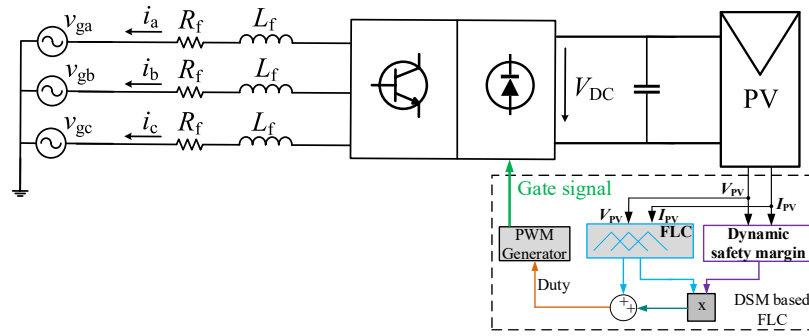


Fig. H.2 General configuration of MPPT using DSM based FLC

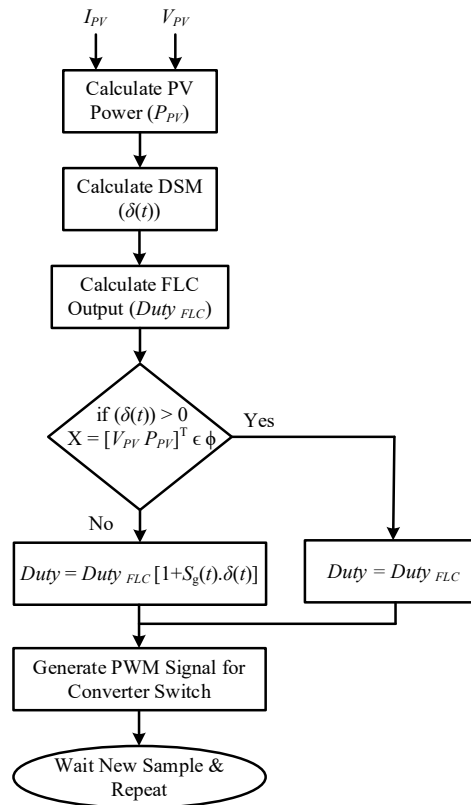


Fig. H.3 Flowchart of the proposed DSM based FLC MPPT

➤ Case Study

A PV array with a flyback converter is followed by a current-controlled voltage source inverter in the case study that uses the MPPT controller based on DSM. For numerous reasons, the flyback converter was chosen. During the off phase, the voltage is changed to a value set by the turns ratio. This enables the use of a diode with lower capacitances and hence quicker switching speeds, as well as a MOSFET with a significantly lower ON resistance. As a result, power losses could be decreased, resulting in increased efficiency. It also offers a large input voltage range and, due to the presence of a high-frequency transformer, provides grid and PV isolation [223]. Furthermore, there is no need to utilize a large transformer to step up the voltage to grid voltage following the inverter. In addition, because it has fewer components than other topologies, it is less expensive and delivers DC-DC in a single stage rather than several stages. It has a higher ripple current and input and output capacitance; however, its efficiency ranges from 75% to 80% [224].

The proposed technique was simulated using the MATLAB™ SIMULINK environment for the PV KYOCERA KC200GT module in various scenarios. The simulation results are presented to assess the efficacy of the suggested single-phase grid-connected PV system model and control algorithms. Fig. H.4 shows PV power curves for various numbers of modules under standard weather conditions of 25 °C and 1000 W/m², as well as partial shade conditions.

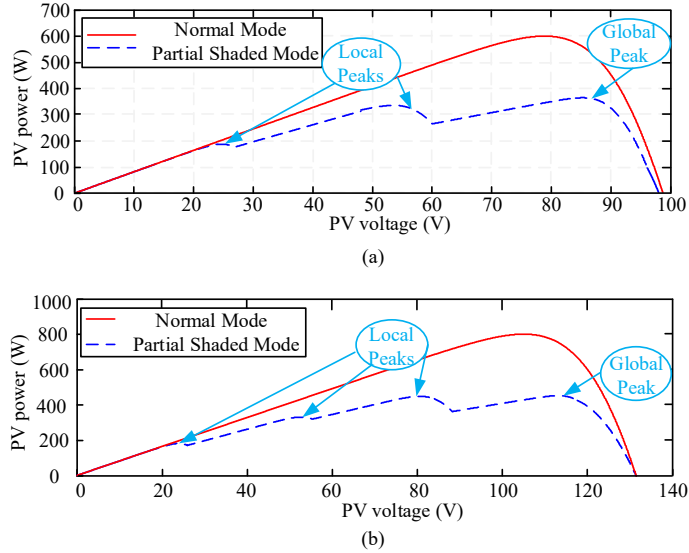


Fig. H.4 PV power curves for (a) three modules (b) four modules at normal and partial shading conditions

The safe region, Φ , of each module, is calculated using the module’s datasheet. The overall safe region will be obtained by connecting two or more modules in series. Then the parameters of equation (106) for two modules, three modules, and four modules, respectively, will be as follow:

$$A = \begin{bmatrix} -90 & -1 \\ -37.5 & 1 \\ 90 & 1 \\ 37.5 & -1 \end{bmatrix}, C = \begin{bmatrix} -4900 \\ -1730 \\ 4390 \\ 1475 \end{bmatrix}, A = \begin{bmatrix} -90 & -1 \\ -37.5 & 1 \\ 90 & 1 \\ 37.5 & -1 \end{bmatrix}, C = \begin{bmatrix} -7350 \\ -2595 \\ 6585 \\ 2212.5 \end{bmatrix}, A = \begin{bmatrix} -90 & -1 \\ -37.5 & 1 \\ 90 & 1 \\ 37.5 & -1 \end{bmatrix}, C = \begin{bmatrix} -9800 \\ -3460 \\ 8780 \\ 2950 \end{bmatrix}. \quad (113)$$

Then by determining the status of the PV system, $X = [V_{PV} P_{PV}]^T$, the observed maximum point under normal conditions is recorded to update the safe region boundary to overcome the approximation of the calculated region of a single module.

Fig. H.5 shows the PV power for the DSM-based FLC while it is partially shaded. The output power is verified by evaluating the global maximum in Fig. H.4 using the results obtained in Fig. H.5 under partial shade conditions.

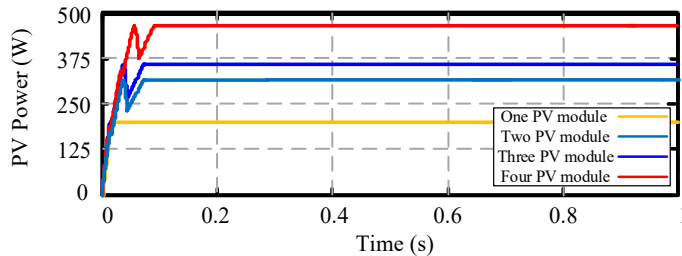


Fig. H.5 PV power curve for different PV modules for DSM based FLC at partially shaded mode

At partial shade conditions, Fig. H.6 displays the output PV voltage for DSM-based FLC and standalone FLC for multiple PV modules. The FLC controller’s output voltage remains constant at the local maxima

of 25 V and 200 W, which is the first maxima point. The FLC output voltage based on DSM, on the other hand, always reaches the global maximum. For example, in the case of four modules, the voltage is 115 V and the power is 450 W, indicating that the proposed method is successful. Table H.2 summarizes the simulation results under shading conditions for various PV module configurations.

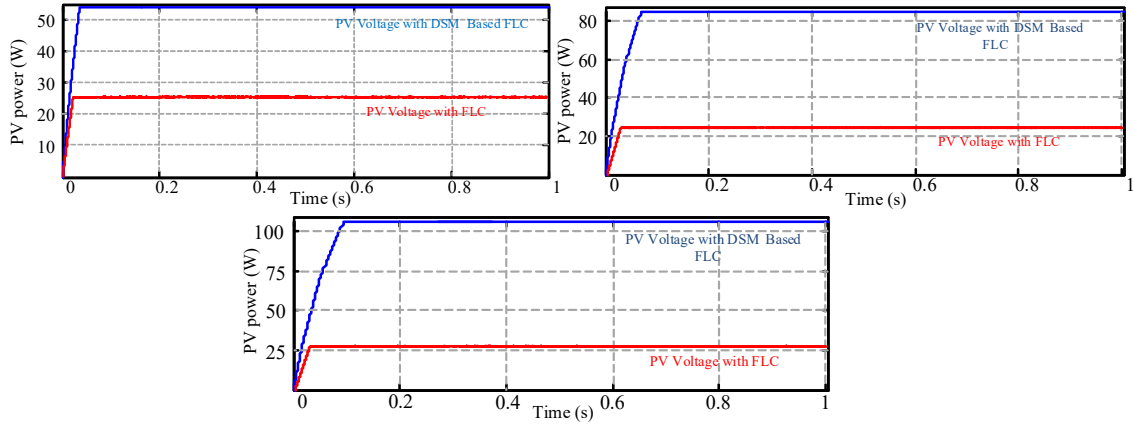


Fig. H.6 PV voltage for (a) one PV module (b) two PV modules (c) four PV modules at partial shading conditions.

Table H.2 Summary of simulation results.

Case	FLC		DSM Based FLC	
	P _{MPPT} (W)	V _{MPPT} (V)	P _{MPPT} (W)	V _{MPPT} (V)
1 PV module	200	25	200	25
2 PV modules	200	25	300	55
3 PV modules	200	25	350	85
4 PV modules	200	25	450	115

It is not necessary to use a P-V scan with this technique; it has a positive impact on grid stability and has a quick response. The determination of the safe operating region is the core issue of the suggested approach. As a result, before adopting the suggested technique, a safe region must be defined offline based on manufacturing data, and then updated or identified online based on historical data. A practical PV system is implemented to validate the proposed method, and the demonstrated results show the productivity of the proposed algorithm.

H.3. MPPT employing adaptive FLC and DSM (practical Case Study)

The proposed MPPT technique is verified through a laboratory PV system prepared as illustrated in Fig. H.8. The control algorithms described in chapter 4 are implemented on a 32-bit, floating-point digital signal processor (DSP) type TMS320F28335 (TEXAS INSTRUMENTS), and the data are recorded using a TDS2024 200 MHz two Channels Digital Real-Time Oscilloscope (Tektronix, Beaverton). The list of the experimental components is shown in Table H.3.

The PV module's power curve has been measured and simulated. They are presented in Fig. H.9 with a maximum power of 80 W at temperature and irradiation of 28 °C and 700 W/m², respectively; these values depend on the atmosphere condition when the experiment was executed. As described in chapter 4, the practical PV curve from the datasheet was used to calculate the safety region (Φ). The flowchart of the proposed MPPT is shown in Fig. H.7.

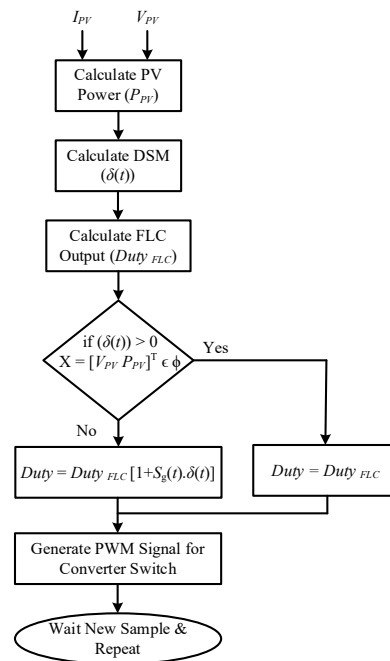


Fig. H.7 Flowchart of the proposed DSM based FLC MPPT

Table H.3 List of experimental components

Component	Description
The selected PV module	80 W NT-80 (E1) (SHARP) [225]
The flyback converter transformer	MYRRA-74070 ETD 44 120–160 W (MYRRA) [226]
The flyback switching frequency	50 kHz
The DC-link capacitor	470 μ F, 250 V
The current and voltage sensors	LA 100-P (LEM), and LV 25-P (LEM) [227], [228]

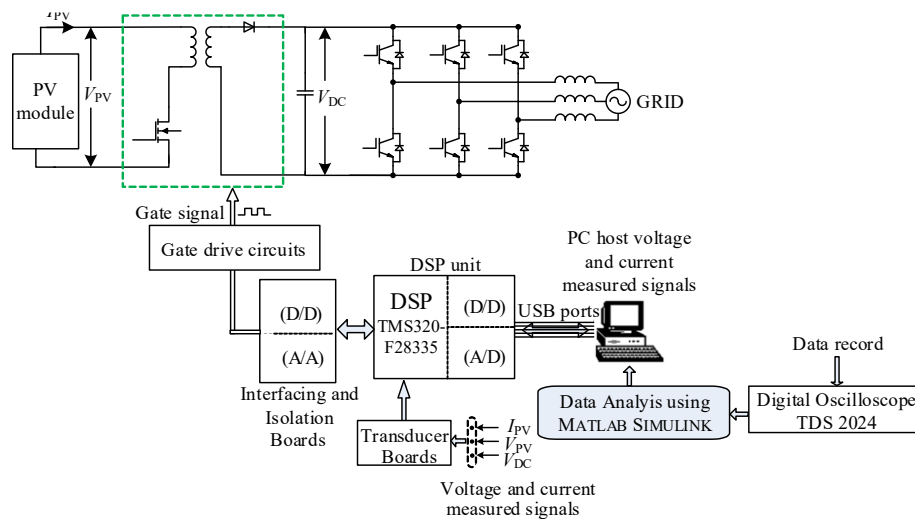


Fig. H.8 Practical system setup

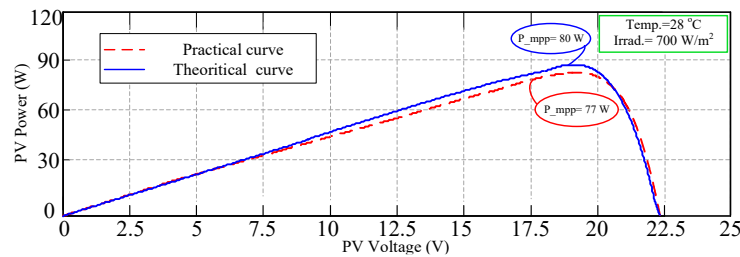


Fig. H.9 Practical and theoretical curves of the PV module at 80 W

Fig. H.8 shows the connection of the test rig, where the input measured signals are: the actual PV voltage, current, and DC bus voltage. The DSP has been programmed using the developed MATLABTM SIMULINK software. The DSP and PC are configured up in a two-level hierarchical control structure, with the DSP acting as an individual control that is directly connected to the field and the PC acting as a supervisory controller. USP port is used to connect the DSP and the PC. The proposed algorithm is then used to generate the appropriate duty cycle of the flyback converter to adjust the voltage operating point depending on the current measurement.

In normal and partial shaded modes, the classical FLC and the DSM-based FLC were evaluated, and the results were shown and analysed. The V_{mpp} signal measured by the DSP during normal operation for the DSM-based FLC technique is shown in Fig. H.10. The result demonstrates the capability to calculate the maximum power output from the PV module accurately. Fig. H.11 depicts the simulation results of a single module voltage of 17.8 V. The voltage obtained from the PV curve about 80 W as seen in Fig. H.9 is remarkably similar. Fig. H.12 displays the PV curve for the practical system under normal and partial shading conditions, while Fig. H.13(a) and Fig. H.13(b) show the extracted power from the PV module under partial shading conditions using FLC with DSM and standalone FLC, respectively. FLC had a power of almost 36 W, which corresponds to the local peak in Fig. H.12. The power of the DSM-based FLC was nearly comparable to the global peak of 80 W in Fig. H.12.

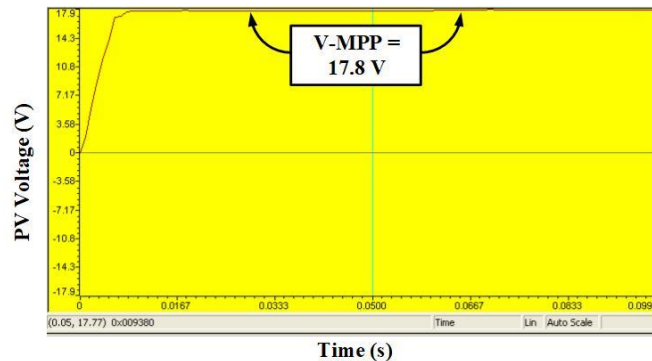


Fig. H.10 The measured PV voltage of DSM based FLC at normal condition

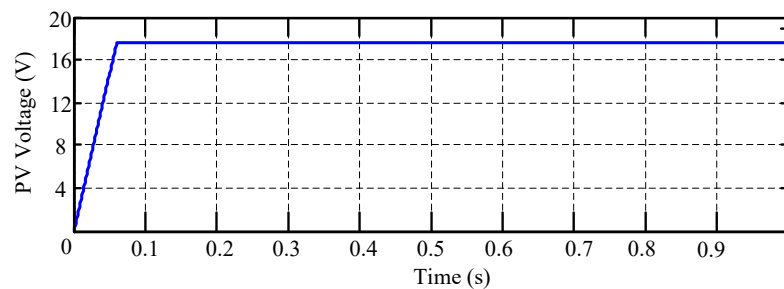


Fig. H.11 PV voltage simulation of DSM based FLC at normal condition

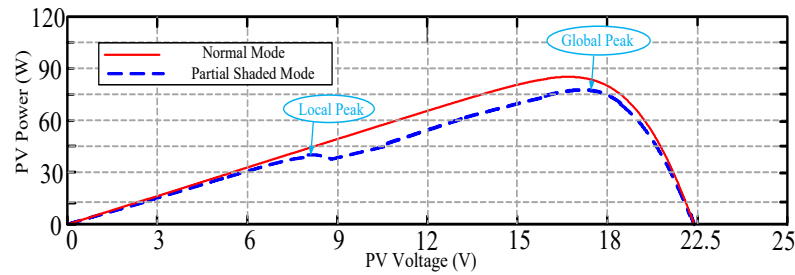


Fig. H.12 PV curve at normal and partial shading conditions

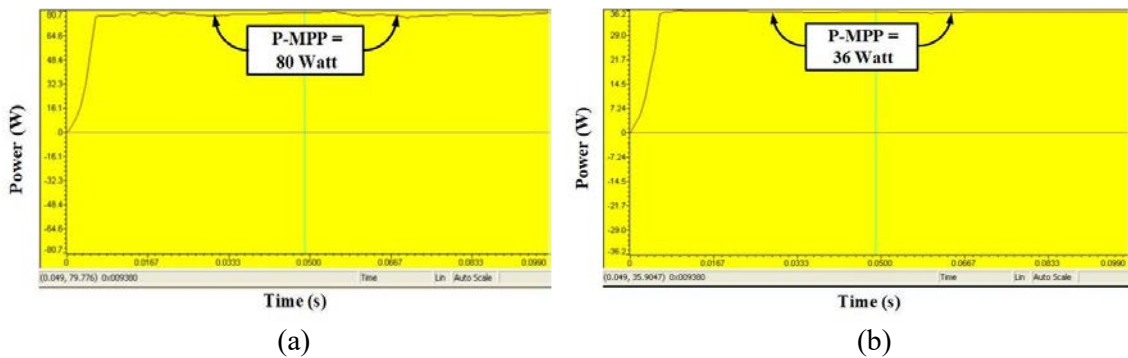


Fig. H.13 PV power for (a) DSM based FLC, (b) FLC at partial shading condition

It is evident from the simulation and practical results that DSM-based FLC is resilient, quick, and capable of tracking the global maximum in shading conditions. Furthermore, it requires less computational effort than the other techniques. Finally, it avoids the need for a P-V scan of the PV system, which significantly influences grid stability.

A multiple-stage topology has been considered that consists of photovoltaic arrays, a DC/DC converter to adapt the photovoltaic voltage to the input of the inverter, and a three-phase inverter; first, the chopper control is implemented. For normal and partial shaded modes, an MPPT technique based on the Fuzzy Logic Controller (FLC) using Dynamic Safety Margin (DSM) as a performance index is presented. For normalizing the FLC, the DSM indicates the present Photovoltaic (PV) status from the safety boundary. A string of different series connections up to four PV modules has been used to ensure the efficacy of the suggested approach.

The simulation results show that the proposed MPPT technique can operate the PV system at the global maximum point, whereas traditional fuzzy MPPT fails to do so in the condition of partial shading. An actual PV system setup successfully validated the proposed method. As the approach does not need a P-V scan, it has a positive influence on grid stability and provides a quick response. However, before adopting the proposed method, a safe region must be defined offline based on manufacturing data, then updated online based on historical data.

It is necessary to highlight that during the study of the protection scheme in MV DS, the PV model was simplified to a constant current source to simplify the system and reduce the total computation time of the simulated cases. Furthermore, because the faults (sags) only last for a limited number of periods, the weather is supposed to remain steady during the faults (sags).

H.4. Mathematical inference of the MPPT under partial shading mode

Two groups of PV cells linked in series within a module could model a partially shaded module. Different levels of irradiance are received by each group. The module consists of r series-connected cells, in which s shaded cells receive irradiance G_1 , and $(r - s)$ shaded cells receiving irradiance G_2 . The PV parameters can be represented as:

$$I_{ph1} = I_{ph} G_1 \quad (114)$$

$$I_{ph2} = I_{ph} G_2 \quad (115)$$

$$N_{s1} = s \quad (116)$$

$$N_{s2} = r - s, \quad (117)$$

where subscripts 1 and 2 refer to the cells receiving irradiance of G_1 and G_2 respectively, I_{ph} is the solar-generated current. Considering the existence of a single bypass diode for each PV module, the output current and voltage at the array terminal can be obtained by solving the following equations:

$$I_{PV} = \begin{cases} I_{Ph}(G_1) - I_{o1} \left[\exp\left(\frac{q(V_{PVm1} + I_{PV} R_s)}{N_{s1} A K T_k}\right) - 1 \right] - \frac{(V_{PVm1} + I_{PV} R_s N_{s1})}{R_p N_{s1}} & I_{PV} > I_{Ph1} \\ I_{Ph}(G_2) - I_{o1} \left[\exp\left(\frac{q(V_{PVm2} + I_{PV} R_s)}{N_{s2} A K T_k}\right) - 1 \right] - \frac{(V_{PVm2} + I_{PV} R_s N_{s2})}{R_p N_{s2}} & I_{PV} < I_{Ph2} \end{cases} \quad (118)$$

$$V_{PV} = \begin{cases} V_{PV1} & I_{PV} > I_{Ph1} \\ V_{PV2} + V_{PV1} & I_{PV} < I_{Ph2} \end{cases}, \quad (119)$$

where A is the diode ideality factor, G is the operating irradiance level (W/m^2), K is the Boltzmann constant, G_r is the nominal irradiance level (W/m^2), N_s is the number of series-connected cells, T_k is the operating temperature (K), V_{PV} is the output voltage, I_{o1} is the diode saturation current, V_{PVm} is the PV module output voltage, I_{PV} is the PV output current and R_s is the series-connected resistance. During partial shading, a segment of the PV cells, which obtains uniform irradiance, still perform at the optimum efficiency. Although the current flow is naturally constant through each cell in a series configuration, the shaded cells need to perform with a reverse bias voltage to provide a current such as the illuminated cells. However, the resulting polarity of the reverse power contributes to power consumption and the decrease in the maximum output power of the partially shaded PV module.

➤ Dynamic Safety Margin

Let \mathbf{x} be the state space in \mathfrak{R}^n , and $\Phi \subseteq \mathbf{x}$ be subspace that defines the safe operation region for some system state variables $\mathbf{x} \in \mathfrak{R}^m$. Φ can be specified by a set of inequalities, $\Phi = \{\mathbf{x} \mid \varphi_i(\mathbf{x}) \leq 0, i=1, \dots, q\}$, where $\varphi_i: \mathfrak{R}^m \rightarrow \mathfrak{R}$. $\varphi_i(\mathbf{x}) > 0$ is the unsafe operation as shown in Fig. H.14, and $\partial\Phi = \{\mathbf{x} \mid \varphi_i(\mathbf{x}) = 0, i=1, \dots, q\} \subset \Phi$ is the boundary of the safe region, where variable q is the number of defined inequalities and m is the number of state variables relevant to safety. Notice that $m \leq n$, where n is the dimension of the state-space. The system trajectory starts from the initial condition, \mathbf{x}_0 , to the operating point \mathbf{x}_s crossing the state space with varying distance to the safety boundary as shown in Figure 5. In this subspace of state variables, DSM is defined as the instantaneous shortest distance, $\delta(t)$, between the current state vector, \mathbf{x} , and $\partial\Phi$. Therefore, the DSM can be obtained by solving the following quadratic programming optimization problem:

$$\min_{\mathbf{x}_p} \left\| \mathbf{x} - \mathbf{x}_p \right\|_2^2, \quad (120)$$

subject to $\mathbf{x}_p \in \partial\Phi$ and the DSM is:

$$\delta = s \ t \cdot \left\| \mathbf{x} - \mathbf{x}_{p0} \right\|_2, \quad (121)$$

where \mathbf{x}_{p0} is the solution of the previous optimization problem and:

$$s \ t = \begin{cases} +1, & \text{if } \mathbf{x} \text{ into the region of safe operation} \\ -1, & \text{if } \mathbf{x} \text{ out of the region of safe operation} \end{cases}$$

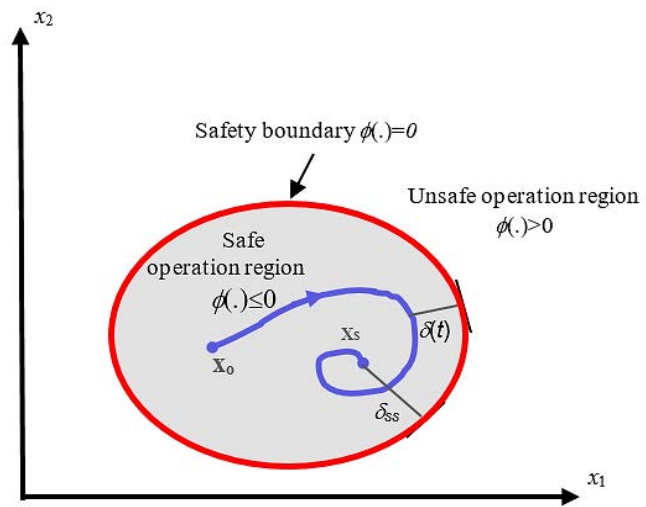


Fig. H.14 DSM definition

List of publications

1. M. Bakkar, S. Bogarra, F. Córcoles, J. Saura and M. Moreno, “Power Control Strategies During Voltage Sags According to Spanish Grid Code,” International Conference on Renewable Energies and Power Quality (ICREPQ’18), (16), Salamanca Spain, 2018, Proceeding. (Attend o the conference and represent the paper personally).
2. Rolán, A., Giménez, P., Yagüe, S., Bogarra, S., Saura, J., Bakkar, M.: “Voltage recovery influence on three-phase grid-connected inverters under voltage sags”, IET Generation, Transmission & Distribution, 2019, 13, (3), pp. 435–443.
3. M. Bakkar, S. Bogarra, A. Rolán, F. Córcoles, J. Saura, “Voltage sag influence on controlled three-phase grid-connected inverters according to the Spanish grid code,” IET generation transmission & distribution, accepted, unpublished, 2020.
4. M. Bakkar and S. Bogarra and F. Córcoles and J. Iglesias.: “Overcurrent protection based on ANNs for smart distribution networks with grid-connected VSIs”, IET Generation Transmission & Distribution, Dec. 2020, Online.
5. M. Bakkar, Ahmed Aboelhassan, M. Abdel-Geliel, and Michael Galea.: “PV Systems Control Using Fuzzy Logic Controller Employing Dynamic Safety Margin under Normal and Partial Shading Conditions”, Energies, 2021, 14, x.
6. Rolan, A.; Bogarra, S.; Bakkar, M. Integration of Distributed Energy Resources to Unbalanced Grids under Voltage Sags with Grid Code Compliance. IEEE Transactions on Smart Grid. 2021.



DEPARTAMENT D'ENGINYERIA
ELÈCTRICA



UNIVERSITAT POLITÈCNICA DE
CATALUNYA